

The ALF (Algorithms for Lattice Fermions) project release 2.4. Documentation for the auxiliary-field quantum Monte Carlo code

ALF collaboration*: F. F. Assaad^{1,2}, M. Bercx¹, F. Goth¹, A. Götz¹, J. S. Hofmann³, E. Huffman⁴, Z. Liu¹, F. Parisen Toldin¹, J. S. E. Portela¹ and J. Schwab¹

1 Institut für Theoretische Physik und Astrophysik,
Universität Würzburg, 97074 Würzburg, Germany

2 Würzburg-Dresden Cluster of Excellence ct.qmat, Am Hubland, 97074 Würzburg, Germany

3 Department of Condensed Matter Physics, Weizmann Institute of Science,
Rehovot, 76100, Israel

4 Perimeter Institute for Theoretical Physics, Waterloo, Ontario N2L 2Y5, Canada

* alf@physik.uni-wuerzburg.de

Abstract

The *Algorithms for Lattice Fermions* package provides a general code for the finite-temperature and projective auxiliary-field quantum Monte Carlo algorithm. The code is engineered to be able to simulate any model that can be written in terms of sums of single-body operators, of squares of single-body operators and single-body operators coupled to a bosonic field with given dynamics. The package includes five pre-defined model classes: SU(N) Kondo, SU(N) Hubbard, SU(N) t-V and SU(N) models with long range Coulomb repulsion on honeycomb, square and N-leg lattices, as well as Z_2 unconstrained lattice gauge theories coupled to fermionic and Z_2 matter. An implementation of the stochastic Maximum Entropy method is also provided. One can download the code from our Git instance at <https://git.physik.uni-wuerzburg.de/ALF/ALF/-/tree/ALF-2.4> and sign in to file issues.



Copyright F. F. Assaad *et al.*

This work is licensed under the Creative Commons

[Attribution-ShareAlike 4.0 International License](#).

Published by the SciPost Foundation.

Received 2023-04-16

Accepted 2025-10-10

Published 20??-??-??

[doi:10.21468/SciPostPhysCodeb.?](https://doi.org/10.21468/SciPostPhysCodeb.)



Check for
updates

1

2

3 This publication is part of a bundle: Please cite both the article and the release you used.

DOI

doi:[10.21468/SciPostPhysCodeb.?](https://doi.org/10.21468/SciPostPhysCodeb.)

doi:[10.21468/SciPostPhysCodeb.?-r?](https://doi.org/10.21468/SciPostPhysCodeb.?-r?)

Type

Article

Codebase release

4

Contents

7	1 Introduction	4
8	1.1 Motivation	4
9	1.2 Definition of the Hamiltonian	6
10	1.3 Outline and what is new	7

11	2 Auxiliary field quantum Monte Carlo: Finite temperature	8
12	2.1 Formulation of the method	8
13	2.1.1 The partition function	10
14	2.1.2 Observables	10
15	2.1.3 Reweighting and the sign problem	12
16	2.2 Updating schemes	13
17	2.2.1 Sequential single spin flips	13
18	2.2.2 Sampling of e^{-S_0}	13
19	2.2.3 Global updates in space	14
20	2.2.4 Global updates in time and space	15
21	2.2.5 Parallel tempering	16
22	2.2.6 Langevin dynamics	17
23	2.3 The Trotter error and checkerboard decomposition	21
24	2.3.1 Asymmetric Trotter decomposition	21
25	2.3.2 Symmetric Trotter decomposition	22
26	2.3.3 The Symm flag	24
27	2.4 Stabilization – A peculiarity of the BSS algorithm	24
28	3 Auxiliary field quantum Monte Carlo: Projective algorithm	26
29	3.1 Specification of the trial wave function	27
30	3.2 Some technical aspects of the projective code	28
31	3.3 Comparison of finite and projective codes	28
32	4 Monte Carlo sampling	28
33	4.1 The Jackknife resampling method	30
34	4.2 An explicit example of error estimation	31
35	4.3 Pseudocode description	32
36	5 Data structures and input/output	34
37	5.1 The Operator type	34
38	5.2 Handling of the fields: The Fields type	36
39	5.3 The Lattice and Unit_cell types	36
40	5.4 The observable types Obser_Vec and Obser_Latt	39
41	5.4.1 Scalar observables	39
42	5.4.2 Equal-time and time-displaced correlation functions	40
43	5.5 The WaveFunction type	41
44	5.6 Specification of the Hamiltonian: The Hamiltonian module	41
45	5.6.1 Flavor symmetries	45
46	5.7 File structure	46
47	5.7.1 Input files	47
48	5.7.2 Output files – Observables	48
49	6 Using the code	50
50	6.1 Quick start	51
51	6.2 Compiling and running	51
52	6.3 Error analysis	53
53	6.4 Parameter optimization	56
54	7 The plain vanilla Hubbard model on the square lattice	57
55	7.1 Defining the parameters	58
56	7.2 Setting the Hamiltonian: Ham_set	58

57	7.3	The lattice: Ham_latt	58
58	7.4	The hopping: Ham_hop	58
59	7.5	The interaction: Ham_V	59
60	7.6	The trial wave function: Ham_Trial	60
61	7.7	Observables	60
62	7.7.1	Allocating space for the observables: Alloc_obs	60
63	7.7.2	Measuring equal-time observables: Obser	61
64	7.7.3	Measuring time-displaced observables: ObserT	62
65	7.8	Flavor symmetries	63
66	7.9	Numerical precision	63
67	7.10	Running the code and testing	63
68	8	Predefined structures	64
69	8.1	Predefined lattices	64
70	8.1.1	Square lattice, Fig. 6(a)	65
71	8.1.2	Bilayer square lattice, Fig. 6(b)	66
72	8.1.3	N-leg ladder lattice, Fig. 6(c)	66
73	8.1.4	Honeycomb lattice, Fig. 6(d)	67
74	8.1.5	Bilayer honeycomb lattice, Fig. 6(e)	67
75	8.1.6	π -flux lattice (deprecated)	67
76	8.2	Generic hopping matrices on Bravais lattices	67
77	8.2.1	Setting up the hopping matrix: The Hopping_Matrix_type	68
78	8.2.2	An example: Nearest neighbor hopping on the honeycomb lattice	70
79	8.2.3	Predefined hoppings	71
80	8.3	Predefined interaction vertices	73
81	8.3.1	SU(N) Hubbard interaction	73
82	8.3.2	M_z -Hubbard interaction	74
83	8.3.3	SU(N) V-interaction	74
84	8.3.4	Fermion-Ising coupling	74
85	8.3.5	Long-range Coulomb repulsion	75
86	8.3.6	J_z - J_z interaction	75
87	8.4	Predefined observables	76
88	8.4.1	Equal-time SU(N) spin-spin correlations	76
89	8.4.2	Equal-time spin correlations	77
90	8.4.3	Equal-time Green function	78
91	8.4.4	Equal-time density-density correlations	78
92	8.4.5	Time-displaced Green function	78
93	8.4.6	Time-displaced SU(N) spin-spin correlations	78
94	8.4.7	Time-displaced spin correlations	78
95	8.4.8	Time-displaced density-density correlations	79
96	8.4.9	Dimer-dimer correlations	79
97	8.4.10	Cotunneling for Kondo models	80
98	8.4.11	Renyi entropy	81
99	8.5	Predefined trial wave functions	82
100	8.5.1	Square	82
101	8.5.2	Honeycomb	82
102	8.5.3	N-leg ladder	82
103	8.5.4	Bilayer square	83
104	8.5.5	Bilayer honeycomb	83

105	9 Model classes	83
106	9.1 SU(N) Hubbard models <code>Hamiltonian_Hubbard_smod.F90</code>	83
107	9.2 SU(N) t-V models <code>Hamiltonian_tV_smod.F90</code>	85
108	9.3 SU(N) Kondo lattice models <code>Hamiltonian_Kondo_smod.F90</code>	86
109	9.4 Models with long range Coulomb interactions <code>Hamiltonian_LRC_smod.F90</code>	89
110	9.5 Z_2 lattice gauge theories coupled to fermion and Z_2 matter <code>Hamiltonian_Z2_smod.F90</code>	90
111	9.5.1 Projective approach	93
112	9.5.2 Observables	93
113	9.5.3 A test case: Z_2 slave spin formulation of the SU(2) Hubbard model	94
115	10 Maximum entropy	95
116	10.1 Quick start	95
117	10.2 General setup	95
118	10.3 Single-particle quantities: <code>Channel=P</code>	97
119	10.4 Particle-hole quantities: <code>Channel=PH</code>	97
120	10.5 Particle-particle quantities: <code>Channel=PP</code>	99
121	10.6 Zero-temperature, projective code: <code>Channel=T0</code>	99
122	10.7 Dynamics of the one-dimensional half-filled Hubbard model	99
123	11 Conclusions and future directions	100
124	A Practical implementation of Wick decomposition of $2n$-point correlation functions of two imaginary times	101
126	B Performance, memory requirements and parallelization	102
127	C Licenses and copyrights	103
128	References	104

130 1 Introduction

131 1.1 Motivation

132 The aim of the ALF project is to provide a general formulation of the auxiliary-field QMC
133 method that enables one to promptly play with different model Hamiltonians at minimal pro-
134 gramming cost. The package also comes with a number of predefined Hamiltonians aimed at
135 producing benchmark results.

136 The auxiliary-field quantum Monte Carlo (QMC) approach is the algorithm of choice to
137 simulate thermodynamic properties of a variety of correlated electron systems in the solid state
138 and beyond [1–6]. Apart from the physics of the canonical Hubbard model [7,8], the topics one
139 can investigate in detail include correlation effects in the bulk and on surfaces of topological
140 insulators [9–12], quantum phase transitions between Dirac fermions and insulators [13–20],
141 deconfined quantum critical points [18, 21–24], constrained and unconstrained lattice gauge
142 theories [21, 25–30], heavy fermion systems [31–36], nematic [37, 38] and magnetic [39, 40]
143 quantum phase transitions in metals, antiferromagnetism in metals [41], superconductivity
144 in spin-orbit split and in topological flat bands [42–44], SU(N) symmetric models [45–50],
145 long-ranged Coulomb interactions in graphene systems [51–55], cold atomic gases [56], low
146 energy nuclear physics [57] that may require formulations in the canonical ensemble [58, 59],

147 entanglement entropies and spectra [60–66], electron-phonon systems [67–69], Landau level
 148 regularization of continuum theories [70,71], Yukawa SYK models [72] and even spin systems
 149 [73] among others. This ever-growing list of topics is based on algorithmic progress and on
 150 recent symmetry-related insights [74–77] that lead to formulations free of the negative sign
 151 problem for a number of model systems with very rich phase diagrams.

152 Auxiliary-field methods can be formulated in a number of very different ways. The fields
 153 define the configuration space \mathcal{C} . They can stem from the Hubbard-Stratonovich (HS) [78]
 154 transformation required to decouple the many-body interacting term into a sum of non-
 155 interacting problems, or they can correspond to bosonic modes with predefined dynamics
 156 such as phonons or gauge fields. In all cases, the result is that the grand-canonical partition
 157 function takes the form

$$Z = \text{Tr}(e^{-\beta \hat{\mathcal{H}}}) = \sum_{\mathcal{C}} e^{-S(\mathcal{C})}, \quad (1)$$

158 where β corresponds to the inverse temperature and S is the action of non-interacting fermions
 159 subject to a space-time fluctuating auxiliary field. The high-dimensional integration over the
 160 fields is carried out stochastically. In this formulation of many-body quantum systems, there is
 161 no reason for the action to be a real number. Thereby $e^{-S(\mathcal{C})}$ cannot be interpreted as a weight.
 162 To circumvent this problem one can adopt re-weighting schemes and sample $|e^{-S(\mathcal{C})}|$. This
 163 invariably leads to the so-called *negative sign problem*, with the associated exponential computa-
 164 tional scaling in system size and inverse temperature [79]. The sign problem is formulation
 165 dependent and, as mentioned above, there has been tremendous progress at identifying an
 166 increasing number of models not affected by the negative sign problem which cover a rich do-
 167 main of collective emergent phenomena. For continuous fields, the stochastic integrations can
 168 be carried out with Langevin dynamics or hybrid methods [80]. However, for many problems
 169 one can get away with discrete fields [81]. In this case, Monte Carlo importance sampling
 170 will often be put to use [82]. We note that due to the non-locality of the fermion determinant
 171 (see below), cluster updates, such as in the loop or stochastic series expansion algorithms for
 172 quantum spin systems [83–85], are hard to formulate for this class of problems. The search
 173 for efficient updating schemes that quickly wander through the configuration space defines
 174 ongoing challenges.

175 Formulations differ not only in the choice of the fields, continuous or discrete, and sam-
 176 pling strategy, but also by the formulation of the action itself. For a given field configuration,
 177 integrating out fermionic degrees of freedom generically leads to a fermionic determinant of
 178 dimension βN where N is the volume of the system. Working with this determinant leads to
 179 the Hirsch-Fye approach [86] and the computational effort scales¹ as $\mathcal{O}(\beta N)^3$. The Hirsch-Fye
 180 algorithm is the method of choice for impurity problems, but has in general been outperformed
 181 by a class of so-called continuous-time quantum Monte Carlo approaches [87–89]. One key
 182 advantage of continuous-time methods is being action based, allowing one to better handle
 183 the retarded interactions obtained when integrating out fermion or boson baths. However,
 184 in high dimensions or at low temperatures, the cubic scaling originating from the fermionic
 185 determinant is expensive. To circumvent this, the hybrid Monte-Carlo approach [5,90,91] ex-
 186 presses the fermionic determinant in terms of a Gaussian integral thereby introducing a new
 187 variable in the Monte Carlo integration. The resulting algorithm is the method of choice for
 188 lattice gauge theories in 3+1 dimensions and has been used to provide *ab initio* estimates of
 189 light hadron masses starting from quantum chromodynamics [92].

190 The approach we adopt lies between the above two extremes. We keep the fermionic deter-
 191 minant, but formulate the problem so as to work only with $N \times N$ matrices. This Blankenbecler,
 192 Scalapino, Sugar (BSS) algorithm scales linearly in imaginary time β , but remains cubic in the
 193 volume N . Furthermore, the algorithm can be formulated either in a projective manner [3,4],

¹Here we implicitly assume the absence of negative sign problem.

adequate to obtain zero temperature properties in the canonical ensemble, or at finite temperatures, in the grand-canonical ensemble [2]. In this documentation we summarize the essential aspects of the auxiliary-field QMC approach, and refer the reader to Refs. [6, 93] for complete reviews.

1.2 Definition of the Hamiltonian

The first and most fundamental part of the project is to define a general Hamiltonian which can accommodate a large class of models. Our approach is to express the model as a sum of one-body terms, a sum of two-body terms each written as a perfect square of a one body term, as well as a one-body term coupled to a bosonic field with dynamics to be specified by the user. Writing the interaction in terms of sums of perfect squares allows us to use generic forms of discrete approximations to the HS transformation [94, 95]. Symmetry considerations are imperative to increase the speed of the code. We therefore include a *color* index reflecting an underlying SU(N) color symmetry as well as a *flavor* index reflecting the fact that after the HS transformation, the fermionic determinant is block diagonal in this index.

The class of solvable models includes Hamiltonians $\hat{\mathcal{H}}$ that have the following general form:

$$\hat{\mathcal{H}} = \hat{\mathcal{H}}_T + \hat{\mathcal{H}}_V + \hat{\mathcal{H}}_I + \hat{\mathcal{H}}_{0,I}, \quad \text{where} \quad (2)$$

$$\hat{\mathcal{H}}_T = \sum_{k=1}^{M_T} \sum_{\sigma=1}^{N_{\text{col}}} \sum_{s=1}^{N_{\text{fl}}} \sum_{x,y} \hat{c}_{x\sigma s}^\dagger T_{xy}^{(ks)} \hat{c}_{y\sigma s} \equiv \sum_{k=1}^{M_T} \hat{T}^{(k)}, \quad (3)$$

$$\hat{\mathcal{H}}_V = \sum_{k=1}^{M_V} U_k \left\{ \sum_{\sigma=1}^{N_{\text{col}}} \sum_{s=1}^{N_{\text{fl}}} \left[\left(\sum_{x,y} \hat{c}_{x\sigma s}^\dagger V_{xy}^{(ks)} \hat{c}_{y\sigma s} \right) + \alpha_{ks} \right] \right\}^2 \equiv \sum_{k=1}^{M_V} U_k (\hat{V}^{(k)})^2, \quad (4)$$

$$\hat{\mathcal{H}}_I = \sum_{k=1}^{M_I} \hat{Z}_k \left(\sum_{\sigma=1}^{N_{\text{col}}} \sum_{s=1}^{N_{\text{fl}}} \sum_{x,y} \hat{c}_{x\sigma s}^\dagger I_{xy}^{(ks)} \hat{c}_{y\sigma s} \right) \equiv \sum_{k=1}^{M_I} \hat{Z}_k \hat{I}^{(k)}. \quad (5)$$

The indices and symbols used above have the following meaning:

- The number of fermion *flavors* is set by N_{fl} . After the HS transformation, the action will be block diagonal in the flavor index.
- The number of fermion *colors* is set² by N_{col} . The Hamiltonian is invariant under $SU(N_{\text{col}})$ rotations.
- N_{dim} is the total number of spacial vertices: $N_{\text{dim}} = N_{\text{unit-cell}} N_{\text{orbital}}$, where $N_{\text{unit-cell}}$ is the number of unit cells of the underlying Bravais lattice and N_{orbital} is the number of orbitals per unit cell.
- The indices x and y label lattice sites where $x, y = 1, \dots, N_{\text{dim}}$.
- Therefore, the matrices $T^{(ks)}$, $V^{(ks)}$ and $I^{(ks)}$ are of dimension $N_{\text{dim}} \times N_{\text{dim}}$.
- The number of interaction terms is labeled by M_V and M_I . $M_T > 1$ would allow for a checkerboard decomposition.
- $\hat{c}_{y\sigma s}^\dagger$ is a second-quantized operator that creates an electron in a Wannier state centered around lattice site y , with color σ , and flavor index s . The operators satisfy the anti-commutation relations:

$$\left\{ \hat{c}_{y\sigma s}^\dagger, \hat{c}_{y'\sigma' s'} \right\} = \delta_{yy'} \delta_{ss'} \delta_{\sigma\sigma'}, \quad \text{and} \quad \left\{ \hat{c}_{y\sigma s}, \hat{c}_{y'\sigma' s'} \right\} = 0. \quad (6)$$

²Note that in the code $N_{\text{col}} \equiv \text{N_SUN}$.

- 225 • α_{ks} is a complex number.

226 The bosonic part of the general Hamiltonian (2) is $\hat{\mathcal{H}}_{0,I} + \hat{\mathcal{H}}_I$ and has the following properties:

- 227 • \hat{Z}_k couples to a general one-body term. We will work in a basis where this operator
 228 is diagonal: $\hat{Z}_k|\phi\rangle = \phi_k|\phi\rangle$. ϕ_k is a real number or an Ising variable. Hence \hat{Z}_k can
 229 correspond to the Pauli matrix $\hat{\sigma}_z$ or to the position operator.
- 230 • The dynamics of the bosonic field is given by $\hat{\mathcal{H}}_{0,I}$. This term is not specified here; it
 231 has to be specified by the user and becomes relevant when the Monte Carlo update
 232 probability is computed in the code.

233 Note that the matrices $T^{(ks)}$, $V^{(ks)}$ and $I^{(ks)}$ explicitly depend on the flavor index s but not on
 234 the color index σ . The color index σ only appears in the second quantized operators such that
 235 the Hamiltonian is manifestly $SU(N_{\text{col}})$ symmetric. We also require the matrices $T^{(ks)}$, $V^{(ks)}$
 236 and $I^{(ks)}$ to be Hermitian.

237 1.3 Outline and what is new

238 In order to use the program, a minimal understanding of the algorithm is necessary. Its code is
 239 written in Fortran, according to the 2008 standard, and natively uses MPI (MPI 3.0 compliant
 240 implementation needed) for parallel runs on supercomputing systems. In this documentation
 241 we aim to present in enough detail both the algorithm and its implementation to allow the
 242 user to confidently use and modify the program.

243 In Sec. 2, we summarize the steps required to formulate the many-body, imaginary-time
 244 propagation in terms of a sum over HS and bosonic fields of one-body, imaginary-time propa-
 245 gators. To simulate a model not already included in ALF, the user has to provide this one-body,
 246 imaginary-time propagator for a given configuration of HS and bosonic fields. In this section
 247 we also touch on how to compute observables and on how we deal with the negative sign
 248 problem. Since version 2.0, ALF has a number of new updating schemes. The package comes
 249 with the possibility to implement global updates in space and time or only in space; we provide
 250 parallel-tempering and Langevin dynamics options; and it is possible to implement symmetric
 251 Trotter decompositions. At the end of the section we comment on the issue of stabilization for
 252 the finite temperature code.

253 In Sec. 3, we describe the projective version of the algorithm, constructed to produce
 254 ground state properties. One can very easily switch between projective and finite tempera-
 255 ture codes, but a trial wave function must be provided for the projective algorithm.

256 One of the key challenges in Monte Carlo methods is to adequately evaluate the stochastic
 257 error. In Sec. 4 we provide an explicit example of how to correctly estimate the error.

258 Section 5 is devoted to the data structures that are needed to implement the model, as
 259 well as to the input and output file structure. The data structures include an `Operator` type
 260 to optimally work with sparse Hermitian matrices, a `Lattice` type to define one- and two-
 261 dimensional Bravais lattices, a generic `Fields` type for the auxiliary fields, two `Observable`
 262 types to handle scalar observables (e.g., total energy) and equal-time or time-displaced two-
 263 point correlation functions (e.g., spin-spin correlations) and finally a `Wavefunction` type to
 264 define the trial wave function in the projective code. At the end of this section we comment
 265 on the file structure.

266 In Sec. 6 we provide details on running the code using the shell. As an alternative the user
 267 can download a separate project, `pyALF` that provides a convenient python interface as well
 268 as Jupyter notebooks.

269 The package has a set of predefined structures that allow easy reuse of lattices, observables,
 270 interactions and trial wave functions. Although convenient, this extra layer of abstraction

271 might render ALF harder to modify. To circumvent this we make available an implementation
 272 of a plain vanilla Hubbard model on the square lattice (see Sec. 7) that shows explicitly how
 273 to implement this basic model without making use of predefined structures. We believe that
 274 this is a good starting point to modify a Hamiltonian from scratch, as exemplified in the pack-
 275 age's [Tutorial](#). Yet another possible starting point is provided by the template Hamiltonian
 276 `Hamiltonian_##NAME##_smod.F90`

277 Sec. 8 introduces the sets of predefined lattices, hopping matrices, interactions, observables
 278 and trial wave functions available. The goal here is to provide a library so as to facilitate
 279 implementation of new Hamiltonians.

280 The package comes with a set of Hamiltonians, described in Sec. 9, which includes: (i)
 281 SU(N) Hubbard models, (ii) SU(N) t-V models, (iii) SU(N) Kondo lattice models, (iv) Models
 282 with long ranged coulomb interactions, and (v) Generic Z_2 lattice gauge theories coupled to
 283 Z_2 matter and fermions. These model classes are built on the predefined structures.

284 In Sec. 10 we describe how to use our implementation of the stochastic analytical continuation
 285 [[96, 97](#)].

286 Finally, in Sec. 11 we list a number of features being considered for future releases of the
 287 ALF package.

288 2 Auxiliary field quantum Monte Carlo: Finite temperature

289 We start this section by deriving the detailed form of the partition function and outlining
 290 the computation of observables (Sec. 2.1.1 - 2.1.3). Next, we present a number of update
 291 strategies, namely local updates, global updates, parallel tempering and Langevin dynamics
 292 (Sec. 2.2). We then discuss the Trotter error, both for symmetric and asymmetric decomposi-
 293 tions (Sec. 2.3) and, finally, we describe the measures we have implemented to make the code
 294 numerically stable (Sec. 2.4).

295 2.1 Formulation of the method

296 Our aim is to compute observables for the general Hamiltonian (2) in thermodynamic equilib-
 297 rium as described by the grand-canonical ensemble. We show below how the grand-canonical
 298 partition function can be rewritten as

$$Z = \text{Tr}\left(e^{-\beta \hat{\mathcal{H}}}\right) = \sum_C e^{-S(C)} + \mathcal{O}(\Delta\tau^2), \quad (7)$$

299 and define the space of configurations C . Note that the chemical potential term is already
 300 included in the definition of the one-body term $\hat{\mathcal{H}}_T$, see Eq. (3), of the general Hamiltonian.
 301 The essential ingredients of the auxiliary-field quantum Monte Carlo implementation in the
 302 ALF package are the following:

- 303 • We discretize the imaginary time propagation: $\beta = \Delta\tau L_{\text{Trotter}}$. Generically this intro-
 304 duces a systematic Trotter error of $\mathcal{O}(\Delta\tau)^2$ [[98](#)]. We note that there has been consid-
 305 erable effort at getting rid of the Trotter systematic error and to formulate a genuine
 306 continuous-time BSS algorithm [[99](#)]. To date, efforts in this direction that are based
 307 on a CT-AUX type formulation [[100, 101](#)] face two issues. The first one is that they are
 308 restricted to a class of models with Hubbard-type interactions

$$(\hat{n}_i - 1)^2 = (\hat{n}_i - 1)^4, \quad (8)$$

309 in order for the basic CT-AUX equation [[102](#)],

$$1 + \frac{U}{K} (\hat{n}_i - 1)^2 = \frac{1}{2} \sum_{s=\pm 1} e^{as(\hat{n}_i - 1)}, \quad \text{with } \frac{U}{K} = \cosh(\alpha) - 1, \quad \text{and } K \in \mathbb{R}, \quad (9)$$

310 to hold. The second issue is that it is hard to formulate a computationally efficient
 311 algorithm. Given this situation, if eliminating the Trotter systematic error is required, it
 312 turns out that extrapolating to small imaginary-time steps using the multi-grid method
 313 [103–105] is a more efficient scheme.

314 There has also been progress in efficient continuous-time methods using techniques that
 315 draw from the Stochastic Series Expansion [106] which can be combined with fermion
 316 bag ideas [107]. However, these techniques are even more restricted to a specific class of
 317 Hamiltonians, those that can be expressed as sums of exponentiated fermionic bilinear
 318 terms $\hat{H} = \sum_i \hat{h}^{(i)}$, where

$$\hat{h}^{(i)} = -\gamma^{(i)} e^{\sum_{jk} a_{jk}^{(i)} \hat{c}_j^\dagger \hat{c}_k + \text{H.c.}}. \quad (10)$$

319 Stabilization can also be costly depending on the parameters, particularly for large α
 320 values [108].

- 321 Having isolated the two-body term, we apply Gauß-Hermite quadrature [109] to the
 322 continuous HS transform and obtain the discrete HS transformation [94, 95]:

$$e^{\Delta\tau\lambda\hat{A}^2} = \frac{1}{4} \sum_{l=\pm 1, \pm 2} \gamma(l) e^{\sqrt{\Delta\tau\lambda}\eta(l)\hat{A}} + \mathcal{O}((\Delta\tau\lambda)^4), \quad (11)$$

323 where the fields η and γ take the values:

$$\begin{aligned} \gamma(\pm 1) &= 1 + \sqrt{6}/3, & \eta(\pm 1) &= \pm \sqrt{2(3 - \sqrt{6})}, \\ \gamma(\pm 2) &= 1 - \sqrt{6}/3, & \eta(\pm 2) &= \pm \sqrt{2(3 + \sqrt{6})}. \end{aligned} \quad (12)$$

324 Since the Trotter error is already of order $(\Delta\tau^2)$ per time slice, this transformation is
 325 next to exact. One can relate the expectation value of the field $\eta(l)$ to the operator \hat{A} by
 326 noting that:

$$\begin{aligned} \frac{1}{4} \sum_{l=\pm 1, \pm 2} \gamma(l) e^{\sqrt{\Delta\tau\lambda}\eta(l)\hat{A}} \left(\frac{\eta(l)}{2\sqrt{\Delta\tau\lambda}} \right) &= e^{\Delta\tau\lambda\hat{A}^2} \hat{A} + \mathcal{O}((\Delta\tau\lambda)^3), \quad \text{and} \\ \frac{1}{4} \sum_{l=\pm 1, \pm 2} \gamma(l) e^{\sqrt{\Delta\tau\lambda}\eta(l)\hat{A}} \left(\frac{(\eta(l))^2 - 2}{4\Delta\tau\lambda} \right) &= e^{\Delta\tau\lambda\hat{A}^2} \hat{A}^2 + \mathcal{O}((\Delta\tau\lambda)^2). \end{aligned} \quad (13)$$

- 327 \hat{Z}_k in Eq. (5) can stand for a variety of operators, such as the Pauli matrix $\hat{\sigma}_z$ – in
 328 which case the Ising spins take the values $s_k = \pm 1$ – or the position operator – such
 329 that $\hat{Z}_k|\phi\rangle = \phi_k|\phi\rangle$, with ϕ_k a real number.
- 330 From the above it follows that the Monte Carlo configuration space C is given by the
 331 combined spaces of bosonic configurations and of HS discrete field configurations:

$$C = \{\phi_{i,\tau}, l_{j,\tau}, \text{ with } i = 1 \cdots M_I, j = 1 \cdots M_V, \tau = 1 \cdots L_{\text{Trotter}}\}. \quad (14)$$

332 Here, the HS fields take the values $l_{j,\tau} = \pm 2, \pm 1$ and $\phi_{i,\tau}$ may, for instance, be a continuous
 333 real field or, if $\hat{Z}_k = \hat{\sigma}_z$, be restricted to ± 1 .

334 **2.1.1 The partition function**

335 With the above, the partition function of the model (2) can be written as follows.

$$\begin{aligned} Z &= \text{Tr}\left(e^{-\beta \hat{\mathcal{H}}}\right) \\ &= \text{Tr}\left[e^{-\Delta\tau \hat{\mathcal{H}}_{0,I}} \prod_{k=1}^{M_V} e^{-\Delta\tau U_k (\hat{V}^{(k)})^2} \prod_{k=1}^{M_I} e^{-\Delta\tau \hat{\sigma}_k \hat{f}^{(k)}} \prod_{k=1}^{M_T} e^{-\Delta\tau \hat{T}^{(k)}}\right]^{L_{\text{Trotter}}} + \mathcal{O}(\Delta\tau^2) \\ &= \sum_C \left(\prod_{k=1}^{M_V} \prod_{\tau=1}^{L_{\text{Trotter}}} \gamma_{k,\tau} \right) e^{-S_0(\{s_{i,\tau}\})} \\ &\quad \times \text{Tr}_F \left\{ \prod_{\tau=1}^{L_{\text{Trotter}}} \left[\prod_{k=1}^{M_V} e^{\sqrt{-\Delta\tau U_k} \eta_{k,\tau} \hat{V}^{(k)}} \prod_{k=1}^{M_I} e^{-\Delta\tau s_{k,\tau} \hat{f}^{(k)}} \prod_{k=1}^{M_T} e^{-\Delta\tau \hat{T}^{(k)}} \right] \right\} + \mathcal{O}(\Delta\tau^2). \end{aligned} \quad (15)$$

336 In the above, the trace Tr runs over the bosonic and fermionic degrees of freedom, and Tr_F
 337 only over the fermionic Fock space. $S_0(\{s_{i,\tau}\})$ is the action corresponding to the bosonic
 338 Hamiltonian, and is only dependent on the bosonic fields so that it can be pulled out of the
 339 fermionic trace. We have adopted the shorthand notation $\eta_{k,\tau} \equiv \eta(l_{k,\tau})$ and $\gamma_{k,\tau} \equiv \gamma(l_{k,\tau})$. At
 340 this point, and since for a given configuration C we are dealing with a free propagation, we
 341 can integrate out the fermions to obtain a determinant:

$$\begin{aligned} \text{Tr}_F \left\{ \prod_{\tau=1}^{L_{\text{Trotter}}} \left[\prod_{k=1}^{M_V} e^{\sqrt{-\Delta\tau U_k} \eta_{k,\tau} \hat{V}^{(k)}} \prod_{k=1}^{M_I} e^{-\Delta\tau s_{k,\tau} \hat{f}^{(k)}} \prod_{k=1}^{M_T} e^{-\Delta\tau \hat{T}^{(k)}} \right] \right\} &= \prod_{s=1}^{N_{\text{fl}}} \left[e^{\sum_{k=1}^{M_V} \sum_{\tau=1}^{L_{\text{Trotter}}} \sqrt{-\Delta\tau U_k} \alpha_{k,s} \eta_{k,\tau}} \right]^{N_{\text{col}}} \\ &\times \prod_{s=1}^{N_{\text{fl}}} \left[\det \left(1 + \prod_{\tau=1}^{L_{\text{Trotter}}} \prod_{k=1}^{M_V} e^{\sqrt{-\Delta\tau U_k} \eta_{k,\tau} V^{(ks)}} \prod_{k=1}^{M_I} e^{-\Delta\tau s_{k,\tau} I^{(ks)}} \prod_{k=1}^{M_T} e^{-\Delta\tau T^{(ks)}} \right) \right]^{N_{\text{col}}}, \end{aligned} \quad (16)$$

342 where the matrices $T^{(ks)}$, $V^{(ks)}$, and $I^{(ks)}$ define the Hamiltonian [Eq. (2) - (5)]. All in all, the
 343 partition function is given by:

$$\begin{aligned} Z &= \sum_C e^{-S_0(\{s_{i,\tau}\})} \left(\prod_{k=1}^{M_V} \prod_{\tau=1}^{L_{\text{Trotter}}} \gamma_{k,\tau} \right) e^{N_{\text{col}} \sum_{s=1}^{N_{\text{fl}}} \sum_{k=1}^{M_V} \sum_{\tau=1}^{L_{\text{Trotter}}} \sqrt{-\Delta\tau U_k} \alpha_{k,s} \eta_{k,\tau}} \\ &\quad \times \prod_{s=1}^{N_{\text{fl}}} \left[\det \left(1 + \prod_{\tau=1}^{L_{\text{Trotter}}} \prod_{k=1}^{M_V} e^{\sqrt{-\Delta\tau U_k} \eta_{k,\tau} V^{(ks)}} \prod_{k=1}^{M_I} e^{-\Delta\tau s_{k,\tau} I^{(ks)}} \prod_{k=1}^{M_T} e^{-\Delta\tau T^{(ks)}} \right) \right]^{N_{\text{col}}} + \mathcal{O}(\Delta\tau^2) \\ &\equiv \sum_C e^{-S(C)} + \mathcal{O}(\Delta\tau^2). \end{aligned} \quad (17)$$

344 In the above, one notices that the weight factorizes in the flavor index. The color index raises
 345 the determinant to the power N_{col} . This corresponds to an explicit $SU(N_{\text{col}})$ symmetry for each
 346 configuration. This symmetry is manifest in the fact that the single particle Green functions
 347 are color independent, again for each given configuration C .

348 **2.1.2 Observables**

349 In the auxiliary-field QMC approach, the single-particle Green function plays a crucial role.
 350 It determines the Monte Carlo dynamics and is used to compute observables. Consider the
 351 observable:

$$\langle \hat{O} \rangle = \frac{\text{Tr}[e^{-\beta \hat{H}} \hat{O}]}{\text{Tr}[e^{-\beta \hat{H}}]} = \sum_C P(C) \langle \langle \hat{O} \rangle \rangle_{(C)}, \quad \text{where } P(C) = \frac{e^{-S(C)}}{\sum_C e^{-S(C)}}, \quad (18)$$

and $\langle\langle \hat{O} \rangle\rangle_{(C)}$ denotes the observed value of \hat{O} for a given configuration C . For a given configuration C one can use Wick's theorem to compute $O(C)$ from the knowledge of the single-particle Green function:

$$G(x, \sigma, s, \tau | x', \sigma', s', \tau') = \langle\langle \mathcal{T} \hat{c}_{x\sigma s}(\tau) \hat{c}_{x'\sigma' s'}^\dagger(\tau') \rangle\rangle_C, \quad (19)$$

where \mathcal{T} denotes the imaginary-time ordering operator. The corresponding equal-time quantity reads

$$G(x, \sigma, s, \tau | x', \sigma', s', \tau) = \langle\langle \hat{c}_{x\sigma s}(\tau) \hat{c}_{x'\sigma' s'}^\dagger(\tau) \rangle\rangle_C. \quad (20)$$

Since, for a given HS field, translation invariance in imaginary-time is broken, the Green function has an explicit τ and τ' dependence. On the other hand it is diagonal in the flavor index, and independent of the color index. The latter reflects the explicit SU(N) color symmetry present at the level of individual HS configurations. As an example, one can show that the equal-time Green function at $\tau = 0$ reads [6]:

$$G(x, \sigma, s, 0 | x', \sigma, s, 0) = \left(\mathbb{1} + \prod_{\tau=1}^{L_{\text{Trotter}}} B_\tau^{(s)} \right)_{x, x'}^{-1}, \quad (21)$$

with

$$B_\tau^{(s)} = \prod_{k=1}^{M_V} e^{\sqrt{-\Delta\tau U_k} \eta_{k,\tau}} V^{(ks)} \prod_{k=1}^{M_I} e^{-\Delta\tau s_{k,\tau} I^{(ks)}} \prod_{k=1}^{M_T} e^{-\Delta\tau T^{(ks)}}. \quad (22)$$

To compute equal-time, as well as time-displaced observables, one can make use of Wick's theorem. A convenient formulation of this theorem for QMC simulations reads:

$$\begin{aligned} & \langle\langle \mathcal{T} \hat{c}_{\underline{x}_1}^\dagger(\tau_1) \hat{c}_{\underline{x}'_1}(\tau'_1) \cdots \hat{c}_{\underline{x}_n}^\dagger(\tau_n) \hat{c}_{\underline{x}'_n}(\tau'_n) \rangle\rangle_C \\ &= \det \begin{bmatrix} \langle\langle \mathcal{T} \hat{c}_{\underline{x}_1}^\dagger(\tau_1) \hat{c}_{\underline{x}'_1}(\tau'_1) \rangle\rangle_C & \langle\langle \mathcal{T} \hat{c}_{\underline{x}_1}^\dagger(\tau_1) \hat{c}_{\underline{x}'_2}(\tau'_2) \rangle\rangle_C & \dots & \langle\langle \mathcal{T} \hat{c}_{\underline{x}_1}^\dagger(\tau_1) \hat{c}_{\underline{x}'_n}(\tau'_n) \rangle\rangle_C \\ \langle\langle \mathcal{T} \hat{c}_{\underline{x}_2}^\dagger(\tau_2) \hat{c}_{\underline{x}'_1}(\tau'_1) \rangle\rangle_C & \langle\langle \mathcal{T} \hat{c}_{\underline{x}_2}^\dagger(\tau_2) \hat{c}_{\underline{x}'_2}(\tau'_2) \rangle\rangle_C & \dots & \langle\langle \mathcal{T} \hat{c}_{\underline{x}_2}^\dagger(\tau_2) \hat{c}_{\underline{x}'_n}(\tau'_n) \rangle\rangle_C \\ \vdots & \vdots & \ddots & \vdots \\ \langle\langle \mathcal{T} \hat{c}_{\underline{x}_n}^\dagger(\tau_n) \hat{c}_{\underline{x}'_1}(\tau'_1) \rangle\rangle_C & \langle\langle \mathcal{T} \hat{c}_{\underline{x}_n}^\dagger(\tau_n) \hat{c}_{\underline{x}'_2}(\tau'_2) \rangle\rangle_C & \dots & \langle\langle \mathcal{T} \hat{c}_{\underline{x}_n}^\dagger(\tau_n) \hat{c}_{\underline{x}'_n}(\tau'_n) \rangle\rangle_C \end{bmatrix}. \end{aligned} \quad (23)$$

Here, we have defined the super-index $\underline{x} = \{x, \sigma, s\}$.

Wick's theorem can be also used to express a reduced density matrix, i.e., the density matrix for a subsystem, in terms of its correlations [110]. Within the framework of Auxiliary-Field QMC, this allows to express a reduced density matrix $\hat{\rho}_A$ for a subsystem A as [60]

$$\hat{\rho}_A = \sum_C P(C) \det(\mathbb{1} - G_A(\tau_0; C)) e^{-c_{\underline{x}, \underline{x}'}^\dagger H^{(A)} c_{\underline{x}, \underline{x}'}}, \quad H^{(A)} \equiv \ln \left\{ \left[(G_A(\tau_0; C))^T \right]^{-1} - \mathbb{1} \right\}, \quad (24)$$

where $G_A(\tau_0; C)$ is the equal-time Green's function matrix restricted on the subsystem A and at a given time-slice τ_0 . In Eq. (24) an implicit summation over repeated indexes $\underline{x}, \underline{x}' \in A$ is assumed. Interestingly, Eq. (24) holds also when A is the entire system: in this case, it provides an alternative expression for the density matrix, or the (normalized) partition function, as a superposition of Gaussian operators. Eq. (24) is the starting point for computing the entanglement Hamiltonian [64] and the Rényi entropies [60, 62, 63]. A short review on various computational approaches to quantum entanglement in interacting fermionic models can be found in Ref. [66]. ALF provides predefined observables to compute the second Rényi entropy and its associated mutual information, see Sec. 8.4.11.

In Sec. 8.4 we describe the equal-time and time-displaced correlation functions that come predefined in ALF. Using the above formulation of Wick's theorem, arbitrary correlation functions can be computed (see Appendix A). We note, however, that the program is limited to the calculation of observables that contain only two different imaginary times.

382 2.1.3 Reweighting and the sign problem

383 In general, the action $S(C)$ will be complex, thereby inhibiting a direct Monte Carlo sampling
 384 of $P(C)$. This leads to the infamous sign problem. The sign problem is formulation dependent
 385 and as noted above, much progress has been made at understanding the class of models that
 386 can be formulated without encountering this problem [74–77]. When the average sign is not
 387 too small, we can nevertheless compute observables within a reweighting scheme. Here we
 388 adopt the following scheme. First note that the partition function is real such that:

$$Z = \sum_C e^{-S(C)} = \sum_C \overline{e^{-S(C)}} = \sum_C \operatorname{Re}[e^{-S(C)}]. \quad (25)$$

389 Thereby³ and with the definition

$$\operatorname{sgn}(C) = \frac{\operatorname{Re}[e^{-S(C)}]}{|\operatorname{Re}[e^{-S(C)}]|}, \quad (26)$$

390 the computation of the observable [Eq. (18)] is re-expressed as follows:

$$\begin{aligned} \langle \hat{O} \rangle &= \frac{\sum_C e^{-S(C)} \langle \langle \hat{O} \rangle \rangle_{(C)}}{\sum_C e^{-S(C)}} \\ &= \frac{\sum_C \operatorname{Re}[e^{-S(C)}] \frac{e^{-S(C)}}{|\operatorname{Re}[e^{-S(C)}]|} \langle \langle \hat{O} \rangle \rangle_{(C)}}{\sum_C \operatorname{Re}[e^{-S(C)}]} \\ &= \frac{\left\{ \sum_C |\operatorname{Re}[e^{-S(C)}]| \operatorname{sgn}(C) \frac{e^{-S(C)}}{|\operatorname{Re}[e^{-S(C)}]|} \langle \langle \hat{O} \rangle \rangle_{(C)} \right\} / \sum_C |\operatorname{Re}[e^{-S(C)}]|}{\left\{ \sum_C |\operatorname{Re}[e^{-S(C)}]| \operatorname{sgn}(C) \right\} / \sum_C |\operatorname{Re}[e^{-S(C)}]|} \\ &= \frac{\langle \operatorname{sgn} \frac{e^{-S}}{|\operatorname{Re}[e^{-S}]|} \langle \langle \hat{O} \rangle \rangle \rangle_{\bar{P}}}{\langle \operatorname{sgn} \rangle_{\bar{P}}}. \end{aligned} \quad (27)$$

391 The average sign is

$$\langle \operatorname{sgn} \rangle_{\bar{P}} = \frac{\sum_C |\operatorname{Re}[e^{-S(C)}]| \operatorname{sgn}(C)}{\sum_C |\operatorname{Re}[e^{-S(C)}]|}, \quad (28)$$

392 and we have $\langle \operatorname{sgn} \rangle_{\bar{P}} \in \mathbb{R}$ per definition. The Monte Carlo simulation samples the probability
 393 distribution

$$\bar{P}(C) = \frac{|\operatorname{Re}[e^{-S(C)}]|}{\sum_C |\operatorname{Re}[e^{-S(C)}]|}, \quad (29)$$

394 such that the nominator and denominator of Eq. (27) can be computed.

395 Notice that, for the Langevin updating scheme with variable Langevin time step, a straight-
 396 forward generalization of the equations above is used, see Sec. 2.2.6.

397 The negative sign problem is still an issue because the average sign is a ratio of two partition
 398 functions and one can argue that

$$\langle \operatorname{sgn} \rangle_{\bar{P}} \propto e^{-\Delta N \beta}, \quad (30)$$

399 where Δ is an intensive positive quantity and $N\beta$ denotes the Euclidean volume. In a Monte
 400 Carlo simulation the error scales as $1/\sqrt{T_{\text{CPU}}}$ where T_{CPU} corresponds to the computational

³The attentive reader will have noticed that for arbitrary Trotter decompositions, the imaginary time propagator is not necessarily Hermitian. Thereby, the above equation is correct only up to corrections stemming from the controlled Trotter systematic error.

401 time. Since the error on the average sign has to be much smaller than the average sign itself,
 402 one sees that:

$$T_{\text{CPU}} \gg e^{2\Delta N \beta}. \quad (31)$$

403 Two comments are in order. First, the presence of a sign problem invariably leads to an ex-
 404 ponential increase of CPU time as a function of the Euclidean volume. And second, Δ is
 405 formulation dependent. For instance, at finite doping, the SU(2) invariant formulation of the
 406 Hubbard model presented in Sec. 9.1 has a much more severe sign problem than the formu-
 407 lation (presented in the same section) where the HS field couples to the z -component of the
 408 magnetization. Optimization schemes minimize Δ have been put forward in [111, 112].

409 2.2 Updating schemes

410 The program allows for different types of updating schemes, which are described below and
 411 summarized in Tab. 1. With the exception of Langevin dynamics, for a given configuration C ,
 412 we propose a new one, C' , with a given probability $T_0(C \rightarrow C')$ and accept it according to the
 413 Metropolis-Hastings acceptance-rejection probability,

$$P(C \rightarrow C') = \min \left(1, \frac{T_0(C' \rightarrow C)W(C')}{T_0(C \rightarrow C')W(C)} \right), \quad (32)$$

414 so as to guarantee the stationarity condition. Here, $W(C) = |\text{Re}[e^{-S(C)}]|$.

415 Predicting how efficient a certain Monte Carlo update scheme will turn out to be for a
 416 given simulation is very hard, so one must typically resort to testing to find out which option
 417 produces best results. Methods to optimize the acceptance of global moves include Hybrid
 418 Monte Carlo [80] as well as self-learning techniques [113, 114]. Langevin dynamics stands
 419 apart, and as we will see does not depend on the Metropolis-Hastings acceptance-rejection
 420 scheme.

421 2.2.1 Sequential single spin flips

422 The program adopts per default a sequential, single spin-flip strategy. It will visit sequentially
 423 each HS field in the space-time operator list and propose a spin flip. Consider the Ising spin
 424 $s_{i,\tau}$. By default (`Propose_S0=.false.`), we will flip it with probability 1, such that for this
 425 local move the proposal matrix is symmetric. If we are considering the HS field $l_{i,\tau}$ we will
 426 propose with probability 1/3 one of the other three possible fields. For a continuous field, we
 427 modify it with a box distribution of width `Amplitude` centered around the origin. The default
 428 value of `Amplitude` is set to unity. These updating rules are defined in the `Fields_mod.F90`
 429 module (see Sec. 5.2). Again, for these local moves, the proposal matrix is symmetric. Hence
 430 in all cases we will accept or reject the move according to

$$P(C \rightarrow C') = \min \left(1, \frac{W(C')}{W(C)} \right). \quad (33)$$

431 This default updating scheme can be overruled by, e.g., setting `Global_tau_moves` to
 432 `.true.` and not setting `Nt_sequential_start` and `Nt_sequential_end` (see Sec. 5.7.1).
 433 It is also worth noting that this type of sequential spin-flip updating does not satisfy detailed
 434 balance, but rather the more fundamental stationarity condition [82].

435 2.2.2 Sampling of e^{-S_0}

436 The package can also propose single spin-flip updates according to a non-vanishing free
 437 bosonic action $S_0(C)$. This sampling scheme is used if the logical variable `Propose_S0` is
 438 set to `.true..` As mentioned previously, this option only holds for Ising variables.

Table 1: Variables required to control the updating scheme. Per default the program carries out sequential, single spin-flip sweeps, and logical variables are set to `.false.`.

Updating schemes	Type	Description
Sequential	logical	(internal variable) If true, the configurations moves through sequential, single spin flips
Propose_S0	logical	If true, proposes sequential local moves according to the probability e^{-S_0} , where S_0 is the free Ising action. This option only works for type=1 operator where the field corresponds to an Ising variable
Global_tau_moves	logical	Whether to carry out global moves on a single time slice. For a given time slice the user can define which part of the operator string is to be computed sequentially. This is specified by the variable <code>N_sequential_start</code> and <code>N_sequential_end</code> . A number of <code>N_tau_Global</code> user-defined global moves on the given time slice will then be carried out
Global_moves	logical	If true, allows for global moves in space and time. A user-defined number <code>N_Global</code> of global moves in space and time will be carried out at the end of each sweep
Langevin	logical	If true, Langevin dynamics is used exclusively (i.e., can only be used in association with tempering)
Tempering	Compiling option	Requires MPI and runs the code in a parallel tempering mode, also see Sec. 2.2.5, 6.2

439 Consider an Ising spin at space-time i, τ in the configuration C . Flipping this spin generates
 440 the configuration C' and we propose this move according to

$$T_0(C \rightarrow C') = \frac{e^{-S_0(C')}}{e^{-S_0(C')} + e^{-S_0(C)}} = 1 - \frac{1}{1 + e^{-S_0(C')}/e^{-S_0(C)}}. \quad (34)$$

441 Note that the function `S0` in the `Hamiltonian_Hubbard_include.h` module computes pre-
 442 cisely the ratio $e^{-S_0(C')}/e^{-S_0(C)}$, therefore $T_0(C \rightarrow C')$ is obtained without any additional cal-
 443 culation. The proposed move is accepted with the probability:

$$P(C \rightarrow C') = \min\left(1, \frac{e^{-S_0(C)}W(C')}{e^{-S_0(C')}W(C)}\right). \quad (35)$$

444 Note that, as can be seen from Eq. (17), the bare action $S_0(C)$ determining the dynamics of the
 445 bosonic configuration in the absence of coupling to the fermions does not enter the Metropolis
 446 acceptance-rejection step.

447 2.2.3 Global updates in space

448 This option allows one to carry out user-defined global moves on a single time slice. This
 449 option is enabled by setting the logical variable `Global_tau_moves` to `.true.`. Recall that
 450 the propagation over a time step $\Delta\tau$ (see Eq. 22) can be written as:

$$e^{-V_{M_I+M_V}(s_{M_I+M_V,\tau})} \dots e^{-V_1(s_{1,\tau})} \prod_{k=1}^{M_T} e^{-\Delta\tau T^{(k)}}, \quad (36)$$

451 where $e^{-V_n(s_n)}$ denotes one element of the operator list containing the HS fields. One
 452 can provide an interval of indices, [Nt_sequential_start, Nt_sequential_end], in
 453 which the operators will be updated sequentially. Setting Nt_sequential_start = 1 and
 454 Nt_sequential_end = $M_I + M_V$ reproduces the sequential single spin flip strategy of the
 455 above section.

456 The variable N_tau_Global sets the number of global moves carried out on each time slice
 457 ntau. Each global move is generated in the routine Global_move_tau, which is provided
 458 by the user in the Hamiltonian file. In order to define this move, one specifies the following
 459 variables:

- 460 • Flip_length: An integer stipulating the number of spins to be flipped.
- 461 • Flip_list(1:Flip_length): Integer array containing the indices of the operators to
 462 be flipped.
- 463 • Flip_value(1:Flip_length): Flip_value(n) is an integer containing the new
 464 value of the HS field for the operator Flip_list(n).
- 465 • T0_Proposal_ratio: Real number containing the quotient

$$\frac{T_0(C' \rightarrow C)}{T_0(C \rightarrow C')}, \quad (37)$$

466 where C' denotes the new configuration obtained by flipping the spins specified in the
 467 Flip_list array. Since we allow for a stochastic generation of the global move, it may
 468 very well be that no change is proposed. In this case, T0_Proposal_ratio takes the
 469 value 0 upon exit of the routine Global_move_tau and no update is carried out.

- 470 • S0_ratio: Real number containing the ratio $e^{-S_0(C')}/e^{-S_0(C)}$.

471 2.2.4 Global updates in time and space

472 The code allows for global updates as well. The user must then provide two additional func-
 473 tions (see Hamiltonian_Hubbard_include.h): Global_move and Delta_S0_global(
 474 Nsigma_old).

475 The subroutine Global_move(T0_Proposal_ratio,nsigma_old,size_clust) pro-
 476 poses a global move. Its single input is the variable nsigma_old of type Field (see
 477 Section 5.2) that contains the full configuration C stored in nsigma_old%f(M_V + M_I,
 478 Ltrot). On output, the new configuration C' , determined by the user, is stored in the two-
 479 dimensional array nsigma, which is a global variable declared in the Hamiltonian module.
 480 Like for the global move in space (Sec. 2.2.3), T0_Proposal_ratio contains the proposal
 481 ratio $\frac{T_0(C' \rightarrow C)}{T_0(C \rightarrow C')}$. Since we allow for a stochastic generation of the global move, it may very well
 482 be that no change is proposed. In this case, T0_Proposal_ratio takes the value 0 upon
 483 exit, and nsigma=nsigma_old. The real-valued size_clust gives the size of the proposed
 484 move (e.g., $\frac{\text{Number of flipped spins}}{\text{Total number of spins}}$). This is used to calculate the average sizes of proposed and ac-
 485 cepted moves, which are printed in the info file. The variable size_clust is not necessary
 486 for the simulation, but may help the user to estimate the effectiveness of the global update.

487 In order to compute the acceptance-rejection ratio, the user must also provide a function
 488 Delta_S0_global(nsigma_old) that computes the ratio $e^{-S_0(C')}/e^{-S_0(C)}$. Again, the con-
 489 figuration C' is given by the field nsigma.

490 The variable N_Global determines the number of global updates performed per sweep.
 491 Note that global updates are expensive, since they require a complete recalculation of the
 492 weight.

493 **2.2.5 Parallel tempering**

494 Exchange Monte Carlo [115], or parallel tempering [116], is a possible route to overcome
 495 sampling issues in parts of the parameter space. Let h be a parameter which one can vary
 496 without altering the configuration space $\{C\}$ and let us assume that for some values of h one
 497 encounters sampling problems. For example, in the realm of spin glasses, h could correspond
 498 to the inverse temperature. Here at high temperatures the phase space is easily sampled,
 499 but at low temperatures simulations get stuck in local minima. For quantum systems, h could
 500 trigger a quantum phase transition where sampling issues are encountered, for example, in the
 501 ordered phase and not in the disordered one. As its name suggests, parallel tempering carries
 502 out in parallel simulations at consecutive values of h : h_1, h_2, \dots, h_n , with $h_1 < h_2 < \dots < h_n$.
 503 One will sample the extended ensemble:

$$P([h_1, C_1], [h_2, C_2], \dots, [h_n, C_n]) = \frac{W(h_1, C_1)W(h_2, C_2)\cdots W(h_n, C_n)}{\sum_{C_1, C_2, \dots, C_n} W(h_1, C_1)W(h_2, C_2)\cdots W(h_n, C_n)}, \quad (38)$$

504 where $W(h, C)$ corresponds to the weight for a given value of h and configuration C . Clearly,
 505 one can sample $P([h_1, C_1], [h_2, C_2], \dots, [h_n, C_n])$ by carrying out n independent runs. How-
 506 ever, parallel tempering includes the following exchange step:

$$\begin{aligned} &[h_1, C_1], \dots, [\textcolor{red}{h_i, C_i}], [\textcolor{blue}{h_{i+1}, C_{i+1}}], \dots, [h_n, C_n] \\ &\rightarrow [h_1, C_1], \dots, [\textcolor{red}{h_i, C_{i+1}}], [\textcolor{blue}{h_{i+1}, C_i}], \dots, [h_n, C_n], \end{aligned} \quad (39)$$

507 which, for a symmetric proposal matrix, will be accepted with probability

$$\min\left(1, \frac{W(h_i, C_{i+1})W(h_{i+1}, C_i)}{W(h_i, C_i)W(h_{i+1}, C_{i+1})}\right). \quad (40)$$

508 In this way a configuration can meander in parameter space h and explore regions where
 509 ergodicity is not an issue. In the context of spin-glasses, a low temperature configuration,
 510 stuck in a local minima, can heat up, overcome the potential barrier and then cool down
 511 again.

512 A judicious choice of the values h_i is important to obtain a good acceptance rate for the
 513 exchange step. With $W(h, C) = e^{-S(h, C)}$, the distribution of the action S reads:

$$\mathcal{P}(h, S) = \sum_C P(h, C) \delta(S(h, C) - S). \quad (41)$$

514 A given exchange step can only be accepted if the distributions $\mathcal{P}(h, S)$ and $\mathcal{P}(h + \Delta h, S)$
 515 overlap. For $\langle S \rangle_h < \langle S \rangle_{h+\Delta h}$ one can formulate this requirement as:

$$\langle S \rangle_h + \langle \Delta S \rangle_h \simeq \langle S \rangle_{h+\Delta h} - \langle \Delta S \rangle_{h+\Delta h}, \quad \text{with} \quad \langle \Delta S \rangle_h = \sqrt{\langle (S - \langle S \rangle_h)^2 \rangle_h}. \quad (42)$$

516 Assuming $\langle \Delta S \rangle_{h+\Delta h} \simeq \langle \Delta S \rangle_h$ and expanding in Δh one obtains:

$$\Delta h \simeq \frac{2\langle \Delta S \rangle_h}{\partial \langle S \rangle_h / \partial h}. \quad (43)$$

517 The above equation becomes transparent for classical systems with $S(h, C) = hH(C)$. In this
 518 case, the above equation reads:

$$\Delta h \simeq 2h \frac{\sqrt{c}}{c + h\langle H \rangle_h}, \quad \text{with} \quad c = h^2 \langle (H - \langle H \rangle_h)^2 \rangle_h. \quad (44)$$

520 Several comments are in order:

- 521 i) Let us identify h with the inverse temperature such that c corresponds to the specific
522 heat. This quantity is extensive, as well as the energy, such that $\Delta h \simeq 1/\sqrt{N}$ where N
523 is the system size.
- 524 ii) Near a phase transition the specific heat can diverge, and h must be chosen with partic-
525 ular care.
- 526 iii) Since the action is formulation dependent, also the acceptance rate of the exchange
527 move equally depend upon the formulation.

528 The quantum Monte Carlo code in the ALF project carries out parallel-tempering runs when
529 the script `configure.sh` is called with the argument `Tempering` before compilation, see
530 Sec. 6.2.

531 2.2.6 Langevin dynamics

532 For models that include continuous real fields $s \equiv \{s_{k,\tau}\}$ there is the option of using Langevin
533 dynamics for the updating scheme, by setting the variable `Langevin` to `.true.`. This cor-
534 responds to a stochastic differential equation for the fields. They acquire a discrete Langevin
535 time t_l with step width δt_l and satisfy the stochastic differential equation

$$s(t_l + \delta t_l) = s(t_l) - Q \frac{\partial S(s(t_l))}{\partial s(t_l)} \delta t_l + \sqrt{2\delta t_l Q} \eta(t_l). \quad (45)$$

536 Here, $\eta(t_l)$ are independent Gaussian stochastic variables satisfying:

$$\langle \eta_{k,\tau}(t_l) \rangle_\eta = 0, \quad \text{and} \quad \langle \eta_{k,\tau}(t_l) \eta_{k',\tau'}(t'_l) \rangle_\eta = \delta_{k,k'} \delta_{\tau,\tau'} \delta_{t_l,t'_l}, \quad (46)$$

537 $S(s(t_l))$ is an arbitrary real action and Q is an arbitrary positive definite matrix. By default Q is
538 equal to the identity matrix, but a proper choice can help accelerate the update scheme, as we
539 discuss below. We refer the reader to Ref. [117] for an in-depth introduction to stochastic dif-
540 ferential equations. To see that the above indeed produces the desired probability distribution
541 in the long Langevin time limit, we can transform the Langevin equation into the correspond-
542 ing Fokker-Plank one. Let $P(s, t_l)$ be the distribution of fields at Langevin time t_l . Then,

$$P(s, t_l + \delta t_l) = \int Ds' P(s', t_l) \left\langle \delta \left(s - \left[s' - Q \frac{\partial S(s')}{\partial s'} \delta t_l + \sqrt{2\delta t_l Q} \eta(t_l) \right] \right) \right\rangle_\eta, \quad (47)$$

543 where δ corresponds to the $L_{\text{trotter}} M_l$ dimensional Dirac δ -function. Taylor expanding up to
544 order δt_l and averaging over the stochastic variable yields:

$$\begin{aligned} P(s, t_l + \delta t_l) &= \int Ds' P(s', t_l) \left(\delta(s' - s) - \frac{\partial}{\partial s'} \delta(s' - s) Q \frac{\partial S(s')}{\partial s'} \delta t_l \right. \\ &\quad \left. + \frac{\partial}{\partial s'} Q \frac{\partial}{\partial s'} \delta(s' - s) \delta t_l \right) + \mathcal{O}(\delta t_l^2). \end{aligned} \quad (48)$$

545 Partial integration and taking the limit of infinitesimal time steps gives the Fokker-Plank equa-
546 tion

$$\frac{\partial}{\partial t_l} P(s, t_l) = \frac{\partial}{\partial s} \left(P(s, t_l) Q \frac{\partial S(s)}{\partial s} + Q \frac{\partial P(s, t_l)}{\partial s} \right). \quad (49)$$

547 The stationary, $\frac{\partial}{\partial t_l} P(s, t_l) = 0$, normalizable, solution to the above equation corresponds to
548 the desired probability distribution:

$$P(s) = \frac{e^{-S(s)}}{\int Ds e^{-S(s)}}. \quad (50)$$

549 Taking into account a potential negative sign problem, the action for our general model reads:

$$\bar{S}(C) = -\ln |\operatorname{Re} \{e^{-S(C)}\}|, \quad (51)$$

550 where $S(C)$ is defined in Eq. (17). Hence,

$$\frac{\partial \bar{S}(C)}{\partial s_{k,\tau}} = \frac{1}{\operatorname{Re} \{e^{i\phi(C)}\}} \operatorname{Re} \left\{ e^{i\phi(C)} \frac{\partial S(C)}{\partial s_{k,\tau}} \right\}, \quad (52)$$

551 with

$$e^{i\phi(C)} = \frac{e^{-S(C)}}{|e^{-S(C)}|}, \quad (53)$$

552 corresponding to the variable PHASE in the ALF-package.

553 Therefore, to formulate the Langevin dynamics we need to estimate the forces:

$$\frac{\partial S(C)}{\partial s_{k,\tau}} = \frac{\partial S_0(C)}{\partial s_{k,\tau}} + \frac{\partial S^F(C)}{\partial s_{k,\tau}}, \quad (54)$$

554 with the fermionic part of the action being

$$S^F(C) = -\ln \left\{ \left(\prod_{k=1}^{M_V} \prod_{\tau=1}^{L_{\text{Trotter}}} \gamma_{k,\tau} \right) e^{N_{\text{col}} \sum_{s=1}^{N_{\text{fl}}} \sum_{k=1}^{M_V} \sum_{\tau=1}^{L_{\text{Trotter}}} \sqrt{-\Delta\tau U_k} a_{k,s} \eta_{k,\tau}} \right. \\ \times \left. \prod_{s=1}^{N_{\text{fl}}} \left[\det \left(\mathbb{1} + \prod_{\tau=1}^{L_{\text{Trotter}}} \prod_{k=1}^{M_V} e^{\sqrt{-\Delta\tau U_k} \eta_{k,\tau}} V^{(ks)} \prod_{k=1}^{M_I} e^{-\Delta\tau s_{k,\tau}} I^{(ks)} \prod_{k=1}^{M_T} e^{-\Delta\tau T^{(ks)}} \right) \right]^{N_{\text{col}}} \right\}. \quad (55)$$

555 The forces must be bounded for Langevin dynamics to work well. If this condition is violated
556 the results produced by the code are *not reliable*.

557 One possible source of divergence is the determinant in the fermionic action. Zeros lead to
558 unbounded forces and, in order to mitigate this problem, we adopt a variable time step. The
559 user provides an upper bound to the fermion force, Max_Force and, if the maximal force in a
560 configuration, Max_Force_Conf, is larger than Max_Force, then the time step is rescaled as

$$\tilde{\delta t}_l = \frac{\text{Max_Force}}{\text{Max_Force_Conf}} * \delta t_l. \quad (56)$$

561 With the adaptive time step, averages are computed as:

$$\langle \hat{O} \rangle = \frac{\sum_n (\tilde{\delta t}_l)_n \operatorname{sgn}(C_n) \frac{e^{-S(C_n)}}{\operatorname{Re} [e^{-S(C_n)}]} \langle \langle \hat{O} \rangle \rangle_{(C_n)}}{\sum_n (\tilde{\delta t}_l)_n \operatorname{sgn}(C_n)}, \quad (57)$$

562 where $\operatorname{sgn}(C_n)$ is defined in Eq. (26). In this context the adaptive time step corresponds to the
563 variable Mc_step_weight required for the measurement routines (see Sec. 5.4).

564 A possible way to reduce autocorrelation times is to employ Fourier acceleration [118,119].
565 As we see from Eq. (50), the choice of the matrix Q does not alter the probability distribution
566 obtained from the Langevin equation. The main idea of Fourier acceleration is to exploit this
567 freedom and use Q to enhance (reduce) the Langevin time step δt_l of slow (fast) modes of the
568 fields s [120]. The modified Langevin equation reads:

$$s(t_l + \delta t_l) = s(t_l) - \hat{F}^{-1} \left[Q \hat{F} \left[\frac{\partial S(s(t_l))}{\partial s(t_l)} \right] \delta t_l + \sqrt{2\delta t_l Q} \hat{F} [\eta(t_l)] \right], \quad (58)$$

569 with \hat{F} being a transformation to independent modes of the field. This generically corresponds
 570 to a Fourier transform, thus the notation. Currently, Fourier acceleration is not implemented
 571 in ALF, but can be included by the user.

572 In order to use Langevin dynamics the user also has to provide the Langevin time step
 573 `Delta_t_Langevin_HMC`, the maximal force `Max_Force`, set `Global_update_`
 574 `scheme=Langevin` in the parameter file. Furthermore, the forces $\frac{\partial S_0(C)}{\partial s_{k,\tau}}$ are to be speci-
 575 fied in the routine `Ham_Langevin_HMC_S0` of the Hamiltonian files. The Langevin update for
 576 a general Hamiltonian is carried out in the module `Langevin_HMC_mod.F90`. In particular
 577 the fermion forces,

$$\frac{\partial S^F(C)}{\partial s_{k,\tau}} = \Delta\tau N_{\text{col}} \sum_{s=1}^{N_{\text{fl}}} \text{Tr} [I^{(ks)} (\mathbb{1} - \mathbf{G}^{(s)}(k, \tau))], \quad (59)$$

578 are computed in this module. In the above, we introduce a Green function that depends on
 579 the time slice τ and the interaction term k to which the corresponding field $s_{k,\tau}$ belongs:

$$G_{x,y}^{(s)}(k, \tau) = \frac{\text{Tr} [\hat{U}_{(s)}^<(k, \tau) \hat{c}_{x,s} \hat{c}_{y,s}^\dagger \hat{U}_{(s)}^>(k, \tau)]}{\text{Tr} [\hat{U}_{(s)}^<(k, \tau) \hat{U}_{(s)}^>(k, \tau)]}, \quad (60)$$

580 where the following definitions are used

$$\hat{U}_{(s)}^<(k', \tau') = \prod_{\tau=\tau'+1}^{L_{\text{Trotter}}} (\hat{U}_{(s)}(\tau)) \prod_{k=1}^{M_V} e^{\sqrt{-\Delta\tau U_k} \eta_{k,\tau'} \hat{c}_s^\dagger V^{(ks)} \hat{c}_s} \prod_{k=k'+1}^{M_I} e^{-\Delta\tau s_{k,\tau'} \hat{c}_s^\dagger I^{(ks)} \hat{c}_s}, \quad (61)$$

$$\hat{U}_{(s)}^>(k', \tau') = \prod_{k=1}^{k'} e^{-\Delta\tau s_{k,\tau'} \hat{c}_s^\dagger I^{(ks)} \hat{c}_s} \prod_{k=1}^{M_T} e^{-\Delta\tau \hat{c}_s^\dagger T^{(ks)} \hat{c}_s} \prod_{\tau=1}^{\tau'-1} (\hat{U}_{(s)}(\tau)), \quad (62)$$

$$\hat{U}_{(s)}(\tau) = \prod_{k=1}^{M_V} e^{\sqrt{-\Delta\tau U_k} \eta_{k,\tau} \hat{c}_s^\dagger V^{(ks)} \hat{c}_s} \prod_{k=1}^{M_I} e^{-\Delta\tau s_{k,\tau} \hat{c}_s^\dagger I^{(ks)} \hat{c}_s} \prod_{k=1}^{M_T} e^{-\Delta\tau \hat{c}_s^\dagger T^{(ks)} \hat{c}_s}. \quad (63)$$

581 The vector \hat{c}_s^\dagger contains all fermionic operators $\hat{c}_{x,s}^\dagger$ of flavor s .

582 During each Langevin step, all fields are updated and the Langevin time is incremented by
 583 δt_l . At the end of a run, the mean and maximal forces encountered during the run are printed
 584 out in the info file.

585 The great advantage of the Langevin updating scheme is the absence of update rejection,
 586 meaning that all fields are updated at each step. As mentioned above, the price we pay for
 587 using Langevin dynamics is ensuring that forces show no singularities. Two other potential
 588 issues should be highlighted:

- 589 • Langevin dynamics is carried out at a finite Langevin time step, thereby introducing a
 590 further source of systematic error.
- 591 • The factor $\sqrt{2\delta t_l}$ multiplying the stochastic variable makes the noise dominant on short
 592 time scales. On these time scales Langevin dynamics essentially corresponds to a random
 593 walk. This has the advantage of allowing one to circumvent potential barriers, but may
 594 render the updating scheme less efficient than the hybrid molecular dynamics approach.

595 Example – Hubbard chain at half-filling

596 Let us consider a 6-site Hubbard chain at half-filling with $U/t = 4$ and $\beta t = 4$. The Hubbard
 597 interaction can be decoupled using a continuous HS transformation, where we introduce a

real auxiliary field $s_{i,\tau}$ for every lattice site i and time slice τ . When the HS fields are coupled to the z -component of the magnetization (see Sec. 9.1), the partition function can be written as

$$Z = \int \left(\prod_{\tau=1}^{L_{\text{Trotter}}} \prod_{i=1}^{N_{\text{unit-cell}}} \frac{ds_{i,\tau}}{\sqrt{2\pi}} e^{-\frac{1}{2}s_{i,\tau}^2} \right) \times \prod_{s=\uparrow,\downarrow} \det \left(\mathbb{1} + \prod_{\tau=1}^{L_{\text{Trotter}}} \prod_{i=1}^{N_{\text{unit-cell}}} \left(e^{-\sqrt{\Delta\tau U} s_{i,\tau} V^{(is)}} \right) e^{-\Delta\tau T} \right) + \mathcal{O}(\Delta\tau^2). \quad (64)$$

The flavor-dependent interaction matrices have only one non-vanishing entry each:

$$V_{x,y}^{(i,s=\uparrow)} = \delta_{x,y} \delta_{x,i}, \quad \text{and} \quad V_{x,y}^{(i,s=\downarrow)} = -\delta_{x,y} \delta_{x,i}.$$

The forces of the Hubbard model are given by:

$$\frac{\partial S(C)}{\partial s_{i,\tau}} = s_{i,\tau} - \sqrt{\Delta\tau U} \sum_{s=\uparrow,\downarrow} \text{Tr} [V^{(is)} (\mathbb{1} - G^{(s)}(i, \tau))], \quad (65)$$

where the Green function is defined by Eq. (60) with

$$\hat{U}_{(s)}^<(i', \tau') = \prod_{\tau=\tau'+1}^{L_{\text{Trotter}}} (\hat{U}_{(s)}(\tau)) \prod_{i=i'+1}^{N_{\text{unit-cell}}} e^{-\sqrt{\Delta\tau U} s_{i,\tau'} \hat{c}_s^\dagger V^{(is)} \hat{c}_s}, \quad (66)$$

$$\hat{U}_{(s)}^>(i', \tau') = \prod_{i=1}^{i'} \left(e^{-\sqrt{\Delta\tau U} s_{i,\tau'} \hat{c}_s^\dagger V^{(is)} \hat{c}_s} \right) e^{-\Delta\tau \hat{c}_s^\dagger T \hat{c}_s} \prod_{\tau=1}^{\tau'-1} (\hat{U}_{(s)}(\tau)), \quad (67)$$

$$\hat{U}_{(s)}(\tau) = \prod_{i=1}^{N_{\text{unit-cell}}} \left(e^{-\sqrt{\Delta\tau U} s_{i,\tau} \hat{c}_s^\dagger V^{(is)} \hat{c}_s} \right) e^{-\Delta\tau \hat{c}_s^\dagger T \hat{c}_s}. \quad (68)$$

One can show that for periodic boundary conditions the forces are not bounded and to make sure that the program does not crash we set `Max_Force = 1.5`.

The results are: the reference, discrete-variable code gives

$$\langle \hat{H} \rangle = -3.4684 \pm 0.0007, \quad (69)$$

while the Langevin code at $\delta t_l = 0.001$ yields

$$\langle \hat{H} \rangle = -3.457 \pm 0.010, \quad (70)$$

and at $\delta t_l = 0.01$

$$\langle \hat{H} \rangle = -3.495 \pm 0.007. \quad (71)$$

At $\delta t_l = 0.001$ the maximal force that occurred during the run was 112, whereas at $\delta t_l = 0.01$ it grew to 524. In both cases the average force was given by 0.45. For larger values of δt_l the maximal force grows and the fluctuations on the energy become larger (for instance, $\langle \hat{H} \rangle = -3.718439 \pm 0.206469$ at $\delta t_l = 0.02$; for this parameter set the maximal force we encountered during the run was of 1658).

Controlling Langevin dynamics when the action has logarithmic divergences is a challenge, and it is not a given that the results are satisfactory. For our specific problem we can solve this issue by considering open boundary conditions. Following an argument put forward in [89], we can show, using world lines, that the determinant is always positive. In this case the action does not have logarithmic divergences and the Langevin dynamics works beautifully well, see Fig. 1.

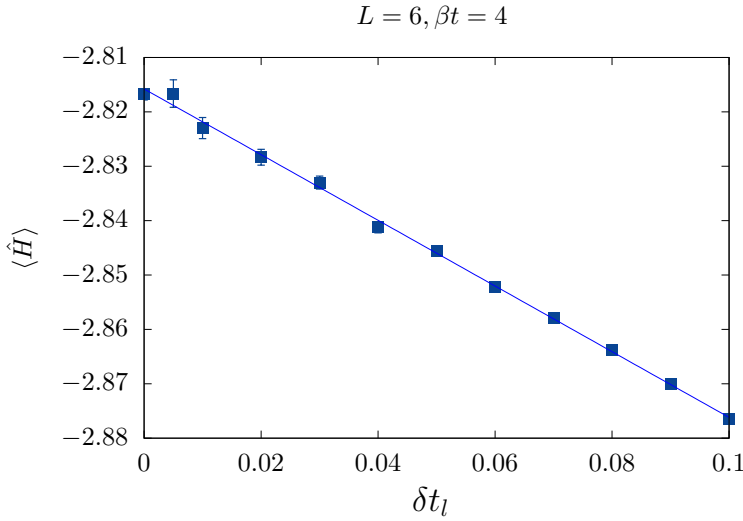


Figure 1: Total energy for the 6-site Hubbard chain at $U/t = 4$, $\beta t = 4$ and with open boundary conditions. For this system it can be shown that the determinant is always positive, so that no singularities occur in the action and, consequently, the Langevin dynamics works very well. The reference data point at $\delta t_l = 0$ comes from the discrete field code for the field coupled to the z-component of the magnetization and reads -2.8169 ± 0.0013 , while the extrapolated value is -2.8176 ± 0.0010 . Throughout the runs the maximal force remained below the threshold of 1.5. The displayed data has been produced by the pyALF script [Langevin.py](#).

620 2.3 The Trotter error and checkerboard decomposition

621 2.3.1 Asymmetric Trotter decomposition

622 In practice, many applications are carried out at finite imaginary time steps, and it is important
 623 to understand the consequences of the Trotter error. How does it scale with system size and
 624 what symmetries does it break? In particular, when investigating a critical point, one should
 625 determine whether the potential symmetry breaking associated with the Trotter decomposition
 626 generates relevant operators.

627 To best describe the workings of the ALF code, we divide the Hamiltonian into hopping
 628 terms $\hat{\mathcal{H}}_T$ and interaction terms $\hat{\mathcal{H}}_V + \hat{\mathcal{H}}_I + \hat{\mathcal{H}}_{0,I}$. Let

$$\hat{\mathcal{H}}_T = \sum_{i=1}^{N_T} \sum_{k \in \mathcal{S}_i^T} \hat{T}^{(k)} \equiv \sum_{i=1}^{N_T} \hat{T}_i. \quad (72)$$

629 Here the decomposition follows the rule that if k and k' belong to the same set \mathcal{S}_i^T then
 630 $[\hat{T}^{(k)}, \hat{T}^{(k')}] = 0$. An important case to consider is that of the checkerboard decomposition.
 631 For the square lattice we can decouple the nearest neighbor hopping into $N_T = 4$ groups, each
 632 consisting of two site hopping processes. This type of checkerboard decomposition is activated
 633 for a set of predefined lattices by setting the flag `Checkerboard` to `.true.`. We will carry
 634 out the same separation for the interaction:

$$\hat{\mathcal{H}}_V + \hat{\mathcal{H}}_I + \hat{\mathcal{H}}_{0,I} = \sum_{i=1}^{N_I} \hat{O}_i, \quad (73)$$

635 where each \hat{O}_i contains a set of commuting terms. For instance, for the Hubbard model, the
 636 above reduces to $U \sum_i \hat{n}_{i,\uparrow} \hat{n}_{i,\downarrow}$ such that $N_I = 1$ and $\hat{O}_1 = U \sum_i \hat{n}_{i,\uparrow} \hat{n}_{i,\downarrow}$.

637 The default Trotter decomposition in the ALF code is based on the equation:

$$e^{-\Delta\tau(\hat{A}+\hat{B})} = e^{-\Delta\tau\hat{A}}e^{-\Delta\tau\hat{B}} + \frac{\Delta\tau^2}{2} [\hat{B}, \hat{A}] + \mathcal{O}(\Delta\tau^3). \quad (74)$$

638 Using iteratively the above the single time step is given by:

$$\begin{aligned} e^{-\Delta\tau\mathcal{H}} &= \prod_{i=1}^{N_O} e^{-\Delta\tau\hat{O}_i} \prod_{j=1}^{N_T} e^{-\Delta\tau\hat{T}_j} \\ &+ \underbrace{\frac{\Delta\tau^2}{2} \left(\sum_{i=1}^{N_O} \sum_{j=1}^{N_T} [\hat{T}_j, \hat{O}_i] + \sum_{j'=1}^{N_T-1} [\hat{T}_{j'}, \hat{T}_{j'}^>] + \sum_{i'=1}^{N_O-1} [\hat{O}_{i'}, \hat{O}_{i'}^>] \right)}_{\equiv \Delta\tau\hat{\lambda}_1} + \mathcal{O}(\Delta\tau^3). \end{aligned} \quad (75)$$

639 In the above, we have introduced the shorthand notation

$$\hat{T}_n^> = \sum_{j=n+1}^{N_T} \hat{T}_j, \quad \text{and} \quad \hat{O}_n^> = \sum_{j=n+1}^{N_O} \hat{O}_j. \quad (76)$$

640 The full propagation then reads

$$\begin{aligned} \hat{U}_{\text{Approx}} &= \left(\prod_{i=1}^{N_O} e^{-\Delta\tau\hat{O}_i} \prod_{j=1}^{N_T} e^{-\Delta\tau\hat{T}_j} \right)^{L_{\text{Trotter}}} = e^{-\beta(\hat{H}+\hat{\lambda}_1)} + \mathcal{O}(\Delta\tau^2) \\ &= e^{-\beta\hat{H}} - \int_0^\beta d\tau e^{-(\beta-\tau)\hat{H}} \hat{\lambda}_1 e^{-\tau\hat{H}} + \mathcal{O}(\Delta\tau^2). \end{aligned} \quad (77)$$

641 The last step follows from time-dependent perturbation theory. The following comments are
642 in order:

- 643 • The error is anti-Hermitian since $\hat{\lambda}_1^\dagger = -\hat{\lambda}_1$. As a consequence, if all the operators as well
644 as the quantity being measured are simultaneously real representable, then the prefactor
645 of the linear in $\Delta\tau$ error vanishes since it ultimately corresponds to computing the trace
646 of an anti-symmetric matrix. This *lucky* cancellation was put forward in Ref. [98]. Hence,
647 under this assumption – which is certainly valid for the Hubbard model considered in
648 Fig. 2 – the systematic error is of order $\Delta\tau^2$.
- 649 • The biggest drawback of the above decomposition is that the imaginary-time propagation
650 is not Hermitian. This can lead to acausal features in imaginary-time correlation
651 functions [121]. To be more precise, the eigenvalues of $H_{\text{Approx}} = -\frac{1}{\beta} \log U_{\text{Approx}}$ need
652 not be real and thus imaginary-time displaced correlation functions may oscillate as a
653 function of imaginary time. This is shown in Fig. 2(a) that plots the absolute value of
654 local time-displaced Green function for the Honeycomb lattice at $U/t = 2$. Sign changes
655 of this quantity involve zeros that, on the considered log-scale, correspond to negative
656 divergences. As detailed in [109], using the non-symmetric Trotter decomposition leads
657 to an additional non-Hermitian second-order error in the measurement of observables
658 O that is proportional to $[T, [T, O]]$. As we see next, these issues can be solved by con-
659 sidering a symmetric Trotter decomposition.

660 2.3.2 Symmetric Trotter decomposition

661 To address the issue described above, the ALF package provides the possibility of using a sym-
662 metric Trotter decomposition,

$$e^{-\Delta\tau(\hat{A}+\hat{B})} = e^{-\Delta\tau\hat{A}/2} e^{-\Delta\tau\hat{B}} e^{-\Delta\tau\hat{A}/2} + \frac{\Delta\tau^3}{12} [2\hat{A} + \hat{B}, [\hat{B}, \hat{A}]] + \mathcal{O}(\Delta\tau^5), \quad (78)$$

663 by setting the `Symm` flag to `.true.`. Before we apply the expression above to a time step, let
 664 us write

$$e^{-\Delta\tau\mathcal{H}} = e^{-\frac{\Delta\tau}{2}\sum_{j=1}^{N_T}\hat{T}_j}e^{-\Delta\tau\sum_{i=1}^{N_I}\hat{O}_i}e^{-\frac{\Delta\tau}{2}\sum_{j=1}^{N_T}\hat{T}_j} + \underbrace{\frac{\Delta\tau^3}{12}[2\hat{T}_0^> + \hat{O}_0^>, [\hat{O}_0^>, \hat{T}_0^>]]}_{\equiv\Delta\tau\hat{\lambda}_{TO}} + \mathcal{O}(\Delta\tau^5). \quad (79)$$

665 Then,

$$\begin{aligned} e^{-\Delta\tau\sum_i^{N_I}\hat{O}_i} &= \left(\prod_{i=1}^{N_O-1} e^{-\frac{\Delta\tau}{2}\hat{O}_i} \right) e^{-\Delta\tau\hat{O}_{N_O}} \left(\prod_{i=N_O-1}^1 e^{-\frac{\Delta\tau}{2}\hat{O}_i} \right) \\ &\quad + \underbrace{\frac{\Delta\tau^3}{12} \sum_{i=1}^{N_O-1} [2\hat{O}_i + \hat{O}_i^>, [\hat{O}_i^>, \hat{O}_i]]}_{\equiv\Delta\tau\hat{\lambda}_O} + \mathcal{O}(\Delta\tau^5), \end{aligned} \quad (80)$$

$$\begin{aligned} e^{-\frac{\Delta\tau}{2}\sum_j^{N_T}\hat{T}_j} &= \left(\prod_{j=1}^{N_T-1} e^{-\frac{\Delta\tau}{4}\hat{T}_j} \right) e^{-\frac{\Delta\tau}{2}\hat{T}_{N_T}} \left(\prod_{j=N_T-1}^1 e^{-\frac{\Delta\tau}{4}\hat{T}_j} \right) \\ &\quad + \underbrace{\frac{\Delta\tau^3}{96} \sum_{j=1}^{N_T-1} [2\hat{T}_j + \hat{T}_j^>, [\hat{T}_j^>, \hat{T}_j]]}_{\equiv\Delta\tau\hat{\lambda}_T} + \mathcal{O}(\Delta\tau^5), \end{aligned} \quad (81)$$

666 and we can derive a closed equation for the free energy density:

$$\begin{aligned} f_{\text{Approx}} &= -\frac{1}{\beta V} \log \text{Tr} \left[\left(\prod_{j=1}^{N_T-1} e^{-\frac{\Delta\tau}{4}\hat{T}_j} \right) e^{-\frac{\Delta\tau}{2}\hat{T}_{N_T}} \left(\prod_{j=N_T-1}^1 e^{-\frac{\Delta\tau}{4}\hat{T}_j} \right) \right. \\ &\quad \times \left(\prod_{i=1}^{N_O-1} e^{-\frac{\Delta\tau}{2}\hat{O}_i} \right) e^{-\Delta\tau\hat{O}_{N_O}} \left(\prod_{i=N_O-1}^1 e^{-\frac{\Delta\tau}{2}\hat{O}_i} \right) \\ &\quad \times \left. \left(\prod_{j=1}^{N_T-1} e^{-\frac{\Delta\tau}{4}\hat{T}_j} \right) e^{-\frac{\Delta\tau}{2}\hat{T}_{N_T}} \left(\prod_{j=N_T-1}^1 e^{-\frac{\Delta\tau}{4}\hat{T}_j} \right) \right]^{L_{\text{Trotter}}} \\ &= f - \frac{1}{V} \langle \hat{\lambda}_{TO} + \hat{\lambda}_O + 2\hat{\lambda}_T \rangle + \mathcal{O}(\Delta\tau^4). \end{aligned} \quad (82)$$

667 The following comments are in order:

- 668 • The approximate imaginary-time propagation from which the f_{Approx} is derived is Her-
 669 mitian. Hence no spurious effects in imaginary-time correlation functions are to be ex-
 670 pected. This is clearly shown in Fig. 2(a).
- 671 • In Fig. 2(b) we have used the ALF-library with `Symm= .true.` with and without checker-
 672 board decomposition. We still expect the systematic error to be of order $\Delta\tau^2$. However
 673 its prefactor is much smaller than that of the aforementioned anti-symmetric decom-
 674 position.
- 675 • We have taken the burden to evaluate explicitly the prefactor of the $\Delta\tau^2$ error on the free
 676 energy density. One can see that for Hamiltonians that are sums of local operators, the
 677 quantity $\langle \hat{\lambda}_{TO} + \hat{\lambda}_O + 2\hat{\lambda}_T \rangle$ scales as the volume V of the system, such that the systematic
 678 error on the free energy density (and on correlation functions that can be computed

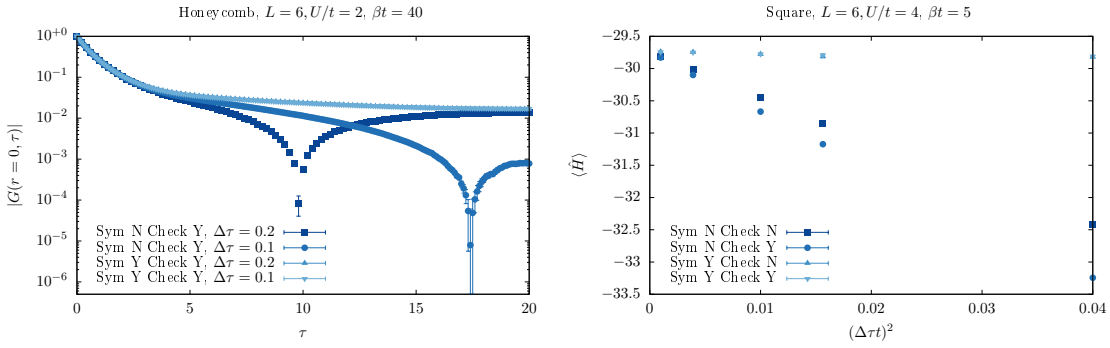


Figure 2: Analysis of Trotter systematic error. Left: We consider a 6×6 Hubbard model on the Honeycomb lattice, $U/t = 2$, half-band filling, inverse temperature $\beta t = 40$, and we have used an HS transformation that couples to the density. The figure plots the local-time displaced Green function. Right: Here we consider the 6×6 Hubbard model at $U/t = 4$, half-band filling, inverse temperature $\beta t = 5$, and we have used the HS transformation that couples to the z -component of spin. We provide data for the four combinations of the logical variables `Sym` and `Checkerboard`, where `Sym = .true.` (.`false.`) indicates a symmetric (asymmetric) Trotter decomposition has been used, and `Checkerboard = .true.` (.`false.`) that the checkerboard decomposition for the hopping matrix has (not) been used. The large deviations between different choices of `Sym` are here $\sim [T, [T, H]]$ as detailed in [109].

679 by adding source terms) will be volume independent. For model Hamiltonians that are
 680 not sums of local terms, care must be taken. A conservative upper bound on the error
 681 is $\langle \hat{\lambda}_{TO} + \hat{\lambda}_O + 2\hat{\lambda}_T \rangle \propto \Delta\tau^2 V^3$, which means that, in order to maintain a constant
 682 systematic error for the free energy density, we have to keep $\Delta\tau V$ constant. Such a
 683 situation has been observed in Ref. [71].

684 Alternative symmetric second order methods as well as the issues with decompositions of
 685 higher order have been detailed in [109].

686 2.3.3 The Symm flag

687 If the `Sym` flag is set to true, then the program will automatically – for the set of predefined
 688 lattices and models – use the symmetric $\Delta\tau$ time step of the interaction and hopping terms.

689 To save CPU time when the `Sym` flag is on we carry out the following approximation:

$$\left[\left(\prod_{j=1}^{N_T-1} e^{-\frac{\Delta\tau}{4} \hat{T}_j} \right) e^{-\frac{\Delta\tau}{2} \hat{T}_{N_T}} \left(\prod_{j=N_T-1}^1 e^{-\frac{\Delta\tau}{4} \hat{T}_j} \right) \right]^2 \simeq \left(\prod_{j=1}^{N_T-1} e^{-\frac{\Delta\tau}{2} \hat{T}_j} \right) e^{-\Delta\tau \hat{T}_{N_T}} \left(\prod_{j=N_T-1}^1 e^{-\frac{\Delta\tau}{2} \hat{T}_j} \right). \quad (83)$$

690 The above is consistent with the overall precision of the Trotter decomposition and more im-
 691 portantly conserves the Hermiticity of the propagation.

692 2.4 Stabilization – A peculiarity of the BSS algorithm

693 From the partition function in Eq. (17) it can be seen that, for the calculation of the Monte
 694 Carlo weight and of the observables, a long product of matrix exponentials has to be formed.
 695 In addition to that, we need to be able to extract the single-particle Green function for a given

696 flavor index at, say, time slice $\tau = 0$. As mentioned above (cf. Eq. (21)), this quantity is given
 697 by:

$$\mathbf{G} = \left(\mathbb{1} + \prod_{\tau=1}^{L_{\text{Trotter}}} \mathbf{B}_\tau \right)^{-1}, \quad (84)$$

698 which can be recast as the more familiar linear algebra problem of finding a solution for the
 699 linear system

$$\left(\mathbb{1} + \prod_{\tau=1}^{L_{\text{Trotter}}} \mathbf{B}_\tau \right) \mathbf{x} = \mathbf{b}. \quad (85)$$

700 The matrices $\mathbf{B}_\tau \in \mathbb{C}^{n \times n}$ depend on the lattice size as well as other physical parameters that
 701 can be chosen such that a matrix norm of \mathbf{B}_τ can be unbound in magnitude. From standard
 702 perturbation theory for linear systems, the computed solution $\tilde{\mathbf{x}}$ would contain a relative error

$$\frac{|\tilde{\mathbf{x}} - \mathbf{x}|}{|\mathbf{x}|} = \mathcal{O}\left(\epsilon \kappa_p \left(\mathbb{1} + \prod_{\tau=1}^{L_{\text{Trotter}}} \mathbf{B}_\tau \right)\right), \quad (86)$$

703 where ϵ denotes the machine precision, which is 2^{-53} for IEEE double-precision numbers, and
 704 $\kappa_p(\mathbf{M})$ is the condition number of the matrix \mathbf{M} with respect to the matrix p -norm. Due to
 705 $\prod_\tau \mathbf{B}_\tau$ containing exponentially large and small scales, as can be seen in Eq. (17), a straightfor-
 706 ward inversion is completely ill-suited, in that its condition number would grow exponentially
 707 with increasing inverse temperature, rendering the computed solution $\tilde{\mathbf{x}}$ meaningless.

708 In order to circumvent this, more sophisticated methods have to be employed. In the realm
 709 of the BSS algorithm there has been a long history [4, 93, 122–125] of using various matrix
 710 factorization techniques. The predominant techniques are either based on the singular value
 711 decomposition (SVD) or on techniques using the QR decomposition. The default stabilization
 712 strategy in the auxiliary-field QMC implementation of the ALF package is to form a product of
 713 QR-decompositions, which is proven to be weakly backwards stable [124]. While algorithms
 714 using the SVD can provide higher stability, though at a higher cost, we note that great care
 715 has to be taken in the choice of the algorithm, which has to achieve a high relative accuracy
 716 [126, 127].

717 As a first step we assume that, for a given integer NWrap , the multiplication of NWrap \mathbf{B}
 718 matrices has an acceptable condition number and, for simplicity, that L_{Trotter} is divisible by
 719 NWrap . We can then write:

$$\mathbf{G} = \left(\mathbb{1} + \prod_{i=1}^{\frac{L_{\text{Trotter}}}{\text{NWrap}}} \underbrace{\prod_{\tau=1}^{\text{NWrap}} \mathbf{B}_{(i-1) \cdot \text{NWrap} + \tau}}_{\equiv \mathcal{B}_i} \right)^{-1}. \quad (87)$$

720 The key idea is to efficiently separate the scales of a matrix from the orthogonal part of a
 721 matrix. This can be achieved with the QR decomposition of a matrix \mathbf{A} in the form $\mathbf{A}_i = \mathbf{Q}_i \mathbf{R}_i$.
 722 The matrix \mathbf{Q}_i is unitary and hence in the usual 2-norm it satisfies $\kappa_2(\mathbf{Q}_i) = 1$. To get a handle
 723 on the condition number of \mathbf{R}_i we consider the diagonal matrix

$$(\mathbf{D}_i)_{n,n} = |(\mathbf{R}_i)_{n,n}|, \quad (88)$$

724 and set $\tilde{\mathbf{R}}_i = \mathbf{D}_i^{-1} \mathbf{R}_i$, which gives the decomposition

$$\mathbf{A}_i = \mathbf{Q}_i \mathbf{D}_i \tilde{\mathbf{R}}_i. \quad (89)$$

725 The matrix \mathbf{D}_i now contains the row norms of the original \mathbf{R}_i matrix and hence attempts to
 726 separate off the total scales of the problem from \mathbf{R}_i . This is similar in spirit to the so-called

727 matrix equilibration which tries to improve the condition number of a matrix through suitably
 728 chosen column and row scalings. Due to a theorem by van der Sluis [128] we know that the
 729 choice in Eq. (88) is almost optimal among all diagonal matrices \mathbf{D} from the space of diagonal
 730 matrices \mathcal{D} , in the sense that

$$\kappa_p((\mathbf{D}_i)^{-1}\mathbf{R}_i) \leq n^{1/p} \min_{\mathbf{D} \in \mathcal{D}} \kappa_p(\mathbf{D}^{-1}\mathbf{R}_i).$$

731 Now, given an initial decomposition $\mathbf{A}_{j-1} = \prod_i \mathcal{B}_i = \mathbf{Q}_{j-1} \mathbf{D}_{j-1} \mathbf{T}_{j-1}$, an update $\mathcal{B}_j \mathbf{A}_{j-1}$ is
 732 formed in the following three steps:

- 733 1. Form $\mathbf{M}_j = (\mathcal{B}_j \mathbf{Q}_{j-1}) \mathbf{D}_{j-1}$. Note the parentheses.
- 734 2. Do a QR decomposition of $\mathbf{M}_j = \mathbf{Q}_j \mathbf{D}_j \mathbf{R}_j$. This gives the final \mathbf{Q}_j and \mathbf{D}_j .
- 735 3. Form the updated \mathbf{T} matrices $\mathbf{T}_j = \mathbf{R}_j \mathbf{T}_{j-1}$.

736 This is a stable but expensive method for calculating the matrix product. Here is where NWrap
 737 comes into play: it specifies the number of plain multiplications performed between the QR
 738 decompositions just described, so that NWrap = 1 corresponds to always performing QR de-
 739 compositions whereas larger values define longer intervals where no QR decomposition will
 740 be performed. Whenever we perform a stabilization, we compare the old result (fast updates)
 741 with the new one (recalculated from the QR stabilized matrices). The difference is docu-
 742 mented as the stability, both for the Green function and for the sign (of the determinant) The
 743 effectiveness of the stabilization *has* to be judged for every simulation from the output file
 744 info (Sec. 5.7.2). For most simulations there are two values to look out for:

- 745 • Precision Green
- 746 • Precision Phase

747 The Green function, as well as the average phase, are usually numbers with a magnitude of
 748 $\mathcal{O}(1)$. For that reason we recommend that NWrap is chosen such that the mean precision is
 749 of the order of 10^{-8} or better (for further recommendations see Sec. 6.4). We include typical
 750 values of Precision Phase and of the mean and the maximal values of Precision Green
 751 in the example simulations discussed in Sec. 7.9.

752 3 Auxiliary field quantum Monte Carlo: Projective algorithm

753 The projective approach is the method of choice if one is interested in ground-state properties.
 754 The starting point is a pair of trial wave functions, $|\Psi_{T,L/R}\rangle$, that are not orthogonal to the
 755 ground state $|\Psi_0\rangle$:

$$\langle \Psi_{T,L/R} | \Psi_0 \rangle \neq 0. \quad (90)$$

756 The ground-state expectation value of any observable \hat{O} can then be computed by propagation
 757 along the imaginary time axis:

$$\frac{\langle \Psi_0 | \hat{O} | \Psi_0 \rangle}{\langle \Psi_0 | \Psi_0 \rangle} = \lim_{\theta \rightarrow \infty} \frac{\langle \Psi_{T,L} | e^{-\theta \hat{H}} e^{-(\beta-\tau)\hat{H}} \hat{O} e^{-\tau \hat{H}} e^{-\theta \hat{H}} | \Psi_{T,R} \rangle}{\langle \Psi_{T,L} | e^{-(2\theta+\beta)\hat{H}} | \Psi_{T,R} \rangle}, \quad (91)$$

758 where β defines the imaginary time range where observables (time displaced and equal time)
 759 are measured and τ varies from 0 to β in the calculation of time-displace observables. The
 760 simulations are carried out at large but finite values of θ so as to guarantee convergence to

761 the ground state within the statistical uncertainty. The trial wave functions are determined up
 762 to a phase, and the program uses this gauge choice to guarantee that

$$\langle \Psi_{T,L} | \Psi_{T,R} \rangle > 0. \quad (92)$$

763 In order to use the projective version of the code, the model's namespace in the parameter
 764 file must set `projector=.true.` and specify the value of the projection parameter `Theta`,
 765 as well as the imaginary time interval `Beta` in which observables are measured.

766 Note that time-displaced correlation functions are computed for a τ ranging from 0 to β .
 767 The implicit assumption in this formulation is that the projection parameter `Theta` suffices
 768 to reach the ground state. Since the computational time scales linearly with `Theta` large
 769 projections parameters are computationally not expensive.

770 3.1 Specification of the trial wave function

771 For each flavor, one needs to specify a left and a right trial wave function. In the ALF, they
 772 are assumed to be the ground state of single-particle trial Hamiltonians $\hat{H}_{T,L/R}$ and hence
 773 correspond to a single Slater determinant each. More specifically, we consider a single-particle
 774 Hamiltonian with the same symmetries, color and flavor, as the original Hamiltonian:

$$\hat{H}_{T,L/R} = \sum_{\sigma=1}^{N_{\text{col}}} \sum_{s=1}^{N_{\text{fl}}} \sum_{x,y}^{N_{\text{dim}}} \hat{c}_{x\sigma s}^{\dagger} h_{xy}^{(s,L/R)} \hat{c}_{y\sigma s}. \quad (93)$$

775 Ordering the eigenvalues of the Hamiltonian in ascending order yields the ground state

$$|\Psi_{T,L/R}\rangle = \prod_{\sigma=1}^{N_{\text{col}}} \prod_{s=1}^{N_{\text{fl}}} \prod_{n=1}^{N_{\text{part},s}} \left(\sum_{x=1}^{N_{\text{dim}}} \hat{c}_{x\sigma s}^{\dagger} U_{x,n}^{(s,L/R)} \right) |0\rangle, \quad (94)$$

776 where

$$U^{\dagger,(s,L/R)} h^{(s,L/R)} U^{(s,L/R)} = \text{Diag}(\epsilon_1^{(s,L/R)}, \dots, \epsilon_{N_{\text{dim}}}^{(s,L/R)}). \quad (95)$$

777 The trial wave function is hence completely defined by the set of orthogonal vectors $U_{x,n}^{(s,L/R)}$
 778 for n ranging from 1 to the number of particles in each flavor sector, $N_{\text{part},s}$. This information is
 779 stored in the `WaveFunction` type defined in the module `WaveFunction_mod` (see Sec. 5.5).
 780 Note that, owing to the $SU(N_{\text{col}})$ symmetry, the color index is not necessary to define the trial
 781 wave function. The user will have to specify the trial wave function in the following way:

```
782 Do s = 1, N_fl
783   Do x = 1, Ndim
784     Do n = 1, N_part(s)
785       WF_L(s)%P(x,n) = U_{x,n}^{(s,L)}
786       WF_R(s)%P(x,n) = U_{x,n}^{(s,R)}
787     Enddo
788   Enddo
789 Enddo
```

792 In the above `WF_L` and `WF_R` are `WaveFunction` arrays of length N_{fl} . ALF comes with a set of
 793 predefined trial wave functions, see Sec. 8.5.

794 Generically, the unitary matrix will be generated by a diagonalization routine such that
 795 if the ground state for the given particle number is degenerate, the trial wave function has a
 796 degree of ambiguity and does not necessarily share the symmetries of the Hamiltonian $\hat{H}_{T,L/R}$.
 797 Since symmetries are the key for guaranteeing the absence of the negative sign problem, vi-
 798 olating them in the choice of the trial wave function can very well lead to a sign problem.
 799 It is hence recommended to define the trial Hamiltonians $\hat{H}_{T,L/R}$ such that the ground state
 800 for the given particle number is non-degenerate. That can be checked using the value of

801 WL_L/R(s)%Degen, which stores the energy difference between the last occupied and first
 802 un-occupied single particle state. If this value is greater than zero, then the trial wave func-
 803 tion is non-degenerate and hence has all the symmetry properties of the trial Hamiltonians,
 804 $\hat{H}_{T,L/R}$. When the projector variable is set to .true., this quantity is listed in the info file.

805 3.2 Some technical aspects of the projective code

806 If one is interested solely in zero-temperature properties, the projective code offers many ad-
 807 vantages. This comes from the related facts that the Green function matrix is a projector, and
 808 that scales can be omitted.

809 In the projective algorithm, it is known [6] that

$$G(x, \sigma, s, \tau | x', \sigma, s, \tau) = \left[1 - U_{(s)}^>(\tau) \left(U_{(s)}^<(\tau) U_{(s)}^>(\tau) \right)^{-1} U_{(s)}^<(\tau) \right]_{x,x'}, \quad (96)$$

810 with

$$U_{(s)}^>(\tau) = \prod_{\tau'=1}^{\tau} \mathbf{B}_{\tau'}^{(s)} P^{(s),R}, \quad \text{and} \quad U_{(s)}^<(\tau) = P^{(s),L,\dagger} \prod_{\tau'=L_{\text{Trotter}}}^{\tau+1} \mathbf{B}_{\tau'}^{(s)}, \quad (97)$$

811 where $\mathbf{B}_{\tau}^{(s)}$ is given by Eq. (22) and $P^{(s),L/R}$ correspond to the $N_{\text{dim}} \times N_{\text{part},s}$ submatrices of
 812 $U^{(s),L/R}$. To see that scales can be omitted, we carry out a singular value decomposition:

$$U_{(s)}^>(\tau) = \tilde{U}_{(s)}^>(\tau) d^> v^>, \quad \text{and} \quad U_{(s)}^<(\tau) = v^< d^< \tilde{U}_{(s)}^<(\tau), \quad (98)$$

813 such that $\tilde{U}_{(s)}^>(\tau)$ corresponds to a set of column-wise orthogonal vectors. It can be readily
 814 seen that scales can be omitted, since

$$G(x, \sigma, s, \tau | x', \sigma, s, \tau) = \left[1 - \tilde{U}_{(s)}^>(\tau) \left(\tilde{U}_{(s)}^<(\tau) \tilde{U}_{(s)}^>(\tau) \right)^{-1} \tilde{U}_{(s)}^<(\tau) \right]_{x,x'}. \quad (99)$$

815 Hence, stabilization is never an issue for the projective code, and arbitrarily large projection
 816 parameters can be reached.

817 The form of the Green function matrix implies that it is a projector: $G^2 = G$. This property
 818 has been used in Ref. [129] to very efficiently compute imaginary-time-displaced correlation
 819 functions.

820 3.3 Comparison of finite and projective codes

821 The finite temperature code operates in the grand canonical ensemble, whereas in the projec-
 822 tive approach the particle number is fixed. On finite lattices, the comparison between both
 823 approaches can only be made at a temperature scale below which a finite-sized charge gap
 824 emerges. In Fig. 3 we consider a semi-metallic phase as realized by the Hubbard model on the
 825 Honeycomb lattice at $U/t = 2$. It is evident that, at a scale below which charge fluctuations
 826 are suppressed, both algorithms yield identical results.

827 4 Monte Carlo sampling

828 Error estimates in Monte Carlo simulations are based on the central limit theorem [131] and
 829 can be a delicate matter, especially as it requires independent measurements and a finite vari-
 830 ance. In this section we give examples of the care that must be taken to satisfy these require-
 831 ments when using a Monte Carlo code. This is part of the common lore of the field and we
 832 cover them briefly in this text. For a deeper understanding of the inherent issues of Markov-
 833 chain Monte Carlo methods we refer the reader to the pedagogical introduction in chapter

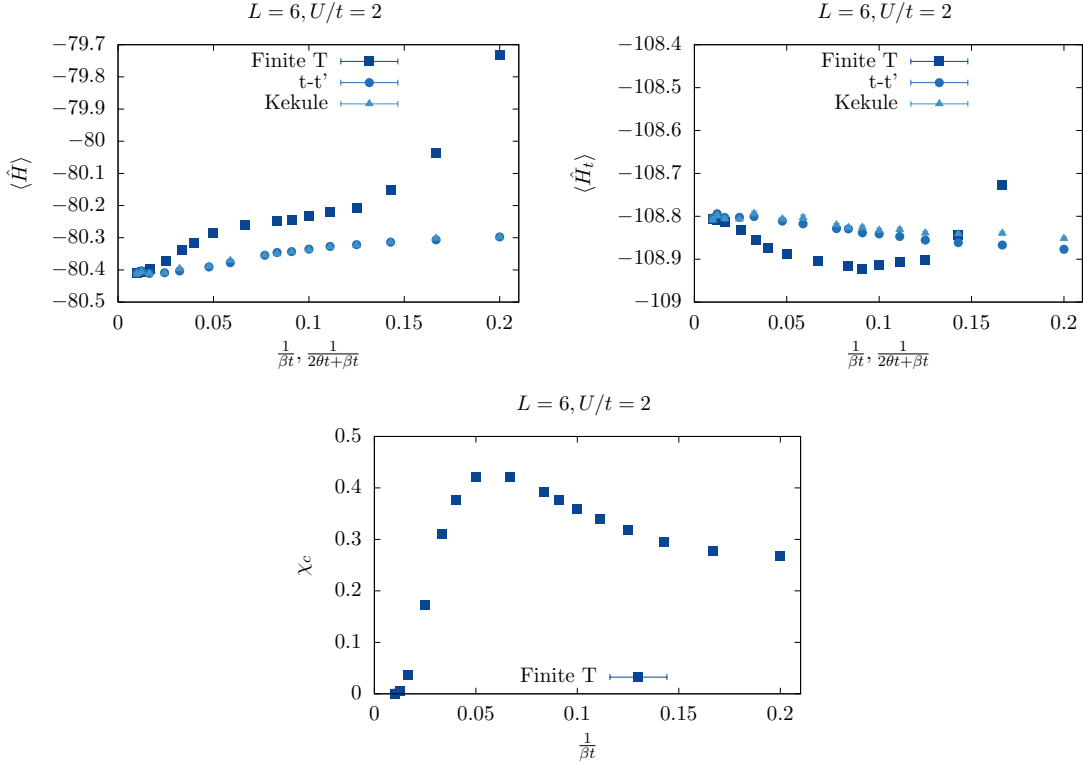


Figure 3: Comparison between the finite-temperature and projective codes for the Hubbard model on a 6×6 Honeycomb lattice at $U/t = 2$ and with periodic boundary conditions. For the projective code (blue and black symbols) $\beta t = 1$ is fixed, while θ is varied. In all cases we have $\Delta\tau t = 0.1$, no checkerboard decomposition, and a symmetric Trotter decomposition. For this lattice size and choice of boundary conditions, the non-interacting ground state is degenerate, since the Dirac points belong to the discrete set of crystal momenta. In order to generate the trial wave function we have lifted this degeneracy by either including a Kékulé mass term [46] that breaks translation symmetry (blue symbols), or by adding a next-next nearest neighbor hopping (black symbols) that breaks the symmetry nematically and shifts the Dirac points away from the zone boundary [130]. As apparent, both choices of trial wave functions yield the same answer, which compares very well with the finite temperature code at temperature scales below the finite-size charge gap.

834 1.3.5 of Krauth [132], the overview article of Sokal [82], the more specialized literature by
 835 Geyer [133] and chapter 6.3 of Neal [134].

836 In general, one distinguishes local from global updates. As the name suggest, the local
 837 update corresponds to a small change of the configuration, e.g., a single spin flip of one of the
 838 $L_{\text{Trotter}}(M_I + M_V)$ field entries (see Sec. 2.2), whereas a global update changes a significant
 839 part of the configuration. The default update scheme of the ALF implementation are local
 840 updates, such that there is a minimum number of moves required for generating an indepen-
 841 dent configuration. The associated time scale is called the autocorrelation time, T_{auto} , and is
 842 generically dependent upon the choice of the observables.

843 We call a *sweep* a sequential propagation from $\tau = 0$ to $\tau = L_{\text{Trotter}}$ and back, such that each
 844 field is visited twice in each sweep. A single sweep will generically not suffice to produce an
 845 independent configuration. In fact, the autocorrelation time T_{auto} characterizes the required
 846 time scale to generate independent values of $\langle\langle \hat{O} \rangle\rangle_C$ for the observable O . This has several

847 consequences for the Monte Carlo simulation:

- 848 • First of all, we start from a randomly chosen field configuration, such that one has to
849 invest a time of *at least* one T_{auto} , but typically many more, in order to generate relevant,
850 equilibrated configurations before reliable measurements are possible. This phase
851 of the simulation is known as the warm-up or burn-in phase. In order to keep the code as
852 flexible as possible (as different simulations might have different autocorrelation times),
853 measurements are taken from the very beginning and, in the analysis phase, the param-
854 eter `n_skip` controls the number of initial bins that are ignored.
- 855 • Second, our implementation averages over bins with NSWEEPS measurements before
856 storing the results on disk. The error analysis requires statistically independent bins in
857 order to generate reliable confidence estimates. If the bins are too small (averaged over
858 a period shorter than T_{auto}), then the error bars are typically underestimated. Most of
859 the time, however, the autocorrelation time is unknown before the simulation is started
860 and, sometimes, single runs long enough to generate appropriately sized bins are not
861 feasible. For this reason, we provide a rebinning facility controlled by the parameter
862 `N_rebin` that specifies the number of bins recombined into each new bin during the
863 error analysis. One can test the suitability of a given bin size by verifying whether an
864 increase in size changes the error estimate (For an explicit example, see Sec. 4.2 and the
865 appendix of Ref. [93]).
- 866 • The `N_rebin` variable can be used to control a further issue. The distribution of the
867 Monte Carlo estimates $\langle\langle \hat{O} \rangle\rangle_C$ is unknown, while a result in the form (mean \pm error)
868 assumes a Gaussian distribution. Every distribution with a finite variance turns into a
869 Gaussian one once it is folded often enough (central limit theorem). Due to the internal
870 averaging (folding) within one bin, many observables are already quite Gaussian. Other-
871 wise one can increase `N_rebin` further, even if the bins are already independent [135].
- 872 • The last issue we mention concerns time-displaced correlation functions. Even if the
873 configurations are independent, the fields within the configuration are still correlated.
874 Hence, the data for $S_{\alpha,\beta}(\mathbf{k}, \tau)$ [see Sec. 5.4; Eq. (123)] and $S_{\alpha,\beta}(\mathbf{k}, \tau + \Delta\tau)$ are also
875 correlated. Setting the switch `N_Cov=1` triggers the calculation of the covariance matrix
876 in addition to the usual error analysis. The covariance is defined by

$$\text{COV}_{\tau\tau'} = \frac{1}{N_{\text{Bin}}} \left\langle (S_{\alpha,\beta}(\mathbf{k}, \tau) - \langle S_{\alpha,\beta}(\mathbf{k}, \tau) \rangle)(S_{\alpha,\beta}(\mathbf{k}, \tau') - \langle S_{\alpha,\beta}(\mathbf{k}, \tau') \rangle) \right\rangle. \quad (100)$$

877 An example where this information is necessary is the calculation of mass gaps extracted
878 by fitting the tail of the time-displaced correlation function. Omitting the covariance
879 matrix will underestimate the error.

880 4.1 The Jackknife resampling method

881 For each observable $\hat{A}, \hat{B}, \hat{C}, \dots$ the Monte Carlo program computes a data set of N_{Bin} (ideally)
882 independent values where for each observable the measurements belong to the same statis-
883 tical distribution. In the general case, we would like to evaluate a function of expectation
884 values, $f(\langle \hat{A} \rangle, \langle \hat{B} \rangle, \langle \hat{C} \rangle \dots)$ – see for example the expression (27) for the observable including
885 reweighting – and are interested in the statistical estimates of its mean value and the standard
886 error of the mean. A numerical method for the statistical analysis of a given function f which
887 properly handles error propagation and correlations among the observables is the Jackknife
888 method, which is, like the related Bootstrap method, a resampling scheme [136]. Here we
889 briefly review the *delete-1 Jackknife* scheme, which consists in generating N_{bin} new data sets of

size $N_{\text{bin}} - 1$ by consecutively removing one data value from the original set. By $A_{(i)}$ we denote the arithmetic mean for the observable \hat{A} , without the i -th data value A_i , namely

$$A_{(i)} \equiv \frac{1}{N_{\text{Bin}} - 1} \sum_{k=1, k \neq i}^{N_{\text{Bin}}} A_k. \quad (101)$$

As the corresponding quantity for the function $f(\langle \hat{A} \rangle, \langle \hat{B} \rangle, \langle \hat{C} \rangle, \dots)$, we define

$$f_{(i)}(\langle \hat{A} \rangle, \langle \hat{B} \rangle, \langle \hat{C} \rangle, \dots) \equiv f(A_{(i)}, B_{(i)}, C_{(i)}, \dots). \quad (102)$$

Following the convention in the literature, we will denote the final Jackknife estimate of the mean by $f_{(.)}$ and its standard error by Δf . The Jackknife mean is given by

$$f_{(.)}(\langle \hat{A} \rangle, \langle \hat{B} \rangle, \langle \hat{C} \rangle, \dots) = \frac{1}{N_{\text{Bin}}} \sum_{i=1}^{N_{\text{Bin}}} f_{(i)}(\langle \hat{A} \rangle, \langle \hat{B} \rangle, \langle \hat{C} \rangle, \dots), \quad (103)$$

and the standard error, including bias correction, is given by

$$(\Delta f)^2 = \frac{N_{\text{Bin}} - 1}{N_{\text{Bin}}} \sum_{i=1}^{N_{\text{Bin}}} [f_{(i)}(\langle \hat{A} \rangle, \langle \hat{B} \rangle, \langle \hat{C} \rangle, \dots) - f_{(.)}(\langle \hat{A} \rangle, \langle \hat{B} \rangle, \langle \hat{C} \rangle, \dots)]^2. \quad (104)$$

For $f = \langle \hat{A} \rangle$, the equations (103) and (104) reduce to the plain sample average and the standard, bias-corrected, estimate of the error.

4.2 An explicit example of error estimation

In the following we use one of our examples, the Hubbard model on a square lattice in the M_z HS decoupling (see Sec. 9.1), to show explicitly how to estimate errors. We show as well that the autocorrelation time is dependent on the choice of observable. In fact, different observables within the same run can have different autocorrelation times and, of course, this time scale depends on the parameter choice. Hence, the user has to check autocorrelations of individual observables for each simulation! Typical regions of the phase diagram that require special attention are critical points where length scales diverge.

In order to determine the autocorrelation time, we calculate the correlation function

$$S_{\hat{O}}(t_{\text{Auto}}) = \sum_{i=1}^{N_{\text{Bin}} - t_{\text{Auto}}} \frac{(O_i - \langle \hat{O} \rangle)(O_{i+t_{\text{Auto}}} - \langle \hat{O} \rangle)}{(O_i - \langle \hat{O} \rangle)(O_i - \langle \hat{O} \rangle)}, \quad (105)$$

where O_i refers to the Monte Carlo estimate of the observable \hat{O} in the i^{th} bin. This function typically shows an exponential decay and the decay rate defines the autocorrelation time. Figure 4(a) shows the autocorrelation functions $S_{\hat{O}}(t_{\text{Auto}})$ for three spin-spin-correlation functions [Eq. (123)] at momentum $\mathbf{k} = (\pi, \pi)$ and at $\tau = 0$:

$\hat{O} = S_{\hat{S}z}$ for the z spin direction, $\hat{O} = (S_{\hat{S}x} + S_{\hat{S}y})/2$ for the xy plane, and $\hat{O} = (S_{\hat{S}x} + S_{\hat{S}y} + S_{\hat{S}z})/3$ for the total spin. The Hubbard model has an SU(2) spin symmetry. However, we chose a HS field which couples to the z -component of the magnetization, M_z , such that each individual configuration breaks this symmetry. Of course, after Monte Carlo averaging one expects restoration of the symmetry. The model, on bipartite lattices, shows spontaneous spin-symmetry breaking at $T = 0$ and in the thermodynamic limit. At finite temperatures, and within the so-called renormalized classical regime, quantum antiferromagnets have a length scale that diverges exponentially with decreasing temperatures [137]. The parameter set chosen for Fig. 4 is non-trivial in the sense that it places the Hubbard model in

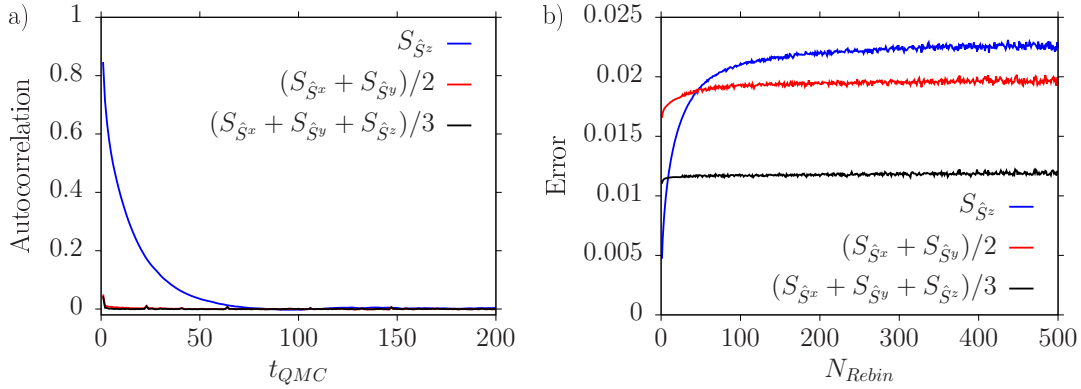


Figure 4: The autocorrelation function $S_{\hat{O}}(t_{Auto})$ (a) and the scaling of the error with effective bin size (b) of three equal-time, spin-spin correlation functions \hat{O} of the Hubbard model in the M_z decoupling (see Sec. 9.1). Simulations were done on a 6×6 square lattice, with $U/t = 4$ and $\beta t = 6$. We used $N_{auto} = 500$ (see Sec. 6) and a total of approximately one million bins. The original bin contained only one sweep and we calculated around one million bins on a single core. The different autocorrelation times for the xy -plane compared to the z -direction can be detected from the decay rate of the autocorrelation function (a) and from the point where saturation of the error sets in (b), which defines the required effective bin size for independent measurements. The improved estimator $(S_{\hat{S}x} + S_{\hat{S}y} + S_{\hat{S}z})/3$ appears to have the smallest autocorrelation time, as argued in the text.

920 this renormalized classical regime where the correlation length is substantial. Figure 4 clearly
 921 shows a very short autocorrelation time for the xy -plane whereas we detect a considerably
 922 longer autocorrelation time for the z -direction. This is a direct consequence of the *long* mag-
 923 netic length scale and the chosen decoupling. The physical reason for the long autocorrelation
 924 time corresponds to the restoration of the SU(2) spin symmetry. This insight can be used to
 925 define an improved, SU(2) symmetric estimator for the spin-spin correlation function, namely
 926 $(S_{\hat{S}x} + S_{\hat{S}y} + S_{\hat{S}z})/3$. Thereby, global spin rotations are no longer an issue and this improved
 927 estimator shows the shortest autocorrelation time, as can be clearly seen in Fig. 4(b). Other
 928 ways to tackle large autocorrelations are global updates and parallel tempering.

929 A simple method to obtain estimates of the mean and its standard error from the time
 930 series of Monte Carlo samples is provided by the aforementioned facility of rebinning. Also
 931 known in the literature as rebatching, it consists in aggregating a fixed number N_{rebin} of
 932 adjacent original bins into a new effective bin. In addition to measuring the decay rate of
 933 the autocorrelation function (Eq. (105)), a measure for the autocorrelation time can be also
 934 obtained by the rebinning method. For a comparison to other methods of estimating the auto-
 935 correlation time we refer the reader to the literature [133, 134, 138]. A reliable error analysis
 936 requires independent bins, otherwise the error is typically underestimated. This behavior is
 937 observed in Fig. 4 (b), where the effective bin size is systematically increased by rebinning. If
 938 the effective bin size is smaller than the autocorrelation time the error will be underestimated.
 939 When the effective bin size becomes larger than the autocorrelation time, converging behavior
 940 sets in and the error estimate becomes reliable.

941 4.3 Pseudocode description

942 The Monte Carlo algorithm as implemented in ALF is summarized in Alg. 1. Key control vari-
 943 ables include:

944	Projector	Uses (=true) the projective instead of finite- T algorithm (see Sec. 3)
945	L_τ	Measures ($\text{Ltau}=1$) time-displaced observables (see Sec. 2.1.2)
946	Tempering	Runs (=true) in parallel tempering mode (see Table 1)
947	Global_moves	Carries out (=true) global moves in a single time slice (see Table 1)
948	Sequential	Carries out (=true) sequential, single spin-flip updates (see Table 1)
949	Langevin	Uses (=true) Langevin dynamics instead of sequential (see Table 1)
950	Per default, the finite-temperature algorithm is used, $\text{Ltau}=0$, and the updating used	
951	is Sequential (i.e., Global_moves, Tempering and Langevin default values are all	
952	<code>.false.</code>).	

Algorithm 1 Basic structure of the QMC implementation in Prog/main.f90

```

954    > INITIALIZATION
955    1: call Fields_Init                                > Set the auxiliary fields
956    2: call Alloc_Ham
957    3: call ham%Ham_Set
958    4: call Nsigma%in
959    5: for n = L_Trotter to 1 do                  > Select Hamiltonian based on ham_name in parameters
960      6:   call Wrapul                               > Set the Hamiltonian and the lattice
961    7: end for

962    > MONTE CARLO RUN
963    8: for n_bc = 1 to N_Bin do                  > Read in an auxiliary-field configuration or generate it randomly
964      9:   for n_sw = 1 to N_Sweep do            > Fill the storage needed for the first actual MC sweep
965        10:     if Tempering then                > Compute propagation matrices and store them at stabilization points
966          11:       call Exchange_Step
967        12:     end if
968        13:     if Global_moves then           > Loop over bins. The bin defines the unit of Monte Carlo time
969          14:       call Global_Updates
970        15:     end if
971        16:     if Langevin then             > Loop over sweeps. Each sweep updates twice (upward and
972          17:       call Langevin_update
973          18:       if Lτ == 1 then           > downward in imaginary time) the space-time lattice of auxil-
974            19:         if Projector then       iary fields
975              20:           call Tau_p
976            21:         else
977              22:           call Tau_m
978            23:         end if
979        24:     end if
980        25:   end if (Langevin)
981        26:   if Sequential then           > UPDATE AND MEASURE equal-time observables
982
983        > UPWARD SWEEP
984        27:   for nτ = 1 to L_Trotter do      > MEASURE time-displaced observables (projective code)
985          28:     call Wrapgrup
986          29:     if nτ == stabilization point in imaginary time then > PROPAGATE Green function from nτ - 1 to nτ, and compute
987            30:       call Wrapur
988
989        > STABILIZE
990        31:   end if
991
992        > DOWNWARD SWEEP
993        32:   for nτ = L_Trotter to 1 do
994         33:     call Wrapgrup
995         34:     if nτ == stabilization point in imaginary time then > Propagate from previous stabilization point to nτ
996           35:       call Wrapur
997
998        > FINALIZE
999        36:   end if
999
9999

```

```

987          ▷ Storage management:
988          - Read from storage: propagation from  $L_{Trotter}$  to  $n_\tau$ 
989          - Write to storage: the just computed propagation
990          call CGR           ▷ Recalculate the Green function at time  $n_\tau$  in a stable way
991          call Control_PrecisionG   ▷ Compare propagated and recalculated Greens
992          end if
993          if  $n_\tau \in [\text{Lobs\_st}, \text{Lobs\_en}]$  then
994              call ham%Obser           ▷ MEASURE the equal-time observables
995          end if
996          end for
997          ▷ DOWNWARD SWEEP
998          for  $n_\tau = L_{Trotter}$  to 1 do
999              ▷ Same steps as for the upward sweep (propagation and estimate update, stabilization,
1000                 equal-time measurements) now downwards in imaginary time
1001              if Projector and  $L_\tau == 1$  and
1002                   $n_\tau$  = stabilization point in imaginary time and
1003                  the projection time  $\theta$  is within the measurement interval then
1004                      call Tau_p           ▷ MEASURE time-displaced observables (projective code)
1005              end if
1006          end for
1007          ▷ MEASURE time-displaced observables (finite temperature)
1008          if  $L_\tau == 1$  and not Projector then
1009              call Tau_m
1010          end if
1011          end if (Sequential)
1012      end for (Sweeps)
1013      call ham%Pr_obs           ▷ Calculate and write to disk measurement averages for current bin
1014      call Nsigma%out           ▷ Write auxiliary field configuration to disk
1015  end for (Bins)

```

1013 5 Data structures and input/output

1014 To manipulate the relevant physical quantities in a general model, we define a set of corre-
 1015 sponding data types. The Operator type (Sec. 5.1) is used to specify the interaction as well
 1016 as the hopping. The handling of the fields is taken care of by the Fields type (Sec. 5.2). To
 1017 define a Bravais lattice as well as a unit cell we introduce the Lattice and Unit_cell types
 1018 (Sec. 5.3). General scalar, equal-time, and time-displaced correlation functions are handled by
 1019 the Observable type (Sec. 5.4). For the projective code, we provide a WaveFunction type
 1020 (Sec. 5.5) to specify the left and right trial wave functions. The Hamiltonian is then specified
 1021 in the Hamiltonian module (Sec. 5.6), making use of the aforementioned types.

1022 5.1 The Operator type

1023 The fundamental data structure in the code is the Operator. It is implemented as a Fortran
 1024 derived data type designed to efficiently define the Hamiltonian (2).

Table 2: Member variables of the `Operator` type. In the left column, the letter X is a placeholder for the letters T and V, indicating hopping and interaction operators, respectively. The highlighted variables must be specified by the user. M_exp and E_exp are allocated only if type = 1, 2.

Variable	Type	Description
Op_X%N	int	Effective dimension N
Op_X%O	cmplx	Matrix O of dimension $N \times N$
Op_X%P	int	Matrix P encoded as a vector of dimension N
Op_X%g	cmplx	Coupling strength g
Op_X%alpha	cmplx	Constant α
Op_X%type	int	Sets the type of HS transformation (1: Ising; 2: discrete HS for perfect-square term; 3: continuous real field)
Op_X%diag	logical	True if O is diagonal
Op_X%U	cmplx	Matrix containing the eigenvectors of O
Op_X%E	dbl	Eigenvalues of O
Op_X%N_non_zero	int	Number of non-vanishing eigenvalues of O
Op_X%M_exp	cmplx	Stores M_exp(:, :, s) = $e^{g\phi(s, \text{type})O(:, :)}$
Op_X%E_exp	cmplx	Stores E_exp(:, s) = $e^{g\phi(s, \text{type})E(:, :)}$

1025 Let the matrix X of dimension $N_{\text{dim}} \times N_{\text{dim}}$ stand for any of the typically sparse, Hermitian
 1026 matrices $T^{(ks)}$, $V^{(ks)}$ and $I^{(ks)}$ that define the Hamiltonian. Furthermore, let $\{z_1, \dots, z_N\}$ denote
 1027 the subset of N indices such that

$$X_{x,y} = \begin{cases} \neq 0, & \text{if } x, y \in \{z_1, \dots, z_N\}, \\ = 0, & \text{otherwise.} \end{cases} \quad (106)$$

1028 Usually, we have $N \ll N_{\text{dim}}$. We define the $N \times N_{\text{dim}}$ matrices P as

$$P_{i,x} = \delta_{z_i, x}, \quad (107)$$

1029 where $i \in [1, \dots, N]$ and $x \in [1, \dots, N_{\text{dim}}]$. The matrix P selects the non-vanishing entries of
 1030 X , which are contained in the rank- N matrix O defined by:

$$X = P^T O P, \quad (108)$$

1031 and

$$X_{x,y} = \sum_{i,j}^N P_{i,x} O_{i,j} P_{j,y} = \sum_{i,j}^N \delta_{z_i, x} O_{ij} \delta_{z_j, y}. \quad (109)$$

1032 Since the P matrices have only one non-vanishing entry per column, they can conveniently be
 1033 stored as a vector P , with entries

$$P_i = z_i. \quad (110)$$

1034 There are many useful identities which emerge from this structure. For example:

$$e^X = e^{P^T O P} = \sum_{n=0}^{\infty} \frac{(P^T O P)^n}{n!} = \mathbb{1} + P^T (e^O - \mathbb{1}) P, \quad (111)$$

1035 since

$$P P^T = \mathbb{1}_{N \times N}. \quad (112)$$

1036 In the code, we define a structure called `Operator` that makes use of the properties de-
 1037 scribed above. This type `Operator` bundles the several components, listed in Table 2 and
 1038 described in the remaining of this section, that are needed to define and use an operator ma-
 1039 trix in the program.

1040 **5.2 Handling of the fields: The Fields type**

1041 The partition function (see Sec. 2.1) consists of terms which, in general, can be written as
 1042 $\gamma e^{g\phi^X}$, where X denotes an arbitrary operator, g is a constant, and γ and ϕ are fields. The
 1043 ALF includes three different types of fields:

1044 $t=1$ This type is for an Ising field, therefore $\gamma = 1$ and $\phi = \pm 1$,

1045 $t=2$ This type is for the generic HS transformation of Eq. (11) where $\gamma \equiv \gamma(l)$ and $\phi = \eta(l)$
 1046 with $l = \pm 1, \pm 2$ [see Eq. (12)],

1047 $t=3$ This type is for continuous fields, i.e., $\gamma = 1$ and $\phi \in \mathbb{R}$.

1048 For such auxiliary fields a dedicated type `Fields` is defined, whose components, listed
 1049 in Table 3, include the variables `Field%f` and `Field%t`, which store the field values and
 1050 types, respectively, and functions such as `Field%flip`, which flips the field values randomly.
 1051 Before using this variable type, the routine `Fields_init(Amplitude)` should be called (its
 1052 argument is optional and the default value is of unity (see Sec. 2.2.1), in order for internal
 1053 variables such as $\eta(l)$ and $\gamma(l)$ [see Eq. (12)] to be initialized.

1054 **5.3 The Lattice and Unit_cell types**

1055 ALF's lattice module can generate one- and two-dimensional Bravais lattices. Both the lattice
 1056 and the unit cell are defined in the module `lattices_v3_mod.F90` and their components are
 1057 detailed in Tables 4 and 5. As its name suggest the module `Predefined_Latt_mod.F90` also
 1058 provides predefined lattices as described in Sec. 8.1. The user who wishes to define his/her
 1059 own lattice has to specify: 1) unit vectors a_1 and a_2 , 2) the size and shape of the lattice, char-
 1060 acterized by the vectors L_1 and L_2 and 3) the unit cell characterized by the number of orbitals
 1061 and their positions. The coordination number of the lattice is specified in the `Unit_cell` data
 1062 type. The lattice is placed on a torus (periodic boundary conditions):

$$\hat{c}_{i+L_1} = \hat{c}_{i+L_2} = \hat{c}_i. \quad (113)$$

1063 The function call

1064 `Call Make_Lattice(L1, L2, a1, a2, Latt)`

1067 generates the lattice `Latt` of type `Lattice`. The reciprocal lattice vectors g_j are defined by:

$$a_i \cdot g_j = 2\pi\delta_{i,j}, \quad (114)$$

1068 and the Brillouin zone BZ corresponds to the Wigner-Seitz cell of the lattice. With $k = \sum_i \alpha_i g_i$,
 1069 the k-space quantization follows from:

$$\begin{bmatrix} L_1 \cdot g_1 & L_1 \cdot g_2 \\ L_2 \cdot g_1 & L_2 \cdot g_2 \end{bmatrix} \begin{bmatrix} \alpha_1 \\ \alpha_2 \end{bmatrix} = 2\pi \begin{bmatrix} n \\ m \end{bmatrix}, \quad (115)$$

1070 such that

$$k = nb_1 + mb_2, \quad \text{with} \quad (116)$$

$$b_1 = \frac{2\pi}{(L_1 \cdot g_1)(L_2 \cdot g_2) - (L_1 \cdot g_2)(L_2 \cdot g_1)} [(L_2 \cdot g_2)g_1 - (L_1 \cdot g_1)g_2],$$

$$b_2 = \frac{2\pi}{(L_1 \cdot g_1)(L_2 \cdot g_2) - (L_1 \cdot g_2)(L_2 \cdot g_1)} [(L_1 \cdot g_1)g_2 - (L_2 \cdot g_2)g_1]. \quad (117)$$

Table 3: Components of a variable of type `Fields` named `Field`. The routine `Fields_init(del)` should be called before the use of this variable type, since it initializes necessary internal variables such as $\eta(l)$, $\gamma(l)$ [see Eq. (12)]. Note that `del` and `amplitude` are private variables of the `fields` module. The integers `n_op` and `Ltrot` are the number of interacting operators per time slice and time slices, respectively, `Group_Comm` (integer) is an MPI communicator defined by the main program, and the optional `In_field` stores the initial field configuration.

Component	Description	
Variable	Type	
<code>Field%t(1:n_op)</code>	int	Sets the HS transformation type (1: Ising; 2: discrete HS for perfect-square term; 3: continuous real field). The index runs through the operator sequence
<code>Field%f(1:n_op, 1:Ltrot)</code>	dble	Defines the auxiliary fields. The first index runs through the operator sequence and the second through the time slices. For $t=1$, $f = \pm 1$; for $t=2$, $f = \pm 1, \pm 2$; and for $t=3$, $f \in \mathbb{R}$
<code>del</code>	dble	Width Δx of box distribution for initial $t=3$ fields, with a default value of 1
<code>amplitude</code>	dble	Random flip width for fields of type $t=3$, defaults to 1
Method(arguments)		
<code>Field%make(n_op,Ltrot)</code>	Reserves memory for the field	
<code>Field%clear()</code>	Clears field from memory	
<code>Field%set()</code>	Sets a random configuration	
<code>Field%flip(n,nt)</code>	Flips the field values randomly for field n on time slice nt . For $t=1$ it flips the sign of the Ising spin. For $t=2$ it randomly choose one of the three other values of l . For $t=3$, $f = f + amplitude*(ranf() - 1/2)$	
<code>Field%phi(n,nt)</code>	Returns ϕ for the n -th operator at the time slice nt	
<code>Field%gamma(n,nt)</code>	Returns γ for the n -th operator at the time slice nt	
<code>Field%i(n,nt)</code>	Returns <code>Field%f</code> rounded to nearest integer (if $t=1$ or 2)	
<code>Field%in(Group_Comm, In_field)</code>	If the file <code>conf_in_np</code> (or <code>conf_in_np.h5</code>) exists it reads the field configuration from this file. Otherwise if <code>In_field</code> is present it sets the fields to <code>In_field</code> . If both <code>conf_in_np.h5</code> and <code>In_field</code> are not provided it sets a random field by calling <code>Field%set()</code> . Here <code>np</code> is the rank number of the process	
<code>Field%out(Group_Comm)</code>	Writes out the field configuration	

1071 The Lattice module also handles the Fourier transformation. For example, the subroutine
 1072 `Fourier_R_to_K` carries out the transformation:

$$S(\mathbf{k}, :, :, :) = \frac{1}{N_{\text{unit-cell}}} \sum_{i,j} e^{-i\mathbf{k} \cdot (\mathbf{i}-\mathbf{j})} S(\mathbf{i}-\mathbf{j}, :, :, :), \quad (118)$$

1073 and `Fourier_K_to_R` the inverse Fourier transform

$$S(\mathbf{r}, :, :, :) = \frac{1}{N_{\text{unit-cell}}} \sum_{\mathbf{k} \in BZ} e^{i\mathbf{k} \cdot \mathbf{r}} S(\mathbf{k}, :, :, :). \quad (119)$$

Table 4: Components of the Lattice type for two-dimensional lattices using as example the default lattice name Latt. The highlighted variables must be specified by the user. Other components of Lattice are generated upon calling: Call `Make_Lattice(L1, L2, a1, a2, Latt)`.

Variable	Type	Description
<code>Latt%a1_p, Latt%a2_p</code>	dble	Unit vectors $\mathbf{a}_1, \mathbf{a}_2$
<code>Latt%L1_p, Latt%L2_p</code>	dble	Vectors $\mathbf{L}_1, \mathbf{L}_2$ that define the topology of the lattice Tilted lattices are thereby possible to implement
<code>Latt%N</code>	int	Number of lattice points, $N_{\text{unit-cell}}$
<code>Latt%list</code>	int	Maps each lattice point $i = 1, \dots, N_{\text{unit-cell}}$ to a real space vector denoting the position of the unit cell: $\mathbf{R}_i = \text{list}(i, 1)\mathbf{a}_1 + \text{list}(i, 2)\mathbf{a}_2 \equiv i_1\mathbf{a}_1 + i_2\mathbf{a}_2$
<code>Latt%invlist</code>	int	Return lattice point from position: $\text{Invlist}(i_1, i_2) = i$
<code>Latt%nnlist</code>	int	Nearest neighbor indices: $j = \text{nnlist}(i, n_1, n_2)$, $n_1, n_2 \in [-1, 1]$, $\mathbf{R}_j = \mathbf{R}_i + n_1\mathbf{a}_1 + n_2\mathbf{a}_2$
<code>Latt%imj</code>	int	$\mathbf{R}_{\text{imj}(i, j)} = \mathbf{R}_i - \mathbf{R}_j$, with $\text{imj}, i, j \in 1, \dots, N_{\text{unit-cell}}$
<code>Latt%BZ1_p, Latt%BZ2_p</code>	dble	Reciprocal space vectors \mathbf{g}_i [See Eq. (114)]
<code>Latt%b1_p, Latt%b2_p</code>	dble	k -quantization [See Eq. (117)]
<code>Latt%listk</code>	int	Maps each reciprocal lattice point $k = 1, \dots, N_{\text{unit-cell}}$ to a reciprocal space vector $\mathbf{k}_k = \text{listk}(k, 1)\mathbf{b}_1 + \text{listk}(k, 2)\mathbf{b}_2 \equiv k_1\mathbf{b}_1 + k_2\mathbf{b}_2$
<code>Latt%invlistk</code>	int	$\text{Invlistk}(k_1, k_2) = k$
<code>Latt%b1_perp_p,</code> <code>Latt%b2_perp_p</code>	dble	Orthonormal vectors to \mathbf{b}_i (for internal use)

1074 In the above, the unspecified dimensions of the structure factor can refer to imaginary-time
 1075 and orbital indices.

1076 The position of an orbital i is given by $\mathbf{R}_i + \delta_i$. \mathbf{R}_i is a point of the Bravais lattice that
 1077 defines a unit cell, and δ_i labels the orbital in the unit cell. This information is stored in the
 1078 array `Unit_cell%Orb_pos` detailed in Table 5.

1079 The total number of orbitals is then given by `Ndim=Lattice%N*Unit_cell%Norb`. To
 1080 keep track of the orbital and unit cell structure, it is useful to define arrays `List(Ndim, 2)`
 1081 and `Inv_list(Latt%N, Unit_cell%Norb)`. For a superindex $x = (i, n)$ labeling the unit
 1082 cell, i , and the orbital, n , of a site on the lattice, we have `List(x, 1)=i`, `List(x, 2)=n` and
 1083 `Inv_list(i, n)=x`.

Table 5: Components of an instance `Latt_unit` of the `Unit_cell` type. The highlighted variables have to be specified by the user. Note that for bilayer lattices the second index of the `Orb_pos` array ranges from 1 to 3.

Variable	Type	Description
<code>Norb</code>	int	Number of orbitals
<code>N_coord</code>	int	Coordination number
<code>Orb_pos(1..Norb, 2[3])</code>	dble	Orbitals' positions, measured from the lattice site

Table 6: Components of a variable of type `Obser_vec`. The contribution listed is that of each configuration C .

Variable	Type	Description	Contribution
N	int	Number of measurements	+1
Ave_sign	dble	Cumulated average sign [Eq. (28)]	$\text{sgn}(C)$
Obs_vec(:)	cmplx	Cumulated vector of observables [Eq. (27)]	$\langle\langle \hat{O}(:) \rangle\rangle_C \frac{e^{-S(C)}}{\text{Re}[e^{-S(C)}]} \text{sgn}(C)$
File_Vec	char	Name of output file	
analysis_mode	char	How to analyze the observable Default value: “identity”	
description(:)	char	Optional description.	Arbitrary number of 64-character lines

5.4 The observable types `Obser_Vec` and `Obser_Latt`

Our definition of the model includes observables [Eq. (27)]. We define two observable types: `Obser_vec` for an array of *scalar* observables such as the energy, and `Obser_Latt` for correlation functions that have the lattice symmetry. In the latter case, translation symmetry can be used to provide improved estimators and to reduce the size of the output. We also obtain improved estimators by taking measurements in the imaginary-time interval $[LOBS_ST, LOBS_EN]$ (see the parameter file in Sec. 5.7.1) thereby exploiting the invariance under translation in imaginary-time. Note that the translation symmetries in space and in time are *broken* for a given configuration C but restored by the Monte Carlo sampling. In general, the user defines size and number of bins in the parameter file, each bin containing a given amount of sweeps. Within a sweep we run sequentially through the HS and bosonic fields, from time slice 1 to time slice L_{Trotter} and back. The results of each bin are written to a file and analyzed at the end of the run.

To accomplish the reweighting of observables (see Sec. 2.1.3), for each configuration the measured value of an observable is multiplied by the factors ZS and ZP:

$$ZS = \text{sgn}(C), \quad (120)$$

$$ZP = \frac{e^{-S(C)}}{\text{Re}[e^{-S(C)}]}. \quad (121)$$

They are computed from the Monte Carlo phase of a configuration,

$$\text{phase} = \frac{e^{-S(C)}}{|e^{-S(C)}|}, \quad (122)$$

which is provided by the main program. Note that each observable structure also includes the average sign [Eq. (28)].

5.4.1 Scalar observables

Scalar observables are stored in the data type `Obser_vec`, described in Table 6. Consider a variable `Obs` of type `Obser_vec`. At the beginning of each bin, a call to `Obser_Vec_Init` in the module `observables_mod.F90` will set `Obs%N=0`, `Obs%Ave_sign=0` and `Obs%Obs_vec(:)=0`. Each time the main program calls the routine `Obser` in the Hamiltonian module, the counter `Obs%N` is incremented by one, the sign [see Eq. (26)] is accumulated in the variable `Obs%Ave_sign`, and the desired observables (multiplied by the sign and $\frac{e^{-S(C)}}{\text{Re}[e^{-S(C)}]}$, see Sec. 2.1.2) are accumulated in the vector `Obs%Obs_vec`.

Table 7: Components of a variable of type `Obser_latt` named `Obs`. Be aware: The types marked with asterisks, `*`, are actually pointers, i.e., when the subroutine `Obser_Latt_make` creates an observable `Obs`, the variables `Latt` and `Latt_unit` do not get copied but linked, meaning modifying them after the creation of `Obs` still affects the observable.

Variable	Type	Description	Contribution
<code>Obs%N</code>	<code>int</code>	Number of measurements	+1
<code>Obs%Ave_sign</code>	<code>dble</code>	Cumulated sign [Eq. (28)]	$\text{sgn}(C)$
<code>Obs%Obs_latt(i-j, τ, α, β)</code>	<code>cmplx</code>	Cumulated correlation function [Eq. (27)]	$\langle\langle \hat{O}_{i,\alpha}(\tau) \hat{O}_{j,\beta} \rangle\rangle_C \times \frac{e^{-S(C)}}{\text{Re}[e^{-S(C)}]} \text{sgn}(C)$
<code>Obs%Obs_latt0(α)</code>	<code>cmplx</code>	Cumulated expected value [Eq. (27)]	$\langle\langle \hat{O}_{i,\alpha} \rangle\rangle_C \times \frac{e^{-S(C)}}{\text{Re}[e^{-S(C)}]} \text{sgn}(C)$
<code>Obs%File_Latt</code>	<code>char</code>	Name of output file	
<code>Obs%Latt</code>	<code>Lattice*</code>	Bravais lattice [Tab. 4]	
<code>Obs%Latt_unit</code>	<code>Unit_cell*</code>	Unit cell [Tab. 5]	
<code>Obs%dtau</code>	<code>dble</code>	Imaginary time step	
<code>Obs%Channel</code>	<code>char</code>	Channel for Maximum Entropy	

1110 At the end of the bin, a call to `Print_bin_Vec` in module `observables_mod.F90` will
 1111 append the result of the bin in the file `File_Vec_scal`. Note that this subroutine will automatically
 1112 append the suffix `_scal` to the the filename `File_Vec`. This suffix is important to facilitate
 1113 automatic analyses of the data at the end of the run. Furthermore, the file `File_Vec_scal_info`
 1114 is created (if it does not exist yet), which contains a string that specifies how to analyze the
 1115 observable and an optional description.

1116 5.4.2 Equal-time and time-displaced correlation functions

1117 The data type `Obser_latt` (see Table 7) is useful for dealing with both equal-time and
 1118 imaginary-time-displaced correlation functions of the form:

$$1119 S_{\alpha,\beta}(\mathbf{k}, \tau) = \frac{1}{N_{\text{unit-cell}}} \sum_{i,j} e^{-i\mathbf{k}\cdot(i-j)} (\langle\langle \hat{O}_{i,\alpha}(\tau) \hat{O}_{j,\beta} \rangle\rangle - \langle\langle \hat{O}_{i,\alpha} \rangle\rangle \langle\langle \hat{O}_{j,\beta} \rangle\rangle), \quad (123)$$

1119 where α and β are orbital indices and i and j lattice positions. Here, translation symmetry of
 1120 the Bravais lattice is explicitly taken into account. The correlation function splits in a correlated
 1121 part $S_{\alpha,\beta}^{(\text{corr})}(\mathbf{k}, \tau)$ and a background part $S_{\alpha,\beta}^{(\text{back})}(\mathbf{k})$:

$$1122 S_{\alpha,\beta}^{(\text{corr})}(\mathbf{k}, \tau) = \frac{1}{N_{\text{unit-cell}}} \sum_{i,j} e^{-i\mathbf{k}\cdot(i-j)} \langle\langle \hat{O}_{i,\alpha}(\tau) \hat{O}_{j,\beta} \rangle\rangle, \quad (124)$$

$$1123 S_{\alpha,\beta}^{(\text{back})}(\mathbf{k}) = \frac{1}{N_{\text{unit-cell}}} \sum_{i,j} e^{-i\mathbf{k}\cdot(i-j)} \langle\langle \hat{O}_{i,\alpha} \rangle\rangle \langle\langle \hat{O}_{j,\beta} \rangle\rangle \\ 1124 = N_{\text{unit-cell}} \langle\langle \hat{O}_\alpha \rangle\rangle \langle\langle \hat{O}_\beta \rangle\rangle \delta(\mathbf{k}), \quad (125)$$

1122 where translation invariance in space and time has been exploited to obtain the last line. The
 1123 background part depends only on the expectation value $\langle\langle \hat{O}_\alpha \rangle\rangle$, for which we use the following
 1124 estimator

$$1125 \langle\langle \hat{O}_\alpha \rangle\rangle \equiv \frac{1}{N_{\text{unit-cell}}} \sum_i \langle\langle \hat{O}_{i,\alpha} \rangle\rangle. \quad (126)$$

Table 8: Components of a variable of type `WaveFunction` named `WF`.

Variable	Type	Description
<code>WF%P(:, :)</code>	<code>cmplx</code>	P is an <code>Ndim</code> × <code>N_part</code> matrix, where <code>N_part</code> is the number of particles
<code>WF%Degen</code>	<code>dble</code>	It stores the energy difference between the last occupied and first unoccupied single particle state and can be used to check for degeneracy

1125 Consider a variable `Obs` of type `Obser_latt`. At the beginning of each bin a call to
 1126 `Obser_Latt_Init` in the module `observables_mod.F90` will initialize the elements of
 1127 `Obs` to zero. Each time the main program calls the `Obser` or `ObserT` routines one accumu-
 1128 lates $\langle \langle \hat{O}_{i,\alpha}(\tau) \hat{O}_{j,\beta} \rangle \rangle_C \frac{e^{-S(C)}}{\text{Re}[e^{-S(C)}]} \text{sgn}(C)$ in `Obs%Obs_latt(i-j, \tau, \alpha, \beta)` and $\langle \langle \hat{O}_{i,\alpha} \rangle \rangle_C \frac{e^{-S(C)}}{\text{Re}[e^{-S(C)}]} \text{sgn}(C)$ in
 1129 `Obs%Obs_latt0(\alpha)`. At the end of each bin, a call to `Print_bin_Latt` in
 1130 the module `observables_mod.F90` will append the result of the bin in the specified file
 1131 `Obs%File_Latt`. Note that the routine `Print_bin_Latt` carries out the Fourier trans-
 1132 formation and prints the results in k -space. We have adopted the following naming con-
 1133 ventions. For equal-time observables, defined by having the second dimension of the array
 1134 `Obs%Obs_latt(i-j, \tau, \alpha, \beta)` set to unity, the routine `Print_bin_Latt` attaches the suf-
 1135 fix `_eq` to `Obs%File_Latt`. For time-displaced correlation functions we use the suffix `_tau`.
 1136 Furthermore, `Print_bin_Latt` will create a corresponding info file with suffix `_eq_info` or
 1137 `_tau_info`, if not already present. The info file contains the channel, number of imaginary time
 1138 steps, length of one imaginary time step, unit cell and the vectors defining the Bravais lattice.

1139 5.5 The `WaveFunction` type

1140 The projective algorithm (Sec. 3) requires a pair of trial wave functions, $|\Psi_{T,L/R}\rangle$, for which
 1141 there is the dedicated `WaveFunction` type, defined in the module `WaveFunction_mod` as
 1142 described in Table 8.

1143 The module `WaveFunction_mod` also includes the routine `WF_overlap(WF_L, WF_R,`
 1144 `Z_norm)` for normalizing the right trial wave function `WF_R` by the factor `Z_norm`, such that
 1145 $\langle \Psi_{T,L} | \Psi_{T,R} \rangle = 1$.

1146 5.6 Specification of the Hamiltonian: The Hamiltonian module

1147 The module `Hamiltonian_main` in `Prog/Hamiltonian_main_mod.F90` defines the inter-
 1148 face for all model-specific variables and subroutines needed by the Monte Carlo algorithm,
 1149 like the hopping, the interaction, the observables, the trial wave function, and optionally up-
 1150 dating schemes (see Sec. 2.2). All Hamiltonians (which is the term we are using for an en-
 1151 capsulated model definition) are derived from this main Hamiltonian. In order to implement
 1152 a new user-defined Hamiltonian, one only has to set up a single submodule of the module
 1153 `Hamiltonian_main`. Accordingly, this documentation focuses almost entirely on this module
 1154 and how to derive a new model from it. The remaining parts of the code may hence be treated
 1155 as a black box.

1156 Table 9 shows all variables declared in `Hamiltonian_main`, they fully define the model.
 1157 Note that the procedures listed in Table 10 are part of the variable `ham`.

1158 To define a new Hamiltonian called `New_model`, one has to do two things:

- 1159 1. Add a new line `New_model` to the file `Prog/Hamiltonians.list`
- 1160 2. Write the new submodule in `Prog/Hamiltonians/Hamiltonian_New_model_`
 1161 `smod.F90`

1162 In this new submodule the user can redefine the procedures listed in Table 10, those have
 1163 to be bound to a new type, which is derived from the Hamiltonian object `ham_base`. The sub-
 1164 module has access to all variables defined in `Hamiltonian_main`, while all variables defined
 1165 in the submodule are encapsulated. To expose the new Hamiltonian, the user has to define

```
1166 module Subroutine Ham_Alloc_New_model
1167   allocate(ham_New_model::ham)
1168 end Subroutine Ham_Alloc_New_model
1169
```

1171 where `ham_New_model` is the name of the new type derived from `ham_base`. The rest of the
 1172 linking is done automatically through the entry in `Prog/Hamiltonians.list`.

1173 Hamiltonian variables to be read in through the parameters file should be written in a
 1174 specific format, since they will be parsed at compile time and subroutines for reading from
 1175 parameters file and writing the HDF5 file will be automatically generated. For each namelist,
 1176 there has to be block of this form:

```
1177 !#PARAMETERS START# <namelist_name>
1178 <var1_type> :: <var1_name> = <var1_default> ! <var1_description>
1179 <var2_type> :: <var2_name> = <var2_default> ! <var2_description>
1180 ...
1181 !#PARAMETERS END#
```

1184 Each of those “namelist specifications” starts with a line containing `#PARAMETERSSTART#`
 1185 and end with a line containing `#PARAMETERSEND#`. The namelist name has to be written
 1186 after `#PARAMETERSSTART#` on the same line. The variable type specification `<varX_type>`
 1187 should be either `real`, `integer`, `character` or `logical`, declared as `real(Kind=Kind(0.`
 1188 `d0))`, `integer`, `character(len=64)` or `logical` respectively. Each variable needs to have
 1189 a default value. The description of the parameters is optional. A variable can be commented
 1190 out, but will still be parsed to be read from parameters. This is to facilitate reading of variables
 1191 that are already defined in `Hamiltonian_main`, e.g. `N_SUN`.

1192 For example, a namelist called `my_parameter_list` containing `N_SUN` and `Beta` could
 1193 look like:

```
1194 !#PARAMETERS START# my_parameter_list
1195 !Integer          :: N_SUN = 2
1196 real(Kind=Kind(0.d0)) :: Beta = 5.d0 ! Inverse temperature
1197 !#PARAMETERS END#
```

1200 The parsing script `parse_ham.py` in `Prog/` has the option `--test_file` for testing the
 1201 namelist specifications, e.g. calling:

```
1202 ./parse_ham.py --test_file Hamiltonians/Hamiltonian_New_model_smod.F90
```

1203 prints out the results from parsing for manual checking. We recommend doing this after every
 1204 change in the namelist.

1205 During compilation, the file `Hamiltonian_New_model_read_write_parameters.F90`
 1206 containing the subroutines `read_parameters` and `write_parameters_hdf5` is generated
 1207 automatically. The former subroutine can be called in `ham_set`, while the latter has to be
 1208 bound to `ham_New_model` through:

```
1209 #ifdef HDF5
1210   procedure, nopass :: write_parameters_hdf5
1211 #endif
```

1214 To help creating a new Hamiltonian, we provide a template `Prog/Hamiltonians/`
 1215 `Hamiltonian_##NAME##_smod.F90`, which can be copied to `Prog/Hamiltonians/`
 1216 `Hamiltonian_New_model_smod.F90` before being modified. To simplify the implementa-
 1217 tion of a new Hamiltonian, ALF comes with a set of predefined structures (Sec. 8) which the
 1218 user can combine together or use as templates.

Table 9: List of the public and private variables declared in the module Hamiltonian. The highlighted variables have to be set in the subroutine `ham_set`.

Public Variable	Type	Description
ham	class(ham_base)	Hamiltonian object. All model dependent procedures are attached to this variable (see Table 10).
Op_V	Operator	Interaction
Op_T	Operator	Hopping
WF_L	WaveFunction	Left trial wave function
WF_R	WaveFunction	Right trial wave function
nsigma	Fields	Fields
Ndim	int	Number of sites
N_Fl	int	Number of flavors
N_SUN	int	Number of colors
Ltrot	int	Total number of trotter slices
Thtrot	int	Number of trotter slices reserved for projection
Projector	logical	Enable projector code
Group_Comm	int	Group communicator for MPI
Symm	logical	Symmetric trotter
Calc_Fl	logical	Explicitly calculation of flavors (optional)
Private Variable	Type	Description
Obs_scal	Obser_Vec	Storage for measured scalar observables
Obs_eq	Obser_Latt	Storage for measured equal time correlations
Obs_tau	Obser_Latt	Storage for measured time displaced correlations

1219 In order to specify a Hamiltonian, we have to set the matrix representation of the
 1220 imaginary-time propagators, $e^{-\Delta\tau T^{(ks)}}$, $e^{\sqrt{-\Delta\tau U_k} \eta_{k\tau} V^{(ks)}}$ and $e^{-\Delta\tau s_{k\tau} I^{(ks)}}$, that appear in the par-
 1221 tition function (17). For each pair of indices (k,s) , these terms have the general form

$$\text{Matrix Exponential} = e^{g \phi(\text{type}) X}. \quad (127)$$

1222 In case of the perfect-square term, we additionally have to set the constant α , see the definition
 1223 of the operators $\hat{V}^{(k)}$ in Eq. (4). The data structures which hold all the above information are
 1224 variables of the type `Operator` (see Table 2). For each pair of indices (k,s) , we store the
 1225 following parameters in an `Operator` variable:

- 1226 • P and O defining the matrix X [see Eq. (108)],
- 1227 • the constants g , α ,
- 1228 • optionally: the type `type` of the discrete fields ϕ .

1229 The latter parameter can take one of three values: Ising (1), discrete HS (2), and real (3), as
 1230 detailed in Sec. 5.2. Note that we have dropped the color index σ , since the implementation
 1231 uses the $SU(N_{\text{col}})$ invariance of the Hamiltonian.

1232 Accordingly, the following data structures fully describe the Hamiltonian (2):

- 1233 • For the hopping Hamiltonian (3), we have to set the exponentiated hopping matrices
 1234 $e^{-\Delta\tau T^{(ks)}}$:

Table 10: Typebound procedures bound to type `ham_base`. To define a new model, at least `Ham_Set` has to be overloaded in the Hamiltonian submodule. For measurements `Alloc_obs`, `Obser` (and `ObserT` for time displaced observables) are necessary. The other procedures are needed for optional features.

Procedure	Description	Section
<code>Ham_Set</code>	Reads in model and lattice parameters from the file <code>parameters</code> . Sets the Hamiltonian, which is commonly split up into subroutines <code>Ham_Latt</code> , <code>Ham_Hop</code> , <code>Ham_V</code> and <code>Ham_Trial</code> <code>Ham_Latt</code> : Sets the Lattice and the <code>Unit_cell</code> as well as the arrays <code>List</code> and <code>Inv_list</code> required for multiorbital problems <code>Ham_hop</code> : Sets the hopping term $\hat{\mathcal{H}}_T$ (i.e., operator <code>Op_T</code>) by calling <code>Op_make</code> and <code>Op_set</code> <code>Ham_V</code> : Sets the interaction term $\hat{\mathcal{H}}_V$ (i.e., operator <code>Op_V</code>) by calling <code>Op_make</code> and <code>Op_set</code> <code>Ham_Trial</code> : Sets the trial wave function for the projective code $ \Psi_{T,L/R}\rangle$ specified by the <code>Wavefunction</code> type	5.6 , 9 5.3 , 7.3 8.1 5.1 , 7.4 , 8.2 5.1 , 7.5 , 8.3 5.5 , 7.6 , 8.5
<code>Alloc_obs</code>	Assigns memory storage to the observable	5.4 , 7.7.1
<code>Obser</code>	Computes the scalar and equal-time observables	5.4 , 7.7.2 , 8.4
<code>ObserT</code>	Computes time-displaced correlation functions	5.4 , 7.7.3 , 8.4
<code>S0</code>	Returns the ratio $e^{S_0(C')}/e^{-S_0(C)}$ for a single spin flip	2.2.2
<code>Global_move_tau</code>	Generates a global move on a given time slice τ . This routine is only called if <code>Global_tau_moves=True</code> and <code>N_Global_tau>0</code>	2.2.3
<code>Override_global_tau_sampling_parameters</code>	Allows setting <code>global_tau</code> parameters at run time	2.2.3
<code>Hamiltonian_set_nsigma</code>	Sets the initial field configuration. This routine is to be modified if one wants to specify the initial configuration. By default the initial configuration is assumed to be random	
<code>Global_move</code>	Handles global moves in time and space	2.2.4
<code>Delta_S0_global</code>	Computes $e^{S_0(C')}/e^{-S_0(C)}$ for a global move	2.2.4
<code>Init_obs</code>	Initializes the observables to zero. Usually, this doesn't have to be modified.	
<code>Pr_obs</code>	Writes the observables to disk by calling <code>Print_bin</code> of the <code>Observables</code> module. Usually this does not have to be modified	
<code>weight_reconstruction</code>	Reconstructs of the weight for “inactive” flavors	5.6.1
<code>GR_reconstruction</code>	Reconstructs the Green function <code>GR</code> for the “inactive” flavors	5.6.1
<code>GRT_reconstruction</code>	Reconstructs the time-displaced Green functions <code>GOT</code> and <code>GTO</code>	5.6.1

1235 In this case $X^{(ks)} = T^{(ks)}$, and a single variable `Op_T` describes the operator matrix

$$\left(\sum_{x,y}^{N_{\text{dim}}} \hat{c}_{xs}^{\dagger} T_{xy}^{(ks)} \hat{c}_{ys} \right), \quad (128)$$

1236 where $k = [1, M_T]$ and $s = [1, N_{\text{fl}}]$. In the notation of the general expression (127), we
 1237 set $g = -\Delta\tau$ (and $\alpha = 0$). In case of the hopping matrix, the type variable takes its
 1238 default value `Op_T%type = 0`. All in all, the corresponding array of structure variables
 1239 is `Op_T(M_T, N_fl)`.

- 1240 • For the interaction Hamiltonian (4), which is of perfect-square type, we have to set the
 1241 exponentiated matrices $e^{\sqrt{-\Delta\tau U_k} \eta_k; V^{(ks)}}$:

1242 In this case, $X = V^{(ks)}$ and a single variable `Op_V` describes the operator matrix:

$$\left[\left(\sum_{x,y}^{N_{\text{dim}}} \hat{c}_{xs}^{\dagger} V_{x,y}^{(ks)} \hat{c}_{ys} \right) + \alpha_{ks} \right], \quad (129)$$

1243 where $k = [1, M_V]$ and $s = [1, N_{\text{fl}}]$, $g = \sqrt{-\Delta\tau U_k}$ and $\alpha = \alpha_{ks}$. The discrete HS
 1244 decomposition which is used for the perfect-square interaction, is selected by setting the
 1245 type variable to `Op_V%type = 2`. All in all, the required structure variables `Op_V` are
 1246 defined using the array `Op_V(M_V, N_fl)`.

- 1247 • For the bosonic interaction Hamiltonian (5), we have to set the exponentiated matrices
 1248 $e^{-\Delta\tau s_k \tau} I^{(ks)}$:

1249 In this case, $X = I^{(k,s)}$ and a single variable `Op_V` then describes the operator matrix:

$$\left(\sum_{x,y}^{N_{\text{dim}}} \hat{c}_{xs}^{\dagger} I_{xy}^{(ks)} \hat{c}_{ys} \right), \quad (130)$$

1250 where $k = [1, M_I]$ and $s = [1, N_{\text{fl}}]$ and $g = -\Delta\tau$ (and $\alpha = 0$). If this operator couples
 1251 to an Ising field, we specify the type variable `Op_V%type=1`. On the other hand, if it
 1252 couples to a scalar field (i.e. real number) then we specify `Op_V%type=3`. All in all, the
 1253 required structure variables are contained in the array `Op_V(M_I, N_fl)`.

- 1254 • In case of a full interaction [perfect-square term (4) and bosonic term (5)], we define
 1255 the corresponding doubled array `Op_V(M_V+M_I, N_fl)` and set the variables separately for
 1256 both ranges of the array according to the above.

1257 5.6.1 Flavor symmetries

1258 This code allows the use of time-reversal or particle-hole symmetry to accelerate the algorithm
 1259 by only explicitly calculating a subset of flavors and reconstructing the complement by symme-
 1260 try. Here, a pair of flavors $(n_{\text{fl}}, \bar{n}_{\text{fl}})$ are related by a unitary or anti-unitary symmetry, including
 1261 particle-hole transformations, such that

$$\mathcal{U}^{-1} \text{Op}_V(i, n_{\text{fl}}) \mathcal{U} = \text{Op}_V(i, \bar{n}_{\text{fl}}); \quad \mathcal{U}^{-1} \text{Op}_T(i, n_{\text{fl}}) \mathcal{U} = \text{Op}_T(i, \bar{n}_{\text{fl}}), \quad (131)$$

1262 for any given i . Note that `Op_V(i, n_fl)` includes a constant shift α to absorb contributions from
 1263 the commutator in case of particle-hole symmetries. For example, the particle-hole symmetry
 1264 requires a non-zero shift $\alpha = 1/2$ in the M_z decoupling of the Hubbard interaction to map the
 1265 upspin to the downspin. This acceleration is activated by allocating `Calc_Fl` in `Ham_Set` and
 1266 setting the “active” flavors `n_fl` to `.True.` and the symmetry-related flavors `bar{n_fl}` to `.False..`

Table 11: Overview of the directories included in the ALF package.

Directory	Description
Prog/	Main program and subroutines
Libraries/	Collection of mathematical routines
Analysis/	Routines for error analysis
Scripts_and_Parameters_files/	Helper scripts and the Start/ directory, which contains the files required to start a run
Documentation/	This documentation
Mathematica/	Mathematica notebooks to evaluate higher order correlation functions with Wicks theorem
testsuite/	An automatic test suite for various parts of the code

1267 This symmetry allows one to reconstruct one flavor, say \bar{n}_{fl} , from the other, n_{fl} . For unitary symmetries, the weight is given by $Z(\bar{n}_{\text{fl}}) = Z(n_{\text{fl}})$, while anti-unitary symmetries lead to
 1268 $Z(\bar{n}_{\text{fl}}) = Z(n_{\text{fl}})^*$. This relation has to be provided by the user in `weight_reconstruction`.
 1269 Up to entry, all weights $Z(n_{\text{fl}})$ have to be explicitly calculated by ALF and the user has to fill
 1270 all “inactive” flavors \bar{n}_{fl} of the array Z . Similarly, the subroutines `GR_reconstruction` and
 1271 `GRT_reconstruction` have to be overridden to provide the symmetry reconstruction of the
 1272 “inactive” flavors \bar{n}_{fl} of the equal-time and time-displaced Green functions out of n_{fl} , respectively.
 1273

1274 Finally we note that if the projective algorithm is used then the trial wave function also
 1275 has to satisfy the aforementioned symmetry. In particular, assume that the trial wave function
 1276 corresponds to the ground state of a single particle Hamiltonian, $\hat{H}_T(n_{\text{fl}})$, then we will require
 1277 that
 1278

$$\mathcal{U}^{-1}\hat{H}_T(n_{\text{fl}})\mathcal{U} = \hat{H}_T(\bar{n}_{\text{fl}}). \quad (132)$$

1279 5.7 File structure

1280 The code package, summarized in Table 11, consists of the program directories `Prog/`,
 1281 `Libraries/`, `Analysis/`, and the directory `Scripts_and_Parameters_files/`, which
 1282 contains supporting scripts and, in its subdirectory `Start`, the input files necessary for a run,
 1283 described in the Sec. 5.7.1 as well as `Mathematica/` that contains Mathematica notebooks to
 1284 evaluate higher order correlation functions with Wicks theorem as described in Appendix A.
 1285 The routines available in the directory `Analysis/` are described in Sec. 6.3, and the testsuite
 1286 in Sec. 6.2.

1287 Below we describe the structure of ALF’s input and output files. Notice that the input/output
 1288 files for the Analysis routines are described in Sec. 6.3.

Table 12: Overview of the input files required for a simulation, which can be found in the subdirectory `Scripts_and_Parameters_files/Start/`.

File	Description
<code>parameters</code>	Defines which Hamiltonian to use and sets the parameters for: lattice, model, QMC process, and error analysis
<code>seeds</code>	List of integer numbers to initialize the random number generator and to start a simulation from scratch

1289 5.7.1 Input files

1290 The package's two input files are described in Table 12. The parameter file `Start/`
 1291 `parameters` has the following form – using as an example the Hubbard model on a square
 1292 lattice (see Sec. 9.1 for the general SU(N) Hubbard and Sec. 7 for a detailed walk-through on
 1293 its plain vanilla version):

```

1294 =====
1295 ! Input variables for a general ALF run
1296 !
1297 -----
1298 &VAR_ham_name          !! Use Hamiltonian defined in
1299 ham_name = "Hubbard"   ! Prog/Hamiltonians/Hamiltonian_{ham_name}_smode.F90
1300 /
1301
1302 &VAR_lattice           !! Parameters defining the specific lattice and base model
1303 L1                   = 6      ! Length in direction a_1
1304 L2                   = 6      ! Length in direction a_2
1305 Lattice_type = "Square" ! Sets a_1 = (1,0), a_2=(0,1), Norb=1, N_coord=2
1306 Model                = "Hubbard" ! Sets the Hubbard model, to be specified in &VAR_Hubbard
1307 /
1308
1309 &VAR_Model_Generic    !! Common model parameters
1310 Checkerboard = .T.       ! Whether checkerboard decomposition is used
1311 Symm        = .T.       ! Whether symmetrization takes place
1312 N_SUM       = 2         ! Number of colors
1313 N_FL        = 1         ! Number of flavors
1314 Phi_X       = 0.d0      ! Twist along the L_1 direction, in units of the flux quanta
1315 Phi_Y       = 0.d0      ! Twist along the L_2 direction, in units of the flux quanta
1316 Bulk        = .T.       ! Twist as a vector potential (.T.); at the boundary (.F.)
1317 N_Phi       = 0         ! Total number of flux quanta traversing the lattice
1318 Dtau        = 0.1d0     ! Thereby Ltrot=Beta/dtau
1319 Beta         = 5.d0      ! Inverse temperature
1320 Projector   = .F.       ! Whether the projective algorithm is used
1321 Theta        = 10.d0    ! Projection parameter
1322 /
1323
1324 &VAR_QMC             !! Variables for the QMC run
1325 Nwrap            = 10     ! Stabilization. Green functions will be computed from
1326                           ! scratch after each time interval Nwrap*Dtau
1327 NSweep           = 20     ! Number of sweeps
1328 NBin              = 5      ! Number of bins
1329 Ltau               = 1      ! 1 to calculate time-displaced Green functions; 0 otherwise
1330 LOBS_ST           = 0      ! Start measurements at time slice LOBS_ST
1331 LOBS_EN           = 0      ! End measurements at time slice LOBS_EN
1332 CPU_MAX           = 0.0    ! Code stops after CPU_MAX hours, if 0 or not
1333                           ! specified, the code stops after Nbin bins
1334 Propose_S0         = .F.    ! Proposes single spin flip moves with probability exp(-S0)
1335 Global_moves        = .F.    ! Allows for global moves in space and time
1336 N_Global            = 1      ! Number of global moves per sweep
1337 Global_tau_moves   = .F.    ! Allows for global moves on a single time slice.
1338 N_Global_tau        = 1      ! Number of global moves that will be carried out on a
1339                           ! single time slice
1340 Nt_sequential_start = 0      ! One can combine sequential & global moves on a time slice
1341 Nt_sequential_end   = -1     ! The program then carries out sequential local moves in the
1342                           ! range [Nt_sequential_start, Nt_sequential_end] followed by
1343                           ! N_Global_tau global moves
1344 Langevin            = .F.    ! Langevin update
1345 Delta_t_Langevin_HMC = 0.01  ! Default time step for Langevin and HMC updates
1346 Max_Force           = 1.5    ! Max Force for Langevin
1347 /
1348
1349 &VAR_errors          !! Variables for analysis programs
1350 n_skip              = 1      ! Number of bins that to be skipped
1351 N_rebin              = 1      ! Rebinning
1352 N_Cov                = 0      ! If set to 1 covariance computed for non-equal-time
1353                           ! correlation functions
1354 N_auto               = 0      ! If > 0 triggers calculation of autocorrelation
1355 N_Back               = 1      ! If set to 1, subtract background in correlation functions
1356 /
1357
1358 &VAR_TEMP             !! Variables for parallel tempering

```

```

1359 N_exchange_steps      = 6    ! Number of exchange moves [see Eq. (39)]
1360 N_Tempering_frequency = 10   ! The frequency in units of sweeps at which the
1361                               ! exchange moves are carried out
1362 mpi_per_parameter_set = 2    ! Number of mpi-processes per parameter set
1363 Tempering_calc_det     = .T. ! Specifies whether the fermion weight has to be taken
1364                               ! into account while tempering. The default is .true.,
1365                               ! and it can be set to .F. if the parameters that
1366                               ! get varied only enter the free bosonic action S_0
1367 /
1368
1369 &VAR_Max_Stoch          !! Variables for Stochastic Maximum entropy
1370 Ngamma      = 400           ! Number of Dirac delta-functions for parametrization
1371 Om_st       = -10.d0         ! Frequency range lower bound
1372 Om_en       = 10.d0         ! Frequency range upper bound
1373 NDis        = 2000          ! Number of boxes for histogram
1374 Nbins       = 250           ! Number of bins for Monte Carlo
1375 Nsweeps     = 70            ! Number of sweeps per bin
1376 NWarm       = 20            ! The NWarm first bins will be omitted
1377 N_alpha     = 14             ! Number of temperatures
1378 alpha_st    = 1.d0           ! Smallest inverse temperature increment for inverse
1379 R           = 1.2d0           ! temperature (see above)
1380 Checkpoint  = .F.           ! Whether to produce dump files, allowing the simulation
1381                               ! to be resumed later on
1382 Tolerance   = 0.1d0          ! Data points for which the relative error exceeds the
1383                               ! tolerance threshold will be omitted.
1384 /
1385
1386 &VAR_Hubbard           !! Variables for the specific model
1387 Mz          = .T.           ! When true, sets the M_z-Hubbard model: Nf=2, demands that
1388                               ! N_sun is even, HS field couples to the z-component of
1389                               ! magnetization; otherwise, HS field couples to the density
1390 Continuous  = .F.           ! Uses (T: continuous; F: discrete) HS transformation
1391 ham_T       = 1.d0           ! Hopping parameter
1392 ham_chem    = 0.d0           ! Chemical potential
1393 ham_U       = 4.d0           ! Hubbard interaction
1394 ham_T2      = 1.d0           ! For bilayer systems
1395 ham_U2      = 4.d0           ! For bilayer systems
1396 ham_Tperp   = 1.d0           ! For bilayer systems
1397 /

```

1399 The program allows for a number of different updating schemes. If no other variables are
1400 specified in the VAR_QMC name space, then the program will run in its default mode, namely
1401 the sequential single spin-flip mode. In particular, note that if Nt_sequential_start and
1402 Nt_sequential_end are not specified and that the variable Global_tau_moves is set to to
1403 true, then the program will carry out only global moves, by setting Nt_sequential_start=1
1404 and Nt_sequential_end=0.

1405 5.7.2 Output files – Observables

1406 The standard output files are listed in Table 13 and Table 14 for plain-text and HDF5 output,
1407 respectively. Notice that, besides these files, which contain direct QMC outputs, ALF can also
1408 produce a number of analysis output files, discussed in Sec. 6.3.

1409 The output of the measured data is organized in bins. One bin corresponds to the arith-
1410 metic average over a fixed number of individual measurements which depends on the chosen
1411 measurement interval [LOBS_ST, LOBS_EN] on the imaginary-time axis and on the number
1412 NSweep of Monte Carlo sweeps. If the user runs an MPI parallelized version of the code, the
1413 average also extends over the number of MPI threads.

1414 The formatting of a single bin’s output depends on the observable type, Obs_vec or Obs_-
1415 Latt:

- 1416 • Observables of type Obs_vec: For each additional bin, a single new line is added to the
1417 output file. In case of an observable with N_size components, the formatting is
1418 $N_size+1 \text{ <measured value, 1> ... <measured value, } N_size \text{ <measured sign>}$

Table 13: Overview of the standard output files if compiled without HDF5. See Sec. 5.4 for the definitions of observables and correlation functions and Table 14 for HDF5 output.

File	Description
info	Summary after completion of the simulation, including parameters of the model and the QMC run and simulation metrics (precision, acceptance rate, wallclock time)
X_scal	Results of equal-time measurements of scalar observables. The placeholder X stands for the observables Kin, Pot, Part, and Ener
X_scal_info	Info on how to analyze the observable and optionally a description.
Y_eq, Y_tau	Results of equal-time and time-displaced measurements of correlation functions. The placeholder Y stands for Green, SpinZ, SpinXY, Den, etc.
Y_eq_info, Y_tau_info	Additional info, like Bravais lattice and unit cell, for equal-time and time-displaced observables
confout_<thread#>	Output files (one per MPI instance) for the HS and bosonic configuration

1419 The counter variable N_size+1 refers to the number of measurements per line, includ-
 1420 ing the phase measurement. This format is required by the error analysis routine (see
 1421 Sec. 6.3). Scalar observables like kinetic energy, potential energy, total energy and par-
 1422 ticle number are treated as a vector of size N_size=1.

- 1423 • Observables of type Obs_Latt: For each additional bin, a new data block is added to
 1424 the output file. The block consists of the expectation values [Eq. (126)] contributing
 1425 to the background part [Eq. (125)] of the correlation function, and the correlated part
 1426 [Eq. (124)] of the correlation function. For imaginary-time displaced correlation func-
 1427 tions, the formatting of the block is given by:

```

1428 <measured sign> <N_orbital> <N_unit_cell> <N_time_slices> <dtau> <Channel>
1429 do alpha = 1, N_orbital
1430   < $\hat{O}_\alpha$ >
1431 enddo
1432 do i = 1, N_unit_cell
1433   <reciprocal lattice vector k(i)>
1434   do tau = 1, N_time_slices
1435     do alpha = 1, N_orbital
1436       do beta = 1, N_orbital
1437         < $S_{\alpha,\beta}^{(corr)}(k(i), \tau)$ >
1438       enddo
1439     enddo
1440   enddo
1441 enddo

```

1442 The same block structure is used for equal-time correlation functions, except for the
 1443 entries <N_time_slices>, <dtau> and <Channel>, which are then omitted. Using
 1444 this structure for the bins as input, the full correlation function $S_{\alpha,\beta}(\mathbf{k}, \tau)$ [Eq. (123)] is
 1445 then calculated by calling the error analysis routine (see Sec. 6.3).

Table 14: Overview of the standard output files if compiled with HDF5. See Sec. 5.4 for the definitions of observables and correlation functions.

File	Description
info	Same as in Tab. 13
data.h5	Contains the same information as the scalar, equal-time correlation and time-displaced correlation operators as in Tab. 13, but in one single HDF5 file. This file also includes all Hamiltonian parameters defined as specified in Sec. 5.6 (see also Fig. 5). Note: The parameter names in the HDF5 file are all lower case
confout_<thread#>.h5	Output files (one per MPI instance) for the HS and bosonic configuration, in HDF5 format

```

data.h5
└── lattice ..... Attached attributes describe Bravais lattice and unit cell
    ├── X_scal..... Attached attribute: analysis_mode
    ├── obser ..... Dataset of shape (NBins, Nobs, 2)
    └── sign..... Dataset of shape (NBins)
    ├── Y_eq Y_tau..... Attached attributes: Channel, dtau
    │   ├── lattice ..... Attached attributes describe Bravais lattice and unit cell
    │   ├── obser ..... Dataset of shape (NBins, Norbs, Norbs, Ntau, Nlatt, 2)
    │   ├── back..... Dataset of shape (NBins, Norbs, 2)
    │   └── sign..... Dataset of shape (NBins)
    └── parameters
        ├── namelist_1..... Attached attributes are the parameters in namelist_1
        ├── ...
        └── namelist_n..... Attached attributes are the parameters in namelist_n

```

Figure 5: Structure of HDF5 output file data.h5. In parameters all n namelists connected with the simulated Hamiltonian can be found.

1446 6 Using the code

1447 In this section we describe the steps for compiling and running the code from the shell, and
 1448 describe how to search for optimal parameter values as well as how to perform the error
 1449 analysis of the data.

1450 The source code of ALF 2.4 is available at <https://git.physik.uni-wuerzburg.de/ALF/ALF/-/tree/ALF-2.4/> and can be cloned with git or downloaded from the repository (make sure to
 1451 choose the appropriate release).

1452 A Python interface, **pyALF**, is also available and can be found, together with a number of
 1453 Jupyter notebooks exploring the interface's capabilities, at <https://git.physik.uni-wuerzburg.de/ALF/pyALF/-/tree/ALF-2.3/>. This interface facilitates setting up simple runs and is ideal
 1454 for setting benchmarks and getting acquainted with ALF. Some of pyALF's notebooks form the
 1455 core of the introductory part of the **ALF Tutorial**, where pyALF's usage is described in more
 1456 detail.

1457 We start out by providing step-by-step instructions that allow a first-time user to go from
 1458 zero to performing a simulation and reading out their first measurement using ALF.

1461 **6.1 Quick start**

1462 The aim of this section is to provide a fruitful and stress-free first contact with the package.
 1463 Ideally, it should be possible to copy and paste the instructions below to a Debian/Ubuntu-
 1464 based Linux shell without further thought.⁴ Explanations and further options and details are
 1465 found in the remaining sections and in the [Tutorial](#).

1466 **Prerequisites:** You should have access to a shell and the permissions to install – or have
 1467 already installed – the numerical packages Lapack and Blas, a Fortran compiler, Python, and
 1468 the tools make and git.

1469 The following commands can be executed in a Debian-based shell⁵ in order to install
 1470 ALF 2.4 and its dependencies, run a demonstration simulation and output one of the mea-
 1471 surements performed:

- 1472 • `sudo apt-get update`
- 1473 • `sudo apt-get install gfortran liblapack-dev python3 make git`
- 1474 • `git clone -b ALF-2.4 https://git.physik.uni-wuerzburg.de/ALF/ALF.git`
- 1475 • `cd ALF`
- 1476 • `source configure.sh GNU noMPI`
- 1477 • `make Hubbard_Plain_Vanilla ana`
- 1478 • `cp -r ./Scripts_and_Parameters_files/Start ./Run && cd ./Run/`
- 1479 • `$ALF_DIR/Prog/ALF.out`
- 1480 • `$ALF_DIR/Analysis/ana.out Ener_scal`
- 1481 • `cat Ener_scalJ`

1482 The last command will output a few lines, including one similar to:

1483 `OBS : 1 -30.009191 0.110961`

1484 which is listing the internal energy of the system and its error.

1485 **6.2 Compiling and running**

1486 The necessary environment variables and the directives for compiling the code are set by the
 1487 script `configure.sh`:

1488 `source configure.sh [MACHINE] [MODE] [STAB]`

1489 If run with no arguments, it lists the available options and sets a generic, serial GNU com-
 1490 piler with minimal flags `-cpp -O3 -ffree-line-length-none -ffast-math`. The pre-
 1491 defined machine configurations and parallelization modes available, as well as the options for
 1492 stabilization schemes for the matrix multiplications (see Sec. 2.4) are shown in Table 15. The
 1493 stabilization scheme choice, in particular, is critical for performance and is discussed further
 1494 in Sec. 6.4.

1495 In order to compile the libraries, the analysis routines and the QMC program at once, just
 1496 execute the single command:

1497 `make`

1498 Related auxiliary directories, object files and executables can be removed by executing the
 1499 command `make clean`. The accompanying Makefile also provides rules for compiling and
 1500 cleaning up the library, the analysis routines and the QMC program separately.

⁴For other systems and distributions see the package's [README](#).

⁵Avoid folder names containing spaces, which are not supported.

Table 15: Available arguments for the script `configure.sh`, called before compilation of the package: predefined machines, parallelization modes, and stabilization schemes (see also Sec. 6.4).

Argument	Selected feature
MACHINE	
GNU	GNU compiler (<code>gfortran/mpifort</code>) for a generic machine (<i>default</i>)
Intel	Intel compiler (<code>ifort/mpiifort</code>) for a generic machine ⁶
PGI	PGI compiler (<code>pgfortran/mpifort</code>) for a generic machine
SuperMUC-NG	Intel compiler (<code>mpiifort</code>) and loads modules for SuperMUC-NG ⁷
JUWELS	Intel compiler (<code>mpiifort</code>) and loads modules for JUWELS ⁸
MODE	
<code>noMPI Serial</code>	No parallelization
<code>MPI</code>	MPI parallelization (<i>default</i> – if a machine is selected)
<code>Tempering</code>	Parallel tempering (Sec. 2.2.5) and the required MPI as well
STAB	
<code>STAB1</code>	Simplest stabilization: UDV (QR-, not SVD-based) decompositions
<code>STAB2</code>	QR-based UDV decompositions with additional normalizations
<code>STAB3</code>	Latest, additionally separates large and small scales (<i>default</i>)
<code>LOG</code>	Logarithmic storage for internal scales, increases accessible ranges
OTHER SWITCHES	
<code>Devel</code>	Compile with additional flags for development and debugging
<code>HDF5</code>	Compile with HDF5 – automatically downloads and installs HDF5 if not present
<code>NO-INTERACTIVE</code>	Do not ask for user confirmation during execution of this script

1501 A suite of tests for individual parts of the code (subroutines, functions, operations, etc.)
 1502 is available at the directory `testsuite`. The tests can be run by executing the following
 1503 sequence of commands (the script `configure.sh` sets environment variables as described
 1504 above):

```
1506 source configure.sh GNU Devel noMPI
1507 gfortran -v
1508 make lib
1509 make ana
1510 make program
1511 cd testsuite
1512 cmake -E make_directory tests
1513 cd tests
1514 cmake -G "Unix Makefiles" -DCMAKE_Fortran_FLAGS_RELEASE=${F90OPTFLAGS} \
1515 -DCMAKE_BUILD_TYPE=RELEASE ..
1516 cmake --build . --target all --config Release
1517 ctest -VV -O log.txt
```

1518 which will output test results and total success rate.

⁶A known issue with the alternative Intel Fortran compiler `ifort` is the handling of automatic, temporary arrays which `ifort` allocates on the stack. For large system sizes and/or low temperatures this may lead to a runtime error. One solution is to demand allocation of arrays above a certain size on the heap instead of the stack. This is accomplished by the `ifort` compiler flag `-heap-arrays [n]` where `[n]` is the minimal size (in kilobytes, for example `n=1024`) of arrays that are allocated on the heap.

⁷Supercomputer at the Leibniz Supercomputing Centre.

⁸Supercomputer at the Jülich Supercomputing Centre.

1519 Starting a simulation

1520 In order to start a simulation from scratch, the following files have to be present: `parameters`
1521 and `seeds` (see Sec. 5.7.1). To run serial simulation, issue the command

1522 \$ALF_DIR/Prog/ALF.out

1523 In order to run with MPI parallelization, the appropriate MPI execution command should be
1524 called. For instance, a program compiled with OpenMPI can be run in parallel by issuing

1525 mpirun -np <number of processes> \$ALF_DIR/Prog/ALF.out

1526 The environment variable `ALF_SHM_CHUNK_SIZE_GB` can be used to reduce the program's
1527 memory footprint by sharing memory between MPI processes on the same node. The variable,
1528 a positive real number, defines the chunk size of the shared memory objects in units of GB.
1529 Typical values are 1.0 or 2.0 GB, but larger values can be used, if otherwise the total number of
1530 MPI communicators so large as to trigger MPI error messages. If `ALF_SHM_CHUNK_SIZE_GB`
1531 is not defined or set to values smaller than one, then the memory is not shared between MPI
1532 processes, which is the default behavior.

1533 To restart the code using the configuration from a previous simulation as a starting point,
1534 first run the script `out_to_in.sh`, which copies outputted field configurations into input files,
1535 before calling the ALF executable. This file is located in the directory `$ALF_DIR/Scripts_`
1536 `and_Parameters_files/Start/`

1537 Notice that, when compiled with DHF5 the code checks whether the parameters stored in
1538 existing data files have the same values as those in the parameter file and exit with an error
1539 when they do not.

1540 6.3 Error analysis

1541 The ALF package includes the analysis programs `ana.out` for plain text bins and
1542 `ana_hdf5.out` for bins in HDF5 format. They perform the same simple error analysis and
1543 correlation function calculations on the three observable types. To perform an error analysis
1544 based on the Jackknife resampling method [136] (Sec. 4.1) of the Monte Carlo bins for a list
1545 of plain-text observables run

1546 \$ALF_DIR/Analysis/ana.out <list of files>

1547 or run

1548 \$ALF_DIR/Analysis/ana.out *

1549 for all observables.

1550 For analyzing observables stored in the HDF5 file `data.h5`, run

1551 \$ALF_DIR/Analysis/ana_hdf5.out <list of observables>

1552 or run

1553 \$ALF_DIR/Analysis/ana_hdf5.out *

1554 for all observables.

1555 The programs `ana.out` and `ana_hdf5.out` are based on the included module `ana_mod`,
1556 which provides subroutines for reading and analyzing ALF Monte Carlo bins, that can be used
1557 to implement more specialized analysis. The three high-level analysis routines employed by
1558 `ana_mod` are listed in Table 16. The files taken as input, as well as the output files are listed
1559 in Table 17.

1560 The error analysis is based on the central limit theorem, which requires bins to be sta-
1561 tistically independent, and also the existence of a well-defined variance for the observable
1562 under consideration (see Sec. 4). The former will be the case if bins are longer than the

Table 16: Overview of analysis subroutines called within `ana.out` and `ana_hdf5.out`.

Program	Description
<code>cov_vec(name)</code>	The bin file name, which should have suffix <code>_scal</code> , is read in, and the corresponding file with suffix <code>_scalJ</code> is produced. It contains the result of the Jackknife rebinning analysis (see Sec. 4)
<code>cov_eq(name)</code>	The bin file name, which should have suffix <code>_eq</code> , is read in, and the corresponding files with suffix <code>_eqJR</code> and <code>_eqJK</code> are produced. They correspond to correlation functions in real and Fourier space, respectively
<code>cov_tau(name)</code>	The bin file name, which should have suffix <code>_tau</code> , is read in, and the directories <code>X_kx_ky</code> are produced for all <code>kx</code> and <code>ky</code> greater or equal to zero. Here <code>X</code> is a place holder from Green, SpinXY, etc., as specified in <code>Alloc_obs(Ltau)</code> (See section 7.7.1). Each directory contains a file <code>g_dat</code> containing the time-displaced correlation function traced over the orbitals. It also contains the covariance matrix if <code>N_cov</code> is set to unity in the parameter file (see Sec. 5.7.1). Besides, a directory <code>X_R0</code> for the local time displaced correlation function is generated. For particle-hole, imaginary-time correlation functions (<code>Channel = "PH"</code>) such as spin and charge, we use the fact that these correlation functions are symmetric around $\tau = \beta/2$ so that we can define an improved estimator by averaging over τ and $\beta - \tau$

1563 autocorrelation time – autocorrelation functions are computed by setting the parameter `N_`
 1564 `auto` to a nonzero value – which has to be checked by the user. In the parameter file de-
 1565 scribed in Sec. 5.7.1, the user can specify how many initial bins should be omitted (variable
 1566 `n_skip`). This number should be comparable to the autocorrelation time. The rebinning vari-
 1567 able `N_rebin` will merge `N_rebin` bins into a single new bin. If the autocorrelation time is
 1568 smaller than the effective bin size, the error should become independent of the bin size and
 1569 thereby of the variable `N_rebin`. The analysis output files listed in Table 17 and are formatted
 1570 in the following way:

- 1571 • For the scalar quantities `X`, the output files `X_scalJ` have the following formatting:

```
1572 Effective number of bins, and bins: <N_bin - N_skip>/<N_rebin> <N_bin>
1573 OBS : 1   <mean(X)>    <error(X)>
1574 OBS : 2   <mean(sign)>  <error(sign)>
```

- 1575 • For the equal-time correlation functions `Y`, the formatting of the output files `Y_eqJR` and
 1576 `Y_eqJK` follows the structure:

```
1577 do i = 1, N_unit_cell
1578   <k_x(i)>  <k_y(i)>
1579   do alpha = 1, N_orbital
1580     do beta = 1, N_orbital
1581       alpha beta Re<mean(Y)> Re<error(Y)> Im<mean(Y)> Im<error(Y)>
1582     enddo
1583   enddo
1584 enddo
```

1585 where `Re` and `Im` refer to the real and imaginary part, respectively.

- 1586 • The imaginary-time displaced correlation functions `Y` are written to the output files `g_R0`
 1587 inside folders `Y_R0`, when measured locally in space; and to the output files `g_kx_ky`
 1588 inside folders `Y_kx_ky` when they are measured k -resolved (where $k = (k_x, k_y)$). The

Table 17: Standard input and output files of the error analysis program `ana.out`.

File	Description
Input	
<code>parameters</code>	Includes error analysis variables <code>N_skip</code> , <code>N_rebin</code> , and <code>N_Cov</code> (see Sec. 5.7.1)
<code>X_scal, Y_eq, Y_tau</code>	Monte Carlo bins (see Table 13)
Output	
<code>X_scalJ</code>	Jackknife mean and error of X, where X stands for Kin, Pot, Part, or Ener
<code>Y_eqJR and Y_eqJK</code>	Jackknife mean and error of Y, which stands for Green, SpinZ, SpinXY, or Den. The suffixes R and K refer to real and reciprocal space, respectively
<code>Y_R0/g_R0</code>	Time-resolved and spatially local Jackknife mean and error of Y, where Y stands for Green, SpinZ, SpinXY, and Den
<code>Y_kx_ky/g_kx_ky</code>	Time resolved and k -dependent Jackknife mean and error of Y, where Y stands for Green, SpinZ, SpinXY, and Den
<code>Part_scal_Auto</code>	Autocorrelation functions $S_{\hat{O}}(t_{\text{Auto}})$ in the range $t_{\text{Auto}} = [0, N_{\text{auto}}]$ for the observable \hat{O}

1589 first line of the file contains the number of imaginary times, the effective number of
 1590 bins, β , the number of orbitals and the channel. Both output files have the following
 1591 formatting:

```
1592 do i = 0, Ltau
1593   tau(i)  <mean( Tr[Y] )>  <error( Tr[Y] )>
1594 enddo
```

1595 where Tr corresponds to the trace over the orbital degrees of freedom. For particle-hole
 1596 quantities at finite temperature, τ runs from 0 to $\beta/2$. In all other cases it runs from 0
 1597 to β .

- 1598 • The file `Y_tauJK` contains the susceptibilities defined as:

$$\chi(\mathbf{q}) = \sum_{n,n'=1}^{\text{Norb}} \int_0^\beta d\tau \left(\langle Y_n(\mathbf{q}, \tau) Y_{n'}(-\mathbf{q}, 0) \rangle - \langle Y_n(\mathbf{q}) \rangle \langle Y_{n'}(-\mathbf{q}) \rangle \delta_{\mathbf{q},0} \right). \quad (133)$$

1599 The output file has the following formatting:

```
1600 do i = 0, Ltau
1601   q_x, q_y, <mean(Real(chi(q)) )>, <error(Real(chi(q)))>, &
1602     & <mean(Im(chi(q)) )>, <error(lmi(chi(q)))>
1603 enddo
```

- 1604 • Setting the parameter `N_auto` to a finite value triggers the computation of autocorrelation
 1605 functions $S_{\hat{O}}(t_{\text{Auto}})$ in the range $t_{\text{Auto}} = [0, N_{\text{auto}}]$. The output is written to the
 1606 file `Part_scal_Auto`, where the data is organized in three columns:

```
1607 tAuto S_{\hat{O}}(t_{\text{Auto}}) error
```

1608 Since these computations are quite time consuming and require many Monte Carlo bins,
 1609 our default is `N_auto=0`.

Table 18: Rules of thumb for obtaining best results and performance from ALF. It is important to fine tune the parameters to the specific model under consideration and perform sanity checks throughout. Most suggestions can severely impact performance and numerical stability if overdone.

Element	Suggestion
Precision Green, Precision Phase theta	Should be found to be <i>small</i> , of order $< 10^{-8}$ (see Sec. 2.4)
dtau	Should be <i>large</i> enough to guarantee convergence to ground state
Nwrap	Should be set <i>small</i> enough to keep Precisions small
Nsweep	Should be set <i>large</i> enough for bins to be of the order of the auto-correlation time
Nbin	Should be set <i>large</i> enough to provide desired statistics
nskip	Should be set <i>large</i> enough to allow for equilibration (\sim auto-correlation time)
Nrebin	Can be set to 1 when Nsweep is large enough; otherwise, and for testing, larger values can be used
Stabilization scheme	Use the default STAB3 – newest and fastest, if it works for your model; alternatives are: STAB1 – simplest, for reference only; STAB2 – with additional normalizations; and LOG – for dealing with more extreme scales (see also Tab. 15)
Parallelism	For some models and systems, restricting parallelism in your BLAS library can improve performance: for OpenBLAS try setting OPENBLAS_NUM_THREADS=1 in the shell
ALF_SHM_CHUNK_SIZE_GB	An environment variable that sets the chunk size in GBs for the memory shared between different MPI processes on the same computing node. By default it is zero (i.e., no sharing), but can be set to, e.g., 1.0 or 2.0 GB or larger if, for instance, the total number of MPI communicators is so large as to trigger MPI error messages.

1610 6.4 Parameter optimization

1611 The finite-temperature, auxiliary-field QMC algorithm is known to be numerically unstable, as
 1612 discussed in Sec. 2.4. The numerical instabilities arise from the imaginary-time propagation,
 1613 which invariably leads to exponentially small and exponentially large scales. As shown in
 1614 Ref. [6], scales can be omitted in the ground state algorithm – thus rendering it very stable –
 1615 but have to be taken into account in the finite-temperature code.

1616 Numerical stabilization of the code is a delicate procedure that has been pioneered in
 1617 Ref. [2] for the finite-temperature algorithm and in Refs. [3, 4] for the zero-temperature, pro-
 1618 jective algorithm. It is important to be aware of the fragility of the numerical stabilization and
 1619 that there is no guarantee that it will work for a given model. It is therefore crucial to always
 1620 check the file `info`, which, apart from runtime data, contains important information concern-
 1621 ing the stability of the code, in particular Precision Green. If the numerical stabilization
 1622 fails, one possible measure is to reduce the value of the parameter Nwrap in the parameter
 1623 file, which will however also impact performance – see Table. 18 for further optimization tips
 1624 for the Monte Carlo algorithm (Sec. 4). Typical values for the numerical precision ALF can
 1625 achieve can be found in Sec. 9.1.

1626 In particular, for the stabilization of the involved matrix multiplications we rely on rou-
 1627 tines from LAPACK. Notice that results are very likely to change depending on the specific
 1628 implementation of the library used.⁹ In order to deal with this possibility, we offer a simple
 1629 baseline which can be used as a quick check as to whether results depend on the library used
 1630 for linear algebra routines. Namely, we have included QR-decomposition related routines of
 1631 the LAPACK-3.7.0 reference implementation from <http://www.netlib.org/lapack/>, which you
 1632 can use by running the script `configure.sh`, (described in Sec. 6), with the flag STAB1 and
 1633 recompiling ALF.¹⁰ The stabilization flags available are described in Tables 15 and 18. The
 1634 performance of the package is further discussed in Sec. B.

1635 7 The plain vanilla Hubbard model on the square lattice

1636 All the data structures necessary to implement a given model have been introduced in the
 1637 previous sections. Here we show how to implement a new model based on the example of the
 1638 Hubbard model.

1639 As stated in Sec. 5.6, for defining a new Hamiltonian calle *New_model* one needs to

- 1640 1. Add a new line containing *New_model* to the file `Prog/Hamiltonians.list`
- 1641 2. Write the corresponding new submodule in `Prog/Hamiltonians/Hamiltonian_`
 1642 `New_model_smod.F90`

1643 Here our *New_model* will be `Hubbard_Plain_Vanilla`. There is a template `Prog/`
 1644 `Hamiltonians/Hamiltonian_##NAME##_smod.F90` that can be used for creating a new
 1645 model.

1646 To get a valid Hamiltonian, one has to specify its parameters, the lattice, the hopping,
 1647 the interaction, the trial wave function (if required), and the observables. Consider the *plain*
 1648 *vanilla* Hubbard model written as:

$$\mathcal{H} = -t \sum_{\langle i,j \rangle, \sigma=\uparrow,\downarrow} (\hat{c}_{i,\sigma}^\dagger \hat{c}_{j,\sigma} + \text{H.c.}) - \frac{U}{2} \sum_i [\hat{c}_{i,\uparrow}^\dagger \hat{c}_{i,\uparrow} - \hat{c}_{i,\downarrow}^\dagger \hat{c}_{i,\downarrow}]^2 - \mu \sum_{i,\sigma} \hat{c}_{i,\sigma}^\dagger \hat{c}_{i,\sigma}. \quad (134)$$

1649 Here $\langle i,j \rangle$ denotes nearest neighbors. We can make contact with the general form of the
 1650 Hamiltonian [see Eq. (2)] by setting: $N_{\text{fl}} = 2$, $N_{\text{col}} \equiv N_{\text{SUN}} = 1$, $M_T = 1$,

$$T_{xy}^{(ks)} = \begin{cases} -t, & \text{if } x, y \text{ are nearest neighbors,} \\ -\mu, & \text{if } x = y, \\ 0m, & \text{otherwise.} \end{cases} \quad (135)$$

1651 $M_V = N_{\text{unit-cell}}$, $U_k = \frac{U}{2}$, $V_{xy}^{(k,s=1)} = \delta_{x,y} \delta_{x,k}$, $V_{xy}^{(k,s=2)} = -\delta_{x,y} \delta_{x,k}$, $\alpha_{ks} = 0$ and $M_I = 0$.
 1652 The coupling of the HS fields to the z -component of the magnetization breaks the SU(2) spin
 1653 symmetry. Nevertheless, the z -component of the spin remains a good quantum number such
 1654 that the imaginary-time propagator – for a given HS field – is block diagonal in this quantum
 1655 number. This corresponds to the flavor index running from 1 to 2, labeling spin up and spin
 1656 down degrees of freedom. We note that in this formulation the hopping matrix can be flavor
 1657 dependent such that a Zeeman magnetic field can be introduced. If the chemical potential
 1658 is set to zero, this will not generate a negative sign problem [74, 139, 140]. The code that
 1659 we describe below can be found in the submodule `Prog/Hamiltonians/Hamiltonian_`
 1660 `Hubbard_Plain_Vanilla_smod.F90`.

⁹The linked library should implement at least the LAPACK-3.4.0 interface.

¹⁰This flag may trigger compiling issues, in particular, the Intel ifort compiler version 10.1 fails for all optimization levels.

1661 **7.1 Defining the parameters**

1662 Defining the parameters as specified in Sec. 5.6, we arrive at:

```

1663 !#PARAMETERS START# VAR_lattice
1664 Character (len=64) :: Model = ''      ! Value irrelevant
1665 Character (len=64) :: Lattice_type = 'Square' ! Possible Values: 'Square'
1666 Integer          :: L1 = 4      ! Length in direction a_1
1667 Integer          :: L2 = 4      ! Length in direction a_2
1668 !#PARAMETERS END#
1670
1671 !#PARAMETERS START# VAR_Hubbard_Plain_Vanilla
1672 !Integer          :: N_SUN = 2
1673 real(Kind=Kind(0.d0)) :: ham_T     = 1.d0      ! Hopping parameter
1674 real(Kind=Kind(0.d0)) :: Ham_chem   = 0.d0      ! Chemical potential
1675 real(Kind=Kind(0.d0)) :: Ham_U     = 4.d0      ! Hubbard interaction
1676 real(Kind=Kind(0.d0)) :: Dtau       = 0.1d0    ! Thereby Ltrot=Beta/dtau
1677 real(Kind=Kind(0.d0)) :: Beta        = 5.d0      ! Inverse temperature
1678 !logical           :: Projector = .false. ! Whether the projective algorithm is used
1679 real(Kind=Kind(0.d0)) :: Theta       = 5.d0      ! Projection parameter
1680 !logical           :: Symm       = .false. ! Whether symmetrization takes place
1681 Integer            :: N_part     = -1      ! Number of particles in trial wave function.
1682                           ! If N_part < 0 -> N_part = L1*L2/2
1683 !#PARAMETERS END#

```

1685 We can test the correct formatting of the parameters by calling:

```
1686 ./parse_ham.py --test_file Hamiltonian_Hubbard_Plain_Vanilla_smod.F90
```

1687 **7.2 Setting the Hamiltonian: Ham_set**

1688 The main program will call the subroutine Ham_set in the submodule Hamiltonian_
 1689 Hubbard_Plain_Vanilla_smod.F90 which specify the model. The routine Ham_set will
 1690 first read the parameter file parameters (see Sec. 5.7.1) Call read_parameters; then
 1691 set the lattice: Call Ham_latt; set the hopping: Call Ham_hop; set the interaction: call
 1692 Ham_V; and if required, set the trial wave function: call Ham_trial. In the subroutine
 1693 Ham_set one will equally have to specify if a symmetry relates different flavors. This func-
 1694 tionality is described in Sec. 5.6.1 and one enables it by allocating tine array Calc_F1.

1695 **7.3 The lattice: Ham_latt**

1696 The routine, which sets the square lattice, reads:

```

1697 a1_p(1) = 1.0 ; a1_p(2) = 0.d0
1698 a2_p(1) = 0.0 ; a2_p(2) = 1.d0
1699 L1_p     = dble(L1)*a1_p
1700 L2_p     = dble(L2)*a2_p
1701 Call Make_Lattice(L1_p, L2_p, a1_p, a2_p, Latt)
1702 Latt_unit%Norb = 1
1703 Latt_unit%N_coord = 2
1704 allocate(Latt_unit%Orb_pos_p(Latt_unit%Norb,2))
1705 Latt_unit%Orb_pos_p(1, :) = [0.d0, 0.d0]
1706 Ndim = Latt%N*Latt_unit%\Norb
1707

```

1709 In its last line, the routine sets the total number of single particle states per flavor and color:
 1710 Ndim = Latt%N*Latt_unit%Norb.

1711 **7.4 The hopping: Ham_hop**

1712 The hopping matrix is implemented as follows. We allocate an array of dimension $1 \times N_{\text{fl}}$ of
 1713 type operator called Op_T and set the dimension for the hopping matrix to $N = N_{\text{dim}}$. The
 1714 operator allocation and initialization is performed by the subroutine Op_make:

```

1715 do nf = 1,N_FL
1716   call Op_make(Op_T(1,nf),Ndim)
1717 enddo
1718

```

1720 Since the hopping does not break down into small blocks, we have $P = \mathbb{1}$ and

```

1721 Do nf = 1, N_FL
1722   Do i = 1,Latt%N
1723     Op_T(1,nf)%P(i) = i
1724   Enddo
1725 Enddo
1726

```

1728 We set the hopping matrix with

```

1729 Do nf = 1, N_FL
1730   Do I = 1, Latt%N
1731     Ix = Latt%nnlist(I,1,0)
1732     Iy = Latt%nnlist(I,0,1)
1733     Op_T(1,nf)%O(I, Ix) = cmplx(-Ham_T, 0.d0, kind(0.D0))
1734     Op_T(1,nf)%O(Ix, I ) = cmplx(-Ham_T, 0.d0, kind(0.D0))
1735     Op_T(1,nf)%O(I, Iy) = cmplx(-Ham_T, 0.d0, kind(0.D0))
1736     Op_T(1,nf)%O(Iy, I ) = cmplx(-Ham_T, 0.d0, kind(0.D0))
1737     Op_T(1,nf)%O(I, I ) = cmplx(-Ham_chem, 0.d0, kind(0.D0))
1738   Enddo
1739   Op_T(1,nf)%g      = -Dtau
1740   Op_T(1,nf)%alpha = cmplx(0.d0,0.d0, kind(0.D0))
1741   Call Op_set(Op_T(1,nf))
1742 Enddo
1743

```

1745 Here, the integer function `Latt%nnlist(I,n,m)` is defined in the lattice module and
 1746 returns the index of the lattice site $I + na_1 + ma_2$. Note that periodic boundary con-
 1747 ditions are already taken into account. The hopping parameter `Ham_T`, as well as
 1748 the chemical potential `Ham_chem` are read from the parameter file. To completely
 1749 define the hopping we further set: `Op_T(1,nf)%g = -Dtau` , `Op_T(1,nf)%alpha =`
 1750 `cmplx(0.d0,0.d0,kind(0.D0))` and call the routine `Op_set(Op_T(1,nf))` so as to gen-
 1751 erate the unitary transformation and eigenvalues as specified in Table 2. Recall that for the
 1752 hopping, the variable `Op_set(Op_T(1,nf))%type` takes its default value of 0. Finally, note
 1753 that, although a checkerboard decomposition is not used here, it can be implemented by con-
 1754 sidering a larger number of sparse hopping matrices.

1755 7.5 The interaction: Ham_V

1756 To implement the interaction, we allocate an array of `Operator` type. The array is called
 1757 `Op_V` and has dimensions $N_{\text{dim}} \times N_{\text{fl}} = N_{\text{dim}} \times 2$. We set the dimension for the interaction term
 1758 to $N = 1$, and allocate and initialize this array of type `Operator` by repeatedly calling the
 1759 subroutine `Op_make`:

```

1760 Allocate(Op_V(Ndim,N_FL))
1761 do nf = 1,N_FL
1762   do i = 1, Ndim
1763     Call Op_make(Op_V(i,nf), 1)
1764   enddo
1765 enddo
1766 Do nf = 1,N_FL
1767   X = 1.d0
1768   if (nf == 2) X = -1.d0
1769   Do i = 1,Ndim
1770     nc = nc + 1
1771     Op_V(i,nf)%P(1) = i
1772     Op_V(i,nf)%O(1,1) = cmplx(1.d0, 0.d0, kind(0.D0))
1773     Op_V(i,nf)%g      = X*SQRT(CMPLX(DTAU*ham_U/2.d0, 0.D0, kind(0.D0)))
1774     Op_V(i,nf)%alpha = cmplx(-0.5d0, 0.d0, kind(0.D0))
1775     Op_V(i,nf)%type   = 2
1776     Call Op_set( Op_V(i,nf) )
1777   Enddo
1778 Enddo
1779

```

1781 The code above makes it explicit that there is a sign difference between the coupling of the
 1782 HS field in the two flavor sectors. Hence, $\text{Op_V}(i, \text{nf})$ encodes $e^{X\sqrt{\Delta\tau U/2}(\hat{c}_{i,\text{nf}}^\dagger \hat{c}_{i,\text{nf}} + \alpha)}$ with
 1783 $X = 1$ for $\text{nf} = 1$ and $X = -1$ for $\text{nf} = 2$. Strictly speaking X can be omitted. However, it
 1784 is required when using the flavor symmetry option in the presence of particle-hole symmetry
 1785 (see Sec. 5.6.1).

1786 7.6 The trial wave function: Ham_Trial

1787 As argued in Sec. 3.1, it is useful to generate the trial wave function from a non-interacting trial
 1788 Hamiltonian. Here we will use the same left and right flavor-independent trial wave functions
 1789 that correspond to the ground state of:

$$\hat{H}_T = -t \sum_i \left[(1 + (-1)^{i_x+i_y} \delta) \hat{c}_i^\dagger \hat{c}_{i+a_x} + (1 - \delta) \hat{c}_i^\dagger \hat{c}_{i+a_y} + \text{H.c.} \right] \equiv \sum_{i,j} \hat{c}_i^\dagger h_{i,j} \hat{c}_i . \quad (136)$$

1790 For the half-filled case, the dimerization $\delta = 0^+$ opens up a gap at half-filling, thus generating
 1791 the desired non-degenerate trial wave function that has the same symmetries (particle-hole
 1792 for instance) as the trial Hamiltonian.

1793 Diagonalization of $h_{i,j}$, $U^\dagger h U = \text{Diag}(\epsilon_1, \dots, \epsilon_{N_{\text{dim}}})$ with $\epsilon_i < \epsilon_j$ for $i < j$, allows us to
 1794 define the trial wave function. In particular, for the half-filled case, we set

```
1795 Do s = 1, N_f1
1796   Do x = 1, Ndim
1797     Do n = 1, N_part
1798       WF_L(s)%P(x,n) = U_x,n
1799       WF_R(s)%P(x,n) = U_x,n
1800     Enddo
1801   Enddo
1802 Enddo
```

1805 with $N_{\text{part}} = N_{\text{dim}}/2$. The variable Degen belonging to the WaveFunction type is given
 1806 by $\text{Degen} = \epsilon_{N_{\text{part}}+1} - \epsilon_{N_{\text{part}}}$. This quantity should be greater than zero for non-degenerate trial
 1807 wave functions.

1808 7.7 Observables

1809 At this point, all the information for starting the simulation has been provided. The code will
 1810 sequentially go through the operator list Op_V and update the fields. Between time slices
 1811 LOBS_ST and LOBS_EN the main program will call the routine $\text{Obser}(\text{GR}, \text{Phase}, \text{Ntau})$,
 1812 which handles equal-time correlation functions, and, if $\text{Ltau}=1$, the routine $\text{ObserT}(\text{NT},$
 1813 $\text{GTO}, \text{GOT}, \text{GOO}, \text{GTT}, \text{PHASE})$ which handles imaginary-time displaced correlation func-
 1814 tions.

1815 Both Obser and ObserT should be provided by the user, who can either implement them-
 1816 selves the observables they want to compute or use the predefined structures of Chap. 8. Here
 1817 we describe how to proceed in order to define an observable.

1818 7.7.1 Allocating space for the observables: Alloc_obs(Ltau)

1819 For four scalar or vector observables, the user will have to declare the following:

```
1820
1821 Allocate ( Obs_scal(4) )
1822 Do I = 1, Size(Obs_scal,1)
1823   select case (I)
1824     case (1)
1825       N = 2;  Filename ="Kin"
1826     case (2)
1827       N = 1;  Filename ="Pot"
1828     case (3)
```

```

1829     N = 1;  Filename ="Part"
1830     case (4)
1831         N = 1,  Filename ="Ener"
1832     case default
1833         Write(6,*) ' Error in Alloc_obs ,
1834     end select
1835     Call Obser_Vec_make(Obs_scal(I), N, Filename)
1836 enddo

```

1838 Here, Obs_scal(1) contains a vector of two observables so as to account for the x - and
 1839 y -components of the kinetic energy, for example.

1840 For equal-time correlation functions we allocate Obs_eq of type Obser_Latt. Here we
 1841 include the calculation of spin-spin and density-density correlation functions alongside equal-
 1842 time Green functions.

```

1843 Allocate ( Obs_eq(5) )
1844 Do I = 1,Size(Obs_eq,1)
1845     select case (I)
1846     case (1)
1847         Filename = "Green"
1848     case (2)
1849         Filename = "SpinZ"
1850     case (3)
1851         Filename = "SpinXY"
1852     case (4)
1853         Filename = "SpinT"
1854     case (5)
1855         Filename = "Den"
1856     case default
1857         Write(6,*) "Error in Alloc_obs"
1858     end select
1859     Nt = 1
1860     Channel = "--"
1861     Call Obser_Latt_make(Obs_eq(I), Nt, Filename, Latt, Latt_unit, Channel, dtau)
1862 Enddo

```

1865 Be aware that Obser_Latt_make does not copy the Bravais lattice Latt and unit cell
 1866 Latt_unit, but links them through pointers to be more memory efficient. One can
 1867 have different lattices attached to different observables by declaring additional instances of
 1868 Type(Lattice) and Type(Unit_cell). For equal-time correlation functions, we set Nt =
 1869 1 and Channel specification is not necessary.

1870 If Ltau = 1, then the code allocates space for time displaced quantities. The same structure
 1871 as for equal-time correlation functions is used, albeit with Nt = Ltrot + 1 and the
 1872 channel should be set. Whith Channel="PH", for instance, the analysis algorithm assumes
 1873 the observable to be particle-hole symmetric. For more details on this parameter, see Sec. 10.

1874 At the beginning of each bin, the main program will set the bin observables to zero by
 1875 calling the routine Init_obs(Ltau). The user does not have to edit this routine.

1876 7.7.2 Measuring equal-time observables: Obser(GR,Phase,Ntau)

1877 Having allocated the necessary memory, we proceed to define the observables. The equal-time
 1878 Green function,

$$GR(x, y, \sigma) = \langle \hat{c}_{x,\sigma} \hat{c}_{y,\sigma}^\dagger \rangle, \quad (137)$$

1879 the phase factor phase [Eq. (122)], and time slice Ntau are provided by the main program.

1880 Here, x and y label both unit cell as well as the orbital within the unit cell. For the Hubbard
 1881 model described here, x corresponds to the unit cell. The Green function does not depend on
 1882 the color index, and is diagonal in flavor. For the SU(2) symmetric implementation there is
 1883 only one flavor, $\sigma = 1$ and the Green function is independent on the spin index. This renders
 1884 the calculation of the observables particularly easy.

1885 An explicit calculation of the potential energy $\langle U \sum_i \hat{n}_{i,\uparrow} \hat{n}_{i,\downarrow} \rangle$ reads

```

1886 Obs_scal(2)%N      = Obs_scal(2)%N + 1
1887 Obs_scal(2)%Ave_sign = Obs_scal(2)%Ave_sign + Real(ZS,kind(0.d0))
1888 Do i = 1,Ndim
1889   Obs_scal(2)%Obs_vec(1)= Obs_scal(2)%Obs_vec(1) +(1-GR(i,i,1))*(1-GR(i,i,2))*Ham_U*ZS*ZP
1890 Enddo
1891

```

1893 Here $ZS = \text{sgn}(C)$ [see Eq. (26)], $ZP = \frac{e^{-S(C)}}{\text{Re}[e^{-S(C)}]}$ [see Eq. (122)] and Ham_U corresponds to
1894 the Hubbard U term.

1895 Equal-time correlations are also computed in this routine. As an explicit example, we
1896 consider the equal-time density-density correlation:

$$\langle \hat{n}_i \hat{n}_j \rangle - \langle \hat{n}_i \rangle \langle \hat{n}_j \rangle, \quad (138)$$

1897 with

$$\hat{n}_i = \sum_{\sigma} \hat{c}_{i,\sigma}^{\dagger} \hat{c}_{i,\sigma}. \quad (139)$$

1898 For the calculation of such quantities, it is convenient to define:

$$\text{GRC}(x,y,s) = \delta_{x,y} - \text{GR}(y,x,s), \quad (140)$$

1899 such that $\text{GRC}(x,y,s)$ corresponds to $\langle \langle \hat{c}_{x,s}^{\dagger} \hat{c}_{y,s} \rangle \rangle$. In the program code, the calculation of the
1900 equal-time density-density correlation function looks as follows:

```

1901 Obs_eq(4)%N = Obs_eq(4)%N + 1           ! Even if it is redundant, each observable
1902                                         ! carries its own counter and sign.
1903 Obs_eq(4)%Ave_sign = Obs_eq(4)%Ave_sign + Real(ZS,kind(0.d0))
1904 Do I = 1,Ndim
1905   Do J = 1,Ndim
1906     imj = latt%imj(I,J)
1907     Obs_eq(4)%Obs_Latt(imj,1,1,1) = Obs_eq(4)%Obs_Latt(imj,1,1,1) + &
1908       & ( (GRC(I,I,1)+GRC(I,I,2)) * (GRC(J,J,1)+GRC(J,J,2)) + &
1909       & GRC(I,J,1)*GR(I,J,1) + GRC(I,J,2)*GR(I,J,2) ) * ZP * ZS
1910   Enddo
1911   Obs_eq(4)%Obs_Latt0(1) = Obs_eq(4)%Obs_Latt0(1) + (GRC(I,I,1)+GRC(I,I,2))*ZP*ZS
1912 Enddo
1913

```

1915 At the end of each bin the main program calls the routine `Pr_obs(LTAU)`. This routine
1916 appends the result for the current bins to the corresponding file, with the appropriate suffix.

1917 7.7.3 Measuring time-displaced observables: `ObserT(NT, GTO, GOT, G00, GTT,` 1918 `PHASE)`

1919 This subroutine is called by the main program at the beginning of each sweep, provided that
1920 $LTAU$ is set to 1. The variable NT runs from 0 to $Ltrot$ and denotes the imaginary time
1921 difference. For a given time displacement, the main program provides:

$$\begin{aligned} \text{GTO}(x,y,s) &= \langle \langle \hat{c}_{x,s}(Nt\Delta\tau) \hat{c}_{y,s}^{\dagger}(0) \rangle \rangle = \langle \langle \mathcal{T} \hat{c}_{x,s}(Nt\Delta\tau) \hat{c}_{y,s}^{\dagger}(0) \rangle \rangle, \\ \text{GOT}(x,y,s) &= -\langle \langle \hat{c}_{y,s}^{\dagger}(Nt\Delta\tau) \hat{c}_{x,s}(0) \rangle \rangle = \langle \langle \mathcal{T} \hat{c}_{x,s}(0) \hat{c}_{y,s}^{\dagger}(Nt\Delta\tau) \rangle \rangle, \\ \text{G00}(x,y,s) &= \langle \langle \hat{c}_{x,s}(0) \hat{c}_{y,s}^{\dagger}(0) \rangle \rangle, \\ \text{GTT}(x,y,s) &= \langle \langle \hat{c}_{x,s}(Nt\Delta\tau) \hat{c}_{y,s}^{\dagger}(Nt\Delta\tau) \rangle \rangle. \end{aligned} \quad (141)$$

1922 In the above we have omitted the color index since the Green functions are color independent.
1923 The time-displaced spin-spin correlations $4\langle \langle \hat{S}_i^z(\tau) \hat{S}_j^z(0) \rangle \rangle$ are then given by:

$$\begin{aligned} 4\langle \langle \hat{S}_i^z(\tau) \hat{S}_j^z(0) \rangle \rangle &= (\text{GTT}(I,I,1) - \text{GTT}(I,I,2)) * (\text{G00}(J,J,1) - \text{G00}(J,J,2)) \\ &\quad - \text{GOT}(J,I,1) * \text{GTO}(I,J,1) - \text{GOT}(J,I,2) * \text{GTO}(I,J,2). \end{aligned} \quad (142)$$

1924 The handling of time-displaced correlation functions is identical to that of equal-time cor-
1925 relations.

1926 **7.8 Flavor symmetries: weight_reconstruction(weight),**
 1927 **GR_reconstruction(GR), and GRT_reconstruction(GTO, GOT)**

1928 At zero chemical potential, and for repulsive interactions, the plain-vanilla Hubbard model
 1929 enjoys a partial particle-hole symmetry which, for each HS field configuration, maps one flavor
 1930 (i.e. spin sector) onto the other:

$$\hat{P}z\hat{c}_{i,\downarrow}^{\dagger}\hat{P}^{-1}=z^*e^{i\mathbf{i}\cdot\mathbf{Q}}\hat{c}_{i,\uparrow}. \quad (143)$$

1931 Here \mathbf{Q} is the antiferromagnetic wave vector. Note that in the presence of an orbital magnetic
 1932 field, or of twisted boundary conditions that couples symmetrically to the flavor (spin) degree
 1933 of freedom, the anti-unitarity of the transformation is required. As a consequence of this
 1934 symmetry, for a given HS field configuration the following holds for the equal-time Green
 1935 function.

$$\begin{aligned} G00(x,y,\uparrow) &= \langle\langle\hat{c}_{x,\uparrow}(0)\hat{c}_{y,\uparrow}^{\dagger}(0)\rangle\rangle = e^{i(y-x)\cdot\mathbf{Q}}\overline{\langle\langle\hat{c}_{x,\downarrow}^{\dagger}(0)\hat{c}_{y,\uparrow}(0)\rangle\rangle} \\ &= \delta_{x,y}-e^{i(y-x)\cdot\mathbf{Q}}\overline{G00(y,x,\downarrow)}. \end{aligned} \quad (144)$$

1936 For the attractive Hubbard model $U < 0$, the up and down sectors are related by time
 1937 reversal symmetry:

$$\hat{T}z\begin{pmatrix} \hat{c}_{i,\uparrow} \\ \hat{c}_{i,\downarrow} \end{pmatrix}\hat{T}^{-1}=z^*i\sigma_y\begin{pmatrix} \hat{c}_{i,\uparrow} \\ \hat{c}_{i,\downarrow} \end{pmatrix}. \quad (145)$$

1938 Of course, we have assumed that the hopping remains invariant under time reversal. As a
 1939 consequence of this symmetry:

$$G00(x,y,\uparrow)=\overline{G00(x,y\downarrow)}. \quad (146)$$

1940 The usage of the flavor symmetry is described in Sec. 5.6.1. Only one flavor has to be
 1941 computed and the routines GR_reconstruction(GR), and GRT_reconstruction(GTO,
 1942 GOT) reconstruct, respectively, the equal-time and time-displaced Green functions for one fla-
 1943 vor given the other. Hence we gain a factor two in computing time. We note that since both
 1944 symmetries are anti-unitary, the weights between the two sectors are related by a complex
 1945 conjugation. This is specified in the routine weight_reconstruction(weight).

1946 7.9 Numerical precision

1947 Information on the numerical stability is included in the following lines of the corresponding
 1948 file info. For a short simulation on a 4×4 lattice at $U/t = 4$ and $\beta t = 10$ we obtain

```
1949 Precision Green Mean, Max : 5.0823874429126405E-011 5.8621144596315844E-006
1950 Precision Phase Max : 0.0000000000000000
1951 Precision tau Mean, Max : 1.5929357848647394E-011 1.0985132530727526E-005
```

1952 showing the mean and maximum difference between the wrapped and from scratch computed
 1953 equal and time-displaced Green functions [6]. A stable code should produce results
 1954 where the mean difference is smaller than the stochastic error. The above example shows a
 1955 very stable simulation since the Green function is of order one.

1956 7.10 Running the code and testing

1957 To test the code, one can carry out high precision simulations. After compilation, the exe-
 1958 cutable ALF.out is found in the directory \$ALF_DIR/Prog/ and can be run from any direc-
 1959 tory containing the files parameters and seeds (See Sec. 5.7).

1960 Alternatively, as we do below, it may be convenient to use pyALF to compile and run the
 1961 code, especially when using one of the scripts or notebooks available.

Table 19: Test results for the `Hubbard_Plain_Vanilla` code on a two-dimensional lattice with default parameters.

	QMC	Exact
Total energy	-13.618 ± 0.002	-13.6224
$\mathbf{Q} = (\pi, \pi)$ spin correlations	3.630 ± 0.006	3.64

1962 **One-dimensional case** The pyALF python script `Hubbard_Plain_Vanilla.py` runs the
 1963 projective version of the code for the four-site Hubbard model. At $\theta t = 10$, $\Delta\tau t = 0.05$ with
 1964 the symmetric Trotter decomposition, we obtain after 40 bins of 2000 sweeps each the total
 1965 energy:

$$\langle \hat{H} \rangle = -2.103750 \pm 0.004825,$$

1966 and the exact result is

$$\langle \hat{H} \rangle_{\text{Exact}} = -2.100396.$$

1967 **Two-dimensional case** For the two-dimensional case, with similar parameters, we obtain the
 1968 results listed in Table 19. The exact results stem from Ref. [141] and the slight discrepancies
 1969 from the exact results can be assigned to the finite value of $\Delta\tau$. Note that all the simulations
 1970 were carried out with the default value of the Hubbard interaction, $U/t = 4$.

1971 8 Predefined structures

1972 The ALF package includes predefined structures, which the user can combine together or use
 1973 as templates for defining new ones. Using the data types defined in the Sec. 5 the following
 1974 modules are available:

- 1975 • lattices and unit cells – `Predefined_Latt_mod.F90`
- 1976 • hopping Hamiltonians – `Predefined_Hop_mod.F90`
- 1977 • interaction Hamiltonians – `Predefined_Int_mod.F90`
- 1978 • observables – `Predefined_Obs_mod.F90`
- 1979 • trial wave functions – `Predefined_Trial_mod.F90`

1980 which we describe in the remaining of this section.

1981 8.1 Predefined lattices

1982 The types `Lattice` and `Unit_cell`, described in Section 5.3, allow us to define arbitrary
 1983 one- and two-dimensional Bravais lattices. The subroutine `Predefined_Latt` provides some
 1984 of the most common lattices, as described below.

1985 The subroutine is called as:

```
1986 Predefined_Latt(Lattice_type, L1, L2, Ndim, List, Invlist, Latt, Latt_Unit)
```

1989 which returns a lattice of size $L_1 \times L_2$ of the given `Lattice_type`, as detailed in Table 20.
 1990 Notice that the orbital position `Latt_Unit%Orb_pos_p(1, :)` is set to zero unless otherwise
 1991 specified.

1992 In order to easily keep track of the orbital and unit cell, `List` and `Invlist` make use of a
 1993 super-index, defined as shown below:

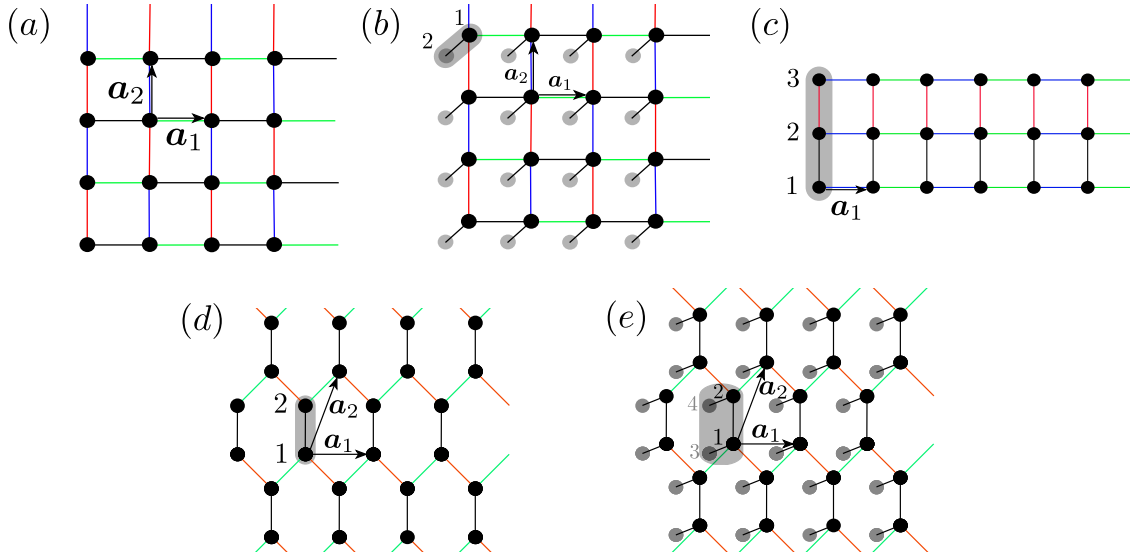


Figure 6: Predefined lattices in ALF: (a) square, (b) bilayer square, (c) 3-leg ladder, (d) honeycomb, and (e) bilayer honeycomb. Nontrivial unit cells are shown as gray regions, while gray sites belong to the second layer in bilayer systems. The links between the orbitals denote the hopping matrix elements and we have assumed, for the purpose of the plot, the absence of hopping in the second layer for bilayer systems. The color coding of the links denotes the checkerboard decomposition.

```

1994 nc = 0
1995      ! Super-index labeling unit cell and orbital
1996 Do I = 1,Latt%N
1997   Do no = 1,Norb
1998     nc = nc + 1
1999     List(nc,1) = I
2000     List(nc,2) = no
2001     Invlist(I,no) = nc
2002   Enddo
2003 Enddo

```

With the above-defined lists one can run through all the orbitals while keeping track of the unit-cell and orbital index. We note that when translation symmetry is completely absent one can work with a single unit cell, and the number of orbitals will then correspond to the number of lattice sites.

8.1.1 Square lattice, Fig. 6(a)

The choice `Lattice_type = "Square"` sets $\mathbf{a}_1 = (1, 0)$ and $\mathbf{a}_2 = (0, 1)$ and for an $L_1 \times L_2$ lattice $\mathbf{L}_1 = L_1 \mathbf{a}_1$ and $\mathbf{L}_2 = L_2 \mathbf{a}_2$:

```

2012
2013 Latt_Unit%N_coord    = 2
2014 Latt_Unit%Norb       = 1
2015 Latt_Unit%Orb_pos_p(1,:) = 0.d0
2016 a1_p(1) = 1.0 ; a1_p(2) = 0.d0
2017 a2_p(1) = 0.0 ; a2_p(2) = 1.d0
2018 L1_p   = dble(L1)*a1_p
2019 L2_p   = dble(L2)*a2_p
2020 Call Make_Lattice( L1_p, L2_p, a1_p, a2_p, Latt )

```

Also, the number of orbitals per unit cell is given by `NORB=1` such that $N_{\text{dim}} \equiv N_{\text{unit-cell}} \cdot \text{NORB} = \text{Latt}%N \cdot \text{NORB}$, since $N_{\text{unit-cell}} = \text{Latt}%N$.

Table 20: Arguments of the subroutine `Predefined_Latt`. Note that the `Pi_Flux` lattice is deprecated, since it can be emulated with the Square lattice with half a flux quanta piercing each plaquette.

Argument	Type	Role	Description
<code>Lattice_type</code>	char	Input	Lattice configuration, which can take the values: - Square - Honeycomb - <code>Pi_Flux</code> (deprecated) - <code>N_leg_ladder</code> - <code>Bilayer_square</code> - <code>Bilayer_honeycomb</code>
<code>L1, L2</code>	int	Input	Lattice sizes (set <code>L2=1</code> for 1D lattices)
<code>Ndim</code>	int	Output	Total number of orbitals
<code>List</code>	int	Output	For every site index $I \in [1, Ndim]$, stores the corresponding lattice position, <code>List(I,1)</code> , and the (local) orbital index, <code>List(I,2)</code>
<code>Invlist</code>	int	Output	For every <code>lattice_position</code> $\in [1, Latt\%N]$ and <code>orbital</code> $\in [1, Norb]$ stores the corresponding site index $I(lattice_position, orbital)$
<code>Latt</code>	Lattice	Output	Sets the lattice
<code>Latt_Unit</code>	Unit_cell	Output	Sets the unit cell

2024 8.1.2 Bilayer square lattice, Fig. 6(b)

2025 The "Bilayer_square" configuration sets:

```

2026
2027 Latt_Unit%Norb      = 2
2028 Latt_Unit%N_coord   = 2
2029 do no = 1,2
2030   Latt_Unit%Orb_pos_p(no,1) = 0.d0
2031   Latt_Unit%Orb_pos_p(no,2) = 0.d0
2032   Latt_Unit%Orb_pos_p(no,3) = real(1-no,kind(0.d0))
2033 enddo
2034 Call Make_Lattice( L1_p, L2_p, a1_p, a2_p, Latt )
2035 Latt%a1_p(1) = 1.0 ; Latt%a1_p(2) = 0.d0
2036 Latt%a2_p(1) = 0.0 ; Latt%a2_p(2) = 1.d0
2037 Latt%L1_p    = dble(L1)*a1_p
2038 Latt%L2_p    = dble(L2)*a2_p

```

2040 8.1.3 N-leg ladder lattice, Fig. 6(c)

2041 The "N_leg_ladder" configuration sets:

```

2042
2043 Latt_Unit%Norb      = L2
2044 Latt_Unit%N_coord   = 1
2045 do no = 1,L2
2046   Latt_Unit%Orb_pos_p(no,1) = 0.d0
2047   Latt_Unit%Orb_pos_p(no,2) = real(no-1,kind(0.d0))
2048 enddo
2049 a1_p(1) = 1.0 ; a1_p(2) = 0.d0
2050 a2_p(1) = 0.0 ; a2_p(2) = 1.d0
2051 L1_p    = dble(L1)*a1_p
2052 L2_p    = a2_p
2053 Call Make_Lattice( L1_p, L2_p, a1_p, a2_p, Latt )

```

2055 8.1.4 Honeycomb lattice, Fig. 6(d)

2056 In order to carry out simulations on the Honeycomb lattice, which is a triangular Bravais lattice
 2057 with two orbitals per unit cell, choose Lattice_type="Honeycomb", which sets

```
2058
2059 a1_p(1) = 1.D0 ; a1_p(2) = 0.d0
2060 a2_p(1) = 0.5D0 ; a2_p(2) = sqrt(3.D0)/2.D0
2061 L1_p = Dble(L1) * a1_p
2062 L2_p = dble(L2) * a2_p
2063 Call Make_Lattice( L1_p, L2_p, a1_p, a2_p, Latt )
2064 Latt_Unit%Norb = 2
2065 Latt_Unit%N_coord = 3
2066 Latt_Unit%Orb_pos_p(1,:) = 0.d0
2067 Latt_Unit%Orb_pos_p(2,:) = (a2_p(:) - 0.5D0*a1_p(:)) * 2.D0/3.D0
```

2069 The coordination number of this lattice is N_coord=3 and the number of orbitals per unit
 2070 cell, NORB=2. The total number of orbitals is therefore $N_{\text{dim}} = \text{Latt}\%N * \text{NORB}$.

2071 8.1.5 Bilayer honeycomb lattice, Fig. 6(e)

2072 The "Bilayer_honeycomb" configuration sets:

```
2073
2074 Latt_Unit%Norb = 4
2075 Latt_Unit%N_coord = 3
2076 Latt_Unit%Orb_pos_p = 0.d0
2077 do n = 1,2
2078   Latt_Unit%Orb_pos_p(1,n) = 0.d0
2079   Latt_Unit%Orb_pos_p(2,n) = (a2_p(n) - 0.5D0*a1_p(n)) * 2.D0/3.D0
2080   Latt_Unit%Orb_pos_p(3,n) = 0.d0
2081   Latt_Unit%Orb_pos_p(4,n) = (a2_p(n) - 0.5D0*a1_p(n)) * 2.D0/3.D0
2082 enddo
2083 Latt_Unit%Orb_pos_p(3,3) = -1.d0
2084 Latt_Unit%Orb_pos_p(4,3) = -1.d0
2085 a1_p(1) = 1.D0 ; a1_p(2) = 0.d0
2086 a2_p(1) = 0.5D0 ; a2_p(2) = sqrt(3.D0)/2.D0
2087 L1_p = dble(L1)*a1_p
2088 L2_p = dble(L2)*a2_p
2089 Call Make_Lattice( L1_p, L2_p, a1_p, a2_p, Latt )
```

2091 8.1.6 π -flux lattice (deprecated)

2092 The "Pi_Flux" lattice has been deprecated, since it can be emulated with the Square lattice
 2093 with half a flux quanta piercing each plaquette. Nonetheless, the configuration is still available,
 2094 and sets:

```
2095
2096 Latt_Unit%Norb = 2
2097 Latt_Unit%N_coord = 4
2098 a1_p(1) = 1.D0 ; a1_p(2) = 1.d0
2099 a2_p(1) = 1.D0 ; a2_p(2) = -1.d0
2100 Latt_Unit%Orb_pos_p(1,:) = 0.d0
2101 Latt_Unit%Orb_pos_p(2,:) = (a1_p(:) - a2_p(:))/2.d0
2102 L1_p = dble(L1) * (a1_p - a2_p)/2.d0
2103 L2_p = dble(L2) * (a1_p + a2_p)/2.d0
2104 Call Make_Lattice( L1_p, L2_p, a1_p, a2_p, Latt )
```

2106 8.2 Generic hopping matrices on Bravais lattices

2107 The module Predefined_Hopping provides a generic way to specify a hopping matrix on a
 2108 multi-orbital Bravais lattice. The only assumption that we make is translation symmetry. We
 2109 allow for twisted boundary conditions in the L_1 and L_2 lattice directions. The twist is given by
 2110 Phi_X and Phi_Y respectively. If the flag bulk=.true., then the twist is implemented with
 2111 a vector potential. Otherwise, if bulk=.false., the twist is imposed at the boundary. The
 2112 routine also accounts for the inclusion of a total number of N_Phi flux quanta traversing the

2113 lattice. All phase factors mentioned above can be flavor dependent. Finally, the checkerboard
 2114 decomposition can also be specified in this module.

2115 **8.2.1 Setting up the hopping matrix: The Hopping_Matrix_type**

2116 All information for setting up a generic hopping matrix on a lattice, including the checkerboard
 2117 decomposition, is specified in the `Hopping_Matrix_type` type, which we describe in the
 2118 remaining of this section. The information stored in this type (see Table 21) fully defines the
 2119 array of operator type `OP_T` that accounts for the single particle propagation in one time step,
 2120 from which the kinetic energy can be derived as well.

2121 **Generic hopping matrices** The generic Hopping Hamiltonian reads:

$$\hat{H}_T = \sum_{(i,\delta),(j,\delta'),s,\sigma} T_{(i,\delta),(j,\delta'),s,\sigma}^{(s)} \hat{c}_{(i,\delta),s,\sigma}^\dagger e^{\frac{2\pi i}{\Phi_0} \int_{i+\delta}^{j+\delta'} A^{(s)}(l) dl} \hat{c}_{(j,\delta'),s,\sigma}, \quad (147)$$

2122 with boundary conditions

$$\hat{c}_{(i+L_i,\delta),s,\sigma}^\dagger = e^{-2\pi i \frac{\Phi_i^{(s)}}{\Phi_0}} e^{\frac{2\pi i}{\Phi_0} \chi_{L_i}^{(s)}(i+\delta)} \hat{c}_{(i,\delta),s,\sigma}^\dagger. \quad (148)$$

2123 Here i labels the unit cell and δ the orbital. Both the twist and vector potential can have a
 2124 flavor dependency. These and the other components of the generic Hopping Hamiltonian are
 2125 described below. For now onwards we will mostly omit the flavor index s .

2126 **Phase factors.** The vector potential accounts for an orbital magnetic field in the z direction
 2127 that is implemented in the Landau gauge: $A(\mathbf{x}) = -B(y, 0, 0)$ with $\mathbf{x} = (x, y, z)$. Φ_0 corre-
 2128 sponds to the flux quanta and the scalar function χ is defined through:

$$A(\mathbf{x} + \mathbf{L}_i) = A(\mathbf{x}) + \nabla \chi_{L_i}(\mathbf{x}). \quad (149)$$

2129 Provided that the bare hopping Hamiltonian, T (i.e., without phases, see Eq. (155)), is
 2130 invariant under lattice translations, \hat{H}_T commutes with magnetic translations that satisfy the
 2131 algebra:

$$\hat{T}_a \hat{T}_b = e^{\frac{2\pi i}{\Phi_0} \mathbf{B} \cdot (\mathbf{a} \times \mathbf{b})} \hat{T}_b \hat{T}_a. \quad (150)$$

2132 On the torus, the uniqueness of the wave functions requires that $\hat{T}_{L_1} \hat{T}_{L_2} = \hat{T}_{L_2} \hat{T}_{L_1}$ such that

$$\frac{\mathbf{B} \cdot (\mathbf{a} \times \mathbf{b})}{\Phi_0} = N_\Phi, \quad (151)$$

2133 with N_Φ an integer. The variable `N_Phi`, specified in the parameter file, denotes the number
 2134 of flux quanta piercing the lattice. The variables `Phi_X` and `Phi_Y` also in the parameter file
 2135 denote the twists – in units of the flux quanta – along the L_1 and L_2 directions. There are
 2136 gauge equivalent ways to insert the twist in the boundary conditions. In the above we have
 2137 inserted the twist as a boundary condition such that for example setting `Phi_1=0.5` corre-
 2138 sponds to anti-periodic boundary conditions along the L_1 axis. Alternatively we can consider
 2139 the Hamiltonian:

$$\hat{H}_T = \sum_{(i,\delta),(j,\delta'),s,\sigma} T_{(i,\delta),(j,\delta'),s,\sigma}^{(s)} \tilde{c}_{(i,\delta),s,\sigma}^\dagger e^{\frac{2\pi i}{\Phi_0} \int_{i+\delta}^{j+\delta'} (A(l) + A_\phi) dl} \tilde{c}_{(j,\delta'),s,\sigma}, \quad (152)$$

2140 with boundary conditions

$$\tilde{c}_{(i+L_i,\delta),s,\sigma}^\dagger = e^{\frac{2\pi i}{\Phi_0} \chi_{L_i}(i+\delta)} \tilde{c}_{(i,\delta),s,\sigma}^\dagger. \quad (153)$$

2141 Here

$$\mathbf{A}_\phi = \frac{\phi_1 |\mathbf{a}_1|}{2\pi |\mathbf{L}_1|} \mathbf{b}_1 + \frac{\phi_2 |\mathbf{a}_2|}{2\pi |\mathbf{L}_2|} \mathbf{b}_2, \quad (154)$$

2142 and \mathbf{b}_i corresponds to the reciprocal lattice vectors satisfying $\mathbf{a}_i \cdot \mathbf{b}_j = 2\pi\delta_{i,j}$. The logical
 2143 variable `bulk` chooses between these two gauge equivalent ways of inserting the twist angle.
 2144 If `bulk=.true.` then we use periodic boundary conditions – in the absence of an orbital field
 2145 – otherwise twisted boundaries are used. The above phase factors are computed in the module
 2146 function:

```
2147 complex function Generic_hopping(i, no_i, n_1, n_2, no_j, N_Phi, Phi_1, Phi_2, Bulk, Latt,
2148 Latt_Unit)
```

2151 which returns the phase factor involved in the hopping of a hole from lattice site $i + \delta_{no_i}$ to
 2152 $i + n_1 \mathbf{a}_1 + n_2 \mathbf{a}_2 + \delta_{no_j}$. Here δ_{no_i} is the position of the no_i orbital in the unit cell i . The
 2153 information for the phases is encoded in the type `Hopping_matrix_type`.

2154 **The Hopping matrix elements.** The hopping matrix is specified assuming only translation
 2155 invariance. (The point group symmetry of the lattice can be broken.) That is, we assume that
 2156 for each flavor index:

$$T_{(i, \delta), (i+n_1 \mathbf{a}_1 + n_2 \mathbf{a}_2, \delta')}^{(s)} = T_{(0, \delta), (n_1 \mathbf{a}_1 + n_2 \mathbf{a}_2, \delta')}^{(s)}. \quad (155)$$

2157 The right hand side of the above equation is given the type `Hopping_matrix_type`.

2158 **The checkerboard decomposition.** Aside from the hopping phases and hopping matrix el-
 2159 ements, the `Hopping_matrix_type` type contains information concerning the checkerboard
 2160 decomposition. In Eq. (72) we wrote the hopping Hamiltonian as:

$$\hat{\mathcal{H}}_T = \sum_{i=1}^{N_T} \sum_{k \in \mathcal{S}_i^T} \hat{T}^{(k)}, \quad (156)$$

2161 with the rule that if k and k' belong to the same set \mathcal{S}_i^T then $[\hat{T}^{(k)}, \hat{T}^{(k')}] = 0$. In the checker-
 2162 board decomposition, $\hat{T}^{(k)}$ corresponds to hopping on a bond. The checkerboard decompo-
 2163 sition depends on the lattice type, as well as on the hopping matrix elements. The required
 2164 information is stored in `Hopping_matrix_type`. In this data type, `N_FAM` corresponds to
 2165 the number of sets (or families) (N_T in the above equation). `L_FAM(1:N_FAM)` corresponds
 2166 to the number of bonds in the set, and finally, `LIST_FAM(1:N_FAM, 1:max(L_FAM(:))`,
 2167 2) contains information concerning the two legs of the bonds. Finally, to be able to generate
 2168 the imaginary time step of length $\Delta\tau$ we have to know by which fraction of $\Delta\tau$ we have to
 2169 propagate each set. This information is given in the array `Prop_Fam`.

2170 As an example we can consider the three-leg ladder lattice of Figure 6(c). Here the number
 2171 of sets (or families) `N_FAM` is equal to four, corresponding to the red, green, black and blue
 2172 bonds. It is clear from the figure that bonds in a given set do not have common legs, so that
 2173 hopping instances on the bonds of a given set commute.

2174 **Usage: The Hopping_Matrix_type** There are `N_bonds` hopping matrix elements emanat-
 2175 ing from a given unit cell, defined so that looping over all of the elements does not overcount
 2176 the bonds. For each bond, the array `List` contains the full information to define the RHS of
 2177 Eq. (155). The hopping amplitudes are stored in the array `T` and the local potentials in the
 2178 array `T_loc` (See Table 21). The `Hopping_Matrix_type` type also contains the information
 2179 for the checkerboard decomposition.

Table 21: Public member variables of the Hopping_Matrix_type type.

Variable	Type	Description
N_bonds	int	Number of hopping matrix elements within and emanating from a unit cell
List(N_bonds,4)	int	List($\bullet,1$) = δ List($\bullet,2$) = δ' List($\bullet,3$) = n_1 List($\bullet,4$) = n_2
T(N_bonds)	cmplx	Hopping amplitude
T_loc(Norb)	cmplx	On site potentials (e.g., chemical potential, Zeeman field)
N_Phi	int	Number of flux quanta piercing the lattice
Phi_X	dble	Twist in a_1 direction
Phi_Y	dble	Twist in a_2 direction
Bulk	logical	Twist as vector potential (T) or boundary condition (F)
N_Fam	int	Number of sets, N_T in Eq. (72)
L_Fam(N_FAM)	int	Number of bonds per set S^T
List_Fam(N_FAM,max(L_FAM(:)),2)	int	List_Fam($\bullet,\bullet,1$) = Unit cell List_Fam($\bullet,\bullet,2$) = Bond number
Prop_Fam(N_FAM)	dble	The fraction of $\Delta\tau$ with which the set will be propagated

2180 The data in the Hopping_matrix_type type suffices to uniquely define the unit step
 2181 propagation for the kinetic energy, and for any combinations of the Checkerboard and Symm
 2182 options (see Sec. 2.3). The propagation is set through the call:

```
2183 Call Predefined_Hoppings_Set_OPT(Hopping_Matrix, List, Invlist, Latt, Latt_unit, Dtau,
2184   Checkerboard, Symm, OP_T)
2185
```

2187 in which the operator array OP_T(*,N_FL) is allocated and defined. In the simplest case,
 2188 where no checkerboard is used, the array's first dimension is unity.

2189 The data in the Hopping_matrix_type type equally suffices to compute the kinetic en-
 2190 ergy. This is carried out in the routine Predefined_Hoppings_Compute_Kin.

2191 8.2.2 An example: Nearest neighbor hopping on the honeycomb lattice

2192 For the honeycomb lattice of Fig. 6(d) the number of bond within and emanating from a unit
 2193 cell is N_bonds = 3. The list array of the Hopping_matrix_type reads:

```
2194 list(1,1) = 1;  list(1,2) = 2;  list(1,3) = 0;  list(1,4) = 0 ! Intra unit-cell hopping
2195 list(2,1) = 2;  list(2,2) = 1;  list(2,3) = 0;  list(2,4) = 1 ! Inter unit-cell hopping
2196 list(3,1) = 1;  list(3,2) = 2;  list(3,3) = 1;  list(3,4) = -1 ! Inter unit-cell hopping
2197 T(1) = -1.0;  T(2) = -1.0;  T(3) = -1.0
2198 T_loc(1) = 0.0;  T_loc(2) = 0.0
2199 ! Hopping
2200 ! Chemical potential
```

2201 In the last two lines, we have set the hopping matrix element for each bond to -1 and the chem-
 2202 ical potential to zero. The fields, can then be specified with the variables N_phi, Phi_x,
 2203 Phi_y. Setting the twists, Phi_x, Phi_y to zero and looping over N_phi from $1 \cdots L^2$ pro-
 2204 duces the single particle spectrum of Fig. 7(a).

2205 For the honeycomb lattice the checkerboard decomposition for the nearest neighbor hop-
 2206 ping consists of three sets: N_Fam = 3 each of length corresponding to the number of unit

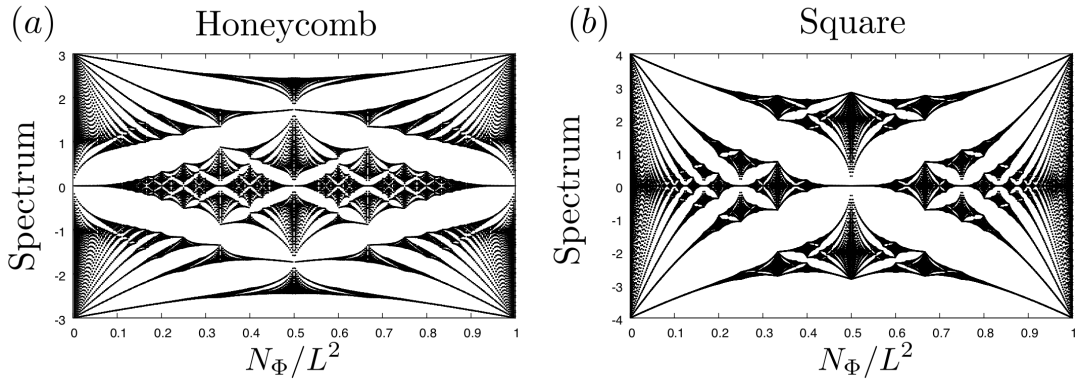


Figure 7: The single particle spectrum of the tight binding model on the honeycomb (a) and square (b) lattices as a function of the flux N_Φ . This corresponds to the well known Hofstadter butterflies.

2207 cells. In Fig. 6(d) these sets are denoted by different colors. In the code, the elements of the
2208 sets are specified as:

```

2209 do I = 1,Latt%N
2210   do nf = 1,N_FAM
2211     List_Fam(nf,I,1) = I ! Unit cell
2212     List_Fam(nf,I,2) = nf ! The bond
2213   enddo
2214 enddo
2215

```

2217 8.2.3 Predefined hoppings

2218 The module provides hopping and checkerboard decompositions, defining a `Hopping_`
2219 `Matrix` (an array of length `N_FL` of type `Hopping_Matrix_type`, see Sec. 8.2.1) for each of
2220 the following predefined lattices.

2221 Square

2222 The call:

```

2223 Call Set_Default_hopping_parameters_square(Hopping_Matrix, T_vec, Chem_vec, Phi_X_vec,
2224   Phi_Y_vec, Bulk, N_Phi_vec, N_FL, List, Invlist, Latt, Latt_unit)
2225

```

2227 defines the `Hopping_Matrix` for the square lattice:

$$\hat{H}_T = \sum_{i,\sigma,s} \left(\left[\sum_{\delta=\{a_1,a_2\}} -t^{(s)} \hat{c}_{i,s,\sigma}^\dagger e^{\frac{2\pi i}{\Phi_0} \int_i^{i+\delta} A^{(s)}(l) dl} \hat{c}_{i+\delta,s,\sigma} + \text{H.c.} \right] - \mu^{(s)} \hat{c}_{i,s,\sigma}^\dagger \hat{c}_{i,s,\sigma} \right). \quad (157)$$

2228 The vectors `T_vec` and `Chem_vec` have length `N_FL` and specify the hopping and the chemical
2229 potentials, while the vectors `Phi_X_vec`, `Phi_Y_vec` and `N_Phi_vec`, also of length `N_FL`,
2230 define the vector potential.

2231 Honeycomb

2232 The call:

```

2233 Call Set_Default_hopping_parameters_honeycomb(Hopping_Matrix, T_vec, Chem_vec, Phi_X_vec,
2234   Phi_Y_vec, Bulk, N_Phi_vec, N_FL, List, Invlist, Latt, Latt_unit)
2235

```

2237 defines the Hopping_Matrix for the honeycomb lattice:

$$\hat{H}_T = \sum_{i,\sigma,s} \left(\sum_{\delta=\{\delta_1, \delta_2, \delta_3\}} -t^{(s)} \hat{c}_{i,s,\sigma}^\dagger e^{\frac{2\pi i}{\Phi_0} \int_i^{i+\delta} A^{(s)}(l) dl} \hat{c}_{i+\delta,s,\sigma} + \text{H.c.} \right) \\ + \sum_{i,\sigma,s} -\mu^{(s)} \left(\hat{c}_{i,s,\sigma}^\dagger \hat{c}_{i,s,\sigma} + \hat{c}_{i+\delta_1,s,\sigma}^\dagger \hat{c}_{i+\delta_1,s,\sigma} \right), \quad (158)$$

2238 where the T_vec and Chem_vec have length N_FL and specify the hopping and the chemical
 2239 potentials, while the vectors Phi_X_vec, Phi_Y_vec and N_Phi_vec, also of length N_FL,
 2240 define the vector potential. Here i runs over sublattice A, and $i + \delta$ over the three nearest
 2241 neighbors of site i .

2242 Square bilayer

2243 The call:

```
2244
2245 Call Set_Default_hopping_parameters_Bilayer_square(Hopping_Matrix, T1_vec, T2_vec,
2246   Tperp_vec, Chem_vec, Phi_X_vec, Phi_Y_vec, Bulk, N_Phi_vec, N_FL, List, Invlist,
2247   Latt, Latt_unit)
```

2249 defines the Hopping_Matrix for the bilayer square lattice:

$$\hat{H}_T = \sum_{i,\sigma,s,n} \left(\left[\sum_{\delta=\{a_1, a_2\}} -t_n^{(s)} \hat{c}_{i,s,\sigma,n}^\dagger e^{\frac{2\pi i}{\Phi_0} \int_i^{i+\delta} A^{(s)}(l) dl} \hat{c}_{i+\delta,s,\sigma,n} + \text{H.c.} \right] - \mu^{(s)} \hat{c}_{i,s,\sigma,n}^\dagger \hat{c}_{i,s,\sigma,n} \right) \\ + \sum_{i,\sigma,s} -t_\perp^{(s)} \left(\hat{c}_{i,s,\sigma,1}^\dagger \hat{c}_{i,s,\sigma,2} + \text{H.c.} \right), \quad (159)$$

2250 where the additional index n labels the layers.

2251 Honeycomb bilayer

2252 The call:

```
2253
2254 Call Set_Default_hopping_parameters_Bilayer_honeycomb(Hopping_Matrix, T1_vec, T2_vec,
2255   Tperp_vec, Chem_vec, Phi_X_vec, Phi_Y_vec, Bulk, N_Phi_vec, N_FL, List, Invlist,
2256   Latt, Latt_unit)
```

2258 defines the Hopping_Matrix for the bilayer honeycomb lattice:

$$\hat{H}_T = \sum_{i,\sigma,s,n} \left(\sum_{\delta=\{\delta_1, \delta_2, \delta_3\}} -t_n^{(s)} \hat{c}_{i,s,\sigma,n}^\dagger e^{\frac{2\pi i}{\Phi_0} \int_i^{i+\delta} A^{(s)}(l) dl} \hat{c}_{i+\delta,s,\sigma,n} + \text{H.c.} \right) \\ + \sum_{i,\sigma,s} -t_\perp^{(s)} \left(\hat{c}_{i,s,\sigma,1}^\dagger \hat{c}_{i,s,\sigma,2} + \hat{c}_{i+\delta_1,s,\sigma,1}^\dagger \hat{c}_{i+\delta_1,s,\sigma,2} + \text{H.c.} \right) \\ + \sum_{i,\sigma,s,n} -\mu^{(s)} \left(\hat{c}_{i,s,\sigma,n}^\dagger \hat{c}_{i,s,\sigma,n} + \hat{c}_{i+\delta_1,s,\sigma,n}^\dagger \hat{c}_{i+\delta_1,s,\sigma,n} \right). \quad (160)$$

2259 Here, the additional index n labels the layer. i runs over the unit cells and $\delta = \{\delta_1, \delta_2, \delta_3\}$
 2260 over the three nearest neighbors.

2261 N-leg ladder

2262 The call:

```

2263 Call Set_Default_hopping_parameters_n_lag_ladder(Hopping_Matrix, T_vec, Tperp_vec, Chem_vec,
2264      Phi_X_vec, Phi_Y_vec, Bulk, N_Phi_vec, N_FL, List, Invlist, Latt, Latt_unit)
2265

```

2267 defines the Hopping_Matrix for the the N-leg ladder lattice:

$$\hat{H}_T = \sum_{i,\sigma,s} \sum_{n=1}^{\text{Norb}} \left(-t^{(s)} \hat{c}_{i,s,\sigma,n}^\dagger e^{\frac{2\pi i}{\Phi_0} \int_i^{i+a_1} A^{(s)}(l) dl} \hat{c}_{i+a_1,s,\sigma,n} + \text{H.c.} - \mu^{(s)} \hat{c}_{i,s,\sigma,n}^\dagger \hat{c}_{i,s,\sigma,n} \right) \\ + \sum_{i,\sigma,s} \sum_{n=1}^{\text{Norb}-1} -t_\perp^{(s)} \left(\hat{c}_{i+\delta_1,s,\sigma,n}^\dagger e^{\frac{2\pi i}{\Phi_0} \int_{(n-1)a_2}^{(n)a_2} A^{(s)}(l) dl} \hat{c}_{i+\delta_1,s,\sigma,n+1} + \text{H.c.} \right). \quad (161)$$

2268 Here, the additional index n defines the orbital. Note that this lattice has open boundary
2269 conditions in the a_2 direction.

2270 8.3 Predefined interaction vertices

2271 In its most general form, an interaction Hamiltonian, expressed in terms of sums of perfect
2272 squares, can be written, as presented in Section 1, as a sum of M_V vertices:

$$\hat{\mathcal{H}}_V = \sum_{k=1}^{M_V} U_k \left\{ \sum_{\sigma=1}^{N_{\text{col}}} \sum_{s=1}^{N_{\text{fl}}} \left[\left(\sum_{x,y} \hat{c}_{x\sigma s}^\dagger V_{xy}^{(ks)} \hat{c}_{y\sigma s} \right) + \alpha_{ks} \right] \right\}^2 \equiv \sum_{k=1}^{M_V} U_k (\hat{V}^{(k)})^2 \quad (4)$$

$$\equiv \sum_{k=1}^{M_V} \hat{\mathcal{H}}_V^{(k)},$$

2273 which are encoded in one or more variables of type `Operator`, described in Sec. 5.1. We often
2274 use arrays of `Operator` type, which should be initialized by repeatedly calling the subroutine
2275 `Op_make`.

2276 The module `Predefined_Int_mod.F90` implements some of the most common of such
2277 interaction vertices $\hat{\mathcal{H}}_V^{(k)}$, as detailed in the remainder of this section, where we drop the su-
2278 perscript (k) when unambiguous.

2279 8.3.1 SU(N) Hubbard interaction

2280 The SU(N) Hubbard interaction on a given site i is given by

$$\hat{\mathcal{H}}_{V,i} = +\frac{U}{N_{\text{col}}} \left[\sum_{\sigma=1}^{N_{\text{col}}} \left(\hat{c}_{i\sigma}^\dagger \hat{c}_{i\sigma} - 1/2 \right) \right]^2. \quad (162)$$

2281 Assuming that no other term in the Hamiltonian breaks the SU(N) color symmetry, then this
2282 interaction term conveniently corresponds to a single operator, obtained by calling, for each
2283 of the N_{dim} sites i :

```

2284 Call Predefined_Int_U_SUN(OP, I, N_SUN, DTAU, U)
2285

```

2287 which defines:

```

2288 Op%P(1) = I
2289 Op%O(1,1) = cmplx(1.d0, 0.d0, kind(0.D0))
2290 Op%alpha = cmplx(-0.5d0, 0.d0, kind(0.D0))
2291 Op%g = SQRT(CMPLX(-DTAU*U/(DBLE(N_SUN)), 0.D0, kind(0.D0)))
2292 Op%type = 2

```

2295 To relate to Eq. (4), we have $V_{xy}^{(is)} = \delta_{x,y} \delta_{x,i}$, $\alpha_{is} = -\frac{1}{2}$ and $U_k = \frac{U}{N_{\text{col}}}$. Here the flavor
2296 index, s , plays no role.

2297 8.3.2 M_z -Hubbard interaction2298
2299 **Call** Predefined_Int_U_MZ(OP_up, Op_do, I, DTAU, U)2301 The M_z -Hubbard interaction is given by

$$\hat{\mathcal{H}}_V = -\frac{U}{2} \sum_i \left[\hat{c}_{i\uparrow}^\dagger \hat{c}_{i\uparrow} - \hat{c}_{i\downarrow}^\dagger \hat{c}_{i\downarrow} \right]^2, \quad (163)$$

2302 which corresponds to the general form of Eq. (4) by setting: $N_{fl} = 2$, $N_{col} \equiv N_{SUN} = 1$,
2303 $M_V = N_{unit-cell}$, $U_k = \frac{U}{2}$, $V_{xy}^{(i,s=1)} = \delta_{x,y} \delta_{x,i}$, $V_{xy}^{(i,s=2)} = -\delta_{x,y} \delta_{x,i}$, and $\alpha_{is} = 0$; and which is
2304 defined in the subroutine Predefined_Int_U_MZ by two operators:

```
2305 Op_up%P(1) = I
2306 Op_up%O(1,1) = cmplx(1.d0, 0.d0, kind(0.D0))
2307 Op_up%alpha = cmplx(0.d0, 0.d0, kind(0.D0))
2308 Op_up%g = SQRT(CMPLX(DTAU*U/2.d0, 0.D0, kind(0.D0)))
2309 Op_up%type = 2
2310
2311 Op_do%P(1) = I
2312 Op_do%O(1,1) = cmplx(1.d0, 0.d0, kind(0.D0))
2313 Op_do%alpha = cmplx(0.d0, 0.d0, kind(0.D0))
2314 Op_do%g = -SQRT(CMPLX(DTAU*U/2.d0, 0.D0, kind(0.D0)))
2315 Op_do%type = 2
2316
```

2318 8.3.3 SU(N) V-interaction

2319
2320 **Call** Predefined_Int_V_SUN(OP, I, J, N_SUN, DTAU, V)

2322 The interaction term of the generalized t-V model, given by

$$\hat{\mathcal{H}}_{V,i,j} = -\frac{V}{N_{col}} \left[\sum_{\sigma=1}^{N_{col}} \left(\hat{c}_{i\sigma}^\dagger \hat{c}_{j\sigma} + \hat{c}_{j\sigma}^\dagger \hat{c}_{i\sigma} \right) \right]^2, \quad (164)$$

2323 is coded in the subroutine Predefined_Int_V_SUN by a single symmetric operator:

```
2324 Op%P(1) = I
2325 Op%P(2) = J
2326 Op%O(1,2) = cmplx(1.d0 ,0.d0, kind(0.D0))
2327 Op%O(2,1) = cmplx(1.d0 ,0.d0, kind(0.D0))
2328 Op%g = SQRT(CMPLX(DTAU*V/real(N_SUN,kind(0.d0)), 0.D0, kind(0.D0)))
2329 Op%alpha = cmplx(0.d0, 0.d0, kind(0.D0))
2330 Op%type = 2
2331
```

2333 8.3.4 Fermion-Ising coupling

2334
2335 **Call** Predefined_Int_Ising_SUN(OP, I, J, DTAU, XI)

2337 The interaction between the Ising and a fermion degree of freedom, given by

$$\hat{\mathcal{H}}_{V,i,j} = \hat{Z}_{i,j} \xi \sum_{\sigma=1}^{N_{col}} \left(\hat{c}_{i\sigma}^\dagger \hat{c}_{j\sigma} + \hat{c}_{j\sigma}^\dagger \hat{c}_{i\sigma} \right), \quad (165)$$

2338 where ξ determines the coupling strength, is implemented in the subroutine Predefined_
2339 Int_Ising_SUN:

```
2340 Op%P(1) = I
2341 Op%P(2) = J
2342 Op%O(1,2) = cmplx(1.d0 ,0.d0, kind(0.D0))
2343 Op%O(2,1) = cmplx(1.d0 ,0.d0, kind(0.D0))
2344 Op%g = cmplx(-DTAU*XI,0.D0,kind(0.D0))
2345 Op%alpha = cmplx(0d0,0.d0, kind(0.D0))
2346 Op%type = 1
2347
```

2349 8.3.5 Long-range Coulomb repulsion

2350 `Call Predefined_Int_LRC(OP, I, DTAU)`

2353 The Long-Range Coulomb (LRC) interaction can be written as

$$\hat{\mathcal{H}}_V = \frac{1}{N} \sum_{i,j} \left(\hat{n}_i - \frac{N}{2} \right) V_{i,j} \left(\hat{n}_j - \frac{N}{2} \right), \quad (166)$$

2354 where

$$\hat{n}_i = \sum_{\sigma=1}^N \hat{c}_{i,\sigma}^\dagger \hat{c}_{i,\sigma}, \quad (167)$$

2355 and i corresponds to a super-index labelling the unit cell and orbital.

2356 The code uses the following HS decomposition:

$$e^{-\Delta\tau\hat{H}_{V,k}} = \int \prod_i d\phi_i e^{-\frac{N\Delta\tau}{4}\phi_i V_{i,j}^{-1}\phi_j - \sum_i i\Delta\tau\phi_i(\hat{n}_i - \frac{N}{2})}. \quad (168)$$

2357 The above holds only provided that the matrix V is positive definite and the implementation
2358 follows Ref. [51].

2359 The LRC interaction is implemented in the subroutine `Predefined_Int_LRC`:

```
2360
2361 Op%P(1) = I
2362 Op%O(1,1) = cmplx(1.d0, 0.d0, kind(0.D0))
2363 Op%alpha = cmplx(-0.5d0, 0.d0, kind(0.D0))
2364 Op%g = cmplx(0.d0, DTAU, kind(0.D0))
2365 Op%type = 3
```

2367 8.3.6 J_z - J_z interaction

2368 `Call Predefined_Int_Jz(OP_up, Op_do, I, J, DTAU, Jz)`

2371 Another predefined vertex is:

$$\hat{\mathcal{H}}_{V,i,j} = -\frac{|J_z|}{2} \left(S_i^z - \text{sgn}|J_z|S_j^z \right)^2 = J_z S_i^z S_j^z - \frac{|J_z|}{2} (S_i^z)^2 - \frac{|J_z|}{2} (S_j^z)^2, \quad (169)$$

2372 which, if particle fluctuations are frozen on the i and j sites, then $(S_i^z)^2 = 1/4$ and the inter-
2373 action corresponds to a J_z - J_z ferromagnetic or antiferromagnetic coupling.

2374 The implementation of the interaction in `Predefined_Int_Jz` defines two operators:

```
2375
2376 Op_up%P(1) = I
2377 Op_up%P(2) = J
2378 Op_up%O(1,1) = cmplx(1.d0, 0.d0, kind(0.D0))
2379 Op_up%O(2,2) = cmplx(-Jz/Abs(Jz), 0.d0, kind(0.D0))
2380 Op_up%alpha = cmplx(0.d0, 0.d0, kind(0.D0))
2381 Op_up%g = SQRT(CMPLX(DTAU*Jz/8.d0, 0.d0, kind(0.D0)))
2382 Op_up%type = 2
2383
2384 Op_do%P(1) = I
2385 Op_do%P(2) = J
2386 Op_do%O(1,1) = cmplx(1.d0, 0.d0, kind(0.d0))
2387 Op_do%O(2,2) = cmplx(-Jz/Abs(Jz), 0.d0, kind(0.d0))
2388 Op_do%alpha = cmplx(0.d0, 0.d0, kind(0.d0))
2389 Op_do%g = -SQRT(CMPLX(DTAU*Jz/8.d0, 0.d0, kind(0.d0)))
2390 Op_do%type = 2
```

Table 22: Arguments taken by the subroutines in the module `Predefined_Obs`. Note that a given method makes use of only a subset of this list, as described in this section. Note also that we use the superindex $i = (i, n_i)$ where i denotes the unit cell and n_i the orbital.

Argument	Type	Description
Latt	Lattice	Lattice as a variable of type <code>Lattice</code> , see Sec. 5.3
Latt_Unit	Unit_cell	Unit cell as a variable of type <code>Unit_cell</code> , see Sec. 5.3
List(Ndim,2)	int	For every site index I, stores the corresponding lattice position, <code>List(I,1)</code> , and the (local) orbital index, <code>List(I,2)</code>
NT	int	Imaginary time τ
GR(Ndim,Ndim,N_FL)	cmplx	Equal-time Green function $GR(i, j, s) = \langle c_{i,s} c_{j,s}^\dagger \rangle$
GRC(Ndim,Ndim,N_FL)	cmplx	$GRC(i, j, s) = \langle c_{i,s}^\dagger c_{j,s} \rangle = \delta_{i,j} - GR(j, i, s)$
GTO(Ndim,Ndim,N_FL)	cmplx	Time-displaced Green function $\langle \langle T\hat{c}_{i,s}(\tau)\hat{c}_{j,s}^\dagger(0) \rangle \rangle$
GOT(Ndim,Ndim,N_FL)	cmplx	Time-displaced Green function $\langle \langle T\hat{c}_{i,s}(0)\hat{c}_{j,s}^\dagger(\tau) \rangle \rangle$
G00(Ndim,Ndim,N_FL)	cmplx	Time-displaced Green function $\langle \langle T\hat{c}_{i,s}(0)\hat{c}_{j,s}^\dagger(0) \rangle \rangle$
GTT(Ndim,Ndim,N_FL)	cmplx	Time-displaced Green function $\langle \langle T\hat{c}_{i,s}(\tau)\hat{c}_{j,s}^\dagger(\tau) \rangle \rangle$
N_SUN	int	Number of fermion colors N_{col}
ZS	cmplx	$ZS = \text{sgn}(C)$, see Sec. 5.4
ZP	cmplx	$ZP = e^{-S(C)} / \text{Re}[e^{-S(C)}]$, see Sec. 5.4
Obs	Obser_Latt	Output: one or more measurement result

2392 8.4 Predefined observables

2393 The types `Obser_Vec` and `Obser_Latt` described in Section 5.4 handle arrays of scalar
 2394 observables and correlation functions with lattice symmetry respectively. The module
 2395 `Predefined_Obs` provides a set of standard equal-time and time-displaced observables, as
 2396 described below. It contains procedures and functions. Procedures provide a complete han-
 2397 dling of the observable structure. That is, they take care, for example, of incrementing the
 2398 counter and of the average sign. On the other hand, functions only provide the Wick decom-
 2399 position result, and the handling of the observable structure is left to the user.

2400 The predefined measurements methods take as input Green functions `GR`, `GTO`, `GOT`, `G00`,
 2401 and `GTT`, defined in Sec. 7.7.2 and 7.7.3, as well as `N_SUN`, time slice `Ntau`, lattice information,
 2402 and so on – see Table 22.

2403 8.4.1 Equal-time SU(N) spin-spin correlations

2404 A measurement of SU(N) spin-spin correlations can be obtained through:

2405 `Call Predefined_Obs_eq_SpinSun_measure(Latt, Latt_unit, List, GR, GRC, N_SUN, ZS, ZP, Obs)`

2408 If `N_FL = 1` then this routine returns

$$Obs(i-j, n_i, n_j) = \frac{2N}{N^2 - 1} \sum_{a=1}^{N^2-1} \langle \langle \hat{c}_{i,n_i}^\dagger T^a \hat{c}_{i,n_i} \hat{c}_{j,n_j}^\dagger T^a \hat{c}_{j,n_j} \rangle \rangle_C, \quad (170)$$

2409 where T^a are the generators of SU(N) satisfying the normalization conditions
 2410 $\text{Tr}[T^a T^b] = \delta_{a,b}/2$, $\text{Tr}[T^a] = 0$, $\hat{c}_{j,n_j}^\dagger = (\hat{c}_{j,n_j,1}^\dagger, \dots, \hat{c}_{j,n_j,N}^\dagger)$ is an N-flavored spinor, j cor-
 2411 responds to the unit-cell index and n_j labels the orbital.

²⁴¹² Using Wick's theorem, valid for a given configuration of fields, we obtain

$$\text{Obs} = \frac{2N}{N^2 - 1} \sum_{a=1}^{N^2-1} \sum_{\alpha, \beta, \gamma, \delta=1}^N T_{\alpha, \beta}^a T_{\gamma, \delta}^a \\ \times \left(\langle \langle \hat{c}_{i, n_i, \alpha}^\dagger \hat{c}_{i, n_i, \beta} \rangle \rangle_C \langle \langle \hat{c}_{j, n_j, \gamma}^\dagger \hat{c}_{j, n_j, \delta} \rangle \rangle_C + \langle \langle \hat{c}_{i, n_i, \alpha}^\dagger \hat{c}_{j, n_j, \delta} \rangle \rangle_C \langle \langle \hat{c}_{i, n_i, \beta}^\dagger \hat{c}_{j, n_j, \gamma} \rangle \rangle_C \right). \quad (171)$$

²⁴¹³ For this SU(N) symmetric code, the Green function is diagonal in the spin index and spin
²⁴¹⁴ independent:

$$\langle \langle \hat{c}_{i, n_i, \alpha}^\dagger \hat{c}_{j, n_j, \beta} \rangle \rangle_C = \delta_{\alpha, \beta} \langle \langle \hat{c}_{i, n_i}^\dagger \hat{c}_{j, n_j} \rangle \rangle_C. \quad (172)$$

²⁴¹⁵ Hence,

$$\text{Obs} = \frac{2N}{N^2 - 1} \sum_{a=1}^{N^2-1} \left([\text{Tr} T^a]^2 \langle \langle \hat{c}_{i, n_i}^\dagger \hat{c}_{i, n_i} \rangle \rangle_C \langle \langle \hat{c}_{j, n_j}^\dagger \hat{c}_{j, n_j} \rangle \rangle_C + \text{Tr}[T^a T^a] \langle \langle \hat{c}_{i, n_i}^\dagger \hat{c}_{j, n_j} \rangle \rangle_C \langle \langle \hat{c}_{i, n_i} \hat{c}_{j, n_j}^\dagger \rangle \rangle_C \right) \\ = N \langle \langle \hat{c}_{i, n_i}^\dagger \hat{c}_{j, n_j} \rangle \rangle_C \langle \langle \hat{c}_{i, n_i} \hat{c}_{j, n_j}^\dagger \rangle \rangle_C. \quad (173)$$

²⁴¹⁶ Note that we can also define the generators of SU(N) as

$$\hat{S}_\nu^\mu(x) = \hat{c}_{x, \mu}^\dagger \hat{c}_{x, \nu} - \delta_{\mu, \nu} \frac{1}{N} \sum_{\alpha=1}^N \hat{c}_{x, \alpha}^\dagger \hat{c}_{x, \alpha}. \quad (174)$$

²⁴¹⁷ With this definition, the spin-spin correlations read:

$$\sum_{\mu, \nu=1}^N \langle \langle \hat{S}_\nu^\mu(x) \hat{S}_\mu^\nu(y) \rangle \rangle_C = (N^2 - 1) \langle \langle \hat{c}_x^\dagger \hat{c}_y \rangle \rangle_C \langle \langle \hat{c}_x \hat{c}_y^\dagger \rangle \rangle_C. \quad (175)$$

²⁴¹⁸ In the above x denotes a super index defining site and orbital. Aside from the normalization,
²⁴¹⁹ this formulation gives the same result.

²⁴²⁰ 8.4.2 Equal-time spin correlations

²⁴²¹ A measurement of the equal-time spin correlations can be obtained by:

```
2422 Call Predefined_Obs_eq_SpinMz_measure(Latt, Latt_unit, List, GR, GRC, N_SUN, ZS, ZP, ObsZ,
2423 ObsXY, ObsXYZ)
```

²⁴²⁶ If $N_FL=2$ and $N_SUN=1$, then the routine returns:

$$\text{ObsZ}(i-j, n_i, n_j) = 4 \langle \langle \hat{c}_{i, n_i}^\dagger S^z \hat{c}_{i, n_i} \hat{c}_{j, n_j}^\dagger S^z \hat{c}_{j, n_j} \rangle \rangle_C - 4 \langle \langle \hat{c}_{i, n_i}^\dagger S^z \hat{c}_{i, n_i} \rangle \rangle_C \langle \langle \hat{c}_{j, n_j}^\dagger S^z \hat{c}_{j, n_j} \rangle \rangle_C, \\ \text{ObsXY}(i-j, n_i, n_j) = 2 \left(\langle \langle \hat{c}_{i, n_i}^\dagger S^x \hat{c}_{i, n_i} \hat{c}_{j, n_j}^\dagger S^x \hat{c}_{j, n_j} \rangle \rangle_C + \langle \langle \hat{c}_{i, n_i}^\dagger S^y \hat{c}_{i, n_i} \hat{c}_{j, n_j}^\dagger S^y \hat{c}_{j, n_j} \rangle \rangle_C \right), \\ \text{ObsXYZ} = \frac{2 \cdot \text{ObsXY} + \text{ObsZ}}{3}. \quad (176)$$

²⁴²⁷ Here $\hat{c}_{i, n_i}^\dagger = (\hat{c}_{i, n_i, \uparrow}^\dagger, \hat{c}_{i, n_i, \downarrow}^\dagger)$ is a two component spinor and $S = \frac{1}{2}\sigma$, with

$$\sigma = \left(\begin{bmatrix} 0 & 1 \\ 1 & 0 \end{bmatrix}, \begin{bmatrix} 0 & -i \\ i & 0 \end{bmatrix}, \begin{bmatrix} 1 & 0 \\ 0 & -1 \end{bmatrix} \right), \quad (177)$$

²⁴²⁸ the Pauli spin matrices.

2429 **8.4.3 Equal-time Green function**

2430 A measurement of the equal-time Green function can be obtained by:

2431 `Call Predefined_Obs_eq_Green_measure(Latt, Latt_unit, List, GR, GRC, N_SUN, ZS, ZP, Obs)`

2434 Which returns:

$$\text{Obs}(i - j, n_i, n_j) = \sum_{\sigma=1}^{N_{\text{col}}} \sum_{s=1}^{N_{\text{fl}}} \langle \hat{c}_{i,n_i,\sigma,s}^\dagger \hat{c}_{j,n_j,\sigma,s} \rangle. \quad (178)$$

2435 **8.4.4 Equal-time density-density correlations**

2436 A measurement of equal-time density-density correlations can be obtained by:

2437 `Call Predefined_Obs_eq_Den_measure(Latt, Latt_unit, List, GR, GRC, N_SUN, ZS, ZP, Obs)`

2440 Which returns:

$$\text{Obs}(i - j, n_i, n_j) = \langle \langle \hat{N}_{i,n_i} \hat{N}_{j,n_j} \rangle - \langle \hat{N}_{i,n_i} \rangle \langle \hat{N}_{j,n_j} \rangle \rangle_C, \quad (179)$$

2441 where

$$\hat{N}_{i,n_i} = \sum_{\sigma=1}^{N_{\text{col}}} \sum_{s=1}^{N_{\text{fl}}} \hat{c}_{i,n_i,\sigma,s}^\dagger \hat{c}_{i,n_i,\sigma,s}. \quad (180)$$

2442 **8.4.5 Time-displaced Green function**

2443 A measurement of the time-displaced Green function can be obtained by:

2444 `Call Predefined_Obs_tau_Green_measure(Latt, Latt_unit, List, NT, GTO, GOT, GOO, GTT, N_SUN,`
 2445 `ZS, ZP, Obs)`

2448 Which returns:

$$\text{Obs}(i - j, \tau, n_i, n_j) = \sum_{\sigma=1}^{N_{\text{col}}} \sum_{s=1}^{N_{\text{fl}}} \langle \langle \hat{c}_{i,n_i,\sigma,s}^\dagger(\tau) \hat{c}_{j,n_j,\sigma,s} \rangle \rangle_C. \quad (181)$$

2449 **8.4.6 Time-displaced SU(N) spin-spin correlations**

2450 A measurement of time-displaced spin-spin correlations for SU(N) models ($N_{\text{fl}} = 1$) can be
 2451 obtained by:

2452 `Call Predefined_Obs_tau_SpinSU_N_measure(Latt, Latt_unit, List, NT, GTO, GOT, GOO, GTT,`
 2453 `N_SUN, ZS, ZP, Obs)`

$$\text{Obs}(i - j, \tau, n_i, n_j) = \frac{2N}{N^2 - 1} \sum_{a=1}^{N^2 - 1} \langle \langle \hat{c}_{i,n_i}^\dagger(\tau) T^a \hat{c}_{i,n_i}(\tau) \hat{c}_{j,n_j}^\dagger T^a \hat{c}_{j,n_j} \rangle \rangle_C, \quad (182)$$

2456 where T^a are the generators of SU(N) (see Sec. 8.4.1 for more details).

2457 **8.4.7 Time-displaced spin correlations**

2458 A measurement of time-displaced spin-spin correlations for Mz models ($N_{\text{fl}} = 2, N_{\text{col}} = 1$) is
 2459 returned by:

2460 `Call Predefined_Obs_tau_SpinMz_measure(Latt, Latt_unit, List, NT, GTO, GOT, GOO, GTT, N_SUN,`
 2461 `ZS, ZP, ObsZ, ObsXY, ObsXYZ)`

2464 Which calculates the following observables:

$$\begin{aligned}\text{ObsZ}(\mathbf{i} - \mathbf{j}, \tau, n_i, n_j) &= 4\langle\langle \hat{c}_{i,n_i}^\dagger(\tau) S^z \hat{c}_{i,n_i}(\tau) \hat{c}_{j,n_j}^\dagger S^z \hat{c}_{j,n_j} \rangle\rangle_C \\ &\quad - 4\langle\langle \hat{c}_{i,n_i}^\dagger S^z \hat{c}_{i,n_i} \rangle\rangle_C \langle\langle \hat{c}_{j,n_j}^\dagger S^z \hat{c}_{j,n_j} \rangle\rangle_C, \\ \text{ObsXY}(\mathbf{i} - \mathbf{j}, \tau, n_i, n_j) &= 2 \left(\langle\langle \hat{c}_{i,n_i}^\dagger(\tau) S^x \hat{c}_{i,n_i}(\tau) \hat{c}_{j,n_j}^\dagger S^x \hat{c}_{j,n_j} \rangle\rangle_C \right. \\ &\quad \left. + \langle\langle \hat{c}_{i,n_i}^\dagger(\tau) S^y \hat{c}_{i,n_i}(\tau) \hat{c}_{j,n_j}^\dagger S^y \hat{c}_{j,n_j} \rangle\rangle_C \right), \\ \text{ObsXYZ} &= \frac{2 \cdot \text{ObsXY} + \text{ObsZ}}{3}. \end{aligned} \quad (183)$$

2465 8.4.8 Time-displaced density-density correlations

2466 A measurement of time-displaced density-density correlations for general SU(N) models is
2467 given by:

```
2468 Call Predefined_Obs_tau_Den_measure(Latt, Latt_unit, List, NT, GTO, GOT, GOO, GTT, N_SUN,
2469 ZS, ZP, Obs)
2470
```

2472 Which returns:

$$\text{Obs}(\mathbf{i} - \mathbf{j}, \tau, n_i, n_j) = \langle\langle \hat{N}_{i,n_i}(\tau) \hat{N}_{j,n_j} \rangle - \langle\hat{N}_{i,n_i}\rangle \langle\hat{N}_{j,n_j}\rangle \rangle_C. \quad (184)$$

2473 The density operator is defined in Eq. (180).

2474 8.4.9 Dimer-dimer correlations

2475 Let

$$\hat{S}_\nu^\mu(x) = \hat{c}_{x,\mu}^\dagger \hat{c}_{x,\nu} - \delta_{\mu,\nu} \frac{1}{N} \sum_{\alpha=1}^N \hat{c}_{x,\alpha}^\dagger \hat{c}_{x,\alpha} \quad (185)$$

2476 be the generators of SU(N). Dimer-Dimer correlations are defined as:

$$\langle\langle \hat{S}_\nu^\mu(x, \tau) \hat{S}_\mu^\nu(y, \tau) \hat{S}_\delta^\gamma(w, \tau) \hat{S}_\gamma^\delta(z) \rangle\rangle_C, \quad (186)$$

2477 where the sum over repeated indices from $1 \cdots N$ is implied. The calculation is carried out for
2478 the self-adjoint antisymmetric representation of SU(N) for which $\sum_{\alpha=1}^N \hat{c}_{x,\alpha}^\dagger \hat{c}_{x,\alpha} = N/2$, such
2479 that the generators can be replaced by:

$$\hat{S}_\nu^\mu(x) = \hat{c}_{x,\mu}^\dagger \hat{c}_{x,\nu} - \delta_{\mu,\nu} \frac{1}{2}. \quad (187)$$

2480 The function

```
2481 Complex (Kind=Kind(0.d0)) function Predefined_Obs_dimer_tau(x, y, w, z, GTO, GOT, GOO, GTT,
2482 N_SUN, N_FL)
2483
```

2485 returns the value of the time-displaced dimer-dimer correlation function. The function

```
2486 Complex (Kind=Kind(0.d0)) function Predefined_Obs_dimer_eq(x, y, w, z, GR, GRC, N_SUN, N_FL)
2487
```

2489 returns the value of the equal time dimer-dimer correlation function:

$$\langle\langle \hat{S}_\nu^\mu(x, \tau) \hat{S}_\mu^\nu(y, \tau) \hat{S}_\delta^\gamma(w, \tau) \hat{S}_\gamma^\delta(z, \tau) \rangle\rangle_C. \quad (188)$$

2490 Here, both GR and GRC are on time slice τ .

2491 To compute the background terms, the function

```
2492 Complex (Kind=Kind(0.d0)) function Predefined_Obs_dimer0_eq(x, y, GR, N_SUN, N_FL)
```

2495 returns

$$\langle \langle \hat{S}_\nu^\mu(x, \tau) \hat{S}_\mu^\nu(y, \tau) \rangle \rangle_C. \quad (189)$$

2496 All routines are programmed for $N_{\text{SUN}} = 2, 4, 6, 8$ at $N_{\text{FL}}=1$. The routines also handle
 2497 the case of broken SU(2) spin symmetry corresponding to $N_{\text{FL}}=2$ and $N_{\text{SUN}}=1$. To carry
 2498 out the Wick decomposition and sums over spin indices, we use the Mathematica notebooks
 2499 DimerDimer_SU2_NFL_2.nb and DimerDimer_SUN_NFL_1.nb.

2500 8.4.10 Cotunneling for Kondo models

2501 The Kondo lattice model (KLM), \hat{H}_{KLM} is obtained by carrying out a canonical Schrieffer-
 2502 Wolf [142] transformation of the periodic Anderson model (PAM), \hat{H}_{PAM} . Hence,
 2503 $ke^{\hat{S}} \hat{H}_{PAM} e^{-\hat{S}} = \hat{H}_{KLM}$ with $\hat{S}^\dagger = -\hat{S}$. Let $\hat{f}_{x,\sigma}$ create an electron on the correlation f-orbital
 2504 of the PAM. Then,

$$e^{\hat{S}} \hat{f}_{x,\sigma'}^\dagger e^{-\hat{S}} \simeq \frac{2V}{U} \left(\hat{c}_{x,-\sigma'}^\dagger \hat{S}_x^{\sigma'} + \sigma' \hat{c}_{x,\sigma'}^\dagger \hat{S}_x^z \right) \equiv \frac{2V}{U} \tilde{\hat{f}}_{x,\sigma'}^\dagger. \quad (190)$$

2505 In the above, it is understood that σ' takes the value 1 (-1) for up (down) spin degrees of
 2506 freedom, that $\hat{S}_x^{\sigma'} = \hat{f}_{x,\sigma'}^\dagger \hat{f}_{x,-\sigma'}$ and that $\hat{S}_x^z = \frac{1}{2} \sum_{\sigma'} \sigma' \hat{f}_{x,\sigma'}^\dagger \hat{f}_{x,\sigma'}$. Finally, $\hat{c}_{x,\sigma'}^\dagger$ corresponds to
 2507 the conduction electron that hybridizes with $\hat{f}_{x,\sigma'}^\dagger$. This form matches that derived in Ref. [143]
 2508 and a calculation of the former equation can be found in Ref. [144]. An identical, but more
 2509 transparent formulation is given in Ref. [145] and reads:

$$\tilde{\hat{f}}_{x,\sigma}^\dagger = \sum_{\sigma'} \hat{c}_{x,\sigma'}^\dagger \boldsymbol{\sigma}_{\sigma',\sigma} \cdot \hat{S}_x, \quad (191)$$

2510 where $\boldsymbol{\sigma}$ denotes the vector of Pauli spin matrices. With the above, one will readily show that
 2511 the $\tilde{\hat{f}}_{x,\sigma}^\dagger$ transforms as $\hat{f}_{x,\sigma}^\dagger$ under an SU(2) spin rotation. The function

```
2512 Complex (Kind=Kind(0.d0)) function Predefined_Obs_Cotunneling(x_c, x, y_c, y, GTO, GOT, GO0,  
2513 GTT, N_SUN, N_FL)
```

2516 returns the value of the time displaced correlation function:

$$\sum_{\sigma} \langle \langle \tilde{\hat{f}}_{x,\sigma}^\dagger(\tau) \tilde{\hat{f}}_{y,\sigma}(0) \rangle \rangle_C. \quad (192)$$

2517 Here, x_c and y_c correspond to the conduction orbitals that hybridize with the x and y f-
 2518 orbitals. The routine works for SU(N) symmetric codes corresponding to $N_{\text{FL}}=1$ and N_{SUN}
 2519 = 2, 4, 6, 8. For the larger N-values, we have replaced the generators of SU(2) with that of
 2520 SU(N). The routine also handles the case where spin-symmetry is broken by e.g. a Zeeman
 2521 field. This corresponds to the case $N_{\text{FL}}=2$ and $N_{\text{SUN}}=1$. Note that the function only car-
 2522 rries out the Wick decomposition and the handling of the observable type corresponding to
 2523 this quantity has to be done by the user. To carry out the Wick decomposition and sums
 2524 over spin indices, we use the Mathematica notebooks Cotunneling_SU2_NFL_2.nb and
 2525 Cotunneling_SUN_NFL_1.nb.

2526 8.4.11 Rényi entropy

2527 The module `entanglement_mod.F90` allows one to compute the 2nd Rényi entropy, S_2 , for
 2528 a subsystem. Using Eq. (24), S_2 can be expressed as a stochastic average of an observable
 2529 constructed from two independent simulations of the model [60]:

$$e^{-S_2} = \sum_{C_1, C_2} P(C_2)P(C_1) \det[G_A(\tau_0; C_1)G_A(\tau_0; C_2) - (1 - G_A(\tau_0; C_1))(1 - G_A(\tau_0; C_2))], \quad (193)$$

2530 where $G_A(\tau_0; C_i)$, $i = 1, 2$ is the Green function matrix restricted to the desired subsystem A
 2531 at a given time-slice τ_0 , and for the configuration C_i of the replica i . The degrees of freedom
 2532 defining the subsystem A are lattice site, flavor index, and color index. We note that although
 2533 formally correct, the method of Ref. [60] suffers from fat tails in the strong coupling limit and
 2534 for large subsystems A . We have recently witnessed major improvements for the computation
 2535 of Rényi entropies [146, 147] based on an incremental approach. It is beyond the scope of this
 2536 version of the ALF library to provide a generic implementation of these new approaches.

2537 Notice that, due to its formulation, sampling S_2 requires an MPI simulation with at least 2
 2538 processes. Also, only real-space partitions are currently supported.

2539 A measurement of the 2nd Rényi entropy can be obtained by:

2540 `Call Predefined_Obs_scal_Renyi_Ent(GRC, List, Nsites, N_SUN, ZS, ZP, Obs)`

2543 which returns the observable `Obs`, for which $\langle \text{Obs} \rangle = e^{-S_2}$. The subsystem A can be defined in a
 2544 number of different ways, which are handled by what we call *specializations* of the subroutine,
 2545 described as follows.

2546 In the most general case, `List(:, N_FL, N_SUN)` is a three-dimensional array that contains
 2547 the list of lattice sites in A for every flavor and color index; `Nsites(N_FL, N_SUN)` is then a bidimensional array that provides the number of lattice sites in the subsystem for every
 2548 flavor and color index; and the argument `N_SUN` must be omitted in the call.

2550 For a subsystem whose degrees of freedom, for a given flavor index, have a common value
 2551 of color indexes, `Predefined_Obs_scal_Renyi_Ent` can be called by providing `List(:, N_FL)` as a bidimensional array that contains the list of lattice sites for every flavor index. In
 2553 this case, `Nsites(N_FL)` provides the number of sites in the subsystem for any given flavor
 2554 index, while `N_SUN(N_FL)` contains the number of color indexes for a given flavor index.

2555 Finally, a specialization exists for the simple case of a subsystem whose lattice degrees of
 2556 freedom are flavor- and color-independent. In this case, `List(:)` is a one-dimensional array
 2557 containing the lattice sites of the subsystem. `Nsites` is the number of sites, and `N_SUN` is
 2558 the number of color indexes belonging to the subsystem. Accordingly, for every element `I` of
 2559 `List`, the subsystem contains all degrees of freedom with site index `I`, any flavor index, and
 2560 1 ... `N_SUN` color index.

2561 **Mutual information** The mutual information between two subsystems A and B is given by

$$I_2 = -\ln\langle \text{Renyi_A} \rangle - \ln\langle \text{Renyi_B} \rangle + \ln\langle \text{Renyi_AB} \rangle, \quad (194)$$

2562 where `Renyi_A`, `Renyi_B`, and `Renyi_AB` are the second Rényi entropies of A , B , and $A \cup B$,
 2563 respectively.

2564 The measurements necessary for computing I_2 are obtained by:

2565 `Call Predefined_Obs_scal_Mutual_Inf(GRC, List_A, Nsites_A, List_B, Nsites_B, N_SUN, ZS, ZP,`
 2566 `Obs)`

2569 which returns the 2nd Rényi entropies mentioned above, stored in the variable `Obs`. Here,
 2570 `List_A` and `Nsites_A` are input parameters describing the subsystem A – with the same

2571 conventions and specializations described above – and `List_B` and `Nsites_B` are the corre-
 2572 sponding input parameters for the subsystem B , while `N_SUM` is assumed to be identical for A
 2573 and B .

2574 8.5 Predefined trial wave functions

2575 When using the projective algorithm (see Sec. 3), trial wave functions must be specified. These
 2576 are stored in variables of the `WaveFunction` type (Sec. 5.5). The ALF package provides a set
 2577 of predefined trial wave functions $|\Psi_{T,L/R}\rangle = WF_L/R$, returned by the call:

```
2578 Call Predefined_TrialWaveFunction(Lattice_type, Ndim, List, Invlist, Latt, Latt_unit,
2579           N_part, N_FL, WF_L, WF_R)
```

2582 Twisted boundary conditions (`Phi_X_vec=0.01`) are implemented for some lattices in order
 2583 to generate non-degenerate trial wave functions. Here the marker “`_vec`” indicates the vari-
 2584 able may assume different values depending on the flavor (e.g., spin up and down). Currently
 2585 predefined trial wave functions are flavor independent.

2586 The predefined trial wave functions correspond to the solution of the non-interacting tight
 2587 binding Hamiltonian on each of the predefined lattices. These solutions are the ground states
 2588 of the predefined hopping matrices (Sec. 8.2) with default parameters, for each lattice, as
 2589 follows.

2590 8.5.1 Square

2591 Parameter values for the predefined trial wave function on the square lattice:

```
2592 Checkerboard = .false.
2593 Symm          = .false.
2594 Bulk          = .false.
2595 N_Phi_vec    = 0
2596 Phi_X_vec    = 0.01d0
2597 Phi_Y_vec    = 0.d0
2598 Ham_T_vec    = 1.d0
2599 Ham_Chem_vec = 0.d0
2600 Dtau          = 1.d0
2601
```

2603 8.5.2 Honeycomb

2604 The twisted boundary condition for the square lattice lifts the degeneracy present at half-band
 2605 filling, but breaks time reversal symmetry as well as the C_4 lattice symmetry. If time reversal
 2606 symmetry is required to avoid the negative sign problem (that would be the case for the attrac-
 2607 tive Hubbard model at finite doping), then this choice of the trial wave function will introduce
 2608 a negative sign. One should then use the trial wave function presented in Sec. 7.6. For the
 2609 Honeycomb case, the trial wave function we choose is the ground state of the tight binding
 2610 model with small next-next-nearest hopping matrix element t' [130]. This breaks the C_3
 2611 symmetry and shifts the Dirac cone away from the zone boundary. Time reversal symmetry is
 2612 however not broken. Alternatively, one could include a small Kekule mass term. As shown in
 2613 Sec. 3.3 both choices of trial wave functions produce good results.

2614 8.5.3 N-leg ladder

2615 Parameter values for the predefined trial wave function on the N-leg ladder lattice:

```
2616
2617 Checkerboard = .false.
2618 Symm          = .false.
2619 Bulk          = .false.
2620 N_Phi_vec    = 0
2621 Phi_X_vec    = 0.01d0
```

```

2622 Phi_Y_vec      = 0.d0
2623 Ham_T_vec      = 1.d0
2624 Ham_Tperp_vec  = 1.d0
2625 Ham_Chem_vec   = 0.d0
2626 Dtau           = 1.d0

```

2628 8.5.4 Bilayer square

2629 Parameter values for the predefined trial wave function on the bilayer square lattice:

```

2630
2631 Checkerboard = .false.
2632 Symm          = .false.
2633 Bulk          = .false.
2634 N_Phi_vec    = 0
2635 Phi_X_vec    = 0.d0
2636 Phi_Y_vec    = 0.d0
2637 Ham_T_vec    = 1.d0
2638 Ham_T2_vec   = 0.d0
2639 Ham_Tperp_vec= 1.d0
2640 Ham_Chem_vec = 0.d0
2641 Dtau          = 1.d0

```

2643 8.5.5 Bilayer honeycomb

2644 Parameter values for the predefined trial wave function on the bilayer honeycomb lattice:

```

2645
2646 Checkerboard = .false.
2647 Symm          = .false.
2648 Bulk          = .false.
2649 N_Phi_vec    = 0
2650 Phi_X_vec    = 0.d0
2651 Phi_Y_vec    = 0.d0
2652 Ham_T_vec    = 1.d0
2653 Ham_T2_vec   = 0.d0
2654 Ham_Tperp_vec= 1.d0
2655 Ham_Chem_vec = 0.d0
2656 Dtau          = 1.d0

```

2658 9 Model classes

2659 The ALF library comes with five model classes: (i) SU(N) Hubbard models, (ii) O(2N) t-V
 2660 models, (iii) Kondo models, (iv) long-range Coulomb models, and (v) generic Z_2 lattice gauge
 2661 theories coupled to Z_2 matter and fermions. Below we detail the functioning of these classes.

2662 9.1 SU(N) Hubbard models Hamiltonian_Hubbard_smod.F90

2663 The parameter space for this model class reads:

```

2664
2665 &VAR_Hubbard          !! Variables for the Hubbard class
2666 Mz      = .T.          ! Whether to use the M_z-Hubbard model: Nf=2; N_SUN must be
2667                  ! even. HS field couples to the z-component of magnetization
2668 ham_T   = 1.d0          ! Hopping parameter
2669 ham_chem = 0.d0          ! Chemical potential
2670 ham_U   = 4.d0          ! Hubbard interaction
2671 ham_T2   = 1.d0          ! For bilayer systems
2672 ham_U2   = 4.d0          ! For bilayer systems
2673 ham_Tperp = 1.d0          ! For bilayer systems
2674 Continuous = .F.          ! For continuous HS decomposition
2675 /

```

2677 In the above listing, `ham_T` and `ham_T2` correspond to the hopping in the first and second
 2678 layers respectively and `ham_Tperp` is to the interlayer hopping. The Hubbard U term has
 2679 an orbital index, `ham_U` for the first and `ham_U2` for the second layers. Finally, `ham_chem`
 2680 corresponds to the chemical potential. If the flag `Mz` is set to `.False.`, then the code simulates
 2681 the following SU(N) symmetric Hubbard model:

$$\hat{H} = \sum_{(i,\delta),(j,\delta')} \sum_{\sigma=1}^N T_{(i,\delta),(j,\delta')} \hat{c}_{(i,\delta),\sigma}^\dagger e^{\frac{2\pi i}{\Phi_0} \int_{i+\delta}^{j+\delta'} A(l) dl} \hat{c}_{(j,\delta'),\sigma} + \sum_i \sum_{\delta} \frac{U_\delta}{N} \left(\sum_{\sigma=1}^N [\hat{c}_{(i,\delta),\sigma}^\dagger \hat{c}_{(i,\delta),\sigma} - 1/2] \right)^2 - \mu \sum_{(i,\delta)} \sum_{\sigma=1}^N \hat{c}_{(i,\delta),\sigma}^\dagger \hat{c}_{(i,\delta),\sigma}. \quad (195)$$

2682 The generic hopping is taken from Eq. (147) with appropriate boundary conditions given by
 2683 Eq. (148). The index i runs over the unit cells, δ over the orbitals in each unit cell and σ
 2684 from 1 to N and encodes the SU(N) symmetry. Note that N corresponds to `N_SUN` in the code.
 2685 The flavor index is set to unity such that it does not appear in the Hamiltonian. The chemical
 2686 potential μ is relevant only for the finite temperature code.

2687 If the variable `Mz` is set to `.True.`, then the code requires `N_SUN` to be even and simulates
 2688 the following Hamiltonian:

$$\hat{H} = \sum_{(i,\delta),(j,\delta')} \sum_{\sigma=1}^{N/2} \sum_{s=1,2} T_{(i,\delta),(j,\delta')} \hat{c}_{(i,\delta),\sigma,s}^\dagger e^{\frac{2\pi i}{\Phi_0} \int_{i+\delta}^{j+\delta'} A(l) dl} \hat{c}_{(j,\delta'),\sigma,s} - \sum_i \sum_{\delta} \frac{U_\delta}{N} \left(\sum_{\sigma=1}^{N/2} [\hat{c}_{(i,\delta),\sigma,2}^\dagger \hat{c}_{(i,\delta),\sigma,2} - \hat{c}_{(i,\delta),\sigma,1}^\dagger \hat{c}_{(i,\delta),\sigma,1}] \right)^2 - \mu \sum_{(i,\delta)} \sum_{\sigma=1}^{N/2} \sum_{s=1,2} \hat{c}_{(i,\delta),\sigma,s}^\dagger \hat{c}_{(i,\delta),\sigma,s}. \quad (196)$$

2689 In this case, the flavor index `N_FL` takes the value 2. Clearly at $N = 2$, both modes correspond
 2690 to the Hubbard model. For N even and $N > 2$ the models differ. In particular in the latter
 2691 Hamiltonian the U(N) symmetry is broken down to $U(N/2) \otimes U(N/2)$.

2692 It the variable `Continuous=.T.` then the code will use the generic HS transformation:

$$e^{\alpha \hat{A}^2} = \frac{1}{\sqrt{2\pi}} \int d\phi e^{-\phi^2/2 + \sqrt{2\alpha} \hat{A}}, \quad (197)$$

2693 as opposed to the discrete version of Eq. 11. If the Langevin flag is set to false, the code will
 2694 use the single spin-flip update:

$$\phi \rightarrow \phi + \text{Amplitude}(\xi - 1/2), \quad (198)$$

2695 where ξ is a random number $\in [0, 1]$ and `Amplitude` is defined in the `Fields_mod.F90`
 2696 module. Since this model class works for all predefined lattices (see Fig. 6) it includes the
 2697 SU(N) periodic Anderson model on the square and Honeycomb lattices. Finally, we note that
 2698 the executable for this class is given by `Hubbard.out`.

2699 As an example, we can consider the periodic Anderson model. Here we choose the
 2700 Bilayer_square lattice `Ham_U = Ham_T2 = 0`, `Ham_U2= U_f`, `Ham_tperp= V` and
 2701 `Ham_T= 1`. The pyALF based python script `Hubbard_PAM.py` produces the data shown in
 2702 Fig. 8 for the L=8 lattice.

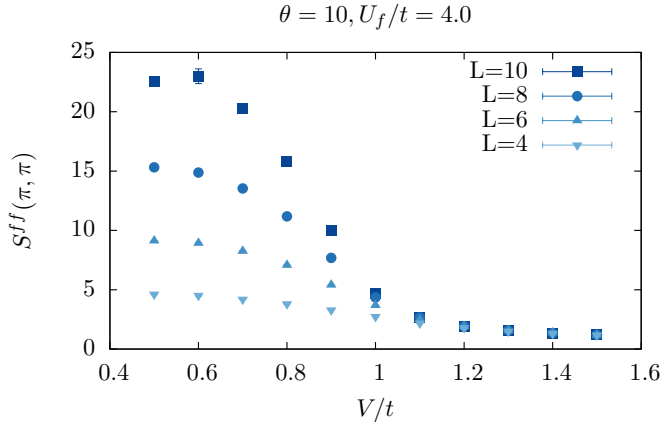


Figure 8: The periodic Anderson model. Here we plot the equal-time spin structure factor of the f-electrons at $\mathbf{q} = (\pi, \pi)$. This quantity is found in the file `SpinZ_eqJK`. The pyALF based python script `Hubbard_PAM.py` produces the data shown for the $L = 8$ lattice. One sees that for the chosen value of U_f/t the competition between the RKKY interaction and Kondo screening drives the system through a magnetic order-disorder transition at $V_c/t \simeq 1$ [148].

2703 9.2 SU(N) t-V models Hamiltonian_tV_smod.F90

2704 The parameter space for this model class reads:

```

2705 &VAR_tV          !! Variables for the t-V class
2706 ham_T      = 1.d0    ! Hopping parameter
2707 ham_chem   = 0.d0    ! Chemical potential
2708 ham_V      = 0.5d0   ! interaction strength
2709 ham_T2     = 1.d0    ! For bilayer systems
2710 ham_V2     = 0.5d0   ! For bilayer systems
2711 ham_Tperp  = 1.d0    ! For bilayer systems
2712 ham_Vperp  = 0.5d0   ! For bilayer systems
2713 ham_Vpervp = 0.5d0   !

```

2716 In the above `ham_T` and `ham_T2` and `ham_Tperp` correspond to the hopping in the first and
 2717 second layers respectively and `ham_Tperp` is to the interlayer hopping. The interaction term
 2718 has an orbital index, `ham_V` for the first and `ham_V2` for the second layers, and `ham_Vpervp` for
 2719 interlayer coupling. Note that we use the same sign conventions here for both the hopping pa-
 2720 rameters and the interaction strength. This implies a relative minus sign between here and the
 2721 U_δ interaction strength of the Hubbard model (see Sec. 9.1). Finally `ham_chem` corresponds
 2722 to the chemical potential. Let us introduce the operator

$$\hat{b}_{\langle(i,\delta),(j,\delta')\rangle} = \sum_{\sigma=1}^N \hat{c}_{(i,\delta),\sigma}^\dagger e^{\frac{2\pi i}{\Phi_0} \int_{i+\delta}^{j+\delta'} A(l) dl} \hat{c}_{(j,\delta'),\sigma} + \text{H.c.} \quad (199)$$

2723 The model is then defined as follows:

$$\begin{aligned} \hat{H} = & \sum_{\langle(i,\delta),(j,\delta')\rangle} T_{(i,\delta),(j,\delta')} \hat{b}_{\langle(i,\delta),(j,\delta')\rangle} + \sum_{\langle(i,\delta),(j,\delta')\rangle} \frac{V_{(i,\delta),(j,\delta')}}{N} (\hat{b}_{\langle(i,\delta),(j,\delta')\rangle})^2 \\ & - \mu \sum_{(i,\delta)} \sum_{\sigma=1}^N \hat{c}_{(i,\delta),\sigma}^\dagger \hat{c}_{(i,\delta),\sigma}. \end{aligned} \quad (200)$$

2724 The generic hopping is taken from Eq. (147) with appropriate boundary conditions given by
 2725 Eq. (148). The index i runs over the unit cells, δ over the orbitals in each unit cell and σ

from 1 to N , encoding the $SU(N)$ symmetry. Note that N corresponds to `N_SUN` in the code. The flavor index is set to unity such that it does not appear in the Hamiltonian. The chemical potential μ is relevant only for the finite temperature code. An example showing how to run this model class can be found in the pyALF based Jupyter notebook `tV_model.ipynb`.

As a concrete example, we can consider the Hamiltonian of the t-V model of $SU(N)$ fermions on the square lattice,

$$\hat{H} = -t \sum_{\langle i,j \rangle} \hat{b}_{\langle i,j \rangle} - \frac{V}{N} \sum_{\langle i,j \rangle} (\hat{b}_{\langle i,j \rangle})^2 - \mu \sum_i \sum_{\sigma=1}^N \hat{c}_{i,\sigma}^\dagger \hat{c}_{i,\sigma}, \quad (201)$$

which can be simulated by setting `ham_T` = t , `ham_V` = V , and `ham_chem` = μ . At half-band filling $\mu = 0$, the sign problem is absent for $V > 0$ and for all values of N [75, 149]. For even values of N no sign problem occurs for $V > 0$ and arbitrary chemical potentials [74].

Note that in the absence of orbital magnetic fields, the model has an $O(2N)$ symmetry. This can be seen by writing the model in a Majorana basis (see e.g. Ref. [21]).

9.3 $SU(N)$ Kondo lattice models `Hamiltonian_Kondo_smod.F90`

The Kondo lattice model we consider is an $SU(N)$ generalization of the $SU(2)$ Kondo-model discussed in [31, 32]. Here we follow the work of Ref. [50]. Let T^a be the $N^2 - 1$ generators of $SU(N)$ that satisfy the normalization condition:

$$\text{Tr}[T^a T^b] = \frac{1}{2} \delta_{a,b}. \quad (202)$$

For the $SU(2)$ case, T^a corresponds to the $T = \frac{1}{2}\boldsymbol{\sigma}$ with $\boldsymbol{\sigma}$ a vector of the three Pauli spin matrices, Eq. (177). The Hamiltonian is defined on bilayer square or honeycomb lattices, with hopping restricted to the first layer (i.e conduction orbitals c_i^\dagger) and spins, f-orbitals, on the second layer.

$$\hat{H} = -t \sum_{\langle i,j \rangle} \sum_{\sigma=1}^N \left(\hat{c}_{i,\sigma}^\dagger e^{\frac{2\pi i}{\Phi_0} \int_i^j \mathbf{A} \cdot d\mathbf{l}} \hat{c}_{j,\sigma} + \text{H.c.} \right) - \mu \sum_{i,\sigma} \hat{c}_{i,\sigma}^\dagger \hat{c}_{i,\sigma} + \frac{U_c}{N} \sum_i \left(\hat{n}_i^c - \frac{N}{2} \right)^2 + \frac{2J}{N} \sum_{i,a=1}^{N^2-1} \hat{T}_i^{a,c} \hat{T}_i^{a,f}. \quad (203)$$

In the above, i is a super-index accounting for the unit cell and orbital,

$$\hat{T}_i^{a,c} = \sum_{\sigma,\sigma'=1}^N \hat{c}_{i,\sigma}^\dagger T_{\sigma,\sigma'}^a \hat{c}_{i,\sigma'}, \quad \hat{T}_i^{a,f} = \sum_{\sigma,\sigma'=1}^N \hat{f}_{i,\sigma}^\dagger T_{\sigma,\sigma'}^a \hat{f}_{i,\sigma'}, \quad \text{and} \quad \hat{n}_i^c = \sum_{\sigma=1}^N \hat{c}_{i,\sigma}^\dagger \hat{c}_{i,\sigma}. \quad (204)$$

Finally, the constraint

$$\sum_{\sigma=1}^N \hat{f}_{i,\sigma}^\dagger \hat{f}_{i,\sigma} \equiv \hat{n}_i^f = \frac{N}{2} \quad (205)$$

holds. Some rewriting has to be carried out so as to implement the model. First, we use the relation:

$$\sum_a T_{\alpha,\beta}^a T_{\alpha',\beta'}^a = \frac{1}{2} \left(\delta_{\alpha,\beta'} \delta_{\alpha',\beta} - \frac{1}{N} \delta_{\alpha,\beta} \delta_{\alpha',\beta'} \right),$$

to show that in the unconstrained Hilbert space,

$$\frac{2J}{N} \sum_{a=1}^{N^2-1} \hat{T}_i^{a,c} \hat{T}_i^{a,f} = -\frac{J}{2N} \sum_i (\hat{D}_i^\dagger \hat{D}_i + \hat{D}_i \hat{D}_i^\dagger) + \frac{J}{N} \left(\frac{\hat{n}_i^c}{2} + \frac{\hat{n}_i^f}{2} - \frac{\hat{n}_i^c \hat{n}_i^f}{N} \right),$$

2750 with

$$\hat{D}_i^\dagger = \sum_{\sigma=1}^N \hat{c}_{i,\sigma}^\dagger \hat{f}_{i,\sigma}.$$

2751 In the constrained Hilbert space, $\hat{n}_i^f = N/2$, the above gives:

$$\frac{2J}{N} \sum_{a=1}^{N^2-1} \hat{T}_i^{a,c} \hat{T}_i^{a,f} = -\frac{J}{4N} \left[(\hat{D}_i^\dagger + \hat{D}_i)^2 + (i\hat{D}_i^\dagger - i\hat{D}_i)^2 \right] + \frac{J}{4}. \quad (206)$$

2752 The perfect square form complies with the requirements of ALF. We still have to impose the
 2753 constraint. To do so, we work in the unconstrained Hilbert space and add a Hubbard U -term
 2754 on the f-orbitals. With this addition, the Hamiltonian we simulate reads:

$$\begin{aligned} \hat{H}_{\text{QMC}} = & -t \sum_{\langle i,j \rangle} \sum_{\sigma=1}^N \left(\hat{c}_{i,\sigma}^\dagger e^{\frac{2\pi i}{\Phi_0} \int_i^j \mathbf{A} \cdot d\mathbf{l}} \hat{c}_{j,\sigma} + \text{H.c.} \right) - \mu \sum_{i,\sigma} \hat{c}_{i,\sigma}^\dagger \hat{c}_{i,\sigma} + \frac{U_c}{N} \sum_i \left(\hat{n}_i^c - \frac{N}{2} \right)^2 \\ & - \frac{J}{4N} \left[(\hat{D}_i^\dagger + \hat{D}_i)^2 + (i\hat{D}_i^\dagger - i\hat{D}_i)^2 \right] + \frac{U_f}{N} \sum_i \left(\hat{n}_i^f - \frac{N}{2} \right)^2. \end{aligned} \quad (207)$$

2755 The key point for the efficiency of the code, is to see that

$$\left[\hat{H}_{\text{QMC}}, \left(\hat{n}_i^f - \frac{N}{2} \right)^2 \right] = 0, \quad (208)$$

2756 such that the constraint is implemented efficiently. In fact, for the finite temperature code at
 2757 inverse temperature β , the unphysical Hilbert space is suppressed by a factor $e^{-\beta U_f / N}$.

2758 The SU(2) case

2759 The SU(2) case is special and allows for a more efficient implementation than the one described
 2760 above. The key point is that for the SU(2) case, the Hubbard term is related to the fermion
 2761 parity,

$$\left(\hat{n}_i^f - 1 \right)^2 = \frac{(-1)^{\hat{n}_i^f} + 1}{2}, \quad (209)$$

2762 such that we can omit the current-term $(i\hat{D}_i^\dagger - i\hat{D}_i)^2$ without violating Eq. (208). As in
 2763 Refs. [31, 32, 150], the Hamiltonian that one will simulate reads:

$$\begin{aligned} \hat{\mathcal{H}} = & \underbrace{-t \sum_{\langle i,j \rangle, \sigma} \left(\hat{c}_{i,\sigma}^\dagger e^{\frac{2\pi i}{\Phi_0} \int_i^j \mathbf{A} \cdot d\mathbf{l}} \hat{c}_{j,\sigma} + \text{H.c.} \right) + \frac{U_c}{2} \sum_i \left(\hat{n}_i^c - 1 \right)^2}_{\equiv \hat{\mathcal{H}}_{tU_c}} \\ & - \frac{J}{4} \sum_i \underbrace{\left(\sum_{\sigma} \hat{c}_{i,\sigma}^\dagger \hat{f}_{i,\sigma} + \hat{f}_{i,\sigma}^\dagger \hat{c}_{i,\sigma} \right)^2}_{\equiv \hat{\mathcal{H}}_{U_f}} + \underbrace{\frac{U_f}{2} \sum_i \left(\hat{n}_i^f - 1 \right)^2}_{\equiv \hat{\mathcal{H}}_{U_f}}. \end{aligned} \quad (210)$$

2764 The relation to the Kondo lattice model follows from expanding the square of the hybridization
 2765 to obtain:

$$\hat{\mathcal{H}} = \hat{\mathcal{H}}_{tU_c} + J \sum_i \left(\hat{s}_i^c \cdot \hat{s}_i^f + \hat{\eta}_i^{z,c} \cdot \hat{\eta}_i^{z,f} - \hat{\eta}_i^{x,c} \cdot \hat{\eta}_i^{x,f} - \hat{\eta}_i^{y,c} \cdot \hat{\eta}_i^{y,f} \right) + \hat{\mathcal{H}}_{U_f}, \quad (211)$$

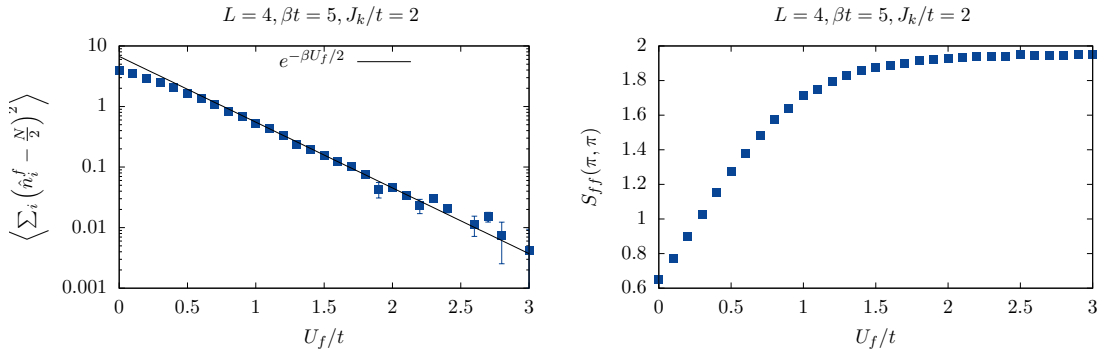


Figure 9: Left: Suppression of charge fluctuations of the f-orbitals as a function of U_f . Right: When charge fluctuations on the f-orbitals vanish, quantities such as the Fourier transform of the f spin-spin correlations at $\mathbf{q} = (\pi, \pi)$ converge to their KLM value. Typically, for the SU(2) case, $\beta U_f > 10$ suffices to reach convergent results. The pyALF script used to produce the data of the plot can be found in [Kondo.py](#).

where the $\hat{\eta}$ -operators relate to the spin-operators via a particle-hole transformation in one spin sector:

$$\hat{\eta}_i^\alpha = \hat{P}^{-1} \hat{S}_i^\alpha \hat{P}, \quad \text{with } \hat{P}^{-1} \hat{c}_{i,\uparrow}^\dagger \hat{P} = (-1)^{i_x+i_y} \hat{c}_{i,\uparrow}^\dagger, \quad \text{and } \hat{P}^{-1} \hat{c}_{i,\downarrow}^\dagger \hat{P} = \hat{c}_{i,\downarrow}^\dagger. \quad (212)$$

Since the $\hat{\eta}^f$ and \hat{S}^f operators do not alter the parity $[(-1)^{\hat{n}_i^f}]$ of the f-sites,

$$[\hat{\mathcal{H}}, \hat{\mathcal{H}}_{U_f}] = 0. \quad (213)$$

Thereby, and for positive values of U , doubly occupied or empty f-sites – corresponding to even parity sites – are suppressed by a Boltzmann factor $e^{-\beta U_f/2}$ in comparison to odd parity sites. Thus, essentially, choosing βU_f adequately allows one to restrict the Hilbert space to odd parity f-sites. In this Hilbert space, $\hat{\eta}^{x,f} = \hat{\eta}^{y,f} = \hat{\eta}^{z,f} = 0$ such that the Hamiltonian (210) reduces to the Kondo lattice model.

QMC implementation

The name space for this model class reads:

```

2776 &VAR_Kondo          !! Variables for the Kondo class
2777 ham_T      = 1.d0    ! Hopping parameter
2778 ham_chem   = 0.d0    ! Chemical potential
2779 ham_Uc     = 0.d0    ! Hubbard interaction on c-orbitals Uc
2780 ham_Uf     = 2.d0    ! Hubbard interaction on f-orbitals Uf
2781 ham_JK     = 2.d0    ! Kondo Coupling J
2782 /
2783

```

Aside from the usual observables we have included the scalar observable `Constraint_scal` that measures

$$\left\langle \sum_i \left(\hat{n}_i^f - \frac{N}{2} \right)^2 \right\rangle. \quad (214)$$

U_f has to be chosen large enough such that the above quantity vanishes within statistical uncertainty. For the square lattice, Fig. 9 plots the aforementioned quantity as a function of U_f for the SU(2) model. As apparent $\left\langle \sum_i \left(\hat{n}_i^f - N/2 \right)^2 \right\rangle \propto e^{-\beta U_f/2}$.

2790 **9.4 Models with long range Coulomb interactions** Hamiltonian_LRC_smod.F90

2791 The model we consider here is defined for N_FL=1, arbitrary values of N_SUN and all the
2792 predefined lattices. It reads:

$$\hat{H} = \sum_{i,j} \sum_{\sigma=1}^N T_{i,j} \hat{c}_{i,\sigma}^\dagger e^{\frac{2\pi i}{\Phi_0} \int_i^j A(l) dl} \hat{c}_{j,\sigma} + \frac{1}{N} \sum_{i,j} \left(\hat{n}_i - \frac{N}{2} \right) V_{i,j} \left(\hat{n}_j - \frac{N}{2} \right) - \mu \sum_i \hat{n}_i. \quad (215)$$

2793 In the above, $i = (i, \delta_i)$ and $j = (j, \delta_j)$ are super-indices encoding the unit-cell and orbital
2794 and $\hat{n}_i = \sum_{\sigma=1}^N \hat{c}_{i,\sigma}^\dagger \hat{c}_{i,\sigma}$. For simplicity, the interaction is specified by two parameters, U and
2795 α that monitor the strength of the onsite interaction and the magnitude of the Coulomb tail
2796 respectively:

$$V_{i,j} \equiv V(i + \delta_i, j + \delta_j) = U \begin{cases} 1, & \text{if } i = j, \\ \frac{\alpha d_{\min}}{\|i - j + \delta_i - \delta_j\|}, & \text{otherwise.} \end{cases} \quad (216)$$

2797 Here d_{\min} is the minimal distance between two orbitals. On a torus, some care has been taken
2798 in defining the distance. Namely, with the lattice size given by the vectors L_1 and L_2 (see
2799 Sec. 8.1),

$$\|i\| = \min_{n_1, n_2 \in \mathbb{Z}} |i - n_1 L_1 - n_2 L_2|. \quad (217)$$

2800 The implementation of the model follows Ref. [51], but supports various lattice geometries.
2801 We use the following HS decomposition:

$$e^{-\Delta\tau \hat{H}_V} \propto \int \prod_i d\phi_i e^{-\frac{N\Delta\tau}{4} \sum_{i,j} \phi_i V_{i,j}^{-1} \phi_j - \sum_i i \Delta\tau \phi_i (\hat{n}_i - \frac{N}{2})}, \quad (218)$$

2802 where ϕ_i is a real variable, V is symmetric and, importantly, has to be positive definite for the
2803 Gaussian integration to be defined. The partition function reads:

$$Z \propto \int \prod_i d\phi_{i,\tau} \underbrace{e^{-\frac{N\Delta\tau}{4} \sum_{i,\tau} \phi_{i,\tau} V_{i,j}^{-1} \phi_{j,\tau}}}_{W_B(\phi)} \underbrace{\text{Tr} \left[\prod_{\tau} e^{-\Delta\tau \hat{H}_T} e^{-\sum_i i \Delta\tau \phi_{i,\tau} (\hat{n}_i - \frac{N}{2})} \right]}_{W_F(\phi)}, \quad (219)$$

2804 such that the weight splits into bosonic and fermionic parts.

2805 For the update, it is convenient to work in a basis where V is diagonal:

$$\text{Diag}(\lambda_1, \dots, \lambda_{\text{Ndim}}) = O^T V O, \quad (220)$$

2806 with $O^T O = 1$ and define:

$$\eta_{i,\tau} = \sum_j O_{i,j}^T \phi_{j,\tau}. \quad (221)$$

2807 On a given time slice τ_u we propose a new field configuration with the probability:

$$T^0(\eta \rightarrow \eta') = \begin{cases} \prod_i \left[P P_B(\eta'_{i,\tau_u}) + (1-P) \delta(\eta_{i,\tau_u} - \eta'_{i,\tau_u}) \right], & \text{for } \tau = \tau_u, \\ \delta(\eta_{i,\tau} - \eta'_{i,\tau}), & \text{for } \tau \neq \tau_u, \end{cases} \quad (222)$$

2808 where

$$P_B(\eta_{i,\tau}) \propto e^{-\frac{N\Delta\tau}{4\lambda_i} \eta_{i,\tau}^2}. \quad (223)$$

2809 $P \in [0, 1]$ and δ denotes the Dirac δ -function. That is, we carry out simple sampling of the
2810 field with probability P and leave the field unchanged with probability $(1 - P)$. P is a free
2811 parameter that does not change the final result but that allows one to adjust the acceptance.

2812 We then use the Metropolis-Hastings acceptance-rejection scheme and accept the move with
 2813 probability

$$\min\left(\frac{T^0(\eta' \rightarrow \eta)W_B(\eta')W_F(\eta')}{T^0(\eta \rightarrow \eta')W_B(\eta)W_F(\eta)}, 1\right) = \min\left(\frac{W_F(\eta')}{W_F(\eta)}, 1\right), \quad (224)$$

2814 where

$$W_B(\eta) = e^{-\frac{N\Delta\tau}{4} \sum_{i,\tau} \eta_{i,\tau}^2 / \lambda_i}, \quad \text{and} \quad W_F(\eta) = \text{Tr}\left[\prod_{\tau} e^{-\Delta\tau \hat{H}_T} e^{-\sum_{i,j} i\Delta\tau O_{i,j} \eta_{j,\tau} (\hat{n}_i - \frac{N}{2})}\right]. \quad (225)$$

2815 Since a local change on a single time slice in the η basis corresponds to a non-local space
 2816 update in the ϕ basis, we use the routine for global updates in space to carry out the update
 2817 (see Sec. 2.2.3).

2818 QMC implementation

2819 The name space for this model class reads:

```
2820
2821 &VAR_LRC          !! Variables for the Long Range Coulomb class
2822 ham_T            = 1.0      ! Specifies the hopping and chemical potential
2823 ham_T2           = 1.0      ! For bilayer systems
2824 ham_Tperp        = 1.0      ! For bilayer systems
2825 ham_chem         = 1.0      ! Chemical potential
2826 ham_U            = 4.0      ! On-site interaction
2827 ham_alpha        = 0.1      ! Coulomb tail magnitude
2828 Percent_change   = 0.1      ! Parameter P
2829 /
2830
```

2831 By setting α to zero we can test this code against the Hubbard code. For a 4×4 square
 2832 lattice at $\beta t = 5$, $U/t = 4$, and half-band filling, Hamiltonian_Hubbard_smod.F90 gives
 2833 $E = -13.1889 \pm 0.0017$ and Hamiltonian_LRC_smod.F90, $E = -13.199 \pm 0.040$. Note that
 2834 for the Hubbard code we have used the default `Mz = .True.`. This option breaks SU(2) spin
 2835 symmetry for a given HS configuration, but produces very precise values of the energy. On the
 2836 other hand, the LRC code is an SU(2) invariant code (as would be choosing `Mz = .False.`)
 2837 and produces more fluctuations in the double occupancy. This partly explains the difference in
 2838 error bars between the two codes. To produce this data, one can run the pyALF python script
 2839 [LRC.py](#).

2840 9.5 Z_2 lattice gauge theories coupled to fermion and Z_2 matter

2841 Hamiltonian_Z2_smod.F90

2842 The Hamiltonian we will consider here reads

$$\begin{aligned} \hat{H} = & -t_{Z_2} \sum_{\langle i,j \rangle, \sigma} \hat{\sigma}_{\langle i,j \rangle}^z (\hat{\Psi}_{i,\sigma}^\dagger \hat{\Psi}_{j,\sigma} + \text{H.c.}) - \mu \sum_{i,\sigma} \hat{\Psi}_{i,\sigma}^\dagger \hat{\Psi}_{i,\sigma} - g \sum_{\langle i,j \rangle} \hat{\sigma}_{\langle i,j \rangle}^x \\ & + K \sum_{\square} \prod_{\langle i,j \rangle \in \partial \square} \hat{\sigma}_{\langle i,j \rangle}^z + J \sum_{\langle i,j \rangle} \hat{\tau}_i^z \hat{\sigma}_{\langle i,j \rangle}^z \hat{\tau}_j^z - h \sum_i \hat{\tau}_i^x \\ & - t \sum_{\langle i,j \rangle, \sigma} \hat{\tau}_i^z \hat{\tau}_j^z (\hat{\Psi}_{i,\sigma}^\dagger \hat{\Psi}_{j,\sigma} + \text{H.c.}) + \frac{U}{N} \sum_i \left[\sum_{\sigma} (\hat{\Psi}_{i,\sigma}^\dagger \hat{\Psi}_{i,\sigma} - 1/2) \right]^2. \end{aligned} \quad (226)$$

2843 The model is defined on a square lattice, and describes fermions,

$$\{\hat{\Psi}_{i,\sigma}^\dagger, \hat{\Psi}_{j,\sigma'}\} = \delta_{i,j} \delta_{\sigma,\sigma'}, \quad \{\hat{\Psi}_{i,\sigma}, \hat{\Psi}_{j,\sigma'}\} = 0, \quad (227)$$

2844 coupled to bond gauge fields,

$$\hat{\sigma}_{\langle i,j \rangle}^z = \begin{bmatrix} 1 & 0 \\ 0 & -1 \end{bmatrix}, \quad \hat{\sigma}_{\langle i,j \rangle}^x = \begin{bmatrix} 0 & 1 \\ 1 & 0 \end{bmatrix}, \quad \{ \hat{\sigma}_{\langle i,j \rangle}^z, \hat{\sigma}_{\langle i',j' \rangle}^x \} = 2(1 - \delta_{\langle i,j \rangle, \langle i',j' \rangle}) \hat{\sigma}_{\langle i,j \rangle}^z \hat{\sigma}_{\langle i',j' \rangle}^x, \quad (228)$$

2845 and Z_2 matter fields:

$$\hat{\tau}_i^z = \begin{bmatrix} 1 & 0 \\ 0 & -1 \end{bmatrix}, \quad \hat{\tau}_i^x = \begin{bmatrix} 0 & 1 \\ 1 & 0 \end{bmatrix}, \quad \{ \hat{\tau}_i^z, \hat{\tau}_{i'}^x \} = 2(1 - \delta_{i,i'}) \hat{\tau}_i^z \hat{\tau}_{i'}^x. \quad (229)$$

2846 Fermions, gauge fields and Z_2 matter fields commute with each other.

2847 Importantly, the model has a local Z_2 symmetry. Consider:

$$\hat{Q}_i = (-1)^{\sum_{\sigma} \hat{\Psi}_{i,\sigma}^{\dagger} \hat{\Psi}_{i,\sigma}} \hat{\tau}_i^x \hat{\sigma}_{i,i+a_x}^x \hat{\sigma}_{i,i-a_x}^x \hat{\sigma}_{i,i+a_y}^x \hat{\sigma}_i^x. \quad (230)$$

2848 One can then show that $\hat{Q}_i^2 = 1$ and that

$$[\hat{Q}_i, \hat{H}] = 0. \quad (231)$$

2849 The above allows us to assign Z_2 charges to the operators. Since $\{\hat{Q}_i, \hat{\Psi}_{i,\sigma}^{\dagger}\} = 0$ we can assign
2850 a Z_2 charge to the fermions. Equivalently $\hat{\tau}_i^z$ has a Z_2 charge and $\hat{\sigma}_{i,j}^z$ carries Z_2 charges
2851 at its ends. Since the total fermion number is conserved, we can assign an electric charge
2852 to the fermions. Finally, the model has an SU(N) color symmetry. In fact, at zero chemical
2853 potential and $U = 0$, the symmetry is enhanced to $O(2N)$ [21]. Aspects of this Hamiltonian
2854 were investigated in Refs. [21, 25, 26, 28–30] and we refer the interested user to these papers
2855 for a discussion of the phases and phase transitions supported by the model.

2856 QMC implementation

2857 The name space for this model class reads:

```

2858 &VAR_Z2_Matter          !! Variables for the Z_2 class
2859 ham_T                  = 1.0      ! Hopping for fermions
2860 ham_TZ2                = 1.0      ! Hopping for orthogonal fermions
2861 ham_chem               = 0.0      ! Chemical potential for fermions
2862 ham_U                  = 0.0      ! Hubbard for fermions
2863 Ham_J                  = 1.0      ! Hopping Z2 matter fields
2864 Ham_K                  = 1.0      ! Plaquette term for gauge fields
2865 Ham_h                  = 1.0      ! sigma^x-term for matter
2866 Ham_g                  = 1.0      ! tau^x-term for gauge
2867 Dtau                   = 0.1d0    ! Thereby Ltrot=Beta/dtau
2868 Beta                    = 10.d0    ! Inverse temperature
2869 Projector              = .False.  ! To enable projective code
2870 Theta                   = 10.0     ! Projection parameter
2871 /

```

2874 We note that the implementation is such that if $Ham_T=0$ ($Ham_TZ2=0$) then all the terms
2875 involving the matter field (Z_2 gauge field) are automatically set to zero. We warn the user
2876 that autocorrelation and warmup times can be large for this model class. At this point, the
2877 model is only implemented for the square lattice and does not support a symmetric Trotter
2878 decomposition.

2879 The key point to implement the model is to define a new bond variable:

$$\hat{\mu}_{\langle i,j \rangle}^z = \hat{\tau}_i^z \hat{\tau}_j^z. \quad (232)$$

2880 By construction, the $\hat{\mu}_{\langle i,j \rangle}^z$ bond variables have a zero flux constraint:

$$\hat{\mu}_{\langle i,i+a_x \rangle}^z \hat{\mu}_{\langle i+a_x, i+a_x+a_y \rangle}^z \hat{\mu}_{\langle i+a_x+a_y, i+a_y \rangle}^z \hat{\mu}_{\langle i+a_y, i \rangle}^z = 1. \quad (233)$$

2881 Consider a basis where $\hat{\mu}_{\langle i,j \rangle}^z$ and $\hat{\tau}_i^z$ are diagonal with eigenvalues $\mu_{\langle i,j \rangle}$ and τ_i respectively.
2882 The map from $\{\tau_i\}$ to $\{\mu_{\langle i,j \rangle}\}$ is unique. The reverse however is valid only up to a global sign.
2883 To pin down this sign (and thereby the relative signs between different time slices) we store
2884 the fields $\mu_{\langle i,j \rangle}$ at every time slice as well as the value of the Ising field at a reference site
2885 $\tau_{i=0}$. Within the ALF, this can be done by adding a dummy operator in the Op_V list to carry
2886 this degree of freedom. With this extra degree of freedom we can switch between the two
2887 representations without loosing any information. To compute the Ising part of the action it is
2888 certainly more transparent to work with the $\{\tau_i\}$ variables. For the fermion determinant, the
2889 $\{\mu_{\langle i,j \rangle}\}$ are more convenient.

2890 Since flipping $\hat{\tau}_i^z$ amounts to changing the sign of the four bond variables emanating from
2891 site i , the identity:

$$\hat{\tau}_i^x = \hat{\mu}_{i,i+a_x}^x \hat{\mu}_{i+a_x,i+a_x+a_y}^x \hat{\mu}_{i+a_x+a_y,i+a_y}^x. \quad (234)$$

2892 holds. Note that $\{\hat{\mu}_{\langle i,j \rangle}^z, \hat{\mu}_{\langle i',j' \rangle}^x\} = 2(1 - \delta_{\langle i,j \rangle, \langle i',j' \rangle}) \hat{\mu}_{\langle i,j \rangle}^z \hat{\mu}_{\langle i',j' \rangle}^x$, such that applying $\hat{\mu}_{\langle i,j \rangle}^x$ on
2893 an eigenstate of $\hat{\mu}_{\langle i,j \rangle}^z$ flips the field.

2894 The model can then be written as:

$$\begin{aligned} \hat{H} = & -t_{Z_2} \sum_{\langle i,j \rangle, \sigma} \hat{\sigma}_{\langle i,j \rangle}^z (\hat{\Psi}_{i,\sigma}^\dagger \hat{\Psi}_{j,\sigma} + \text{H.c.}) - \mu \sum_{i,\sigma} \hat{\Psi}_{i,\sigma}^\dagger \hat{\Psi}_{i,\sigma} - g \sum_{\langle i,j \rangle} \hat{\sigma}_{\langle i,j \rangle}^x + K \sum_{\square} \prod_{\langle i,j \rangle \in \partial \square} \hat{\sigma}_{\langle i,j \rangle}^z \\ & + J \sum_{\langle i,j \rangle} \hat{\mu}_{\langle i,j \rangle}^z \hat{\sigma}_{\langle i,j \rangle}^z - h \sum_i \hat{\mu}_{i,i+a_x}^x \hat{\mu}_{i+a_x,i+a_x+a_y}^x \hat{\mu}_{i+a_x+a_y,i+a_y}^x \hat{\mu}_{i+a_y,i}^x \\ & - t \sum_{\langle i,j \rangle, \sigma} \hat{\mu}_{i,j}^z (\hat{\Psi}_{i,\sigma}^\dagger \hat{\Psi}_{j,\sigma} + \text{H.c.}) + \frac{U}{N} \sum_i \left[\sum_{\sigma} (\hat{\Psi}_{i,\sigma}^\dagger \hat{\Psi}_{i,\sigma} - 1/2) \right]^2, \end{aligned} \quad (235)$$

2895 subject to the constraint of Eq. (233).

2896 To formulate the Monte Carlo, we work in a basis in which $\hat{\mu}_{\langle i,j \rangle}^z$, $\hat{\tau}_0^z$ and $\hat{\sigma}_{\langle i,j \rangle}^z$ are diagonal:

$$\hat{\mu}_{\langle i,j \rangle}^z |\underline{s}\rangle = \mu_{\langle i,j \rangle} |\underline{s}\rangle, \quad \hat{\sigma}_{\langle i,j \rangle}^z |\underline{s}\rangle = \sigma_{\langle i,j \rangle} |\underline{s}\rangle, \quad \hat{\tau}_0^z |\underline{s}\rangle = \tau_0 |\underline{s}\rangle, \quad (236)$$

2897 with $\underline{s} = (\{\mu_{\langle i,j \rangle}\}, \{\sigma_{\langle i,j \rangle}\}, \tau_0)$. In this basis,

$$Z = \sum_{s_1, \dots, s_{L_\tau}} e^{-S_0(\{\underline{s}_\tau\})} \text{Tr}_F \left[\prod_{\tau=1}^{L_\tau} e^{-\Delta \tau \hat{H}_F(\underline{s}_\tau)} \right], \quad (237)$$

2898 where

$$\begin{aligned} S_0(\{\underline{s}_\tau\}) = & -\ln \left[\prod_{\tau=1}^{L_\tau} \langle \underline{s}_{\tau+1} | e^{-\Delta \tau \hat{H}_I} | \underline{s}_\tau \rangle \right], \\ \hat{H}_I = & -g \sum_{\langle i,j \rangle} \hat{\sigma}_{\langle i,j \rangle}^x + K \sum_{\square} \prod_{\langle i,j \rangle \in \partial \square} \hat{\sigma}_{\langle i,j \rangle}^z + J \sum_{\langle i,j \rangle} \hat{\mu}_{\langle i,j \rangle}^z \hat{\sigma}_{\langle i,j \rangle}^z \\ & - h \sum_i \hat{\mu}_{i,i+a_x}^x \hat{\mu}_{i+a_x,i+a_x+a_y}^x \hat{\mu}_{i+a_x+a_y,i+a_y}^x \hat{\mu}_{i+a_y,i}^x, \end{aligned}$$

2899 and

$$\begin{aligned} \hat{H}_F(\underline{s}) = & -t_{Z_2} \sum_{\langle i,j \rangle, \sigma} \sigma_{\langle i,j \rangle} (\hat{\Psi}_{i,\sigma}^\dagger \hat{\Psi}_{j,\sigma} + \text{H.c.}) - \mu \sum_{i,\sigma} \hat{\Psi}_{i,\sigma}^\dagger \hat{\Psi}_{i,\sigma} \\ & - t \sum_{\langle i,j \rangle, \sigma} \mu_{i,j} (\hat{\Psi}_{i,\sigma}^\dagger \hat{\Psi}_{j,\sigma} + \text{H.c.}) + \frac{U}{N} \sum_i \left[\sum_{\sigma} (\hat{\Psi}_{i,\sigma}^\dagger \hat{\Psi}_{i,\sigma} - 1/2) \right]^2. \end{aligned}$$

2900 In the above, $|s_{L_\tau+1}\rangle = |s_1\rangle$. With a further HS transformation of the Hubbard term (see
 2901 Sec. 8.3.1) the model is readily implemented in the ALF. Including this HS field, l , [see Eq. (11)]
 2902 yields the configuration space:

$$C = (\{\mu_{\langle i,j \rangle, \tau}\}, \{\sigma_{\langle i,j \rangle, \tau}\}, \{\tau_{0,\tau}\}, \{l_{i,\tau}\}), \quad (238)$$

2903 where the variables μ , τ and σ take the values ± 1 and l the values $\pm 1, \pm 2$.

2904 The initial configuration as well as the moves have to respect the zero flux constraint of
 2905 Eq. (233). Therefore, single spin flips of the μ fields are prohibited and the minimal move
 2906 one can carry out on a given time slice is the following. We randomly choose a site i and
 2907 propose a move where: $\mu_{i,i+a_x} \rightarrow -\mu_{i,i+a_x}$, $\mu_{i,i-a_x} \rightarrow -\mu_{i,i-a_x}$, $\mu_{i,i+a_y} \rightarrow -\mu_{i,i+a_y}$ and
 2908 $\mu_{i,i-a_y} \rightarrow -\mu_{i,i-a_y}$. One can carry out such moves by using the global move in real space
 2909 option presented in Sec. 2.2.3 and 5.7.1.

2910 9.5.1 Projective approach

2911 The program also supports a zero temperature implementation. Our choice of the trial wave
 2912 function does not break any symmetries of the model and reads:

$$|\Psi_T\rangle = |\Psi_T^F\rangle \otimes_{\langle i,j \rangle} |+\rangle_{\langle i,j \rangle} \otimes_i |+\rangle_i. \quad (239)$$

2913 For the fermion part we use a Fermi sea with small dimerization to avoid the negative sign
 2914 problem at half-filling (see Sec. 7.6). For the Ising part the trial wave function is diagonal in
 2915 the $\hat{\sigma}_{\langle i,j \rangle}^x$ and $\hat{\tau}_i^x$ operators:

$$\hat{\sigma}_{\langle i,j \rangle}^x |+\rangle_{\langle i,j \rangle} = |+\rangle_{\langle i,j \rangle}, \quad \text{and} \quad \hat{\tau}_i^x |+\rangle_i = |+\rangle_i. \quad (240)$$

2916 An alternative choice would be to choose a charge density wave fermionic trial wave func-
 2917 tion. This violates the partial particle-hole symmetry of the model at $U = \mu = 0$ and effectively
 2918 imposes the constraint $\hat{Q}_i = 1$.

2919 9.5.2 Observables

2920 Apart from the standard observables discussed in Sec. 8.4 the code computes additionally

$$\langle \hat{\sigma}_{\langle i,j \rangle}^x \rangle, \quad \text{and} \quad \langle \hat{\tau}_j^x \rangle,$$

2921 which are written to file X_scal;

$$\langle \hat{\sigma}_{\langle i,i+a_x \rangle}^z \hat{\sigma}_{\langle i+a_x, i+a_x+a_y \rangle}^z \hat{\sigma}_{\langle i+a_x+a_y, i+a_y \rangle}^z \hat{\sigma}_{\langle i+a_y, i \rangle}^z \rangle,$$

2922 and

$$\langle \hat{\mu}_{\langle i, i+a_x \rangle}^z \hat{\mu}_{\langle i+a_x, i+a_x+a_y \rangle}^z \hat{\mu}_{\langle i+a_x+a_y, i+a_y \rangle}^z \hat{\mu}_{\langle i+a_y, i \rangle}^z \rangle,$$

2923 written to file Flux_scal; and also $\langle \hat{Q}_i \rangle$ (file Q_scal). Note that the flux over a plaquette of
 2924 the $\hat{\mu}_{\langle i,j \rangle}^z$ is equal to unity by construction so that this observable provides a sanity check. The
 2925 file Q_eq contains the two-point correlation $\langle \hat{Q}_i \hat{Q}_j \rangle - \langle \hat{Q}_i \rangle \langle \hat{Q}_j \rangle$ and Greenf_eq the equal-time
 2926 fermion Green function $\langle \hat{\tau}_i^z \hat{\psi}_{i,\sigma}^\dagger \hat{\tau}_j^z \hat{\psi}_{j,\sigma} \rangle$.

2927 **9.5.3 A test case: Z_2 slave spin formulation of the SU(2) Hubbard model**

2928 In this subsection, we demonstrate that the code can be used to simulate the attractive Hubbard
 2929 model in the Z_2 -slave spin formulation [151]:

$$\hat{H} = -t \sum_{\langle i,j \rangle, \sigma} \hat{c}_{i,\sigma}^\dagger \hat{c}_{j,\sigma} - U \sum_i (\hat{n}_{i,\uparrow} - 1/2)(\hat{n}_{i,\downarrow} - 1/2). \quad (241)$$

2930 In the Z_2 slave spin representation, the physical fermion, $\hat{c}_{i,\sigma}$, is fractionalized into an Ising
 2931 spin carrying Z_2 charge and a fermion, $\hat{\Psi}_{i,\sigma}$, carrying Z_2 and global $U(1)$ charge:

$$\hat{c}_{i,\sigma}^\dagger = \hat{\tau}_i^z \hat{\Psi}_{i,\sigma}^\dagger. \quad (242)$$

2932 To ensure that we remain in the correct Hilbert space, the constraint:

$$\hat{\tau}_i^x - (-1)^{\sum_\sigma \hat{\Psi}_{i,\sigma}^\dagger \hat{\Psi}_{i,\sigma}} = 0, \quad (243)$$

2933 has to be imposed locally. Since $(\hat{\tau}_i^x)^2 = 1$, the latter is equivalent to

$$\hat{Q}_i = \hat{\tau}_i^x (-1)^{\sum_\sigma \hat{\Psi}_{i,\sigma}^\dagger \hat{\Psi}_{i,\sigma}} = 1. \quad (244)$$

2934 Using

$$(-1)^{\sum_\sigma \hat{\Psi}_{i,\sigma}^\dagger \hat{\Psi}_{i,\sigma}} = \prod_\sigma (1 - 2\hat{\Psi}_{i,\sigma}^\dagger \hat{\Psi}_{i,\sigma}) = 4 \prod_\sigma (\hat{c}_{i,\sigma}^\dagger \hat{c}_{i,\sigma} - 1/2), \quad (245)$$

2935 the Z_2 slave spin representation of the Hubbard model now reads:

$$\hat{H}_{Z_2} = -t \sum_{\langle i,j \rangle, \sigma} \hat{\tau}_i^z \hat{\tau}_j^z \hat{\Psi}_{i,\sigma}^\dagger \hat{\Psi}_{j,\sigma} - \frac{U}{4} \sum_i \hat{\tau}_i^x. \quad (246)$$

2936 Importantly, the constraint commutes with Hamiltonian:

$$[\hat{H}_{Z_2}, \hat{Q}_i] = 0. \quad (247)$$

2937 Hence one can foresee that the constraint will be dynamically imposed (we expect a finite-
 2938 temperature Ising phase transition below which \hat{Q}_i orders) and that at $T = 0$ on a finite lattice
 2939 both models should give the same results.

2940 A test run for the 8×8 lattice at $U/t = 4$ and $\beta t = 40$ gives:

k	$\langle n_k \rangle_H$	$\langle n_k \rangle_{H_{Z_2}}$
(0, 0)	$1.93348548 \pm 0.00011322$	$1.93333895 \pm 0.00010405$
$(\pi/4, \pi/4)$	$1.90120688 \pm 0.00014854$	$1.90203726 \pm 0.00017943$
$(\pi/2, \pi/2)$	$0.99942957 \pm 0.00091377$	$1.00000000 \pm 0.00000000$
$(3\pi/4, 3\pi/4)$	$0.09905425 \pm 0.00015940$	$0.09796274 \pm 0.00017943$
(π, π)	$0.06651452 \pm 0.00011321$	$0.06666105 \pm 0.00010405$

2941 Here a Trotter time step of $\Delta \tau t = 0.05$ was used in order to minimize the systematic error
 2942 which should be different between the two codes. The Hamiltonian is invariant under a par-
 2943 tial particle-hole transformation (see Ref. [21]). Since \hat{Q}_i is odd under this transformation,
 2944 $\langle \hat{Q}_i \rangle = 0$. To asses whether the constraint is well imposed, the code, for this special case,
 2945 computes the correlation function:

$$S_Q(\mathbf{q}) = \sum_i \langle \hat{Q}_i \hat{Q}_0 \rangle. \quad (248)$$

2946 For the above run we obtain $S_Q(\mathbf{q} = \mathbf{0}) = 63.4 \pm 1.7$ which, for this 8×8 lattice, complies with
 2947 a ferromagnetic ordering of the Ising \hat{Q}_i variables. The pyALF python script that produces this
 2948 data can be found in [Z2_Matter.py](#). This code was used in Refs. [28, 29].

2950 10 Maximum entropy

2951 If we want to compare the data we obtain from Monte Carlo simulations with experiments,
 2952 we must extract spectral information from the imaginary-time output. This can be achieved
 2953 through the maximum entropy method (MaxEnt), which generically computes the image $A(\omega)$
 2954 for a given data set $g(\tau)$ and kernel $K(\tau, \omega)$:

$$g(\tau) = \int_{\omega_{\text{start}}}^{\omega_{\text{end}}} d\omega K(\tau, \omega) A(\omega). \quad (249)$$

2955 The ALF package includes a standard implementation of the stochastic MaxEnt, as
 2956 formulated in the article of K. Beach [97], in the module Libraries/Modules/
 2957 maxent_stoch_mod.F90. Its wrapper is found in Analysis/Max_SAC.F90 and the Green
 2958 function is read from the output of the cov_tau.F90 analysis program.

2959 In the next section we provide a quick guide on how this facility can be used, followed by
 2960 sections with more detailed information.

2961 10.1 Quick start

- 2962 • Before running the simulation, set in the file parameters the variable Ltau=1, so that
 2963 the necessary time-displaced Green functions are calculated; also set a large enough
 2964 number of bins
- 2965 • Also in the parameters file, set N_Cov=0 (for shorter runs; N_Cov=1 might give more
 2966 reliable error estimates)
- 2967 • Run the Monte Carlo simulation and the analysis:
 \$ALF_DIR/Prog/ALF.out
 \$ALF_DIR/Analysis/ana.out *
- 2968 • Then enter the desired results directory, e.g., Green_0.00_0.00 (they're named in the
 2969 pattern Variable_name_kx_ky) and copy the parameter file to it:
 cd Green_0.00_0.00/ && cp ../parameters .
- 2970 • Run MaxEnt:
 \$ALF_DIR/Analysis/Max_SAC.out

2971 For many purposes it is practical to script some of the steps above, and an example of such
 2972 a script can be found in \$ALF_DIR/Scripts_and_Parameters_files/Spectral.sh.

2973 10.2 General setup

2974 The stochastic MaxEnt is essentially a parallel-tempering Monte Carlo simulation. For a dis-
 2975 crete set of τ_i points, $i \in 1 \cdots n$, the goodness-of-fit functional, which we take as the energy
 2976 reads

$$\chi^2(A) = \sum_{i,j=1}^n \left[g(\tau_i) - \overline{g(\tau_i)} \right] C^{-1}(\tau_i, \tau_j) \left[g(\tau_j) - \overline{g(\tau_j)} \right], \quad (250)$$

2977 with $\overline{g(\tau_i)} = \int d\omega K(\tau_i, \omega) A(\omega)$ and C the covariance matrix. The set of N_α inverse tempera-
 2978 tures considered in the parallel tempering is given by $\alpha_m = \alpha_{st} R^m$, for $m = 1 \cdots N_\alpha$ and a con-
 2979 stant R . The phase space corresponds to all possible spectral functions satisfying a given sum
 2980 rule and the required positivity. Finally, the partition function reads $Z = \int \mathcal{D}A e^{-\alpha \chi^2(A)}$ [97],
 2981 such that for a given “inverse temperature” α , the image is given by:

$$\langle A(\omega) \rangle = \frac{\int \mathcal{D}A e^{-\alpha \chi^2(A)} A(\omega)}{\int \mathcal{D}A e^{-\alpha \chi^2(A)}}. \quad (251)$$

2986 In the code, the spectral function is parametrized by a set of N_γ Dirac δ functions:

$$A(\omega) = \sum_{i=1}^{N_\gamma} a_i \delta(\omega - \omega_i). \quad (252)$$

2987 To produce a histogram of $A(\omega)$ we divide the frequency range in `Ndis` intervals.

2988 Besides the parameters included in the namelist `VAR_Max_Stoch` set in the file
 2989 `parameters` (see Sec. 5.7), also the variable `N_cov`, from the namelist `VAR_errors`, is re-
 2990 quired to run the maxent code. Recalling: `N_cov = 1` (`N_cov = 0`) sets that the covariance
 2991 will (will not) be taken into account.

2992 Input files

2993 In addition to the aforementioned parameter file, the MaxEnt program requires the output of
 2994 the analysis of the time-displaced functions. The program `Anaylsis/ana.out` (see Sec. 6.3)
 2995 generates, for each k -point, a directory named `Variable_name_kx_ky`. In this directory the
 2996 file `g_kx_ky` contains the required information for the MaxEnt code, which is formatted as
 2997 follows:

```
2998 <# of tau-points> <# of bins > <beta> <Norb> <Channel>
2999 do tau = 1, # of tau-points
3000    $\tau$ ,  $\sum_\alpha \langle S_{\alpha,\alpha}^{(\text{corr})}(k, \tau) \rangle$ , error
3001 enddo
3002 do tau1 = 1, # of tau-points
3003   do tau2 = 1, # of tau-points
3004      $C(\tau_1, \tau_2)$ 
3005   enddo
3006 enddo
```

3007 Output files

3008 The code produces the following output files:

- 3009 • The files `Aom_n` contains the average spectral function at inverse temperature α_n . This
 3010 corresponds to $\langle A_n(\omega) \rangle = \frac{1}{Z} \int D\Omega(\omega) e^{-\alpha_n \chi^2(A)} A(\omega)$. The file contains three columns: ω ,
 3011 $\langle A_n(\omega) \rangle$, and $\Delta \langle A_n(\omega) \rangle$.
- 3012 • The files `Aom_ps_n` contain the average image over the inverse temperatures α_n to α_{N_γ} ,
 3013 see Ref. [97] for more details. Its first three columns have the same meaning as for the
 3014 files `Aom_n`.
- 3015 • The file `Green` contains the Green function, obtained from the spectral function through

$$G(\omega) = -\frac{1}{\pi} \int d\Omega \frac{A(\Omega)}{\omega - \Omega + i\delta}, \quad (253)$$

3016 where $\delta = \Delta\omega = (\omega_{\text{end}} - \omega_{\text{start}})/\text{Ndis}$ and the image corresponds to that of the file
 3017 `Aom_ps_n` with $n = N_\alpha - 10$. The first column of the Green file is a place holder for
 3018 post-processing. The last three columns correspond to $\omega, \text{Re } G(\omega), -\text{Im } G(\omega)/\pi$.

- 3019 • One of the most important output files is `energies`, which lists $\alpha_n, \langle \chi^2 \rangle, \Delta \langle \chi^2 \rangle$.
- 3020 • `best_fit` gives the values of a_i and ω_i (recall that $A(\omega) = \sum_{i=1}^{N_\gamma} a_i \delta(\omega - \omega_i)$) corre-
 3021 sponding to the last configuration of the lowest temperature run.

- The file `data_out` facilitates crosschecking. It lists τ , $g(\tau)$, $\Delta g(\tau)$, and $\int d\omega K(\tau, \omega)A(\omega)$, where the image corresponds to the best fit (i.e. the lowest temperature). This data should give an indication of how good the fit actually is. Note that `data_out` contains only the data points that have passed the tolerance test.
- Two dump files are also generated, `dump_conf` and `dump_Aom`. Since the MaxEnt is a Monte Carlo code, it is possible to improve the data by continuing a previous simulation. The data in the dump files allow you to do so. These files are only generated if the variable `checkpoint` is set to `.true.`.

The essential question is: Which image should one use? There is no ultimate answer to this question in the context of the stochastic MaxEnt. The only rule of thumb is to consider temperatures for which the χ^2 is comparable to the number of data points.

10.3 Single-particle quantities: Channel=P

For the single-particle Green function,

$$\langle \hat{c}_k(\tau) \hat{c}_k^\dagger(0) \rangle = \int d\omega K_p(\tau, \omega) A_p(k, \omega), \quad (254)$$

with

$$K_p(\tau, \omega) = \frac{1}{\pi} \frac{e^{-\tau\omega}}{1 + e^{-\beta\omega}}, \quad (255)$$

and, in the Lehmann representation,

$$A_p(k, \omega) = \frac{\pi}{Z} \sum_{n,m} e^{-\beta E_n} (1 + e^{-\beta\omega}) |\langle n | c_n | m \rangle|^2 \delta(E_m - E_n - \omega). \quad (256)$$

Here $(\hat{H} - \mu \hat{N})|n\rangle = E_n|n\rangle$. Note that $A_p(k, \omega) = -\text{Im } G^{\text{ret}}(k, \omega)$, with

$$G^{\text{ret}}(k, \omega) = -i \int dt \Theta(t) e^{i\omega t} \langle \{\hat{c}_k(t), \hat{c}_k^\dagger(0)\} \rangle. \quad (257)$$

Finally the sum rule reads

$$\int d\omega A_p(k, \omega) = \pi \langle \{\hat{c}_k, \hat{c}_k^\dagger\} \rangle = \pi (\langle \hat{c}_k(\tau=0) \hat{c}_k^\dagger(0) \rangle + \langle \hat{c}_k(\tau=\beta) \hat{c}_k^\dagger(0) \rangle). \quad (258)$$

Using the `Max_Sac.F90` with `Channel="P"` will load the above kernel in the MaxEnt library. In this case the back transformation is set to unity. Note that for each configuration of fields we have $\langle \langle \hat{c}_k(\tau=0) \hat{c}_k^\dagger(0) \rangle \rangle_C + \langle \langle \hat{c}_k(\tau=\beta) \hat{c}_k^\dagger(0) \rangle \rangle_C = \langle \langle \{\hat{c}_k, \hat{c}_k^\dagger\} \rangle \rangle_C = 1$, hence, if both the $\tau=0$ and $\tau=\beta$ data points are included, the covariance matrix will have a zero eigenvalue and the χ^2 measure is not defined. Therefore, for the particle channel the program omits the $\tau=\beta$ data point. There are special particle-hole symmetric cases where the $\tau=0$ data point shows no fluctuations – in such cases the code omits the $\tau=0$ data point as well.

10.4 Particle-hole quantities: Channel=PH

Imaginary-time formulation

For particle-hole quantities such as spin-spin or charge-charge correlations, the kernel reads

$$\langle \hat{S}(q, \tau) \hat{S}(-q, 0) \rangle = \frac{1}{\pi} \int d\omega \frac{e^{-\tau\omega}}{1 - e^{-\beta\omega}} \chi''(q, \omega). \quad (259)$$

3049 This follows directly from the Lehmann representation

$$\chi''(q, \omega) = \frac{\pi}{Z} \sum_{n,m} e^{-\beta E_n} |\langle n | \hat{S}(q) | m \rangle|^2 \delta(\omega + E_n - E_m) (1 - e^{-\beta \omega}). \quad (260)$$

3050 Since the linear response to a Hermitian perturbation is real, $\chi''(q, \omega) = -\chi''(-q, -\omega)$ and
 3051 hence $\langle \hat{S}(q, \tau) \hat{S}(-q, 0) \rangle$ is a symmetric function around $\beta = \tau/2$ for systems with inversion
 3052 symmetry – the ones we consider here. When Channel=PH the analysis program ana.out
 3053 uses this symmetry to provide an improved estimator.

3054 The stochastic MaxEnt requires a sum rule, and hence the kernel and image have to be
 3055 adequately redefined. Let us consider $\coth(\beta \omega/2) \chi''(q, \omega)$. For this quantity, we have the
 3056 sum rule, since

$$\int d\omega \coth(\beta \omega/2) \chi''(q, \omega) = 2\pi \langle \hat{S}(q, \tau=0) \hat{S}(-q, 0) \rangle, \quad (261)$$

3057 which is just the first point in the data. Therefore,

$$\langle \hat{S}(q, \tau) \hat{S}(-q, 0) \rangle = \int d\omega \underbrace{\frac{1}{\pi} \frac{e^{-\tau \omega}}{1 - e^{-\beta \omega}}}_{K_{pp}(\tau, \omega)} \underbrace{\tanh(\beta \omega/2) \coth(\beta \omega/2) \chi''(q, \omega)}_{A(\omega)}, \quad (262)$$

3058 and one computes $A(\omega)$. Note that since χ'' is an odd function of ω one restricts the integration
 3059 range to positive values of ω . Hence:

$$\langle \hat{S}(q, \tau) \hat{S}(-q, 0) \rangle = \int_0^\infty d\omega \underbrace{(K(\tau, \omega) + K(\tau, -\omega))}_{K_{ph}(\tau, \omega)} A(\omega). \quad (263)$$

3060 In the code, ω_{start} is set to zero by default and the kernel K_{ph} is defined in the routine XKER_ph.

3061 In general, one would like to produce the dynamical structure factor that gives the susceptibility according to

$$S(q, \omega) = \chi''(q, \omega) / (1 - e^{-\beta \omega}). \quad (264)$$

3063 In the code, the routine BACK_TRANS_ph transforms the image A to the desired quantity:

$$S(q, \omega) = \frac{A(\omega)}{1 + e^{-\beta \omega}}. \quad (265)$$

3064 Matsubara-frequency formulation

3065 The ALF library uses imaginary time. It is, however, possible to formulate the MaxEnt in
 3066 Matsubara frequencies. Consider:

$$\chi(q, i\Omega_m) = \int_0^\beta d\tau e^{i\Omega_m \tau} \langle \hat{S}(q, \tau) \hat{S}(-q, 0) \rangle = \frac{1}{\pi} \int d\omega \frac{\chi''(q, \omega)}{\omega - i\Omega_m}. \quad (266)$$

3067 Using the fact that $\chi''(q, \omega) = -\chi''(-q, -\omega) = -\chi''(q, -\omega)$ one obtains

$$\begin{aligned} \chi(q, i\Omega_m) &= \frac{1}{\pi} \int_0^\infty d\omega \left(\frac{1}{\omega - i\Omega_m} - \frac{1}{-\omega - i\Omega_m} \right) \chi''(q, \omega) \\ &= \frac{2}{\pi} \int_0^\infty d\omega \frac{\omega^2}{\omega^2 + \Omega_m^2} \frac{\chi''(q, \omega)}{\omega} \\ &\equiv \int_0^\infty d\omega K(\omega, i\Omega_m) A(q, \omega), \end{aligned} \quad (267)$$

3068 with

$$K(\omega, i\Omega_m) = \frac{\omega^2}{\omega^2 + \Omega_m^2}, \quad \text{and} \quad A(q, \omega) = \frac{2}{\pi} \frac{\chi''(q, \omega)}{\omega}. \quad (268)$$

3069 The above definitions produce an image that satisfies the sum rule:

$$\int_0^\infty d\omega A(q, \omega) = \frac{1}{\pi} \int_{-\infty}^\infty d\omega \frac{\chi''(q, \omega)}{\omega} \equiv \chi(q, i\Omega_m = 0). \quad (269)$$

3070 10.5 Particle-particle quantities: Channel=PP

3071 Similarly to the particle-hole channel, the particle-particle channel is also a bosonic correlation
 3072 function. Here, however, we do not assume that the imaginary time data is symmetric
 3073 around the $\tau = \beta/2$ point. We use the kernel K_{pp} defined in Eq. (262) and consider the whole
 3074 frequency range. The back transformation yields

$$\frac{\chi''(\omega)}{\omega} = \frac{\tanh(\beta\omega/2)}{\omega} A(\omega). \quad (270)$$

3075 10.6 Zero-temperature, projective code: Channel=T0

3076 In the zero temperature limit, the spectral function associated to an operator \hat{O} reads:

$$A_o(\omega) = \pi \sum_n |\langle n | \hat{O} | 0 \rangle|^2 \delta(E_n - E_0 - \omega), \quad (271)$$

3077 such that

$$\langle 0 | \hat{O}^\dagger(\tau) \hat{O}(0) | 0 \rangle = \int d\omega K_0(\tau, \omega) A_o(\omega), \quad (272)$$

3078 with

$$K_0(\tau, \omega) = \frac{1}{\pi} e^{-\tau\omega}. \quad (273)$$

3079 The zeroth moment of the spectral function reads

$$\int d\omega A_o(\omega) = \pi \langle 0 | \hat{O}^\dagger(0) \hat{O}(0) | 0 \rangle, \quad (274)$$

3080 and hence corresponds to the first data point.

3081 In the zero-temperature limit one does not distinguish between particle, particle-hole, or
 3082 particle-particle channels. Using the `Max_Sac.F90` with `Channel="T0"` loads the above ker-
 3083 nel in the MaxEnt library. In this case the back transformation is set to unity. The code will
 3084 also cut-off the tail of the imaginary time correlation function if the relative error is greater
 3085 than the variable `Tolerance`.

3086 10.7 Dynamics of the one-dimensional half-filled Hubbard model

3087 To conclude this section, we show the example of the one-dimensional Hubbard model, which
 3088 is known to show spin-charge separation (see Ref. [152] and references therein). The data of
 3089 Fig. 10 was produced with the pyALF python script `Hubbard_1D.py`, and the spectral function
 3090 plots with the bash script `Spectral.sh`.

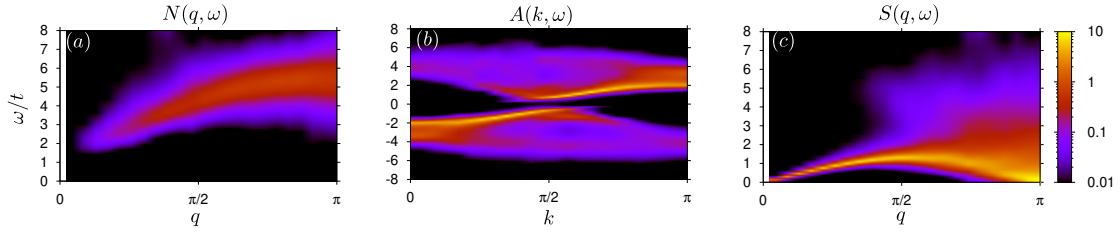


Figure 10: Dynamics of the one-dimensional half-filled Hubbard model on a 46-site chain, with $U/t=4$ and $\beta t = 10$. (a) Dynamical charge structure factor, (b) single particle spectral function and (c) dynamical spin structure factor. Data obtained using the pyALF python script [Hubbard_1D.py](#), considering 400 bins of 200 sweeps each and taking into account the covariance matrix for the MaxEnt. The parameters for the MaxEnt that differ from the default values are also listed in the python script.

3091 11 Conclusions and future directions

3092 In its present form, the auxiliary-field QMC code of the ALF project allows us to simulate
 3093 a large class of non-trivial models, both efficiently and at minimal programming cost. The
 3094 package contains many advanced functionalities, including a projective formulation, various
 3095 updating schemes, better control of Trotter errors, predefined structures that facilitate reuse,
 3096 a large class of models, continuous fields and, finally, stochastic analytical continuation code.
 3097 Also the usability of the code has been continuously improved. In particular the [pyALF](#) project
 3098 provides a Python interface to the ALF which substantially facilitates running the code for
 3099 established models. This ease of use renders ALF a powerful tool to for benchmarking new
 3100 algorithms.

3101 There are further capabilities that we would like to see in future versions of ALF. Introducing
 3102 time-dependent Hamiltonians, for instance, will require some rethinking, but will allow,
 3103 for example, to access entanglement properties of interacting fermionic systems [61–63].
 3104 Moreover, the auxiliary field approach is not the only method to simulate fermionic systems.
 3105 It would be desirable to include additional lattice fermion algorithms such as the CT-INT
 3106 [89, 153]. Lastly, increased compatibility with other software projects is certainly an improve-
 3107 ment to look forward to, and one priority is making ALF be able to read in external Hamilto-
 3108 nians.

3109 Acknowledgments

3110 We are very grateful to B. Danu, S. Beyl, M. Hohenadler, M. Raczkowski, T. Sato, M. Ulybyshev,
 3111 Z. Wang, and M. Weber for their constant support during the development of this project.
 3112 We equally thank G. Hager, M. Wittmann, and G. Wellein for useful discussions and overall
 3113 support. And we extend our special thanks to the user community for its valuable feedback.
 3114 FFA would also like to thank T. Lang and Z. Y. Meng for developments of the auxiliary field
 3115 code as well as to T. Grover. Part of the optimization of the code was carried out during the
 3116 Porting and Tuning Workshop 2016 offered by the Forschungszentrum Jülich. Calculations
 3117 performed to extensively test this package were carried out both on SuperMUC-NG at the
 3118 Leibniz Supercomputing Centre and on JURECA [154] at the Jülich Supercomputing Centre.
 3119 We thank both institutions for the generous allocation of computing time.

3120 **Funding information** MB, FFA and FG thank the Bavarian Competence Network for Tech-
3121 nical and Scientific High Performance Computing (KONWIHR) for financial support. FG, JH,
3122 and JS thank the SFB-1170 for financial support under projects Z03 and C01. F.P.T is funded
3123 by the Deutsche Forschungsgemeinschaft (DFG, German Research Foundation) – project num-
3124 ber 414456783. JSEP thanks the DFG for financial support under the project AS120/14-1,
3125 dedicated to the further development of the ALF library.

3126 A Practical implementation of Wick decomposition of $2n$ -point 3127 correlation functions of two imaginary times

3128 In this Appendix we briefly outline how to compute $2n$ point correlation functions of the form:

$$\lim_{\epsilon \rightarrow 0} \sum_{\sigma_1, \sigma'_1, \dots, \sigma_n, \sigma'_n, s_1, s'_1 \dots s_n, s'_n} f(\sigma_1, \sigma'_1, \dots, \sigma_n, \sigma'_n, s_1, s'_1 \dots s_n, s'_n) \\ \langle \langle \mathcal{T} \left(\hat{c}_{x_1, \sigma_1, s_1}^\dagger(\tau_{1,\epsilon}) \hat{c}_{x'_1, \sigma'_1, s'_1}(\tau'_{1,\epsilon}) - a_1 \right) \cdots \left(\hat{c}_{x_n, \sigma_n, s_n}^\dagger(\tau_{n,\epsilon}) \hat{c}_{x'_n, \sigma'_n, s'_n}(\tau'_{n,\epsilon}) - a_n \right) \rangle \rangle_C . \quad (\text{A.1})$$

3129 Here, σ is a color index and s a flavor index such that

$$\langle \langle \mathcal{T} \hat{c}_{x, \sigma, s}^\dagger(\tau) \hat{c}_{x', \sigma', s'}(\tau') \rangle \rangle_C = \langle \langle \mathcal{T} \hat{c}_{x, \sigma, s}^\dagger(\tau) \hat{c}_{x', \sigma', s'}(\tau') \rangle \rangle_C \delta_{s, s'} \delta_{\sigma, \sigma'} . \quad (\text{A.2})$$

3130 That is, the single-particle Green function is diagonal in the flavor index and color independent.
3131 To define the time ordering we will assume that all times differ but that $\lim_{\epsilon \rightarrow 0} \tau_{n,\epsilon}$ as well as
3132 $\lim_{\epsilon \rightarrow 0} \tau'_{n,\epsilon}$ take the values 0 or τ . Let

$$G_s(I, J) = \lim_{\epsilon \rightarrow 0} \langle \langle \mathcal{T} c_{x_I, s}^\dagger(\tau_{I,\epsilon}) c_{x_J, s}(\tau'_{J,\epsilon}) \rangle \rangle_C . \quad (\text{A.3})$$

3133 The $G_s(I, J)$ are uniquely defined by the time-displaced correlation functions that enter the
3134 ObserT routine in the Hamiltonian files. They are defined in Eq. (141) and read:

$$\begin{aligned} \text{GT0}(x, y, s) &= \langle \langle \hat{c}_{x,s}(\tau) \hat{c}_{y,s}^\dagger(0) \rangle \rangle_C = \langle \langle \mathcal{T} \hat{c}_{x,s}(\tau) \hat{c}_{y,s}^\dagger(0) \rangle \rangle_C , \\ \text{GOT}(x, y, s) &= -\langle \langle \hat{c}_{y,s}^\dagger(\tau) \hat{c}_{x,s}(0) \rangle \rangle_C = \langle \langle \mathcal{T} \hat{c}_{x,s}(0) \hat{c}_{y,s}^\dagger(\tau) \rangle \rangle_C , \\ \text{G00}(x, y, s) &= \langle \langle \hat{c}_{x,s}(0) \hat{c}_{y,s}^\dagger(0) \rangle \rangle_C , \\ \text{GTT}(x, y, s) &= \langle \langle \hat{c}_{x,s}(\tau) \hat{c}_{y,s}^\dagger(\tau) \rangle \rangle_C . \end{aligned} \quad (\text{A.4})$$

3135 For instance, let $\tau_{I,\epsilon} > \tau'_{J,\epsilon}$ and $\lim_{\epsilon \rightarrow 0} \tau_{I,\epsilon} = \lim_{\epsilon \rightarrow 0} \tau'_{J,\epsilon} = \tau$. Then

$$G_s(I, J) = \langle \langle c_{x_I, s}^\dagger(\tau) c_{x_J, s}(\tau) \rangle \rangle_C = \delta_{x_I, x_J} - \text{GTT}(x_J, x_I, s) . \quad (\text{A.5})$$

3136 Using the formulation of Wick's theorem of Eq. (23), Eq. (A.1) reads:

$$\sum_{\sigma_1, \sigma'_1, \dots, \sigma_n, \sigma'_n, s_1, s'_1 \dots s_n, s'_n} f(\sigma_1, \sigma'_1, \dots, \sigma_n, \sigma'_n, s_1, s'_1 \dots s_n, s'_n) \\ \det \begin{bmatrix} G_{s_1}(1, 1) \delta_{s_1, s'_1} \delta_{\sigma_1, \sigma'_1} - a_1 & G_{s_1}(1, 2) \delta_{s_1, s'_2} \delta_{\sigma_1, \sigma'_2} & \dots & G_{s_1}(1, n) \delta_{s_1, s'_n} \delta_{\sigma_1, \sigma'_n} \\ G_{s_2}(2, 1) \delta_{s_2, s'_1} \delta_{\sigma_2, \sigma'_1} & G_{s_2}(2, 2) \delta_{s_2, s'_2} \delta_{\sigma_2, \sigma'_2} - a_2 & \dots & G_{s_2}(2, n) \delta_{s_2, s'_n} \delta_{\sigma_2, \sigma'_n} \\ \vdots & \vdots & \ddots & \vdots \\ G_{s_n}(n, 1) \delta_{s_n, s'_1} \delta_{\sigma_n, \sigma'_1} & G_{s_n}(n, 2) \delta_{s_n, s'_2} \delta_{\sigma_n, \sigma'_2} & \dots & G_{s_n}(n, n) \delta_{s_n, s'_n} \delta_{\sigma_n, \sigma'_n} - a_n \end{bmatrix} . \quad (\text{A.6})$$

3137 The symbolic evaluation of the determinant as well as the sum over the color and flavor indices
3138 can be carried out with Mathematica. This produces a long expression in terms of the functions
3139 $G(I, J, s)$ that can then be included in the code. The Mathematica notebooks that we use can
3140 be found in the directory `Mathematica` of the ALF directory. As an open source alternative to
3141 Mathematica, the user can consider the Sympy Python library.

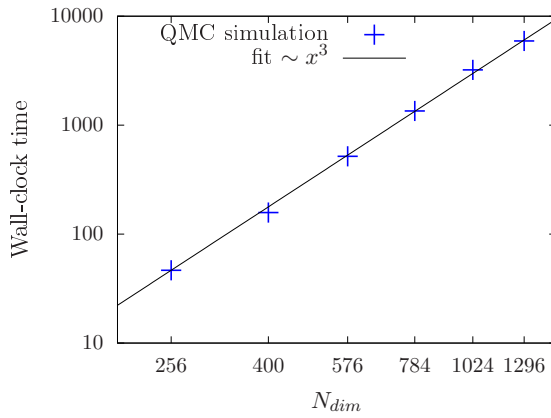


Figure 11: Volume scaling behavior of the auxiliary field QMC code of the ALF project on SuperMUC (phase 2/Haswell nodes) at the LRZ in Munich. The number of sites N_{dim} corresponds to the system volume. The plot confirms that the leading scaling order is due to matrix multiplications such that the runtime is dominated by calls to ZGEMM.

3142 B Performance, memory requirements and parallelization

3143 As mentioned in the introduction, the auxiliary field QMC algorithm scales linearly in inverse
 3144 temperature β and as a cube in the volume N_{dim} . Using fast updates, a single spin flip requires
 3145 $(N_{\text{dim}})^2$ operations to update the Green function upon acceptance. As there are $L_{\text{Trotter}} \times N_{\text{dim}}$
 3146 spins to be visited, the total computational cost for one sweep is of the order of $\beta(N_{\text{dim}})^3$. This
 3147 operation alongside QR-decompositions required for stabilization dominates the performance,
 3148 see Fig. 11. A profiling analysis of our code shows that 80-90% of the CPU time is spent in
 3149 ZGEMM calls of the BLAS library provided in the MKL package by Intel. Consequently, the
 3150 single-core performance is next to optimal.

3151 For the implementation which scales linearly in β , one has to store $2 \times N_{\text{fl}} \times L_{\text{Trotter}} / \text{NWarp}$
 3152 intermediate propagation matrices of dimension $N_{\text{dim}} \times N_{\text{dim}}$. Hence the memory cost scales
 3153 as βN_{dim}^2 and for large lattices and/or low temperatures this dominates the total memory
 3154 requirements that can exceed 2 GB memory for a sequential version.

3155 The above estimates of βN_{dim}^3 for CPU time and βN_{dim}^2 for memory implicitly assume Hamiltonians where the interaction is a sum of local terms. Recently Landau level projection schemes
 3156 for the regularization of continuum field theories have been introduced in the realm of the
 3157 auxiliary field QMC algorithm [70, 71]. In this case the interaction is not local, such that the
 3158 matrices stored in the `Op_V` array of `Observable` type are of dimension of N_{dim} . Since the
 3159 dimension of the `Op_V` array scales as N_{dim} , the memory requirement scales as N_{dim}^3 . In these
 3160 algorithms, a single field couples to a $N_{\text{dim}} \times N_{\text{dim}}$ matrix, such that updating it scales as N_{dim}^3 .
 3161 Furthermore, and as mentioned in Sec. 2.3, for non-local Hamiltonians the Trotter time step
 3162 has to be scaled as $1/N_{\text{dim}}$ so as to maintain a constant systematic error. Taking all of this
 3163 into account, yields a CPU time that scales as βN_{dim}^5 . Hence this approach is expensive both
 3164 in memory and CPU time.

3166 At the heart of Monte Carlo schemes lies a random walk through the given configuration
 3167 space. This is easily parallelized via MPI by associating one random walker to each MPI task.
 3168 For each task, we start from a random configuration and have to invest the autocorrelation
 3169 time T_{auto} to produce an equilibrated configuration. Additionally we can also profit from an
 3170 OpenMP parallelized version of the BLAS/LAPACK library for an additional speedup, which
 3171 also effects equilibration overhead $N_{\text{MPI}} \times T_{\text{auto}} / N_{\text{OMP}}$, where N_{MPI} is the number of cores and

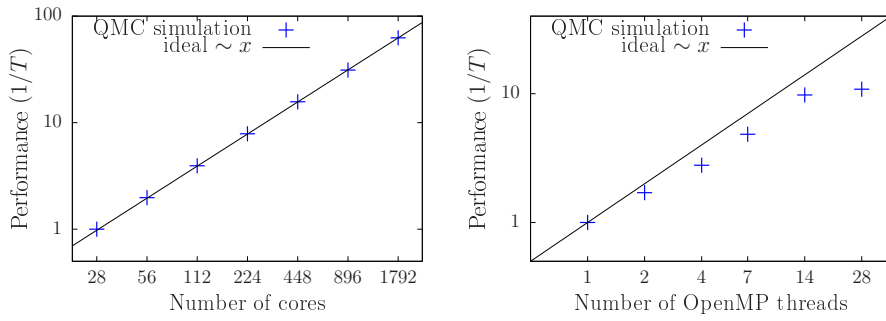


Figure 12: MPI (left) and OpenMP (right) scaling behavior of the auxiliary field QMC code of the ALF project on SuperMUC (phase 2/Haswell nodes) at the LRZ in Munich. The MPI performance data was normalized to 28 cores and was obtained using a problem size of $N_{\text{dim}} = 400$. This is a medium to small system size that is the least favorable in terms of MPI synchronization effects. The OpenMP performance data was obtained using a problem size of $N_{\text{dim}} = 1296$. Employing 2 and 4 OpenMP threads introduces some synchronization/management overhead such that the per-core performance is slightly reduced, compared to the single thread efficiency. Further increasing the amount of threads to 7 and 14 keeps the efficiency constant. The drop in performance of the 28 thread configuration is due to the architecture as the threads are now spread over both sockets of the node. To obtain the above results, it was crucial to pin the processes in a fashion that keeps the OpenMP threads as compact as possible.

3172 N_{OMP} the number of OpenMP threads. For a given number of independent measurements
 3173 N_{meas} , we therefore need a wall-clock time given by

$$T = \frac{T_{\text{auto}}}{N_{\text{OMP}}} \left(1 + \frac{N_{\text{meas}}}{N_{\text{MPI}}} \right). \quad (\text{B.1})$$

3174 As we typically have $N_{\text{meas}}/N_{\text{MPI}} \gg 1$, the speedup is expected to be almost perfect, in accordance
 3175 with the performance test results for the auxiliary field QMC code on SuperMUC (see
 3176 Fig. 12 (left)).

3177 For many problem sizes, 2 GB memory per MPI task (random walker) suffices such that we
 3178 typically start as many MPI tasks as there are physical cores per node. Due to the large amount
 3179 of CPU time spent in MKL routines, we do not profit from the hyper-threading option. For large
 3180 systems, the memory requirement increases and this is tackled by increasing the amount of
 3181 OpenMP threads to decrease the stress on the memory system and to simultaneously reduce
 3182 the equilibration overhead (see Fig. 12 (right)). For the displayed speedup, it was crucial
 3183 to pin the MPI tasks as well as the OpenMP threads in a pattern which keeps the threads as
 3184 compact as possible to profit from a shared cache. This also explains the drop in efficiency
 3185 from 14 to 28 threads where the OpenMP threads are spread over both sockets.

3186 We store the field configurations of the random walker as checkpoints, such that a long
 3187 simulation can be easily split into several short simulations. This procedure allows us to take
 3188 advantage of chained jobs using the dependency chains provided by the batch system.

3189 C Licenses and copyrights

3190 The ALF code is provided as an open source software such that it is available to all and we hope
 3191 that it will be useful. If you benefit from this code we ask that you acknowledge the ALF collab-

3192 oration as mentioned on our website <https://alf.physik.uni-wuerzburg.de>. The git repository
3193 at <https://git.physik.uni-wuerzburg.de/ALF/ALF> gives us the tools to create a small but vi-
3194 brant community around the code and provides a suitable entry point for future contributors
3195 and future developments. The website is also the place where the original source files can be
3196 found. Its public release make it necessary to add copyright headers to our source code, which
3197 is licensed under a GPL license to keep the source as well as any future work in the community.
3198 And the Creative Commons licenses are a good way to share our documentation and it is also
3199 well accepted by publishers. Therefore this document is licensed to you under a CC-BY-SA
3200 license. This means you can share it and redistribute it as long as you cite the original source
3201 and license your changes under the same license. The details are in the file `license.CCBYSA`,
3202 which you should have received with this documentation. To express our desire for a proper
3203 attribution we decided to make this a visible part of the license. To that end we have exer-
3204 cised the rights of section 7 of GPL version 3 and have amended the license terms with an
3205 additional paragraph that expresses our wish that if an author has benefited from this code
3206 that he/she should consider giving back a citation as specified on alf.physik.uni-wuerzburg.de.
3207 This is not something that is meant to restrict your freedom of use, but something that we
3208 strongly expect to be good scientific conduct. The original GPL license can be found in the file
3209 `license.GPL` and the additional terms can be found in `license.additional`. In favour
3210 to our users, the ALF code contains part of the Lapack implementation version 3.6.1 from
3211 <http://www.netlib.org/lapack>. Lapack is licensed under the modified BSD license whose full
3212 text can be found in `license.BSD`.

3213 With that being said, we hope that the ALF code will prove to you to be a suitable and
3214 high-performance tool that enables you to perform quantum Monte Carlo studies of solid state
3215 models of unprecedented complexity.

3216

3217 The ALF project's contributors.

3218 COPYRIGHT

3219 Copyright © 2016-2022, The ALF Project.
3220 The ALF Project Documentation is licensed under a Creative Commons Attribution-ShareAlike
3221 4.0 International License. You are free to share and benefit from this documentation as long
3222 as this license is preserved and proper attribution to the authors is given. For details see the
3223 ALF project website alf.physik.uni-wuerzburg.de and the file `license.CCBYSA`.

3224 References

- 3225 [1] R. Blankenbecler, D. J. Scalapino and R. L. Sugar, *Monte Carlo calculations of coupled boson-fermion systems. I*, Phys. Rev. D **24**, 2278 (1981),
3226 doi:[10.1103/PhysRevD.24.2278](https://doi.org/10.1103/PhysRevD.24.2278).
- 3228 [2] S. R. White, D. J. Scalapino, R. L. Sugar, E. Y. Loh, J. E. Gubernatis and R. T. Scalettar,
3229 *Numerical study of the two-dimensional Hubbard model*, Phys. Rev. B **40**, 506 (1989),
3230 doi:[10.1103/PhysRevB.40.506](https://doi.org/10.1103/PhysRevB.40.506).
- 3231 [3] G. Sugiyama and S. E. Koonin, *Auxiliary field Monte-Carlo for quantum many-body*
3232 *ground states*, Ann. Phys. **168**, 1 (1986), doi:[10.1016/0003-4916\(86\)90107-7](https://doi.org/10.1016/0003-4916(86)90107-7).
- 3233 [4] S. Sorella, S. Baroni, R. Car and M. Parrinello, *A novel technique for the simula-*
3234 *tion of interacting fermion systems*, Europhys. Lett. **8**, 663 (1989), doi:[10.1209/0295-5075/8/7/014](https://doi.org/10.1209/0295-5075/8/7/014).

- 3236 [5] S. Duane, A. D. Kennedy, B. J. Pendleton and D. Roweth, *Hybrid Monte Carlo*, Phys. Lett.
3237 B **195**, 216 (1987), doi:[10.1016/0370-2693\(87\)91197-X](https://doi.org/10.1016/0370-2693(87)91197-X).
- 3238 [6] F. F. Assaad and H. G. Evertz, *World-line and determinantal quantum Monte Carlo meth-*
3239 *ods for spins, phonons and electrons*, in *Computational many-particle physics*, Springer,
3240 Berlin, Heidelberg, Germany, ISBN 9783540746850 (2008), doi:[10.1007/978-3-540-74686-7_10](https://doi.org/10.1007/978-3-540-74686-7_10).
- 3242 [7] D. J. Scalapino, *Numerical studies of the 2D Hubbard model*, in *Handbook of high-*
3243 *temperature superconductivity*, Springer, New York, USA, ISBN 9780387687346 (2007),
3244 doi:[10.1007/978-0-387-68734-6_13](https://doi.org/10.1007/978-0-387-68734-6_13).
- 3245 [8] J. P. F. LeBlanc et al., *Solutions of the two-dimensional Hubbard model: Benchmarks*
3246 *and results from a wide range of numerical algorithms*, Phys. Rev. X **5**, 041041 (2015),
3247 doi:[10.1103/PhysRevX.5.041041](https://doi.org/10.1103/PhysRevX.5.041041) [preprint doi:[10.48550/arXiv.1505.02290](https://arxiv.org/abs/1505.02290)].
- 3248 [9] M. Hohenadler, T. C. Lang and F. F. Assaad, *Correlation effects in quantum Spin-*
3249 *Hall insulators: A quantum Monte Carlo study*, Phys. Rev. Lett. **106**, 100403 (2011),
3250 doi:[10.1103/PhysRevLett.106.100403](https://doi.org/10.1103/PhysRevLett.106.100403) [preprint doi:[10.48550/arXiv.1011.5063](https://arxiv.org/abs/1011.5063)].
- 3251 [10] D. Zheng, G.-M. Zhang and C. Wu, *Particle-hole symmetry and interaction*
3252 *effects in the Kane-Mele-Hubbard model*, Phys. Rev. B **84**, 205121 (2011),
3253 doi:[10.1103/PhysRevB.84.205121](https://doi.org/10.1103/PhysRevB.84.205121) [preprint doi:[10.48550/arXiv.1011.5858](https://arxiv.org/abs/1011.5858)].
- 3254 [11] F. F. Assaad, M. Bercx and M. Hohenadler, *Topological invariant and quantum spin mod-*
3255 *els from magnetic π fluxes in correlated topological insulators*, Phys. Rev. X **3**, 011015
3256 (2013), doi:[10.1103/PhysRevX.3.011015](https://doi.org/10.1103/PhysRevX.3.011015) [preprint doi:[10.48550/arXiv.1204.4728](https://arxiv.org/abs/1204.4728)].
- 3257 [12] J. S. Hofmann, F. F. Assaad, R. Queiroz and E. Khalaf, *Search for correlation-induced*
3258 *adiabatic paths between distinct topological insulators*, Phys. Rev. Res. **2**, 023390 (2020),
3259 doi:[10.1103/PhysRevResearch.2.023390](https://doi.org/10.1103/PhysRevResearch.2.023390) [preprint doi:[10.48550/arXiv.1912.07614](https://arxiv.org/abs/1912.07614)].
- 3260 [13] F. F. Assaad and I. F. Herbut, *Pinning the order: The nature of quantum critical-*
3261 *ity in the Hubbard model on honeycomb lattice*, Phys. Rev. X **3**, 031010 (2013),
3262 doi:[10.1103/PhysRevX.3.031010](https://doi.org/10.1103/PhysRevX.3.031010) [preprint doi:[10.48550/arXiv.1304.6340](https://arxiv.org/abs/1304.6340)].
- 3263 [14] F. P. Toldin, M. Hohenadler, F. F. Assaad and I. F. Herbut, *Fermionic quantum critical-*
3264 *ity in honeycomb and π -flux Hubbard models: Finite-size scaling of renormalization-*
3265 *group-invariant observables from quantum Monte Carlo*, Phys. Rev. B **91**, 165108 (2015),
3266 doi:[10.1103/PhysRevB.91.165108](https://doi.org/10.1103/PhysRevB.91.165108) [preprint doi:[10.48550/arXiv.1411.2502](https://arxiv.org/abs/1411.2502)].
- 3267 [15] Y. Otsuka, S. Yunoki and S. Sorella, *Universal quantum criticality in the metal-insulator*
3268 *transition of two-dimensional interacting Dirac electrons*, Phys. Rev. X **6**, 011029 (2016),
3269 doi:[10.1103/PhysRevX.6.011029](https://doi.org/10.1103/PhysRevX.6.011029) [preprint doi:[10.48550/arXiv.1510.08593](https://arxiv.org/abs/1510.08593)].
- 3270 [16] S. Chandrasekharan and A. Li, *Quantum critical behavior in three di-*
3271 *mensional lattice Gross-Neveu models*, Phys. Rev. D **88**, 021701 (2013),
3272 doi:[10.1103/PhysRevD.88.021701](https://doi.org/10.1103/PhysRevD.88.021701) [preprint doi:[10.48550/arXiv.1304.7761](https://arxiv.org/abs/1304.7761)].
- 3273 [17] V. Ayyar and S. Chandrasekharan, *Massive fermions without fermion bilinear conden-*
3274 *sates*, Phys. Rev. D **91**, 065035 (2015), doi:[10.1103/PhysRevD.91.065035](https://doi.org/10.1103/PhysRevD.91.065035) [preprint
3275 doi:[10.48550/arXiv.1410.6474](https://arxiv.org/abs/1410.6474)].
- 3276 [18] Y. Liu, Z. Wang, T. Sato, M. Hohenadler, C. Wang, W. Guo and F. F. Assaad, *Superconduc-*
3277 *tivity from the condensation of topological defects in a quantum spin-Hall insulator*, Nat.
3278 Commun. **10**, 2658 (2019), doi:[10.1038/s41467-019-10372-0](https://doi.org/10.1038/s41467-019-10372-0).

- 3279 [19] Z.-X. Li, Y.-F. Jiang, S.-K. Jian and H. Yao, *Fermion-induced quantum critical points*, Nat.
3280 Commun. **8**, 314 (2017), doi:[10.1038/s41467-017-00167-6](https://doi.org/10.1038/s41467-017-00167-6).
- 3281 [20] M. Raczkowski, R. Peters, T. T. Phùng, N. Takemori, F. F. Assaad, A. Honecker and J.
3282 Vahedi, *Hubbard model on the honeycomb lattice: From static and dynamical mean-field*
3283 *theories to lattice quantum Monte Carlo simulations*, Phys. Rev. B **101**, 125103 (2020),
3284 doi:[10.1103/PhysRevB.101.125103](https://doi.org/10.1103/PhysRevB.101.125103) [preprint doi:[10.48550/arXiv.1908.04307](https://arxiv.org/abs/1908.04307)].
- 3285 [21] F. F. Assaad and T. Grover, *Simple fermionic model of deconfined phases and phase tran-*
3286 *sitions*, Phys. Rev. X **6**, 041049 (2016), doi:[10.1103/PhysRevX.6.041049](https://doi.org/10.1103/PhysRevX.6.041049) [preprint
3287 doi:[10.48550/arXiv.1607.03912](https://arxiv.org/abs/1607.03912)].
- 3288 [22] T. Sato, M. Hohenadler and F. F. Assaad, *Dirac fermions with competing orders: Non-*
3289 *Landau transition with emergent symmetry*, Phys. Rev. Lett. **119**, 197203 (2017),
3290 doi:[10.1103/PhysRevLett.119.197203](https://doi.org/10.1103/PhysRevLett.119.197203) [preprint doi:[10.48550/arXiv.1707.03027](https://arxiv.org/abs/1707.03027)].
- 3291 [23] T. Sato, M. Hohenadler, T. Grover, J. McGreevy and F. F. Assaad, *Topological terms on*
3292 *topological defects: A quantum Monte Carlo study*, Phys. Rev. B **104**, L161105 (2021),
3293 doi:[10.1103/PhysRevB.104.L161105](https://doi.org/10.1103/PhysRevB.104.L161105) [preprint doi:[10.48550/arXiv.2005.08996](https://arxiv.org/abs/2005.08996)].
- 3294 [24] Z. Wang, Y. Liu, T. Sato, M. Hohenadler, C. Wang, W. Guo and F. F. As-
3295 *saad, Doping-induced quantum spin Hall insulator to superconductor transition*,
3296 Phys. Rev. Lett. **126**, 205701 (2021), doi:[10.1103/PhysRevLett.126.205701](https://doi.org/10.1103/PhysRevLett.126.205701) [preprint
3297 doi:[10.48550/arXiv.2006.13239](https://arxiv.org/abs/2006.13239)].
- 3298 [25] S. Gazit, M. Randeria and A. Vishwanath, *Emergent Dirac fermions and broken symme-*
3299 *tries in confined and deconfined phases of Z_2 gauge theories*, Nat. Phys. **13**, 484 (2017),
3300 doi:[10.1038/nphys4028](https://doi.org/10.1038/nphys4028) [preprint doi:[10.48550/arXiv.1607.03892](https://arxiv.org/abs/1607.03892)].
- 3301 [26] S. Gazit, F. F. Assaad, S. Sachdev, A. Vishwanath and C. Wang, *Confinement*
3302 *transition of Z_2 gauge theories coupled to massless fermions: Emergent quantum*
3303 *chromodynamics and $SO(5)$ symmetry*, Proc. Natl. Acad. Sci. **115**, E6987 (2018),
3304 doi:[10.1073/pnas.1806338115](https://doi.org/10.1073/pnas.1806338115) [preprint doi:[10.48550/arXiv.1804.01095](https://arxiv.org/abs/1804.01095)].
- 3305 [27] X. Y. Xu, Y. Qi, L. Zhang, F. F. Assaad, C. Xu and Z. Y. Meng, *Monte Carlo study of lat-*
3306 *tice compact quantum electrodynamics with fermionic matter: The parent state of quan-*
3307 *tum phases*, Phys. Rev. X **9**, 021022 (2019), doi:[10.1103/PhysRevX.9.021022](https://doi.org/10.1103/PhysRevX.9.021022) [preprint
3308 doi:[10.48550/arXiv.1807.07574](https://arxiv.org/abs/1807.07574)].
- 3309 [28] M. Hohenadler and F. F. Assaad, *Fractionalized metal in a Falicov-Kimball model*,
3310 Phys. Rev. Lett. **121**, 086601 (2018), doi:[10.1103/PhysRevLett.121.086601](https://doi.org/10.1103/PhysRevLett.121.086601) [preprint
3311 doi:[10.48550/arXiv.1804.05858](https://arxiv.org/abs/1804.05858)].
- 3312 [29] M. Hohenadler and F. F. Assaad, *Orthogonal metal in the Hubbard model with liber-*
3313 *ated slave spins*, Phys. Rev. B **100**, 125133 (2019), doi:[10.1103/PhysRevB.100.125133](https://doi.org/10.1103/PhysRevB.100.125133)
3314 [preprint doi:[10.48550/arXiv.1906.11937](https://arxiv.org/abs/1906.11937)].
- 3315 [30] S. Gazit, F. F. Assaad and S. Sachdev, *Fermi surface reconstruction without symmetry*
3316 *breaking*, Phys. Rev. X **10**, 041057 (2020), doi:[10.1103/PhysRevX.10.041057](https://doi.org/10.1103/PhysRevX.10.041057) [preprint
3317 doi:[10.48550/arXiv.1906.11250](https://arxiv.org/abs/1906.11250)].
- 3318 [31] F. F. Assaad, *Quantum Monte Carlo simulations of the half-filled two-dimensional*
3319 *Kondo lattice model*, Phys. Rev. Lett. **83**, 796 (1999), doi:[10.1103/PhysRevLett.83.796](https://doi.org/10.1103/PhysRevLett.83.796)
3320 [preprint doi:[10.48550/arXiv.cond-mat/9904178](https://arxiv.org/abs/cond-mat/9904178)].

- 3321 [32] S. Capponi and F. F. Assaad, *Spin and charge dynamics of the ferromagnetic and anti-*
3322 *ferromagnetic two-dimensional half-filled Kondo lattice model*, Phys. Rev. B **63**, 155114
3323 (2001), doi:[10.1103/PhysRevB.63.155114](https://doi.org/10.1103/PhysRevB.63.155114) [preprint doi:[10.48550/arXiv.cond-mat/0010393](https://arxiv.org/abs/cond-mat/0010393)].
- 3325 [33] T. Sato, F. F. Assaad and T. Grover, *Quantum Monte Carlo simulation*
3326 *of frustrated Kondo lattice models*, Phys. Rev. Lett. **120**, 107201 (2018),
3327 doi:[10.1103/PhysRevLett.120.107201](https://doi.org/10.1103/PhysRevLett.120.107201) [preprint doi:[10.48550/arXiv.1711.03116](https://arxiv.org/abs/1711.03116)].
- 3328 [34] J. S. Hofmann, F. F. Assaad and T. Grover, *Fractionalized Fermi liquid in a frustrated Kondo*
3329 *lattice model*, Phys. Rev. B **100**, 035118 (2019), doi:[10.1103/PhysRevB.100.035118](https://doi.org/10.1103/PhysRevB.100.035118)
3330 [preprint doi:[10.48550/arXiv.1807.08202](https://arxiv.org/abs/1807.08202)].
- 3331 [35] B. Danu, F. F. Assaad and F. Mila, *Exploring the Kondo effect of an extended impurity*
3332 *with chains of Co adatoms in a magnetic field*, Phys. Rev. Lett. **123**, 176601 (2019),
3333 doi:[10.1103/PhysRevLett.123.176601](https://doi.org/10.1103/PhysRevLett.123.176601) [preprint doi:[10.48550/arXiv.1903.08622](https://arxiv.org/abs/1903.08622)].
- 3334 [36] B. Danu, M. Vojta, F. F. Assaad and T. Grover, *Kondo breakdown in a spin-1/2*
3335 *chain of adatoms on a Dirac semimetal*, Phys. Rev. Lett. **125**, 206602 (2020),
3336 doi:[10.1103/PhysRevLett.125.206602](https://doi.org/10.1103/PhysRevLett.125.206602) [preprint doi:[10.48550/arXiv.2005.10278](https://arxiv.org/abs/2005.10278)].
- 3337 [37] Y. Schattner, S. Lederer, S. A. Kivelson and E. Berg, *Ising nematic quantum critical*
3338 *point in a metal: A Monte Carlo study*, Phys. Rev. X **6**, 031028 (2016),
3339 doi:[10.1103/PhysRevX.6.031028](https://doi.org/10.1103/PhysRevX.6.031028) [preprint doi:[10.48550/arXiv.1511.03282](https://arxiv.org/abs/1511.03282)].
- 3340 [38] O. Grossman, J. S. Hofmann, T. Holder and E. Berg, *Specific heat of a quantum criti-*
3341 *cal metal*, Phys. Rev. Lett. **127**, 017601 (2021), doi:[10.1103/PhysRevLett.127.017601](https://doi.org/10.1103/PhysRevLett.127.017601)
3342 [preprint doi:[10.48550/arXiv.2009.11280](https://arxiv.org/abs/2009.11280)].
- 3343 [39] X. Y. Xu, K. Sun, Y. Schattner, E. Berg and Z. Y. Meng, *Non-Fermi liquid at*
3344 *(2 + 1)D ferromagnetic quantum critical point*, Phys. Rev. X **7**, 031058 (2017),
3345 doi:[10.1103/PhysRevX.7.031058](https://doi.org/10.1103/PhysRevX.7.031058) [preprint doi:[10.48550/arXiv.1612.06075](https://arxiv.org/abs/1612.06075)].
- 3346 [40] Z. H. Liu, G. Pan, X. Y. Xu, K. Sun and Z. Y. Meng, *Itinerant quantum critical*
3347 *point with fermion pockets and hotspots*, Proc. Natl. Acad. Sci. **116**, 16760 (2019),
3348 doi:[10.1073/pnas.1901751116](https://doi.org/10.1073/pnas.1901751116) [preprint doi:[10.48550/arXiv.1808.08878](https://arxiv.org/abs/1808.08878)].
- 3349 [41] E. Berg, M. A. Metlitski and S. Sachdev, *Sign-problem-free quantum Monte*
3350 *Carlo of the onset of antiferromagnetism in metals*, Science **338**, 1606 (2012),
3351 doi:[10.1126/science.1227769](https://doi.org/10.1126/science.1227769) [preprint doi:[10.48550/arXiv.1206.0742](https://arxiv.org/abs/1206.0742)].
- 3352 [42] H.-K. Tang, X. Yang, J. Sun and H.-Q. Lin, *Berezinskii-Kosterlitz-Thouless phase transition*
3353 *of spin-orbit coupled Fermi gas in optical lattice*, Europhys. Lett. **107**, 40003 (2014),
3354 doi:[10.1209/0295-5075/107/40003](https://doi.org/10.1209/0295-5075/107/40003).
- 3355 [43] J. S. Hofmann, E. Berg and D. Chowdhury, *Superconductivity, pseudogap, and*
3356 *phase separation in topological flat bands*, Phys. Rev. B **102**, 201112 (2020),
3357 doi:[10.1103/PhysRevB.102.201112](https://doi.org/10.1103/PhysRevB.102.201112) [preprint doi:[10.48550/arXiv.1912.08848](https://arxiv.org/abs/1912.08848)].
- 3358 [44] V. Peri, Z.-D. Song, B. A. Bernevig and S. D. Huber, *Fragile topology and flat-band*
3359 *superconductivity in the strong-coupling regime*, Phys. Rev. Lett. **126**, 027002 (2021),
3360 doi:[10.1103/PhysRevLett.126.027002](https://doi.org/10.1103/PhysRevLett.126.027002) [preprint doi:[10.48550/arXiv.2008.02288](https://arxiv.org/abs/2008.02288)].
- 3361 [45] F. F. Assaad, *Phase diagram of the half-filled two-dimensional SU(N) Hubbard-*
3362 *Heisenberg model: A quantum Monte Carlo study*, Phys. Rev. B **71**, 075103 (2005),
3363 doi:[10.1103/PhysRevB.71.075103](https://doi.org/10.1103/PhysRevB.71.075103) [preprint doi:[10.48550/arXiv.cond-mat/0406074](https://arxiv.org/abs/cond-mat/0406074)].

- 3364 [46] T. C. Lang, Z. Y. Meng, A. Muramatsu, S. Wessel and F. F. Assaad, *Dimerized solids and*
3365 *resonating plaquette order in $SU(N)$ -Dirac fermions*, Phys. Rev. Lett. **111**, 066401 (2013),
3366 doi:[10.1103/PhysRevLett.111.066401](https://doi.org/10.1103/PhysRevLett.111.066401) [preprint doi:[10.48550/arXiv.1306.3258](https://doi.org/10.48550/arXiv.1306.3258)].
- 3367 [47] F. H. Kim, K. Penc, P. Nataf and F. Mila, *Linear flavor-wave theory for fully anti-*
3368 *symmetric $SU(N)$ irreducible representations*, Phys. Rev. B **96**, 205142 (2017),
3369 doi:[10.1103/PhysRevB.96.205142](https://doi.org/10.1103/PhysRevB.96.205142) [preprint doi:[10.48550/arXiv.1711.05089](https://doi.org/10.48550/arXiv.1711.05089)].
- 3370 [48] D. Wang, Y. Li, Z. Cai, Z. Zhou, Y. Wang and C. Wu, *Competing orders in the 2D half-*
3371 *filled $SU(2N)$ Hubbard model through the pinning-field quantum Monte Carlo simulations*,
3372 Phys. Rev. Lett. **112**, 156403 (2014), doi:[10.1103/PhysRevLett.112.156403](https://doi.org/10.1103/PhysRevLett.112.156403) [preprint
3373 doi:[10.48550/arXiv.1305.3571](https://doi.org/10.48550/arXiv.1305.3571)].
- 3374 [49] F. H. Kim, F. F. Assaad, K. Penc and F. Mila, *Dimensional crossover in the $SU(4)$ Heisen-*
3375 *berg model in the six-dimensional antisymmetric self-conjugate representation revealed by*
3376 *quantum Monte Carlo and linear flavor-wave theory*, Phys. Rev. B **100**, 085103 (2019),
3377 doi:[10.1103/PhysRevB.100.085103](https://doi.org/10.1103/PhysRevB.100.085103) [preprint doi:[10.48550/arXiv.1906.06938](https://doi.org/10.48550/arXiv.1906.06938)].
- 3378 [50] M. Raczkowski and F. F. Assaad, *Phase diagram and dynamics of the*
3379 *$SU(N)$ symmetric Kondo lattice model*, Phys. Rev. Res. **2**, 013276 (2020),
3380 doi:[10.1103/PhysRevResearch.2.013276](https://doi.org/10.1103/PhysRevResearch.2.013276) [preprint doi:[10.48550/arXiv.1910.07540](https://doi.org/10.48550/arXiv.1910.07540)].
- 3381 [51] M. Hohenadler, F. P. Toldin, I. F. Herbut and F. F. Assaad, *Phase diagram of the Kane-Mele-*
3382 *Coulomb model*, Phys. Rev. B **90**, 085146 (2014), doi:[10.1103/PhysRevB.90.085146](https://doi.org/10.1103/PhysRevB.90.085146)
3383 [preprint doi:[10.48550/arXiv.1407.2708](https://doi.org/10.48550/arXiv.1407.2708)].
- 3384 [52] H.-K. Tang, E. Laksono, J. N. B. Rodrigues, P. Sengupta, F. F. Assaad and
3385 S. Adam, *Interaction-driven metal-insulator transition in strained graphene*, Phys.
3386 Rev. Lett. **115**, 186602 (2015), doi:[10.1103/PhysRevLett.115.186602](https://doi.org/10.1103/PhysRevLett.115.186602) [preprint
3387 doi:[10.48550/arXiv.1505.04188](https://doi.org/10.48550/arXiv.1505.04188)].
- 3388 [53] H.-K. Tang, J. N. Leaw, J. N. B. Rodrigues, I. F. Herbut, P. Sengupta, F. F. As-
3389 saad and S. Adam, *The role of electron-electron interactions in two-dimensional*
3390 *Dirac fermions*, Science **361**, 570 (2018), doi:[10.1126/science.aao2934](https://doi.org/10.1126/science.aao2934) [preprint
3391 doi:[10.48550/arXiv.1808.03648](https://doi.org/10.48550/arXiv.1808.03648)].
- 3392 [54] M. Raczkowski and F. F. Assaad, *Interplay between the edge-state magnetism and long-*
3393 *range Coulomb interaction in zigzag graphene nanoribbons: Quantum Monte Carlo*
3394 *study*, Phys. Rev. B **96**, 115155 (2017), doi:[10.1103/PhysRevB.96.115155](https://doi.org/10.1103/PhysRevB.96.115155) [preprint
3395 doi:[10.48550/arXiv.1707.02065](https://doi.org/10.48550/arXiv.1707.02065)].
- 3396 [55] J. N. Leaw, H.-K. Tang, P. Sengupta, F. F. Assaad, I. F. Herbut and S. Adam,
3397 *Electronic ground state in bilayer graphene with realistic Coulomb interactions*,
3398 Phys. Rev. B **100**, 125116 (2019), doi:[10.1103/PhysRevB.100.125116](https://doi.org/10.1103/PhysRevB.100.125116) [preprint
3399 doi:[10.48550/arXiv.1903.06177](https://doi.org/10.48550/arXiv.1903.06177)].
- 3400 [56] M. Rigol, A. Muramatsu, G. G. Batrouni and R. T. Scalettar, *Local quantum*
3401 *criticality in confined fermions on optical lattices*, Phys. Rev. Lett. **91**, 130403
3402 (2003), doi:[10.1103/PhysRevLett.91.130403](https://doi.org/10.1103/PhysRevLett.91.130403) [preprint doi:[10.48550/arXiv.cond-mat/0304028](https://doi.org/10.48550/arXiv.cond-mat/0304028)].
- 3404 [57] D. Lee, *Lattice simulations for few- and many-body systems*, Prog. Part.
3405 Nucl. Phys. **63**, 117 (2009), doi:[10.1016/j.ppnp.2008.12.001](https://doi.org/10.1016/j.ppnp.2008.12.001) [preprint
3406 doi:[10.48550/arXiv.0804.3501](https://doi.org/10.48550/arXiv.0804.3501)].

- 3407 [58] Z. Wang, F. F. Assaad and F. P. Toldin, *Finite-size effects in canonical and grand-canonical*
3408 *quantum Monte Carlo simulations for fermions*, Phys. Rev. E **96**, 042131 (2017),
3409 doi:[10.1103/PhysRevE.96.042131](https://doi.org/10.1103/PhysRevE.96.042131) [preprint doi:[10.48550/arXiv.1706.01874](https://arxiv.org/abs/1706.01874)].
- 3410 [59] T. Shen, Y. Liu, Y. Yu and B. M. Rubenstein, *Finite temperature auxiliary field quantum*
3411 *Monte Carlo in the canonical ensemble*, J. Chem. Phys. **153**, 204108 (2020),
3412 doi:[10.1063/5.0026606](https://doi.org/10.1063/5.0026606) [preprint doi:[10.48550/arXiv.2010.09813](https://arxiv.org/abs/2010.09813)].
- 3413 [60] T. Grover, *Entanglement of interacting fermions in quantum Monte Carlo calculations*,
3414 Phys. Rev. Lett. **111**, 130402 (2013), doi:[10.1103/PhysRevLett.111.130402](https://doi.org/10.1103/PhysRevLett.111.130402) [preprint
3415 doi:[10.48550/arXiv.1307.1486](https://arxiv.org/abs/1307.1486)].
- 3416 [61] P. Broecker and S. Trebst, *Rényi entropies of interacting fermions from determinantal*
3417 *quantum Monte Carlo simulations*, J. Stat. Mech.: Theory Exp. P08015 (2014),
3418 doi:[10.1088/1742-5468/2014/08/p08015](https://doi.org/10.1088/1742-5468/2014/08/p08015).
- 3419 [62] F. F. Assaad, T. C. Lang and F. P. Toldin, *Entanglement spectra of interacting*
3420 *fermions in quantum Monte Carlo simulations*, Phys. Rev. B **89**, 125121 (2014),
3421 doi:[10.1103/PhysRevB.89.125121](https://doi.org/10.1103/PhysRevB.89.125121) [preprint doi:[10.48550/arXiv.1311.5851](https://arxiv.org/abs/1311.5851)].
- 3422 [63] F. F. Assaad, *Stable quantum Monte Carlo simulations for entanglement spectra of interacting*
3423 *fermions*, Phys. Rev. B **91**, 125146 (2015), doi:[10.1103/PhysRevB.91.125146](https://doi.org/10.1103/PhysRevB.91.125146)
3424 [preprint doi:[10.48550/arXiv.1501.01418](https://arxiv.org/abs/1501.01418)].
- 3425 [64] F. P. Toldin and F. F. Assaad, *Entanglement Hamiltonian of interacting fermionic models*,
3426 Phys. Rev. Lett. **121**, 200602 (2018), doi:[10.1103/PhysRevLett.121.200602](https://doi.org/10.1103/PhysRevLett.121.200602) [preprint
3427 doi:[10.48550/arXiv.1804.03163](https://arxiv.org/abs/1804.03163)].
- 3428 [65] F. P. Toldin, T. Sato and F. F. Assaad, *Mutual information in heavy-fermion systems*,
3429 Phys. Rev. B **99**, 155158 (2019), doi:[10.1103/PhysRevB.99.155158](https://doi.org/10.1103/PhysRevB.99.155158) [preprint
3430 doi:[10.48550/arXiv.1811.11194](https://arxiv.org/abs/1811.11194)].
- 3431 [66] F. P. Toldin and F. F. Assaad, *Entanglement studies of interacting fermionic models*, J. Phys.:
3432 Conf. Ser. **1163**, 012056 (2019), doi:[10.1088/1742-6596/1163/1/012056](https://doi.org/10.1088/1742-6596/1163/1/012056) [preprint
3433 doi:[10.48550/arXiv.1810.06595](https://arxiv.org/abs/1810.06595)].
- 3434 [67] C. Chen, X. Y. Xu, J. Liu, G. Batrouni, R. Scalettar and Z. Y. Meng,
3435 *Symmetry-enforced self-learning Monte Carlo method applied to the Holstein model*,
3436 Phys. Rev. B **98**, 041102 (2018), doi:[10.1103/PhysRevB.98.041102](https://doi.org/10.1103/PhysRevB.98.041102) [preprint
3437 doi:[10.48550/arXiv.1802.06177](https://arxiv.org/abs/1802.06177)].
- 3438 [68] C. Chen, X. Y. Xu, Z. Y. Meng and M. Hohenadler, *Charge-density-wave transitions of Dirac*
3439 *fermions coupled to phonons*, Phys. Rev. Lett. **122**, 077601 (2019),
3440 doi:[10.1103/PhysRevLett.122.077601](https://doi.org/10.1103/PhysRevLett.122.077601) [preprint doi:[10.48550/arXiv.1809.07903](https://arxiv.org/abs/1809.07903)].
- 3441 [69] O. Bradley, G. G. Batrouni and R. T. Scalettar, *Superconductivity and charge density*
3442 *wave order in the two-dimensional Holstein model*, Phys. Rev. B **103**, 235104 (2021),
3443 doi:[10.1103/PhysRevB.103.235104](https://doi.org/10.1103/PhysRevB.103.235104) [preprint doi:[10.48550/arXiv.2011.11703](https://arxiv.org/abs/2011.11703)].
- 3444 [70] M. Ippoliti, R. S. K. Mong, F. F. Assaad and M. P. Zaletel, *Half-filled Landau levels: A*
3445 *continuum and sign-free regularization for three-dimensional quantum critical points*, Phys. Rev. B **98**, 235108 (2018), doi:[10.1103/PhysRevB.98.235108](https://doi.org/10.1103/PhysRevB.98.235108) [preprint
3446 doi:[10.48550/arXiv.1810.00009](https://arxiv.org/abs/1810.00009)].

- 3448 [71] Z. Wang, M. P. Zaletel, R. S. K. Mong and F. F. Assaad, *Phases of the (2 + 1) dimensional*
3449 *SO(5) nonlinear sigma model with topological term*, Phys. Rev. Lett. **126**, 045701 (2021),
3450 doi:[10.1103/PhysRevLett.126.045701](https://doi.org/10.1103/PhysRevLett.126.045701) [preprint doi:[10.48550/arXiv.2003.08368](https://doi.org/10.48550/arXiv.2003.08368)].
- 3451 [72] G. Pan, W. Wang, A. Davis, Y. Wang and Z. Y. Meng, *Yukawa-SYK model*
3452 *and self-tuned quantum criticality*, Phys. Rev. Res. **3**, 013250 (2021),
3453 doi:[10.1103/PhysRevResearch.3.013250](https://doi.org/10.1103/PhysRevResearch.3.013250) [preprint doi:[10.48550/arXiv.2001.06586](https://doi.org/10.48550/arXiv.2001.06586)].
- 3454 [73] H. Zhang et al., *Coexistence and interaction of spinons and magnons in an antifer-*
3455 *romagnet with alternating antiferromagnetic and ferromagnetic quantum spin chains*,
3456 Phys. Rev. Lett. **125**, 037204 (2020), doi:[10.1103/PhysRevLett.125.037204](https://doi.org/10.1103/PhysRevLett.125.037204) [preprint
3457 doi:[10.48550/arXiv.2006.10922](https://doi.org/10.48550/arXiv.2006.10922)].
- 3458 [74] C. Wu and S.-C. Zhang, *Sufficient condition for absence of the sign problem in*
3459 *the fermionic quantum Monte Carlo algorithm*, Phys. Rev. B **71**, 155115 (2005),
3460 doi:[10.1103/PhysRevB.71.155115](https://doi.org/10.1103/PhysRevB.71.155115) [preprint doi:[10.48550/arXiv.cond-mat/0407272](https://doi.org/10.48550/arXiv.cond-mat/0407272)].
- 3461 [75] E. F. Huffman and S. Chandrasekharan, *Solution to sign problems in half-*
3462 *filled spin-polarized electronic systems*, Phys. Rev. B **89**, 111101 (2014),
3463 doi:[10.1103/PhysRevB.89.111101](https://doi.org/10.1103/PhysRevB.89.111101) [preprint doi:[10.48550/arXiv.1311.0034](https://doi.org/10.48550/arXiv.1311.0034)].
- 3464 [76] Z.-X. Li, Y.-F. Jiang and H. Yao, *Solving the fermion sign problem in quantum Monte*
3465 *Carlo simulations by Majorana representation*, Phys. Rev. B **91**, 241117 (2015),
3466 doi:[10.1103/PhysRevB.91.241117](https://doi.org/10.1103/PhysRevB.91.241117) [preprint doi:[10.48550/arXiv.1408.2269](https://doi.org/10.48550/arXiv.1408.2269)].
- 3467 [77] Z. C. Wei, C. Wu, Y. Li, S. Zhang and T. Xiang, *Majorana positivity and the fermion*
3468 *sign problem of quantum Monte Carlo simulations*, Phys. Rev. Lett. **116**, 250601 (2016),
3469 doi:[10.1103/PhysRevLett.116.250601](https://doi.org/10.1103/PhysRevLett.116.250601) [preprint doi:[10.48550/arXiv.1601.01994](https://doi.org/10.48550/arXiv.1601.01994)].
- 3470 [78] J. Hubbard, *Calculation of partition functions*, Phys. Rev. Lett. **3**, 77 (1959),
3471 doi:[10.1103/PhysRevLett.3.77](https://doi.org/10.1103/PhysRevLett.3.77).
- 3472 [79] M. Troyer and U.-J. Wiese, *Computational complexity and fundamental limita-*
3473 *tions to fermionic quantum Monte Carlo simulations*, Phys. Rev. Lett. **94**, 170201
3474 (2005), doi:[10.1103/PhysRevLett.94.170201](https://doi.org/10.1103/PhysRevLett.94.170201) [preprint doi:[10.48550/arXiv.cond-mat/0408370](https://doi.org/10.48550/arXiv.cond-mat/0408370)].
- 3476 [80] S. Duane and J. B. Kogut, *Hybrid stochastic differential equations applied to quantum*
3477 *chromodynamics*, Phys. Rev. Lett. **55**, 2774 (1985), doi:[10.1103/PhysRevLett.55.2774](https://doi.org/10.1103/PhysRevLett.55.2774).
- 3478 [81] J. E. Hirsch, *Discrete Hubbard-Stratonovich transformation for fermion lattice models*,
3479 Phys. Rev. B **28**, 4059 (1983), doi:[10.1103/PhysRevB.28.4059](https://doi.org/10.1103/PhysRevB.28.4059).
- 3480 [82] A. Sokal, *Monte Carlo methods in statistical mechanics: Foundations and new algo-*
3481 *rithms*, in *Functional integration: Basics and applications*, Springer, Boston, USA, ISBN
3482 9781489903211 (1997), doi:[10.1007/978-1-4612-0319-8_6](https://doi.org/10.1007/978-1-4612-0319-8_6).
- 3483 [83] H. G. Evertz, G. Lana and M. Marcu, *Cluster algorithm for vertex models*, Phys. Rev. Lett.
3484 **70**, 875 (1993), doi:[10.1103/PhysRevLett.70.875](https://doi.org/10.1103/PhysRevLett.70.875) [preprint doi:[10.48550/arXiv.cond-mat/9211006](https://doi.org/10.48550/arXiv.cond-mat/9211006)].
- 3486 [84] A. W. Sandvik, *Stochastic series expansion method with operator-loop update*,
3487 Phys. Rev. B **59**, R14157 (1999), doi:[10.1103/PhysRevB.59.R14157](https://doi.org/10.1103/PhysRevB.59.R14157) [preprint
3488 doi:[10.48550/arXiv.cond-mat/9902226](https://doi.org/10.48550/arXiv.cond-mat/9902226)].

- 3489 [85] O. F. Syljuåsen and A. W. Sandvik, *Quantum Monte Carlo with directed loops*,
3490 Phys. Rev. E **66**, 046701 (2002), doi:[10.1103/PhysRevE.66.046701](https://doi.org/10.1103/PhysRevE.66.046701) [preprint
3491 doi:[10.48550/arXiv.cond-mat/0202316](https://arxiv.org/abs/cond-mat/0202316)].
- 3492 [86] J. E. Hirsch and R. M. Fye, *Monte Carlo method for magnetic impurities in metals*, Phys.
3493 Rev. Lett. **56**, 2521 (1986), doi:[10.1103/PhysRevLett.56.2521](https://doi.org/10.1103/PhysRevLett.56.2521).
- 3494 [87] E. Gull, A. J. Millis, A. I. Lichtenstein, A. N. Rubtsov, M. Troyer and
3495 P. Werner, *Continuous-time Monte Carlo methods for quantum impurity mod-
3496 els*, Rev. Mod. Phys. **83**, 349 (2011), doi:[10.1103/RevModPhys.83.349](https://doi.org/10.1103/RevModPhys.83.349) [preprint
3497 doi:[10.48550/arXiv.1012.4474](https://arxiv.org/abs/1012.4474)].
- 3498 [88] F. F. Assaad, *Continuous-time QMC solvers for electronic systems in fermionic and bosonic*
3499 *baths*, in *DMFT at 25: Infinite dimensions: Lecture notes of the autumn school on cor-
3500 related electrons*, Forschungszentrum Jülich, Jülich, Germany, ISBN 9783893369539
3501 (2014).
- 3502 [89] F. F. Assaad and T. C. Lang, *Diagrammatic determinantal quantum Monte Carlo*
3503 *methods: Projective schemes and applications to the Hubbard-Holstein model*,
3504 Phys. Rev. B **76**, 035116 (2007), doi:[10.1103/PhysRevB.76.035116](https://doi.org/10.1103/PhysRevB.76.035116) [preprint
3505 doi:[10.48550/arXiv.cond-mat/0702455](https://arxiv.org/abs/cond-mat/0702455)].
- 3506 [90] R. T. Scalettar, D. J. Scalapino and R. L. Sugar, *New algorithm for the numerical simula-
3507 tion of fermions*, Phys. Rev. B **34**, 7911 (1986), doi:[10.1103/PhysRevB.34.7911](https://doi.org/10.1103/PhysRevB.34.7911).
- 3508 [91] S. Beyl, F. Goth and F. F. Assaad, *Revisiting the hybrid quantum Monte Carlo*
3509 *method for Hubbard and electron-phonon models*, Phys. Rev. B **97**, 085144 (2018),
3510 doi:[10.1103/PhysRevB.97.085144](https://doi.org/10.1103/PhysRevB.97.085144) [preprint doi:[10.48550/arXiv.1708.03661](https://arxiv.org/abs/1708.03661)].
- 3511 [92] S. Dürr et al., *Ab initio determination of light hadron masses*, Science **322**, 1224 (2008),
3512 doi:[10.1126/science.1163233](https://doi.org/10.1126/science.1163233) [preprint doi:[10.48550/arXiv.0906.3599](https://arxiv.org/abs/0906.3599)].
- 3513 [93] F. F. Assaad, *Quantum Monte Carlo methods on lattices: The determinantal method*,
3514 in *Quantum simulations of complex many-body systems: From theory to algorithms*,
3515 lecture notes, John von Neumann Institute for Computing, Jülich, Germany, ISBN
3516 9783000090578 (2002).
- 3517 [94] Y. Motome and M. Imada, *A quantum Monte Carlo method and its applications to multi-
3518 orbital Hubbard models*, J. Phys. Soc. Jpn. **66**, 1872 (1997), doi:[10.1143/JPSJ.66.1872](https://doi.org/10.1143/JPSJ.66.1872)
3519 [preprint doi:[10.48550/arXiv.cond-mat/9705069](https://arxiv.org/abs/cond-mat/9705069)].
- 3520 [95] F. F. Assaad, M. Imada and D. J. Scalapino, *Charge and spin structures of a $d_{x^2-y^2}$ su-
3521 perconductor in the proximity of an antiferromagnetic Mott insulator*, Phys. Rev. B **56**,
3522 15001 (1997), doi:[10.1103/PhysRevB.56.15001](https://doi.org/10.1103/PhysRevB.56.15001) [preprint doi:[10.48550/arXiv.cond-mat/9706173](https://arxiv.org/abs/cond-mat/9706173)].
- 3524 [96] A. W. Sandvik, *Stochastic method for analytic continuation of quantum Monte Carlo data*,
3525 Phys. Rev. B **57**, 10287 (1998), doi:[10.1103/PhysRevB.57.10287](https://doi.org/10.1103/PhysRevB.57.10287).
- 3526 [97] K. S. D. Beach, *Identifying the maximum entropy method as a special limit of stochastic*
3527 *analytic continuation*, (arXiv preprint) doi:[10.48550/arXiv.cond-mat/0403055](https://arxiv.org/abs/cond-mat/0403055).
- 3528 [98] R. M. Fye, *New results on Trotter-like approximations*, Phys. Rev. B **33**, 6271 (1986),
3529 doi:[10.1103/PhysRevB.33.6271](https://doi.org/10.1103/PhysRevB.33.6271).

- 3530 [99] M. Iazzi and M. Troyer, *Efficient continuous-time quantum Monte Carlo algorithm for fermionic lattice models*, Phys. Rev. B **91**, 241118 (2015),
3531 doi:[10.1103/PhysRevB.91.241118](https://doi.org/10.1103/PhysRevB.91.241118) [preprint doi:[10.48550/arXiv.1411.0683](https://doi.org/10.48550/arXiv.1411.0683)].
- 3533 [100] S. M. A. Rombouts, K. Heyde and N. Jachowicz, *Quantum Monte Carlo method for fermions, free of discretization errors*, Phys. Rev. Lett. **82**, 4155 (1999),
3534 doi:[10.1103/PhysRevLett.82.4155](https://doi.org/10.1103/PhysRevLett.82.4155) [preprint doi:[10.48550/arXiv.cond-mat/9805255](https://doi.org/10.48550/arXiv.cond-mat/9805255)].
- 3536 [101] E. Gull, P. Werner, O. Parcollet and M. Troyer, *Continuous-time auxiliary-field Monte Carlo for quantum impurity models*, Europhys. Lett. **82**, 57003 (2008), doi:[10.1209/0295-5075/82/57003](https://doi.org/10.1209/0295-5075/82/57003).
- 3539 [102] S. Rombouts, K. Heyde and N. Jachowicz, *A discrete Hubbard-Stratonovich decomposition for general, fermionic two-body interactions*, Phys. Lett. A **242**, 271 (1998), doi:[10.1016/S0375-9601\(98\)00197-2](https://doi.org/10.1016/S0375-9601(98)00197-2) [preprint doi:[10.48550/arXiv.cond-mat/9804290](https://doi.org/10.48550/arXiv.cond-mat/9804290)].
- 3543 [103] D. Rost, E. V. Gorelik, F. Assaad and N. Blümer, *Momentum-dependent pseudogaps in the half-filled two-dimensional Hubbard model*, Phys. Rev. B **86**, 155109 (2012),
3544 doi:[10.1103/PhysRevB.86.155109](https://doi.org/10.1103/PhysRevB.86.155109) [preprint doi:[10.48550/arXiv.1205.6788](https://doi.org/10.48550/arXiv.1205.6788)].
- 3546 [104] D. Rost, F. Assaad and N. Blümer, *Quasi-continuous-time impurity solver for the dynamical mean-field theory with linear scaling in the inverse temperature*, Phys. Rev. E **87**, 053305 (2013), doi:[10.1103/PhysRevE.87.053305](https://doi.org/10.1103/PhysRevE.87.053305) [preprint doi:[10.48550/arXiv.1303.2004](https://doi.org/10.48550/arXiv.1303.2004)].
- 3549 [105] N. Blümer, *Multigrid Hirsch-Fye quantum Monte Carlo method for dynamical mean-field theory*, (arXiv preprint) doi:[10.48550/arXiv.0801.1222](https://doi.org/10.48550/arXiv.0801.1222).
- 3551 [106] L. Wang, Y.-H. Liu and M. Troyer, *Stochastic series expansion simulation of the $t-V$ model*, Phys. Rev. B **93**, 155117 (2016), doi:[10.1103/PhysRevB.93.155117](https://doi.org/10.1103/PhysRevB.93.155117) [preprint doi:[10.48550/arXiv.1602.02095](https://doi.org/10.48550/arXiv.1602.02095)].
- 3554 [107] E. Huffman and S. Chandrasekharan, *Fermion bag approach to Hamiltonian lattice field theories in continuous time*, Phys. Rev. D **96**, 114502 (2017),
3555 doi:[10.1103/PhysRevD.96.114502](https://doi.org/10.1103/PhysRevD.96.114502) [preprint doi:[10.48550/arXiv.1709.03578](https://doi.org/10.48550/arXiv.1709.03578)].
- 3557 [108] E. Huffman and S. Chandrasekharan, *Fermion-bag inspired Hamiltonian lattice field theory for fermionic quantum criticality*, Phys. Rev. D **101**, 074501 (2020),
3558 doi:[10.1103/PhysRevD.101.074501](https://doi.org/10.1103/PhysRevD.101.074501) [preprint doi:[10.48550/arXiv.1912.12823](https://doi.org/10.48550/arXiv.1912.12823)].
- 3560 [109] F. Goth, *Higher order auxiliary field quantum Monte Carlo methods*, J. Phys.:
3561 Conf. Ser. **2207**, 012029 (2022), doi:[10.1088/1742-6596/2207/1/012029](https://doi.org/10.1088/1742-6596/2207/1/012029) [preprint
3562 doi:[10.48550/arXiv.2009.04491](https://doi.org/10.48550/arXiv.2009.04491)].
- 3563 [110] I. Peschel, *Calculation of reduced density matrices from correlation functions*, J. Phys. A:
3564 Math. Gen. **36**, L205 (2003), doi:[10.1088/0305-4470/36/14/101](https://doi.org/10.1088/0305-4470/36/14/101).
- 3565 [111] Z.-Q. Wan, S.-X. Zhang and H. Yao, *Mitigating the fermion sign problem by automatic differentiation*, Phys. Rev. B **106**, L241109 (2022), doi:[10.1103/PhysRevB.106.L241109](https://doi.org/10.1103/PhysRevB.106.L241109)
3566 [preprint doi:[10.48550/arXiv.2010.01141](https://doi.org/10.48550/arXiv.2010.01141)].
- 3568 [112] D. Hangleiter, I. Roth, D. Nagaj and J. Eisert, *Easing the Monte Carlo sign
3569 problem*, Sci. Adv. **6**, eabb8341 (2020), doi:[10.1126/sciadv.abb8341](https://doi.org/10.1126/sciadv.abb8341) [preprint
3570 doi:[10.48550/arXiv.1906.02309](https://doi.org/10.48550/arXiv.1906.02309)].

- 3571 [113] J. Liu, Y. Qi, Z. Y. Meng and L. Fu, *Self-learning Monte Carlo method*,
3572 Phys. Rev. B **95**, 041101 (2017), doi:[10.1103/PhysRevB.95.041101](https://doi.org/10.1103/PhysRevB.95.041101) [preprint
3573 doi:[10.48550/arXiv.1610.03137](https://arxiv.org/abs/1610.03137)].
- 3574 [114] X. Y. Xu, Y. Qi, J. Liu, L. Fu and Z. Y. Meng, *Self-learning quantum Monte*
3575 *Carlo method in interacting fermion systems*, Phys. Rev. B **96**, 041119 (2017),
3576 doi:[10.1103/PhysRevB.96.041119](https://doi.org/10.1103/PhysRevB.96.041119) [preprint doi:[10.48550/arXiv.1612.03804](https://arxiv.org/abs/1612.03804)].
- 3577 [115] K. Hukushima and K. Nemoto, *Exchange Monte Carlo method and application to spin glass*
3578 *simulations*, J. Phys. Soc. Jpn. **65**, 1604 (1996), doi:[10.1143/JPSJ.65.1604](https://doi.org/10.1143/JPSJ.65.1604) [preprint
3579 doi:[10.48550/arXiv.cond-mat/9512035](https://arxiv.org/abs/cond-mat/9512035)].
- 3580 [116] C. J. Geyer, *Markov chain Monte Carlo maximum likelihood*, in *Computing science and*
3581 *statistics: Proceedings of the 23rd symposium on the interface*, Interface Foundation of
3582 North America, Fairfax Station, USA (1991).
- 3583 [117] C. W. Gardiner, *Handbook of stochastic methods for physics, chemistry and the nat-*
3584 *ural sciences*, Springer, Berlin, Heidelberg, Germany, ISBN 9783540156079 (1985),
3585 doi:[10.1007/978-3-662-02452-2](https://doi.org/10.1007/978-3-662-02452-2).
- 3586 [118] G. G. Batrouni, G. R. Katz, A. S. Kronfeld, G. P. Lepage, B. Svetitsky and K. G.
3587 Wilson, *Langevin simulations of lattice field theories*, Phys. Rev. D **32**, 2736 (1985),
3588 doi:[10.1103/PhysRevD.32.2736](https://doi.org/10.1103/PhysRevD.32.2736).
- 3589 [119] G. G. Batrouni and R. T. Scalettar, *Langevin simulations of a long-range electron-phonon*
3590 *model*, Phys. Rev. B **99**, 035114 (2019), doi:[10.1103/PhysRevB.99.035114](https://doi.org/10.1103/PhysRevB.99.035114) [preprint
3591 doi:[10.48550/arXiv.1808.08973](https://arxiv.org/abs/1808.08973)].
- 3592 [120] C. Davies, G. Batrouni, G. Katz, A. Kronfeld, P. Lepage, P. Rossi, B. Svetitsky and K.
3593 Wilson, *Langevin simulations of lattice field theories using Fourier acceleration*, J. Stat.
3594 Phys. **43**, 1073 (1986), doi:[10.1007/BF02628331](https://doi.org/10.1007/BF02628331).
- 3595 [121] S. Beyl, *Hybrid quantum Monte Carlo for condensed matter models*, PhD thesis, Julius-
3596 Maximilians-Universität Würzburg, Würzburg, Germany (2020), doi:[10.25972/OPUS-19122](https://doi.org/10.25972/OPUS-19122).
- 3598 [122] E. Loh, J. Gubernatis, R. Scalettar, R. Sugar and S. White, *Stable matrix-multiplication*
3599 *algorithms for low-temperature numerical simulations of fermions*, in *Interacting elec-*
3600 *trons in reduced dimensions*, Springer, Boston, USA, ISBN 9781461278696 (1989),
3601 doi:[10.1007/978-1-4613-0565-1](https://doi.org/10.1007/978-1-4613-0565-1).
- 3602 [123] E. Y. Loh, J. E. Gubernatis, R. T. Scalettar, S. R. White, D. J. Scalapino and R. L. Sugar,
3603 *Numerical stability and the sign problem in the determinant quantum Monte Carlo method*,
3604 Int. J. Mod. Phys. C **16**, 1319 (2005), doi:[10.1142/S0129183105007911](https://doi.org/10.1142/S0129183105007911).
- 3605 [124] Z. Bai, C. Lee, R.-C. Li and S. Xu, *Stable solutions of linear systems involving*
3606 *long chain of matrix multiplications*, Linear Algebra Appl. **435**, 659 (2011),
3607 doi:[10.1016/j.laa.2010.06.023](https://doi.org/10.1016/j.laa.2010.06.023).
- 3608 [125] C. Bauer, *Fast and stable determinant quantum Monte Carlo*, SciPost Phys.
3609 Core **2**, 011 (2020), doi:[10.21468/SciPostPhysCore.2.2.011](https://doi.org/10.21468/SciPostPhysCore.2.2.011) [preprint
3610 doi:[10.48550/arXiv.2003.05286](https://arxiv.org/abs/2003.05286)].
- 3611 [126] J. Demmel and K. Veselić, *Jacobi's method is more accurate than QR*, SIAM J. Matrix
3612 Anal. Appl. **13**, 1204 (1992), doi:[10.1137/0613074](https://doi.org/10.1137/0613074).

- 3613 [127] J. Dongarra, M. Gates, A. Haidar, J. Kurzak, P. Luszczek, S. Tomov and I. Yamazaki,
3614 *The singular value decomposition: Anatomy of optimizing an algorithm for extreme scale*,
3615 SIAM Rev. **60**, 808 (2018), doi:[10.1137/17M1117732](https://doi.org/10.1137/17M1117732).
- 3616 [128] A. van der Sluis, *Condition numbers and equilibration of matrices*, Numer. Math. **14**, 14
3617 (1969), doi:[10.1007/BF02165096](https://doi.org/10.1007/BF02165096).
- 3618 [129] M. Feldbacher and F. F. Assaad, *Efficient calculation of imaginary-time-displaced*
3619 *correlation functions in the projector auxiliary-field quantum Monte Carlo algo-*
3620 *rithm*, Phys. Rev. B **63**, 073105 (2001), doi:[10.1103/PhysRevB.63.073105](https://doi.org/10.1103/PhysRevB.63.073105) [preprint
3621 doi:[10.48550/arXiv.cond-mat/0009447](https://arxiv.org/abs/cond-mat/0009447)].
- 3622 [130] D. Ixert, F. F. Assaad and K. P. Schmidt, *Mott physics in the half-filled Hubbard*
3623 *model on a family of vortex-full square lattices*, Phys. Rev. B **90**, 195133 (2014),
3624 doi:[10.1103/PhysRevB.90.195133](https://doi.org/10.1103/PhysRevB.90.195133) [preprint doi:[10.48550/arXiv.1408.0022](https://arxiv.org/abs/1408.0022)].
- 3625 [131] J. W. Negele and H. Orland, *Quantum many body systems*, Addison-Wesley, Redwood
3626 City, USA, ISBN 9780201125931 (1988).
- 3627 [132] W. Krauth, *Statistical mechanics: Algorithms and computations*, Oxford University Press,
3628 Oxford, UK, ISBN 9780198515364 (2006).
- 3629 [133] C. J. Geyer, *Practical Markov chain Monte Carlo*, Stat. Sci. **7**, 473 (1992),
3630 doi:[10.1214/ss/1177011137](https://doi.org/10.1214/ss/1177011137).
- 3631 [134] R. M. Neal, *Probabilistic inference using Markov chain Monte Carlo methods*, Department
3632 of Computer Science, University of Toronto Toronto, Ontario, Canada (1993), <https://www.cs.columbia.edu/~blei/fogm/2025F/readings/Neal1993.pdf>.
- 3634 [135] M. Bercx, J. S. Hofmann, F. F. Assaad and T. C. Lang, *Spontaneous particle-hole symme-*
3635 *try breaking of correlated fermions on the Lieb lattice*, Phys. Rev. B **95**, 035108 (2017),
3636 doi:[10.1103/PhysRevB.95.035108](https://doi.org/10.1103/PhysRevB.95.035108) [preprint doi:[10.48550/arXiv.1610.03314](https://arxiv.org/abs/1610.03314)].
- 3637 [136] B. Efron and C. Stein, *The Jackknife estimate of variance*, Ann. Stat. **9**, 586 (1981),
3638 doi:[10.1214/aos/1176345462](https://doi.org/10.1214/aos/1176345462).
- 3639 [137] S. Chakravarty, B. I. Halperin and D. R. Nelson, *Low-temperature behavior of*
3640 *two-dimensional quantum antiferromagnets*, Phys. Rev. Lett. **60**, 1057 (1988),
3641 doi:[10.1103/PhysRevLett.60.1057](https://doi.org/10.1103/PhysRevLett.60.1057).
- 3642 [138] M. B. Thompson, *A comparison of methods for computing autocorrelation time*, (arXiv
3643 preprint) doi:[10.48550/arXiv.1011.0175](https://arxiv.org/abs/1011.0175).
- 3644 [139] I. Milat, F. Assaad and M. Sigrist, *Field induced magnetic ordering transition in Kondo*
3645 *insulators*, Eur. Phys. J. B **38**, 571 (2004), doi:[10.1140/epjb/e2004-00154-5](https://doi.org/10.1140/epjb/e2004-00154-5).
- 3646 [140] M. Bercx, T. C. Lang and F. F. Assaad, *Magnetic field induced semimetal-to-canted-*
3647 *antiferromagnet transition on the honeycomb lattice*, Phys. Rev. B **80**, 045412 (2009),
3648 doi:[10.1103/PhysRevB.80.045412](https://doi.org/10.1103/PhysRevB.80.045412) [preprint doi:[10.48550/arXiv.0902.2922](https://arxiv.org/abs/0902.2922)].
- 3649 [141] A. Parola, S. Sorella, M. Parrinello and E. Tosatti, *d-wave, dimer, and chiral*
3650 *states in the two-dimensional Hubbard model*, Phys. Rev. B **43**, 6190 (1991),
3651 doi:[10.1103/PhysRevB.43.6190](https://doi.org/10.1103/PhysRevB.43.6190).
- 3652 [142] J. R. Schrieffer and P. A. Wolff, *Relation between the Anderson and Kondo Hamiltonians*,
3653 Phys. Rev. **149**, 491 (1966), doi:[10.1103/PhysRev.149.491](https://doi.org/10.1103/PhysRev.149.491).

- 3654 [143] T. A. Costi, *Kondo effect in a magnetic field and the magnetoresistivity of Kondo al-*
3655 *loys*, Phys. Rev. Lett. **85**, 1504 (2000), doi:[10.1103/PhysRevLett.85.1504](https://doi.org/10.1103/PhysRevLett.85.1504) [preprint
3656 doi:[10.48550/arXiv.cond-mat/0004302](https://arxiv.org/abs/cond-mat/0004302)].
- 3657 [144] M. Raczkowski and F. F. Assaad, *Emergent coherent lattice behavior in Kondo nanosystems*,
3658 Phys. Rev. Lett. **122**, 097203 (2019), doi:[10.1103/PhysRevLett.122.097203](https://doi.org/10.1103/PhysRevLett.122.097203) [preprint
3659 doi:[10.48550/arXiv.1809.00930](https://arxiv.org/abs/1809.00930)].
- 3660 [145] M. Maltseva, M. Dzero and P. Coleman, *Electron cotunneling into a Kondo lattice*,
3661 Phys. Rev. Lett. **103**, 206402 (2009), doi:[10.1103/PhysRevLett.103.206402](https://doi.org/10.1103/PhysRevLett.103.206402) [preprint
3662 doi:[10.48550/arXiv.0910.1138](https://arxiv.org/abs/0910.1138)].
- 3663 [146] J. D’Emidio, R. Orús, N. Laflorencie and F. de Juan, *Universal features of entangle-*
3664 *ment entropy in the honeycomb Hubbard model*, Phys. Rev. Lett. **132**, 076502 (2024),
3665 doi:[10.1103/PhysRevLett.132.076502](https://doi.org/10.1103/PhysRevLett.132.076502) [preprint doi:[10.48550/arXiv.2211.04334](https://arxiv.org/abs/2211.04334)].
- 3666 [147] G. Pan, Y. D. Liao, W. Jiang, J. D’Emidio, Y. Qi and Z. Y. Meng, *Stable com-*
3667 *putation of entanglement entropy for two-dimensional interacting fermion systems*,
3668 Phys. Rev. B **108**, L081123 (2023), doi:[10.1103/PhysRevB.108.L081123](https://doi.org/10.1103/PhysRevB.108.L081123) [preprint
3669 doi:[10.48550/arXiv.2303.14326](https://arxiv.org/abs/2303.14326)].
- 3670 [148] M. Vekić, J. W. Cannon, D. J. Scalapino, R. T. Scalettar and R. L. Sugar,
3671 *Competition between antiferromagnetic order and spin-liquid behavior in the two-*
3672 *dimensional periodic Anderson model at half filling*, Phys. Rev. Lett. **74**, 2367 (1995),
3673 doi:[10.1103/PhysRevLett.74.2367](https://doi.org/10.1103/PhysRevLett.74.2367) [preprint doi:[10.48550/arXiv.cond-mat/9408026](https://arxiv.org/abs/cond-mat/9408026)].
- 3674 [149] Z.-X. Li, Y.-F. Jiang and H. Yao, *Majorana-time-reversal symmetries: A funda-*
3675 *mental principle for sign-problem-free quantum Monte Carlo simulations*, Phys.
3676 Rev. Lett. **117**, 267002 (2016), doi:[10.1103/PhysRevLett.117.267002](https://doi.org/10.1103/PhysRevLett.117.267002) [preprint
3677 doi:[10.48550/arXiv.1601.05780](https://arxiv.org/abs/1601.05780)].
- 3678 [150] K. S. D. Beach, P. A. Lee and P. Monthoux, *Field-induced antiferromagnetism in the Kondo*
3679 *insulator*, Phys. Rev. Lett. **92**, 026401 (2004), doi:[10.1103/PhysRevLett.92.026401](https://doi.org/10.1103/PhysRevLett.92.026401)
3680 [preprint doi:[10.48550/arXiv.cond-mat/0306336](https://arxiv.org/abs/cond-mat/0306336)].
- 3681 [151] A. Rüegg, S. D. Huber and M. Sigrist, *Z_2 -slave-spin theory for strongly correlated*
3682 *fermions*, Phys. Rev. B **81**, 155118 (2010), doi:[10.1103/PhysRevB.81.155118](https://doi.org/10.1103/PhysRevB.81.155118) [preprint
3683 doi:[10.48550/arXiv.0912.3801](https://arxiv.org/abs/0912.3801)].
- 3684 [152] A. Abendschein and F. F. Assaad, *Temperature dependence of spectral func-*
3685 *tions for the one-dimensional Hubbard model: Comparison with experiments*,
3686 Phys. Rev. B **73**, 165119 (2006), doi:[10.1103/PhysRevB.73.165119](https://doi.org/10.1103/PhysRevB.73.165119) [preprint
3687 doi:[10.48550/arXiv.cond-mat/0601222](https://arxiv.org/abs/cond-mat/0601222)].
- 3688 [153] A. N. Rubtsov, V. V. Savkin and A. I. Lichtenstein, *Continuous-time quan-*
3689 *tum Monte Carlo method for fermions*, Phys. Rev. B **72**, 035122 (2005),
3690 doi:[10.1103/PhysRevB.72.035122](https://doi.org/10.1103/PhysRevB.72.035122) [preprint doi:[10.48550/arXiv.cond-mat/0411344](https://arxiv.org/abs/cond-mat/0411344)].
- 3691 [154] D. Krause and P. Thörnig, *JURECA: General-purpose supercomputer at Jülich Supercom-*
3692 *puting Centre*, J. Large-Scale Res. Facil. **2**, A62 (2016), doi:[10.17815/jlsrf-2-121](https://doi.org/10.17815/jlsrf-2-121).